ADVANCED ELECTRODE MATERIALS FOR ELECTROCHEMICAL SUPERCAPACITORS

By Yisong Su, B.S., M.S.

A Thesis Submitted to the School of Graduate Studies in Partial Fulfillment of the Requirements for the Degree Doctor of Philosophy

DOCTOR OF PHILOSOPHY (2015) McMaster University

Department of Materials Science & Engineering Hamilton, Ontario

TITLE: Advanced Electrode Materials for Electrochemical Supercapacitor

AUTHOR: Yisong Su, M.S., (King Abdullah University of Science and Technology, Thuwal, Saudi Arabia), B.S., (Beihang University, Beijing, China)

SUPERVISOR: Igor Zhitomirsky, Distinguished Engineering Professor, Ph.D., P.Eng.

NUMBER OF PAGES: XXXII, 222

Abstract

Advanced dispersants were discovered for the fabrication of homogeneous suspensions of multi-walled carbon nanotubes (MWCNT), graphene, and manganese dioxide (MnO_2) in both ethanol and water. Thin films of MWCNT, graphene, MnO_2, composite films of MWCNT-MnO_2 and MWCNT-graphene were prepared using electrophoretic deposition (EPD) and electrolytic deposition (ELD) methods. The mechanisms of dispersion and deposition were investigated. Cathodic EPD was achieved for MWCNT and graphene using positively charged dispersants. Co-deposition of MWCNT and MnO_2 was performed using a co-dispersant, which dispersed both MWCNT and MnO_2 in ethanol. Composite films were tested for electrochemical supercapacitor (ES) purposes.

Pulse ELD was used to deposit porous MnO_2 coatings on Ni foam substrates from $KMnO_4$ solutions. Cathodic deposition offered advantages, compared to anodic deposition, because the problems, related to anodic dissolution of metallic substrates, can be avoided. The pulse ON/OFF times had significant influence on the morphology and structure of MnO_2 films, which further determined the capacitive performance. The influence of MnO_2 film thickness on specific capacitance (SC) was investigated.

Porous and conductive vanadium nitride (VN) was synthesized using melamine as a reducing agent. To further improve film conductivity and specific surface area, MWCNT were incorporated into VN matrix during synthesis. VN-MWCNT composite electrodes and VN-MWCNT/MnO_2-MWCNT asymmetric supercapacitor cells were fabricated and tested. The electrodes and cells exhibited excellent electrochemical capacitive performance with good cyclic stability. The asymmetric supercapacitor device showed a

voltage window up to 1.8 V, which was the combination of voltage window of VN-MWCNT (-0.9 V-0 V) and MnO_2-MWCNT (0 V-0.9 V).

Polypyrrole (PPy) coated MWCNT were synthesized in ethanol with ammonium peroxydisulfate (APS) solution as an oxidant. The effects of dopants to PPy morphology and conductivity was investigated. Dopants with electrochemical active groups were selected for the synthesis of PPy nanoparticles, where dopants also contributed to the capacitance of the polymer based materials. Both PPy-MWCNT/PPY-MWCNT symmetric supercapacitors and VN-MWCNT/PPY-MWCNT asymmetric supercapacitors were fabricated and tested, where the voltage windows were 0.9 V for the former and 1.3 V for the later. The increase of voltage window was ascribed to the asymmetric structure and negative voltage window of VN-MWCNT composite.

Key words: colloid, dispersion, electrophoretic deposition, manganese dioxide, polypyrrole, carbon nanotubes, graphene, vanadium nitride, asymmetric, supercapacitor.

Acknowledgement

I hereby sincerely acknowledge all the people who helped and supported me during my Ph.D study, without whom I would not be able to complete this thesis.

Foremost, I express my sincere gratitude to my supervisor, Dr. Igor Zhitomirsky, for his kind guidance, motivation, and continuous financial support on my research, for his patience and tolerance, and for his positive influence to my life. It is an honour working with you and I really enjoy it.

I would like to thank my committee members, Dr. Joey Kish and Dr. Dmitri Malakhow, for their guidance and help to my research, committee meetings, proposal exam, and comprehensive exam. I would also like to thank Dr. Gianluigi Botton, Dr. Adrian Kitai, Dr. Gu Xu, and Dr. Tony Petric for their participating my proposal exam and comprehensive exam. My sincere thanks also go to Dr. Peter Kruse and Dr. Aiping Yu for their attending of my Ph.D. thesis defense.

I have taken several courses during my Ph.D. study and I am thankful to these teachers offered these courses, Dr. Joey Kish, Dr. Gu Xu, Dr. Igor Zhitomirsky, and Dr. James Britten.

Many technicians have helped me testing samples and analyzing results. I am grateful to Steve Koprich for his SEM training, Victoria Jarvis for her XRD training, Steve Kornic for FTIR and UV-vis tests, Frank Gibbs for TGA and DTA tests, Babak Shalchi Amirkhiz and Carmen Andrei for TEM traning.

I thank my fellow groupmates in the laboratory: Dr. Xin Pang, Dr. Yaohui Wang, Mustafa Ata, Yanchao Sun, Lijia Yang, Xiaofei Zhu, Shilei Chen, Kaiyuan Shi, Yangshui Liu, Yeling Zhu, Dan Luo, Parick Wojtal, and Tianshi Zhang for the useful discussions of research projects and presentations, and the fun we have together after work. I appreciate the experience of working together with you.

I will forever be thankful to my family for their support of my study aboard. Final, I would like to thank my wife. She is always there cheering me up and stands by me through good and bad times.

Declaration of Academic Achievements

This dissertation was used to fulfill the requirements of Ph.D. degree. The major research project was undertaken from September 2011 to April 2015.

The author of this dissertation and the supervisor are the major contributor to the presented materials. As the primary author, contributions included but not limited to literature review, proposal and approaches, experiments setup, materials synthesis, film preparation, electrochemical tests, materials characterization, data analysis, and journal paper writing.

The results of this dissertation were published in 9 papers in peer-reviewed journals. The published papers are listed below.

1. Su Y, Zhitomirsky I. Electrophoretic nanotechnology of composite electrodes for electrochemical supercapacitors. Journal of Physical Chemistry B. 2012;117:1563-70.
2. Su Y, Zhitomirsky I. Electrophoretic assembly of organic molecules and composites for electrochemical supercapacitors. Journal of Colloid and Interface Science. 2012;392:247-55.
3. Su Y, Zhitomirsky I. Cataphoretic assembly of cationic dyes and deposition of carbon nanotube and graphene films. Journal of Colloid and Interface Science. 2013;399:46-53.
4. Su Y, Zhitomirsky I. Electrophoretic deposition of graphene, carbon nanotubes and composite films using methyl violet dye as a dispersing agent. Colloids and Surfaces A: Physicochemical and Engineering Aspects. 2013;436:97-103.

5. Su Y, Zhitomirsky I. Hybrid MnO_2/carbon nanotube-VN/carbon nanotube supercapacitors. Journal of Power Sources. 2014;267:235-42.
6. Su Y, Zhitomirsky I. Pulse Electrosynthesis of MnO_2 Electrodes for Supercapacitors. Advanced Engineering Material. 2014;16:760-6.
7. Su Y, Zhitomirsky I. Asymmetric electrochemical supercapacitor, based on polypyrrole coated carbon nanotube electrodes. Applied Energy. 2014;(in press).
8. Su Y, Zhitomirsky I. Influence of Dopants on Performance of Polypyrrole Coated Carbon Nanotube Electrodes and Devices. Journal of the Electrochemical Society. 2015;162:A5013-A9

In addition to the work presented here, I co-authored and contributed to one peer-reviewed publication relevant to this thesis in the course of my graduate studies.

9. Shi K, Su Y, Zhitomirsky I. Characterization of Ni plaque based polypyrrole electrodes prepared by pulseelectropolymerization. Materials Letter. 2013;96:135-8.

Table of Contents

List of Figures

List of Tables

List of Abbreviations and Symbols

A (unit)	Ampere
AC	Activated Carbon
AHDA	4-Amino-5-Hydroxynaphthalene-2,7-Disulfonic Acid Monosodium Salt Hydrate (AHDA)
APS	Ammonium Peroxydisulfate
aq.	Aqueous
C	Capacitor
C (unit)	Coulumb
CCA	Calconcarboxylic Acid
C_{dl}	Double-layer capacitance
CFB	Chromotrope FB
CHR-BS	Sulfonazo III Sodium Salt
C_m	Mass normalized specific capacitance
cm (unit)	Centimeter
CNT	Carbon Nanotubes
C_s	Areal normalized specific capacitance
CV	Cyclic Voltammetry

C_{φ}	Pseudocapacitance
DAGB	Diamine Green Black
DTA	Differential Thermal Analysis
E_d	Energy density
EDLC	Electrochemical Double Layer Capacitor
EIS	Electrochemical Impedance Spectroscopy
ELD	Electrolytic Deposition
EPD	Electrophoretic Deposition
ES	Electrochemical Supercapacitors
ESR	Equivalent Series Resistance
F	Faraday constant (96 485 F mol-1)
F (unit)	Farad
FTIR	Fourier transform infrared Spectroscopy
g (unit)	Gram
h (unit)	Hour
IHP	Inner Helmholtz Plane (IHP)
kg (unit)	Kilogram
L (unit)	Liter
Li-ion	Lithium-ion Battery

M (unit)	Mole per liter
mM (unit)	Millimole per liter
m (unit)	Meter
mg (unit)	Milligram
min (unit)	Minute
mL (unit)	Millilitre
MV	Methyl Violet
mV (unit)	Millivoltage
MWCNT	Multi-walled Carbon Nanotubes
Ni-MH	Nickel-Metal Hydride Battery
nm (unit)	Nanometer
OHP	Outer Helmholtz Plane (OHP)
PAni	Polyaniline
PBH	1-Pyrenebutyric Acid
P_d	Power density
PEDOT	Poly(3,4-ethylenedioxythiophene)
PNMA	Poly(n-methyl aniline)
PPy	Polypyrrole
PTh	Poly(thiophene)

PVB	Polyvinyl butyral
p.z.c.	Point of zero charge
Q	Electric charge
QCM	Quartz Crystal Microbalance
R	Ideal Gas Constant (8.314 J mol^{-1} K^{-1})
R_f	Faradaic leakage resistance
S (unit)	Siemens
s (unit)	Second
SC	Specific Capacitance
SEM	Scanning Electron Microscope
SPADNS	Sulfanilic Acid Azochromotrop
T	Absolute temperature (K)
TEM	Transmission Electron Microscope
TGA	Thermogravimetric Analysis
UV-vis	Ultraviolet-Visible Spectroscopy
V (unit)	Voltage
V_A	Attraction energy
V_R	Repulsion energy
V_T	Total internal energy

W (unit)	Watt
Wh (unit)	Watt-hour
XRD	X-Ray Diffraction
Ω (unit)	Ohm
π	Pi (3.1416)
ξ	Zeta potential
μm (unit)	Micrometer
μV (unit)	Micro voltage
℃ (unit)	Celsius degree

Chapter 1 Introduction

The concern of the depletion of fossil energy results in vast interest in technologies in renewable energy such as solar cells, wind farms, tidal electricity generations etc.[1, 2] For the discontinuous producing of electricity and uneven electricity usage during a day, efficient and reliable energy storage systems are needed.[3] With the development of electric vehicles and hybrid vehicles, energy storage systems need to meet high capacity and high power to satisfy the requirements for mileage and speed. Batteries and supercapacitors are in the front line of electrochemical energy storage systems. In past decades, spectacular advances in electrochemistry resulted in the invention of lithium ion (Li-ion) batteries and nickel-metal hydride (Ni-MH) batteries.[4, 5] These new batteries have both high energy density and power density and hence widely used in many fields such as vehicles, computers, portable entertainment and telecommunication devices. Electrochemical supercapacitors (ES) have also been undergoing decades development since the conception was proposed by Conway B.E. in 1970s but with much less attraction from electrochemical community until very recently.[6] The uprising of investigations in ES was caused from the need in improvement of power of batteries,[3] which is desperately needed for many applications such as flash light in cameras, hybrid and electric vehicles. ES intrinsically have the ability of high power density, even though its energy density is one magnitude less than that of Li-ion battery (Fig.1.1). The coupling of battery and supercapacitor can provide steady energy supply and peak power demands. Electrochemical double-layer capacitors (EDLC) have advantages of the use of low cost and environmental friendly raw materials and extremely long cycle life etc.[7]

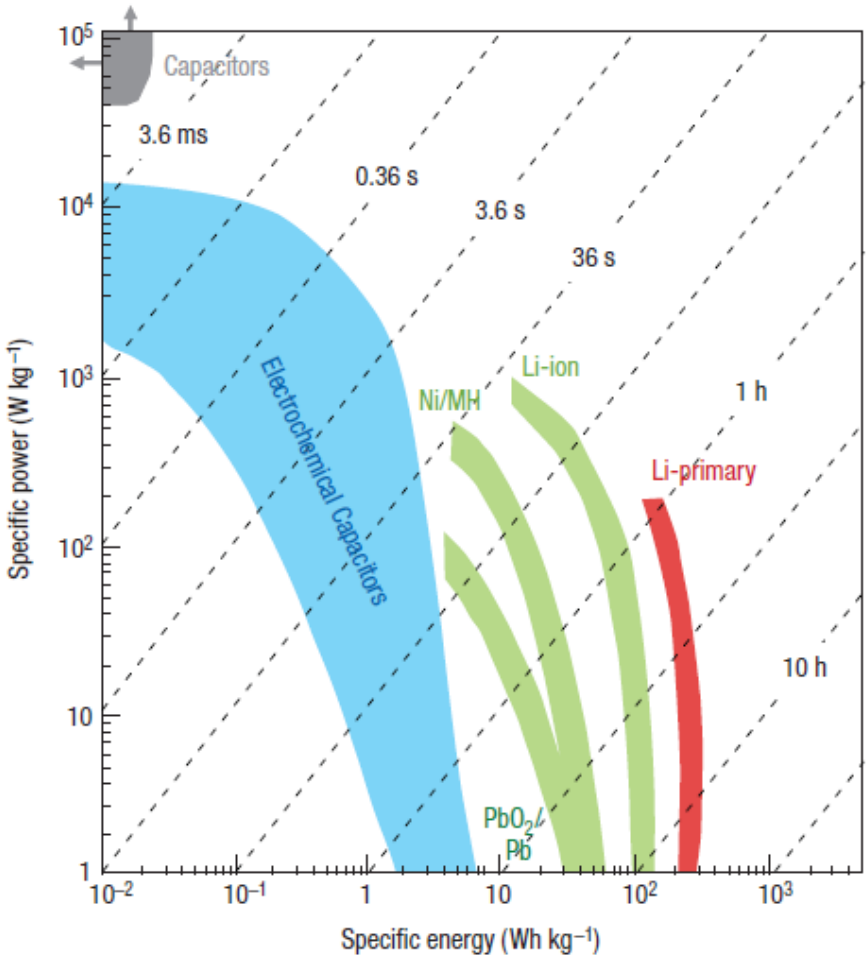

Fig.1.1 Specific power against specific energy, also called a Ragone plot, for various electrical energy storage devices.[3]

The total capacitance of ES is determined by two different energy storage mechanisms, double-layer capacitance and pseudocapacitance. The double-layer capacitance origins from electrostatic storage of separated charges at Helmholtz double layers, where one layer at electrode surface and another layer in electrolyte. Pseudocapacitance is caused by redox reaction where electrons transfer between electrolyte and electrode in a faradaic process. The total capacitance is estimated to be the sum of double-layer capacitance and pseudocapacitance. However, one of these two mechanisms always dominates the total

capacitance, such as double-layer capacitance for carbon electrodes including activated carbon (AC), carbon nanotubes (CNT), graphene etc., and pseudocapacitance for transition metal oxide and conducting polymers, such as MnO_2, RuO_2, NiO, polyaniline, polypyrrole etc. Carbon materials have advantages in specific surface area and conductivity. On the other hand, pseudocapacitive materials have high specific capacitance (SC). Therefore, it is beneficial to utilize both high surface area and conductivity of carbon materials and high SC of pseudocapacitive materials by combining them together to form composite materials.

The surface area and conductivity of carbon materials and SC of pseudocapacitive materials have to be maintained during synthesis to optimize capacitive performance. Carbon materials and pseudocapacitive materials can form morphologies of either nanoscale mixtures or core-shell structures, which provide highest contacting surface between carbon materials and pseudocapacitive materials. Electrophoretic deposition (EPD) is a promising method for the fabrication of composites with morphology of nanoscale mixture and *in situ* chemical synthesis is a good method to synthesize core-shell structures. To achieve these morphologies, both carbon materials and pseudocapacitive materials are needed to be dispersed into solvent homogeneously. Criteria in choosing dispersants for CNT, graphene, and other pseudocapacitive materials must be developed. It is important to note that some dispersants for CNT can cause dramatic aggregation and agglomeration of MnO_2 nanoparticles, therefore co-deposition of CNT and MnO_2 couldn't be achieved.

ES includes both anode and cathode immersed in electrolyte and separated by a membrane separator. Symmetric ES include the same anode and cathode materials, while

asymmetric ES has two different materials for anode and cathode. To achieve the best capacitive performance, the capacitance of cathode and anode must be matched to equal each other. Pseudocapacitive oxide materials, such as MnO_2 and RuO_2 are under investigation for applications in anodes, while the most important materials for cathode are carbons (e.g. AC, CNT, graphene). Pseudocapacitive materials have great advantage in SC but carbon materials have much better capacitance retention, which makes it very difficult to balance the capacitance of both anode and cathode in whole charge/discharge rates range. The low SC and density of carbon materials make the cathode much larger and heavier than anode, so the gravimetric and volumetric capacitance of whole device are substantially reduced. Therefore advanced cathode materials must be found to fit the SC and retention of anode made of pseudocapacitive materials.

In this investigation, advanced dispersants were discovered and chosen for dispersing CNT, graphene, polypyrrole (PPy), and MnO_2 in water and ethanol solvents. Advanced dispersants were developed for co-dispersion of different materials, such as MnO_2, CNT and graphene. In the synthesis of electrochemically active materials, dispersants also played roles of sacrificing agents in synthesis of MnO_2 and dopants for PPy to improve its capacitive performance. The morphologies obtained at different conditions were analyzed and optimized in order to achieve the best electrochemical performance. MnO_2 nanoparticles and CNT were mixed together on the nanoscale using co-dispersants and the films prepared by EPD method from the mixed suspensions showed good capacitive performance. PPy was coated on the surface of CNT using additives which could disperse CNT in ethanol and work as dopant for PPy. Vanadium nitride was chosen as cathode material for the fabrication of MnO_2/VN asymmetric supercapacitor and PPy/VN

asymmetric supercapacitor. The capacitance of both anode and cathode and capacitance retention in whole charge/discharge rates range were fitted very well.

References

[1] Dai S, Ren D, Chou C-L, Finkelman RB, Seredin VV, Zhou Y. Geochemistry of trace elements in Chinese coals: A review of abundances, genetic types, impacts on human health, and industrial utilization. International Journal of Coal Geology 2012;94:3-21.

[2] Dresselhaus MS, Thomas IL. Alternative energy technologies. Nature. 2001;414:332-7.

[3] Simon P, Gogotsi Y. Materials for electrochemical capacitors. Nature Materials 2008;7:845-54.

[4] Tarascon JM, Armand M. Issues and challenges facing rechargeable lithium batteries. Nature. 2001;414:359-67.

[5] Yürüm Y. Hydrogen energy system: production and utilization of hydrogen and future aspects: Springer; 1995.

[6] Conway BE. Electrochemical supercapacitors: scientific fundamentals and technological applications: Springer US; 1999.

[7] Jayalakshmi M, Balasubramanian K. Simple capacitors to supercapacitors - an overview. International Journal of Electrochemical Science 2008;3:1196-217.

Chapter 2 Literature Review

2.1 The development of capacitors and supercapacitors

From the ancient Greece story of rubbed amber with fur attracting dust to the invention of Leyden jar in the middle 18 century, which was credited as the first artificial capacitor, human being spent thousands years in understanding the mechanism of static electricity. Benjamin Franklin improved the design of Leyden jar to flat capacitor during his work on electricity, which substantially reduced capacitor volume and increased convenience and reliability. In 1881, von Helmholtz reached a key conclusion that Faraday's laws implied that a fundamental unit of electrical charge was universally involved.[1] His great contribution paved the way for development of the quantitative and more fundamental science of electrochemistry and for a quantitative science of the electrical nature of matter.

The principle that a capacitor can store electrical energy has been known from 1745. If a voltage is applied to a two-plate capacitor, a charge of +Q on positive plate and a charge of -Q on negative plate are accumulated, where the stored energy (E) is ½ CV^2, where C is the capacitance of this capacitor. The proposal of using this principle for storing electrical energy was firstly claimed and patented by Becker in 1957, in which two porous carbon electrodes and aqueous electrolyte was used and the capacitance of double layer, C_{dl}, arose from the electrode/electrolyte interfaces.[2] This capacitor is lately categorized into EDLC, where carbon is ideal material for it. Carbon black and amorphous carbon have such a high surface to volume ratio that the SC of carbon can reach as high as 200 F g^{-1}.[3] Carbon can also provide good mechanical integrity and is

unreactive in many electrolytes and has ideal capacitative behavior in a large potential voltage range (~ 1.0 V in aqueous electrolyte and ~ 3.5 V in non-aqueous electrolyte).[4]

A different principle of developing ES was originated from 1975 by Conway in Ottawa[5], which based on the concept developed by D. Craig. The new ES is called "pseudocapacitor", where "pseudocapacitance", C_{φ}, arise from the potential dependence of electrochemical adsorption or electrochemical deposition. Then potential dependence of oxide redox systems is also discovered and utilized for pseudocapacitor, especially those with large degree of reversibility and high cyclability (higher than 10^5 cycles).

For pseudocapacitor, there is a continuous dependence of charge, Q, from Faradaic oxidation or reduction, upon the electrode potential, V, where the derivative (dQ/dV) corresponding to the pseudocapacitance, C_{φ}, which is directly measurable and utilizable.

Compared with conventional capacitors, EDLC and pseudocapacitor have a capacitance of as high as tens of Farads, rather than mF, in a very small area or volume, e.g., 1 cm^2 or cm^3. For this reason, the terms "supercapacitor" or "ultracapacitor" was used for these two types of devices. Recently, a more general term "electrochemical capacitors" has been used to refer these systems.

2.2 Classification of capacitors

The capacitors can be generally classified as follows: (i) electrostatic capacitors, (ii) electrolytic capacitor, (iii) EDLC, (iv) ES based on pseudocapacitance, and (v) hybrid supercapacitor, in aspects of energy storage mechanism, capacitor construction, and electrode materials. The classification is in general and the differences of different categories are not strict.

(i) Electrostatic capacitors

An electrostatic capacitor is composed by two metal electrodes paralleling to each other and separated by a dielectric (Fig.2.1). The dielectric is an insulator inserted between two metal plates. The strength of dielectric determines the potential field the capacitor can endure. The field over this value can breakdown the capacitor, causing permanent damage. So a proper dielectric is critical for a capacitor, for example, air has a dielectric strength of 3×10^6 V m^{-1} and paper has a dielectric strength around 16×10^6 V m^{-1}. The increase of dielectric strength can improve the operating voltage window of a capacitor and hence more charges can be stored in two metal plates. The capacitance (C) with unit of Farad (F) is defined as the ratio between charges (Q) with unit of coulomb on plate and the potential difference (U), C=Q/C.

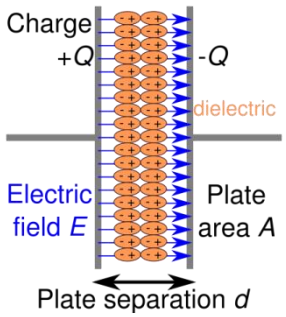

Fig.2.1 Schematic illustration of charged electrostatic capacitor with a plate area of A, distance between two plate of d and surface charge of Q and a dielectric inserted between two plates.

(ii) Electrolytic capacitor

Different from conventional capacitor, electrolyte was used to be one electrode for electrolytic capacitor to achieve high capacitance. The construction of electrolytic capacitor was shown in Fig.2.2, which included two conducting metal foils, where one of

them was coated with a layer of insulating oxide to work as dielectric. A piece of paper soaked in electrolyte was used as a spacer. The foil with an oxide layer works as anode. The electrolyte and the other foil worked as cathode. The most used metal for electrolytic capacitor is aluminum, where the aluminum oxide has a dielectric constant of ~ 10, which is much larger than polymer insulators. The dielectric strength of aluminum oxide is ~ 25 $\times 10^6$ V m^{-1}.[6] For the electrolyte aspect, boric acid and sodium borate are commonly used as electrolytes for electrolytic capacitor, usually with adding of sugar or ethylene glycol to suppress evaporation. The capacitance of electrolytic capacitance varies from less than 1 μF to ~ 1 F with working voltage up to several hundred volts. Due to its large working voltage and capacitance, it has much larger energy density than conventional capacitor.

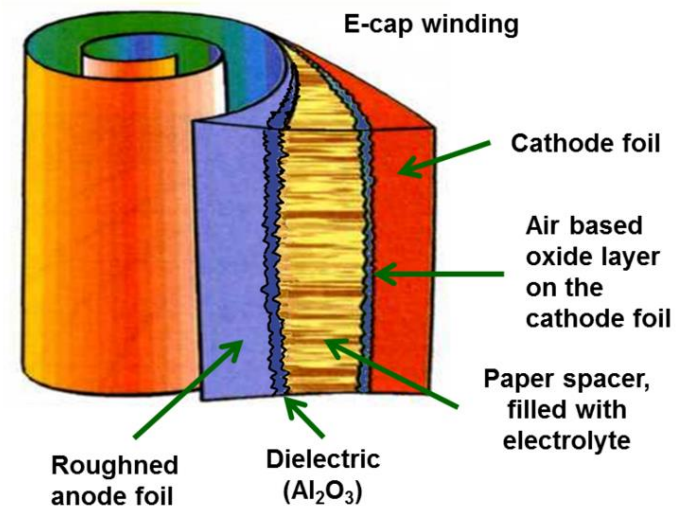

Fig.2.2 Diagram of electrolytic capacitor showing internal construction

(iii) Electrochemical Double Layer Capacitor

Double layer capacitance was firstly researched and proposed by von Helmholtz in 19th century. The Fig.2.3c schematically illustrated the double-layer interface model

(Grahame model),[7] which is a combination of two different charges distribution models, Helmholtz model (Fig.2.3a) and Gouy–Chapman point charge model (Fig.2.3b), which is also called diffusing layer. Between ion layer and electrode surface, one layer or multiple layers of solvents, highly oriented and polarized, attached on the electrode surface. In the new model, the Helmholtz layer was separated into two different layers. The inner layer, from electrode surface to compactly attached solvent layer, was named Inner Helmholtz Plane (IHP). The second layer, from attached solvent to solvated ions, was named Outer Helmholtz Plane (OHP). The layer beyond the OHP was still called diffusing layer. The total capacitance of the double-layer inter face was given in Eq.2.1,

$$\frac{1}{C_{dl}} = \frac{1}{C_{IHP}} + \frac{1}{C_{OHP}} + \frac{1}{C_{diff}} \qquad \textbf{(Eq.}2.1\textbf{)}$$

corresponding to a series relationship between C_{IHP}, C_{OHP}, and C_{diff} as illustrated in the following circuit.

Apparently, the total capacitance C would be dominated by the smallest capacitance among C_{IHP}, C_{OHP}, and C_{diff} on account of the reciprocal form. However, C_{diff} was usually much larger than C_{IHP} and C_{OHP} so the contribution of diffusion layer to the double-layer capacitance was neglected in many cases. The IHP could be considered as a dielectric layer so the C_{IHP} and C_{OHP} could be combined to C_H, which was a fairly reasonable estimation of double-layer capacitance and could be calculated using equation $C= \varepsilon A/d$. In EDLC, the electrodes are porous carbon materials with extremely large specific surface area (e.g. 1000 – 2000 m^2/cm^3).[8] The dielectric layer is replaced with a

molecular layer of electrolyte, which results in nanometer d. Two extremes in specific surface area and separation distance results in extremely high capacitance.

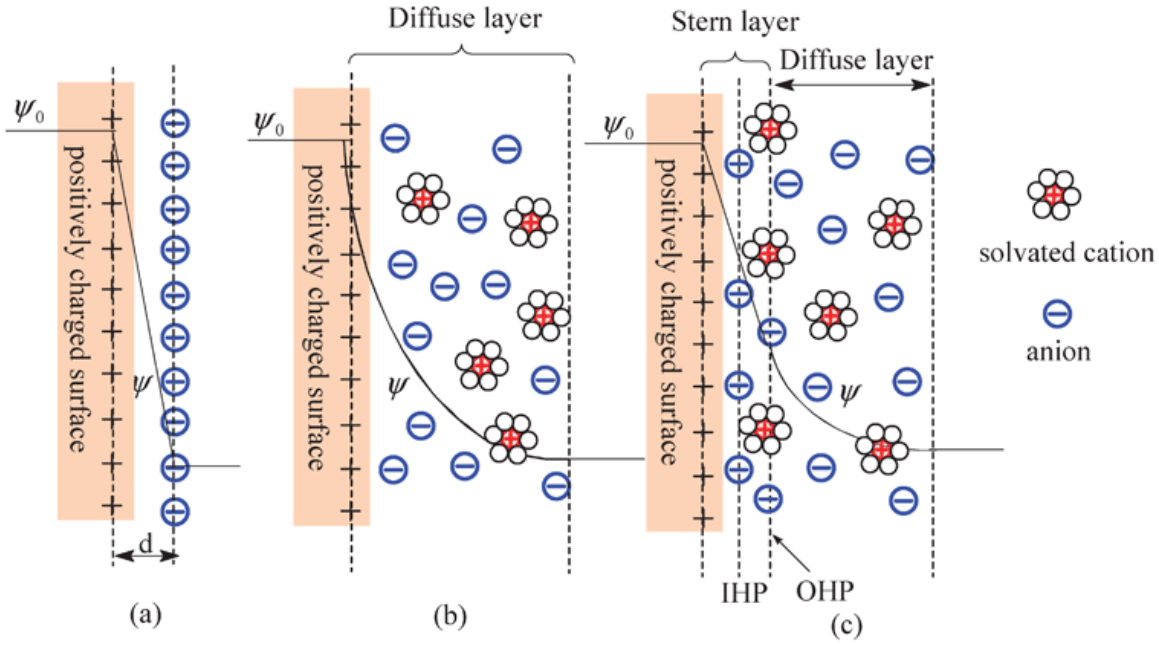

Fig.2.3 Models of the electrical double layer at a positively charged surface: (a) the Helmholtz model, (b) the Gouy–Chapman model, and (c) the Stern model, showing the IHP and OHP.[7]

(iv) Electrochemical capacitors based on pseudocapacitance

Pseudocapacitance arises from reversible electrochemical reactions on electrode surface. The pseudocapacitance originates from the thermodynamic relationship between extent of charge (ΔQ) and the change of potential (ΔU), C=ΔQ/ΔU or C=dQ/dV. The fundamental difference between battery and ES is time of charging and discharging, which is in the order of seconds for ES and hours for battery. The energy storage mechanism for both battery and pseudocapacitor is Faradaic process, which is different form non-Faradaic process of EDLC. So the energy storage in EDLC is lower than that of

battery in order of several magnitudes. Fig.2.4 shows the specific energy versus charging time for EDLC, pseudocapacitor, and battery in general.[9] The specific energy of battery is optimized when charging time is longer than ~ 10 min. Short charging time causes resistive losses of energy and generates much heat, which could lead to explosion and result in safety issues. The EDLC has no safety problem on fast charging-discharging due to its extremely small internal resistance, usually on the level of several micro Ohms, which is several Ohms for battery. However, the specific energy of EDLC is kept on a much lower level than battery. Between EDLC and battery there is a region of best performance in the time domain of ~ 10 s to ~ 10 minutes, which is the region for pseudocapacitive materials. The motivation of researching pseudocapacitance is to find or fabricate a pseudocapacitive materials with both high energy density and power density, a combination of advantages of both battery and EDLC.

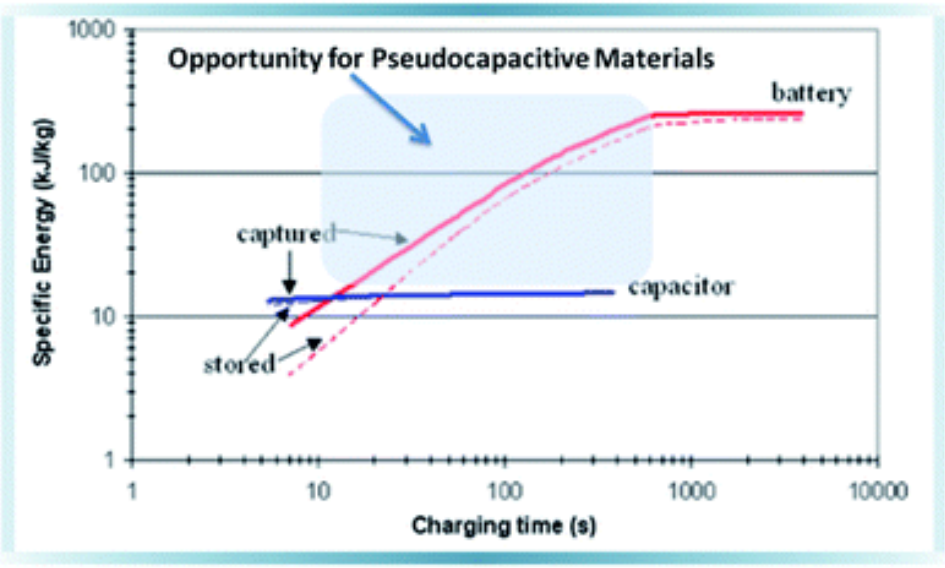

Fig.2.4 Energy *vs.* charging time for an EDLC and a lithium-ion battery. The region between ~ 10 s and 10 minutes represents the time domain where high-rate pseudocapacitive materials could offer higher energy and power densities than lithium-

ion batteries and EDLCs.[9]

Electrochemical mechanisms which can result in pseudocapacitance were investigated by B. E. Conway in 1970s and classified into three different groups, (i) underpotential deposition (Fig.2.5a), (ii) redox pseudocapacitance (Fig.2.5b), and (iii) intercalation pseudocapacitance (Fig.2.5c).[10] Underpotential deposition is a phenomenon of electrochemical deposition of ions on electrode surface forming a layer of adsorbed ions at potential above the Nernst equilibrium potential for reduction process, or vice versa. Redox pseudocapacitance arises from electrochemical adsorption of ions on electrode surface with a concomitant faradaic charge transfer process. Intercalation pseudocapacitance is a result of ion intercalation into tunnels or layers of a redox-active material, accompanied with faradaic charge transfer process but with no crystallographic phase change.

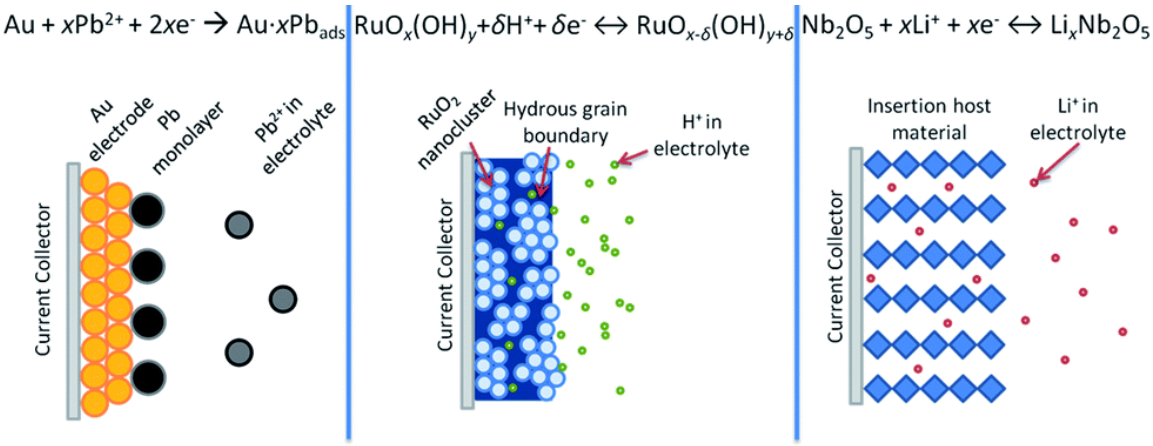

Fig.2.5 Different types of reversible redox mechanisms that give rise to pseudocapacitance: (a) underpotential deposition, (b) redox pseudocapacitance, and (c) intercalation pseudocapacitance.

For all three mechanism, the extent of charge and potential have an electrochemical

relationship (Eq.2.2) due to electrochemical reactions at electrode/electrolyte interface,

$$E \sim E^0 - \frac{RT}{nF} ln\left(\frac{X}{1-X}\right) \quad \textbf{(Eq.}2.2\textbf{)}$$

where E is potential, E^0 is standard electrode potential, R is the ideal gas constant (8.314 J mol^{-1} K^{-1}), T is absolute temperature, n is the number of transferred charges, F is the Faraday constant (96 485 C mol^{-1}), and X is the fractional extent of reaction. The charge, Q, is directly related to the extent of reaction, X. So the capacitance, C=dQ/dV, can be expressed in Eq.2.3,

$$C = \left(\frac{nF}{m}\right)\frac{X}{E} \quad \textbf{(Eq.}2.3\textbf{)}$$

where m is the molecular weight of the active material.

Table 2.1 Comparison between double-layer capacitance and pseudocapacitance

Double-layer capacitance	**Pseudocapacitance**
Non Faradaic	Involves Faradaic process
20–50 μF cm^{-2}	2000 μF cm^{-2} for single-state process; 200–500 μF cm^{-2} for multi-state, overlapping processes
C fairly constant with potential, except through the point of zero charge (p.z.c.)	C fairly constant with potential for RuO_2; for single-state process, exhibits marked maximum
Highly reversible charging/discharging	Quite reversible but has intrinsic electrode kinetic rate limitation determined by potential dependent faradaic leakage resistance (R_f).
Has restricted voltage range (in contrast to non-electrochemical electrostatic capacitor)	Has restricted voltage range
Exhibits mirror-image voltammograms	Exhibits mirror-image voltammograms

(v) Hybrid supercapacitor

In a supercapacitor system, both the storage mechanism of EDLC and pseudocapacitor are observed simultaneously even though one of them dominates over the other.[11] The comparison of EDLC and pseudo-capacitor is shown in the Table 2.1.[12]

Table 2.2 Summary of the different types of hybrid supercapacitors[13]

Type of supercapacitor	**Electrode material**		**Dominate charge storage mechanism**	**Advantages/ disadvantages**
Asymmetric hybrid supercapacitor	Anode:	Pseudocapacitive materials	Pseudocapacitance	High energy density and power density, good cyclability
	Cathode:	Carbon	Double-layer capacitance	
Symmetric hybrid supercapacitor	Anode:	Redox metal oxide or polymer	Pseudocapacitance	High energy density, moderate cost and stability
	Cathode:	Redox metal oxide or polymer	Pseudocapacitance	
Battery-like hybrid supercapacitor	Anode:	Li-ion intercalation materials	Lithiation/delithiation	High energy density, high cost
	Cathode:	Carbon	Double-layer capacitance	

Both double-layer capacitance and pseudocapacitance can be utilized in single ES device to form a hybrid system. Because both Faradaic process and non-Faradaic process are used, better energy and power performance is achievable, with extra benefits such as cycling stability. The hybrid system can be divided into three categories, asymmetric hybrid supercapacitor, symmetric hybrid supercapacitor, and battery-like hybrid supercapacitor. Asymmetric hybrid supercapacitor has one electrode where double-layer

capacitance dominates and another electrode where pseudocapacitance dominates. Symmetric hybrid supercapacitor has two different electrodes where for both of them pseudocapacitance dominates. For battery-like hybrid supercapacitor, one electrode is Li-ion battery electrode, where Li ions intercalation is the main mechanism for energy storage, while the other electrode is using capacitance to store energy. A summary of all different hybrid supercapacitors is given in Table 2.2.[13]

Many combinations of anode and cathode had been tested in either aqueous or organic electrolyte. Pseudocapacitive electrode materials were widely used to improve the energy density of ES devices, usually with sacrifice of capacitance retention and cycling stability due to its low conductivity and redox reactions during charge-discharge. In the meantime, capacitance of both anode and cathode should be balanced to match each other to obtain the highest device capacitance, since the total capacitance of ES device was dominated by the electrode with lower capacitance ($1/C_{total} = 1/C_{anode} + 1/C_{cathode}$). However, due to different capacitance retention versus charge-discharge rates, capacitance of anode and cathode could not be matched at all charge-discharge rates.

The hybrid system could extend the voltage window of ES device. By using AC as cathode and MnO_2 as anode, an ES with voltage window up to 2 V in aqueous electrolyte was achieved. The high voltage window was ascribed to overvoltage of water decomposition on MnO_2 and high specific surface area of carbon.[14] Another example was that combination of carbon electrode and PbO_2 electrode resulted in a voltage window of 2.1 V in H_2SO_4 electrolyte.[15]

2.3 Energy storage and power performance of ES

To store energy (E) into a capacitor, work (W) must be done to separate or store charges in anode and cathode. For an ideal capacitor, the total work of charging a capacitor is the energy the capacitor stored, as given in Eq.2.4

$$E = W = \int_0^Q U dq = \int_0^Q \frac{q}{c} dq = \frac{Q^2}{2C} = \frac{1}{2} C U^2 \qquad \textbf{(Eq.}2.4\textbf{)}$$

where Q is the total stored charges, C is the capacitance, and U is the working voltage of the capacitor. The power (P) of a capacitor is the instant energy delivery ability, which depends on the fluctuating voltage (U(t)), as given in Eq.2.5

$$P = \frac{dW}{dt} = \frac{d}{dt}\left(\frac{1}{2} C U^2\right) = C U(t) \frac{dU}{dt} \qquad \textbf{(Eq.}2.5\textbf{)}$$

So stored energy and power of capacitors are positively linear proportional to the capacitance C. Voltage window of capacitors have strong influence on both energy and power. To increase energy storage and power of a capacitor, it is necessary to increase its capacitance and voltage window.

In scientific papers, maximum power (P_{max}) is widely used to characterize power delivery performance of an ES. In this case, a simple RC circuit is considered, where ESR (R_s) is equivalent series resistance, corresponding to total resistance related to ionic resistance of electrolyte, electrode resistance of electrode, resistance due to ion penetration through membrane separator, and interface resistance between electrode and current collector.

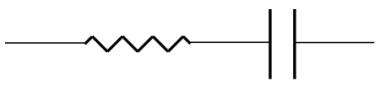

The discharge current (I) can cause the reduction of initial voltage (U_i) to the real time voltage $U=U_i-IR_s$. The corresponding power $P=UI=U_iI-I^2R_s$. To reach the maximum power, $dP/dI=0$. So $I_{Pmax}=U_i/2R_s$ and $V_{Pmax}=U_i-IR_s=U_i/2$. Then the P_{max} has the formula as given in Eq.2.6,

$$P_{max} = \frac{U_{max}^2}{4R_s} \quad \textbf{(Eq.}2.6\textbf{)}$$

Fig.2.6 shows the construction of a supercapacitor, which consists of two current collectors, two electrodes, electrolyte, and a membrane separator. The internal resistance of an ES was directly related to ESR. To improve the power performance, the ESR, more specifically the internal resistance, must be minimized. The internal resistance was determined by resistance of current collector, electrode materials, and electrolyte, and the interfacial resistance of current collector/electrode, and electrode/electrolyte.

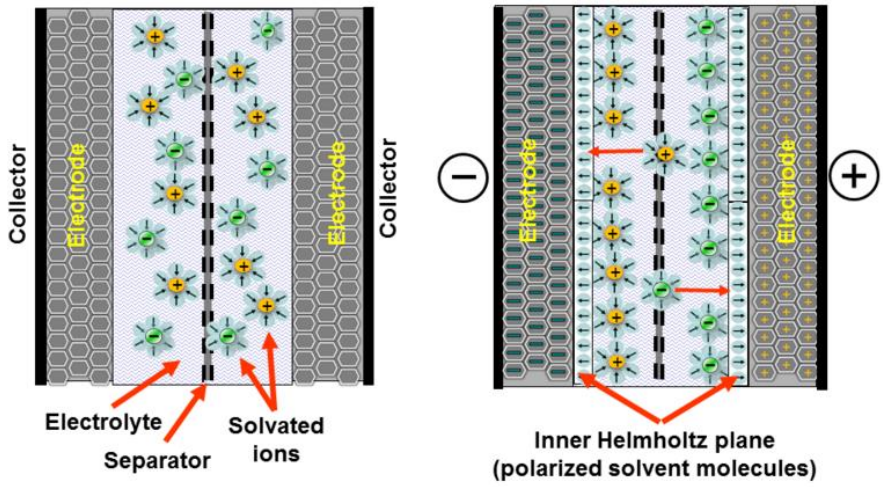

Fig.2.6 Illustration of discharged (left) and charged (right) supercapacitor

(i) Current collector

To minimize the internal resistance and maximize the SC of an ES, proper current

collector must be chosen. Current collectors must be highly conductive and stable under high potential in different electrolytes. There should also be a good interface contact between current collector and active materials. To achieve these goals, surface treatment for metal current collector was necessary. It was proven that polished aluminum current collector could reduce the interfacial resistance between active material and aluminum current collector. A further surface treatment could even improve its stability in electrolyte at high potential.[16]

Unlike metal foils, which only one layer active material could be deposited or pasted on, Ni foam had great advantages in increasing interfacial area between current collector and active materials, hence the internal resistance was controlled in a reasonable range. The active material loading reached as high as 50 mg cm^{-2}, which was hundreds times heavier than that on metal foils.[17, 18] Other current collectors using the same mechanism included Ni plaque,[19] carbonized sponge,[20] carbon aerogel,[21] vertical grown CNT etc.[22] Unlike Ni foam, carbon current collectors had great advantages in electrochemical stability under high potential, large specific surface area, high SC, low density, and environmental friendly, which made carbon-based materials an ideal candidate for current collector, such as AC carbon aerogel, carbon fibers, aligned CNT, and layered graphene.

(ii) Membrane separator

The purpose of membrane separator in an ES was to separate anode and cathode to prevent short circuit, which can trigger the conversion of chemical energy to heat and cause irreversible damage to ES devices. In the meantime, membrane contained numerous pores and tunnels to enable free pass through diffusion of ions and electrolyte

molecules. The important parameters of a membrane separator are thickness, permeability, absorbency, chemical stability, pore sizes, puncture resistance, tensile strength, and thermal properties.

The membrane should have good permeability because the internal resistance was proportional to the permeability. The permeability reflected how easily ions and molecules moving through it. Absorbency is the ability to absorb electrolyte, which directly reveal the wetting ability of membrane separator to electrolyte. Good absorbency could substantially reduce internal resistance. Moreover, membrane separator should have good chemical stability in different electrolyte and cycling stability under high potential, which had great influence on ES and battery life.

There were requirements on thickness, tensile strength and puncture resistance for membrane separators. Electrodes and current collectors were not smooth and the rough edges were strong enough to pierce separator if it was not thick enough. However, thickness of membrane separator had influence to internal resistance and permeability. So the thickness must be chosen after testing.

(iii) Electrolyte

Electrolyte for ES can be categorized into aqueous, organic, and liquid salts (ionic liquids). Electrochemical stability and ionic conductivity are the two main criteria for selection of an electrolyte. Electrochemical stability determines the voltage window and hence has great influence on energy and power density. Ionic conductivity, on the other hand, affects the internal resistance and further influences the power density as shown in Eq.2.6.

Aqueous electrolyte includes acid (e.g. H_2SO_4, HCl), alkali (e.g. KOH, NaOH), and neutral pH solution (e.g. Na_2SO_4, Li_2SO_4). Aqueous electrolytes have high ionic conductivity (up to ~ 1 S cm^{-1}), and hence high power performance is achievable. However, water has an electrochemical stability window of 1.23 V, which results in a narrow voltage window for ES, usually less than 1 V, and hence low energy density.[23] In comparison to aqueous electrolytes, organic electrolytes have much larger electrochemical stability voltage window, which is up to ~ 3 V, with the sacrifice of ionic conductivity and SC (Table 2.3, Fig.2.7).[24, 25] The high voltage window results in high energy density as indicated by Eq.2.6. For this reason, most commercial ES industries use organic electrolytes. Propylene carbonate and acetonitrile are widely used solvents for organic electrolytes and tetraethylammonium tetrafluoroborate is the commonly used salt to dissolve into solvents. The ionic conductivity of organic electrolyte increases with the concentration of dissolved salt until the maximum conductivity is reached.[26] Ionic liquids are molten salts in room temperature, which recently have been considered as a promising electrolytes for ES. Advantages of ionic liquids include low vapor pressure, broad electrochemical stability window, and good thermal property etc.[27-30] But it has limitation in ionic conductivity, especially on room temperature, which substantially reduces the power performance.[31]

Table 2.3 The specific capacitance of selected electrode materials[24]

Material	Electrolyte	F g-1	F cm-3
Carbon cloth	KOH	200	70
	Organic	100	35
Particulate from SiC	KOH	175	126
	Organic	100	72
Particulate from TiC	KOH	220	110
	Organic	120	60

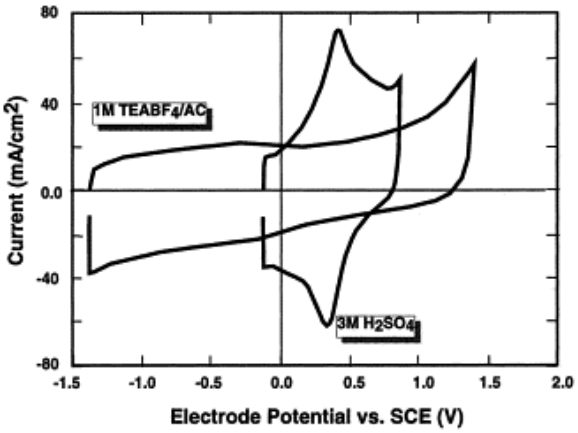

Fig.2.7 Cyclic voltammograms of activated glassy carbon electrodes at 100 mV s^{-1} in 3M H_2SO_4 (aq.) and in 1 M $TEABF_4$ in acetonitrile. Both electrodes received the same electrochemical activation.[25]

2.4 Electrode materials for ES

SC of an ES is strongly depended on electrode materials. Developing materials with high SC can substantially improve the energy storage. Electrode resistance is a key component of ESR, so electrode with high conductivity can result in better power performance. In some cases, electrode materials can enlarge the voltage window of an ES. So there is a necessary to investigate electrode materials.

(i) Carbon materials

Carbon materials included AC, carbon nanofibers, and graphene, corresponding to 0, 1, and 2 dimensions materials. For carbon materials, the dominated capacitance mechanism was double-layer capacitance.

The SC has strong relationship with specific surface area of electrode materials. However, not all area contributes to SC. The area with contribution to SC is places with good contact to electrolyte, which is referred accessible surface. It is for this reason, SC doesn't increase linearly with specific surface area.[32-34] Pore size plays a key role in

determining accessible specific surface area.

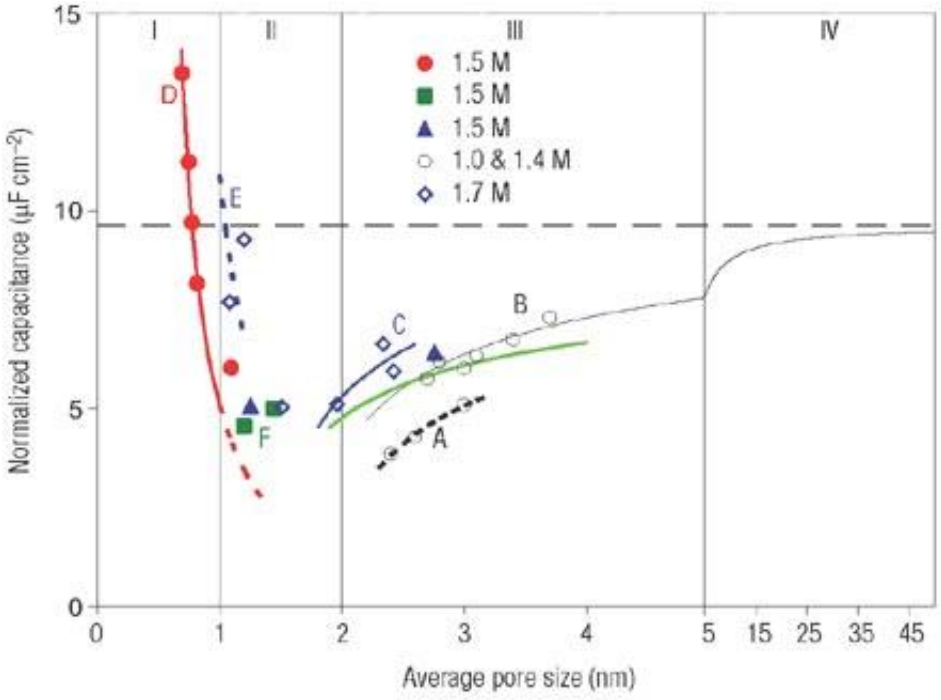

Fig.2.8 SC normalized by specific surface area as a function of pore size for different carbon samples tested in same electrolyte.[14]

Obviously, particles with smaller pore size have larger specific surface. However, it is suggested that solvated ions could not access pores with diameter less than 0.5 nm, even 1 nm for some larger hydrated ions and solvated ions in organic electrolyte.[33, 35, 36] As the pore size increased to 2 to 5 nm, which was about 2 times larger than a solvated ion, capacitance started increasing with pore numbers moderately.[37, 38] However, research showed that particles with balanced microporosity (<2 nm) and mesoporosity (2-50 nm) resulted in best capacitive performance. These experiments indicated that desolvated ions could access micropores and hence contributed to SC of ES.[39] In an experiment where mean pore size could be fine-tuned,[40] the normalized capacitance was gradually declining with mean pore size until a critical value of ~ 1.5 nm, then the

normalized capacitance increased sharply with reducing of mean pore size to the ion size (Fig.2.8). Different models are applied for different zones in Fig.2.8.

The general purpose of increasing porosity was to increase specific surface area for better capacitive performance. However, during the process of increasing porosity, other aspects, such as pore shape, pore size distribution, surface functional group, and electrical conductivity, had to be taken into consideration as well. Electrode materials with large porosity leaded to low density, and hence the volumetric capacitance could even be reduced for high porosity materials.[41] So a compromise between gravimetric capacitance and volumetric capacitance existed for electrode materials with high porosity.

Except specific surface area, introducing surface functional groups was considered as another way to improve capacitive performance, including alcohol, carbonyl, epoxide, and carboxylic acid etc.[42-46] It was suggested that functional groups or heteroatoms (O, N, B, S etc.) in carbon materials could help absorbing ions from electrolyte. For the bad wetting performance of carbon materials, the introducing of functional groups could significantly ameliorate their hydrophilicity/lipophilicity, leading to high electrode/electrolyte contacting area and hence improve their capacitive performance. The methods of introducing surface functional groups included oxidation using strong acid (e.g. nitric acid) or alkali hydroxide (e.g. KOH).[25] Treated carbon materials with surface functional group could have a SC improvement of 5-10 %.[47] However, these functional groups might gradually decompose into electrolyte after many cycles, especially those oxygen-containing acidic groups.[48] Another problem with introducing functional groups was the rising of electrical resistance due to increasing defects in carbon materials, especially in single-walled CNT and single-layered graphene. The

existence of functional groups and heteroatoms in their structure blocked the transportation of electrons.

AC was the most widely used electrode materials for supercapacitors, especially in industry, due to its low price, high specific surface, and moderate conductivity. Electrons transportation between different particles was inefficient by either hopping to trap states of neighbor particles or diffusing within the extended states.[49] In contrast, carbon nanofibers, including CNT, had a continuous pathway of electron transportation along the longitude direction, and hence substantially reduced electrode resistance. It was for this reason, CNT and carbon fibers were better electrode materials than AC for ES application with good power performance. Relatively high specific surface area was also reachable for carbon nanofibers, which resulted in acceptable capacitive performance. Graphene, graphene oxide, and reduced graphene oxide were also used as electrode materials for ES. In comparison to AC and carbon fibers, graphene and its derivatives had much higher specific surface area and electronic conductivity, both of them were beneficial to ES and hence they attracted researchers' attention immediately when it was first discovered in 2004.[50] Reduced graphene oxide, which was rich in surface functional groups and hydrophilic, while high electronic conductivity was maintained, also attracted significant attention as electrode material, with even higher SC than graphene and graphene oxide.

(ii) Transition metal oxides

For all transition metal oxides, pseudocapacitance was the dominated contribution to total capacitance. These oxides included MnO_2, NiO, Co_2O_3, TiO_2, V_2O_5, RuO_2 etc. The fundamental requirements of metal oxide for ES were (i) electric conductivity, (ii) oxidation state change with no phase change, and (iii) reversible redox reaction. In most

cases, metal oxides were coupled with carbon materials for the using of electrode materials for ES. The purposes of introducing carbon materials included increasing specific surface area and increasing electrode conductivity.

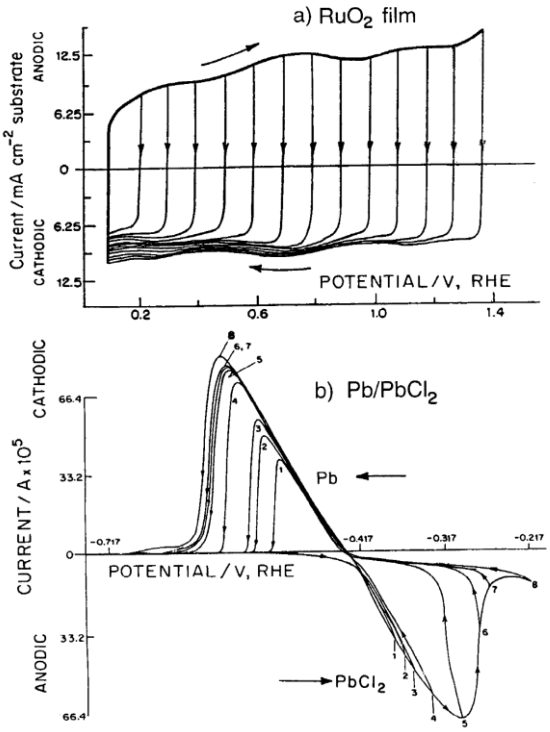

Fig.2.9 (a) CVs for RuO_2 in 1 M aqueous H_2SO_4 showing mirror image symmetry and responses to successive switching along the scanned potential range. (b) CVs for Pb-$PbCl_2$ battery electrode showing typical irreversibility arising with 3-dimensional materials undergoing chemical phase changes.[51]

Some of the metal oxides were also used in battery, such as MnO_2 and Co_2O_3. The difference between battery and supercapacitor was that, for supercapacitor a linear potential change with time could generate a steady current. s=dU/dt, which resulted in a mirror image cyclic voltamogram (CV). However, such a mirror voltamogram is not observed in the case of battery materials (Fig.2.9).[51] The mechanism for this difference

was that electrochemical reactions in ES were reversible. In contrast, battery type process were rarely reversible, and substantially different voltage range was required for its oxidation and reduction processes.

Metal oxides for ES should have several conjunctive reversible redox reactions to form wide operating range of potential. It was proven by the intercalation of Li^+ into MoO_2 shown in Fig.2.10. Under extremely slow scan rate, the CV of Li^+ intercalation showed two identical peaks, corresponding to two different stages of its quasi-2-dimensional intercalation of Li^+ into MnO_2.[51] However, scan rates for ES, usually in the range of 1-500 mV s^{-1}, were much faster than that of batteries. For this reason, distinguished peaks were absent, but continuous and constant current was observed (Fig.2.11). The deviation from constant current and rectangular shape was caused by many reasons, including reversibility of redox reaction, electrode resistance, potential scan rates etc.

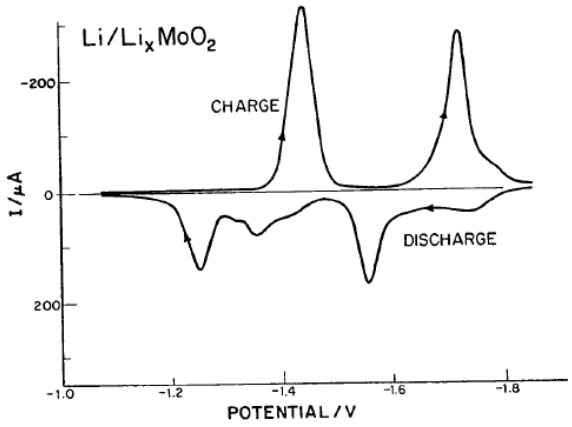

Fig.2.10 Slow CV (9μV s^{-1}) for pseudocapacitance associated with Li^+ intercalation into MoO_2.[51]

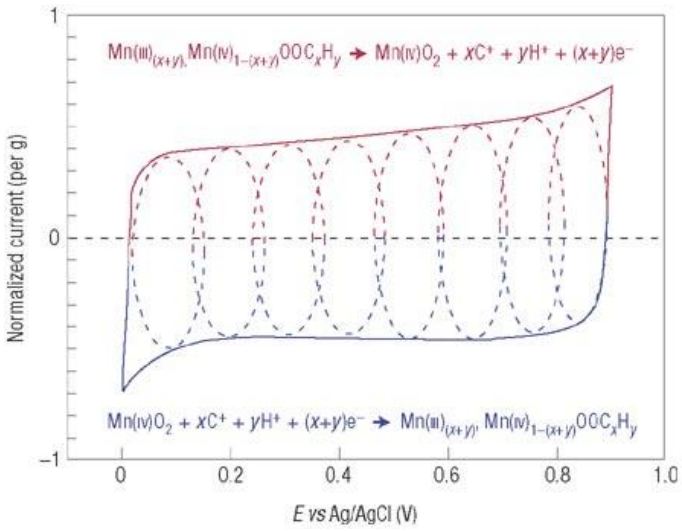

Fig.2.11 The schematic of CV for a MnO_2 electrode cell in mild aqueous electrolyte (0.1 M K_2SO_4) shows the successive multiple surface redox reactions leading to the pseudo-capacitive charge storage mechanism.[14]

MnO_2 was firstly studied in 1999 for the application in pseudocapacitors.[52] The theoretical SC of MnO_2 was 1380 F g^{-1}.[53] However, the high capacitance could only be obtained in nanoscale thin film electrodes.[53, 54] So far, only 10% to 30% of the theoretical value could be achieved for electrodes with thick MnO_2 films. The redox reaction of MnO_2 in charge-discharge was given in Fig.2.11. MnO_2 electrode materials have advantages of low cost, resource abundance, environmental friendly, and good capacitive performance. However, its electronic conductivity was depended on its crystalline structure, but generally very low, from 10^{-7} to 10^{-3} S cm^{-1}.[55] So the transporting length of free electron in MnO_2 was very short, and hence only thin layer on MnO_2 particle surface had contribution to its pseudocapacitance.[53] Another problem with MnO_2 electrodes was than Mn^{3+} formed during redox reaction, no matter what electrolyte was used. This process caused a dissolution of MnO_2 electrode and loss of

capacity. So the cycling performance of MnO_2 electrode was worse than that of EDLC.[56]

RuO_2 was the first electrode material thoroughly researched for pseudocapacitance in 1970s.[57] Unlike MnO_2, RuO_2 possessed good electronic conductivity (~ 10^4 S cm^{-1} for bulk single crystal). It also has high theoretical SC of ~ 1500 F g^{-1}. It was for these reasons, $RuO_2 \cdot nH_2O$ electrode with mass loading up to 30 mg cm^{-2} resulted in a SC as high as 720 F cm^{-2}.[58] Once it was coupled with AC to improve both conductivity and specific surface area, the SC of RuO_2 was improved to 1340 F g^{-1} for thin film electrode, which was close to its theoretical value.[59] The drawback of RuO_2 for electrode materials was the price and resource abundance, which was why RuO_2 supercapacitors were only used for military applications.

Oxides with spinel structure were also widely used for ES, including Mn_3O_4,[60] Fe_3O_4,[61] and Co_3O_4,[62] and mixed metal spinel such as $MnFe_2O_4$.[63] Spinel crystal structure has a molecular form of AB_2O_4, with tremendous 3-dimentional passways for ion diffusion. Like MnO_2, Mn_3O_4 , $MnFe_2O_4$ also had poor electronic conductivity, which lead to low SC for heavy mass loading electrodes, varying from 10 to 300 F g^{-1} with a rectangular CVs.[60, 63] However, Co_3O_4 had a combined behaviors of both ES and battery due to the formation of oxyhydroxides during charge-discharge, as shown in Eq.2.7.[64]

$$M_3O_4 + OH^- + H_2O \leftrightarrow 3MOOH + e^- \quad \textbf{(Eq. 2.7)}$$

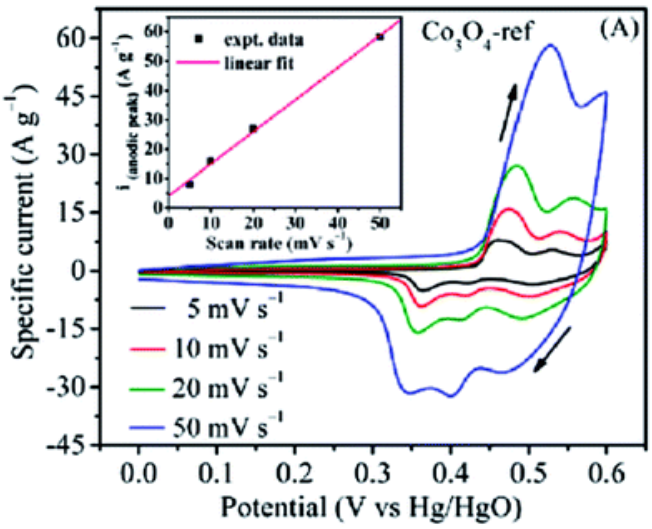

Fig.2.12 CVs for a composite electrode consisting of Co_3O_4 nanowires in 1 M KOH from 5 to 50 mV s^{-1}. The inset shows the linear dependence of the anodic peak on the sweep rate, indicative of pseudocapacitive behavior.[64]

The reaction of forming oxyhydroxides is a two phase reaction, involving phase transition and hence constant potential during charge-discharge. The phase transition limited the cycling and power performance of ES based on Co_3O_4, even though energy density could be larger than conventional ES. The metal oxyhydroxide could be further oxidized to metal oxide particles as shown in Eq.2.8. The CVs of Co_3O_4 are presented in Fig.2.12, where several redox peaks were observed, corresponding to phase transition reactions and oxidation reaction. Thus the energy storage of such kind materials combined pseudocapacitance and battery contribution.

$$MOOH + OH^- \leftrightarrow CoO_2 + H_2O + e^- \quad \textbf{(Eq.}2.8\textbf{)}$$

(iii) Transition metal nitrides

Transition metal nitrides shared many common properties with transition metal oxides or oxyhydoxides, such as two or more oxidation states, and highly reversible

electrochemical reaction. Unlike metal oxides, nitrides have a voltage window in negative range, and high electronic conductivity. Because of high SC and density, the volumetric capacitances of nitrides were much higher than that of EDLC. So nitrides could substitute carbon materials in the fabrication of ES devices.

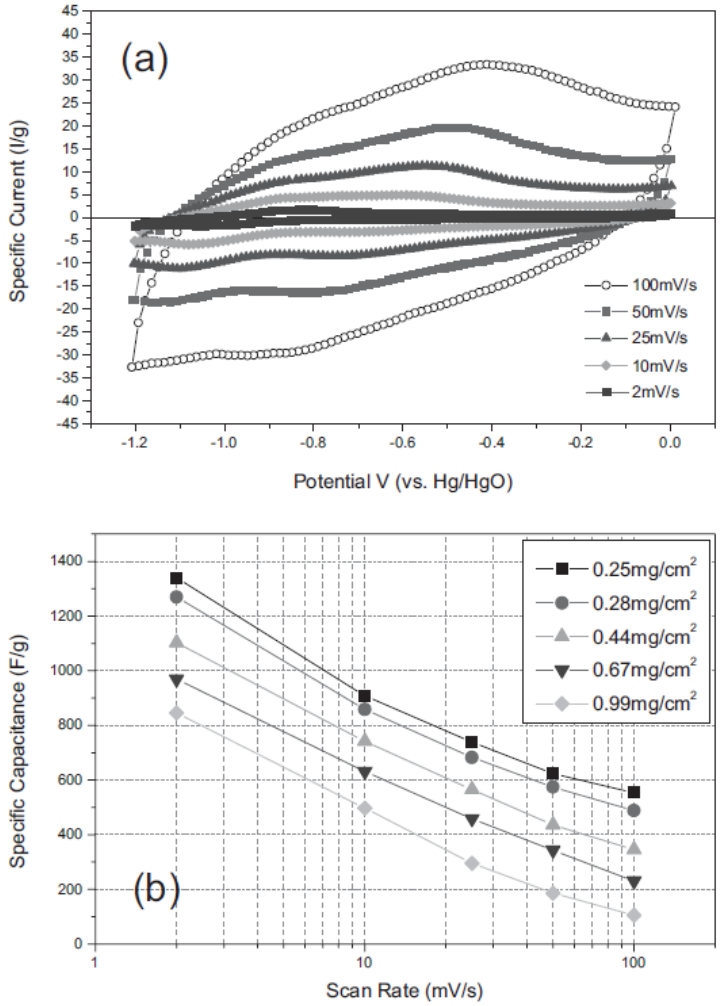

Fig.2.13 The (a) CVs of VN nanocrystals synthesized at 400 ℃ at various scan rates (2-100 mV s^{-1}) in 1 M KOH electrolyte (ΔV: 0 to -1.2 V) and (b) specific capacitance versus scan rates with different active material loading.[65]

VN was firstly reported to have pseudocapacitive behavior in 2006.[65] The electronic conductivity of VN was up to 82 S cm^{-1}, much higher than that of V_2O_5 (10^{-6} S cm^{-1}). The

CVs of VN in KOH electrolyte are given in Fig.2.13, where obviously several redox peaks existed. The voltage window was extended from 0 to -1.2 V. The highest SC of 1340 F g^{-1} was achieved at 2 mV s^{-1} (Fig.2.13).[65] However, SCs from other experiments only varied from 50 to 300 F g^{-1}.[66-69]

The origin of pseudocapacitance was believed to be attributed to the coating layer of V_2O_5 on VN particles, as illustrated in Fig.2.14. The three redox peaks of CVs were ascribed to transition of oxidation states from II, III and IV in an alkali electrolyte.[65, 70] XPS experiments proved the existence of vanadium oxide in the particles and a transition of oxidation states of vanadium atoms during charge/discharge. So the following charge-discharge (Eq.2.9) mechanism was proposed

$$VN_xO_y + OH^- \leftrightarrow VN_xO_y \| OH^- + VN_xO_y\text{-}OH \qquad \textbf{(Eq. 2.9)}$$

where $VN_xO_y \| OH^-$ represented the double layer of hydroxide ions adsorbed on no specific sites of the surface of VN_xO_y. VN_xO_y-OH stood for successive oxidation of VN_xO_y by hydroxyl species, which arose much pseudocapacitance.

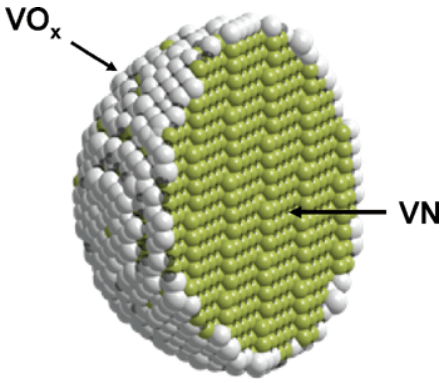

Fig.2.14 Illustration of vanadium oxide coated VN.[65]

Other nitrides included TiN,[71] and MoN,[69] with negative voltage window and pseudocapacitance. The common limitation of transition metal nitrides was the cycling

performance. One thousand cycles in aqueous electrolyte could result in only 10 to 60 % of their original SC.[22, 65, 72] It was found that potential window had great influence on the capacitance retention for VN. Small voltage window resulted in a better cycling performance, with sacrifice of SC.[68] Further investigations regarding to transition metal nitride were focused on improving cycling stability and capacitive performance.

(iv) Conducting polymers

Conducting polymers were polymers with conjugated bonds along their backbones. The conjugated bonds provided conductivity to polymer. The most studied polymer for application of ES were PPy (Fig.2.15F), polyaniline (Fig.2.15D), and other derivatives of polythiophene (Fig.2.15).[73]

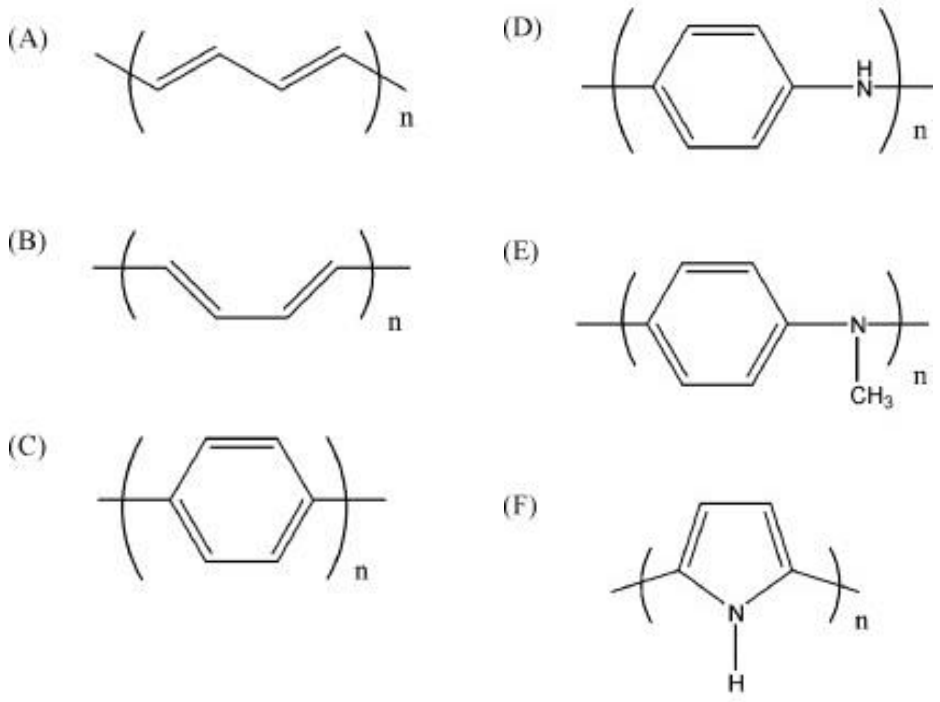

Fig.2.15 Various conducting polymer structures. (A) Trans-poly(acetylene), (B) cis-poly(acetylene), (C) poly(p-phenylene), (D) polyaniline (PAni), (E) poly(n-methyl

aniline) (PNMA), (F) polypyrrole (PPy).

Table 2.4 summarized these polymers with their dopant level, theoretical SC, and typically measured SC.[74] The reason that conducting polymers had higher SC than carbon materials was because they underwent redox reactions during charge-discharge, not simply adsorption/desorption of ions as existed in carbon materials. But the improvement of SC was associated with sacrifice of power performance since redox reaction took longer time than adsorption/desorption. The conductivity of conducting polymers was highly depended on dopant level, from 1 S cm^{-1} to 10^3 S cm^{-1}.[75, 76] Nevertheless, it was still much higher than that of transition metal oxides or nitrides, which paved the way for good power performance. Other advantages of conducting polymers included low cost, resource abundance etc.

Table 2.4 Theoretical and experimental specific capacitances of conducting polymers.[74]

Conducting polymer	Mw (g mol^{-1})	Dopant level	Potential range (V)	Theoretical SC (F g-1)	Measured SC (F g^{-1})
PAni	93	0.5	0.7	750	240
PPy	67	0.33	0.8	620	530
PTh	84	0.33	0.8	485	-
PEDOT	142	0.33	1.2	210	92

Conducting polymers could be either p-doped with anions (A^-) (Eq.2.10) when oxidized or n-doped with cations (C^+) (Eq.2.11) when reduced. The discharge reaction was the reverse of these reactions. The doping-undoping process was the charge-discharge process, which essentially was the insertion-deinsertion of counter ions in polymer chains. The conductivities of conducting polymers were highly depended on doped states. However, they were more conductive than most metal oxides in general, which resulted

in better capacitance retention and power performance. Table 2.5 summarized conductivity of different polymers.[74]

$$Cp + nA^- \rightarrow Cp^{n+}(A^-)_n + ne^- \text{ (p-doping)} \quad \textbf{(Eq. 2.10)}$$

$$Cp + ne^- + nC^+ \rightarrow Cp^{n-}(C^+)_n \text{ (n-doping)} \quad \textbf{(Eq. 2.11)}$$

Table 2.5 Typical conductivity of different conducting polymers

Polymer	Conductivity (S cm^{-1})
PAni	0.1 - 5[77-79]
PPy	10 - 50[80]
Polythiophene (PTh)	300-400[75]

(v) Composite materials

Double-layer capacitive materials had good capacitance retention, power performance, and cycling stability for its high conductivity and high specific surface area, but with drawbacks of low energy density. Pseudocapacitive materials offered high energy density with sacrifice of cycling stability and power delivery because of its redox reactions during charge-discharge and low conductivity. Hybrid system could be used to combine advantages of both double-layer capacitive materials and pseudocapacitive materials to produce composites with good capacitive, cycling stability, power, and energy storage performances.

The general idea was using the high conductivity and high specific surface area carbon materials and high SC of pseudocapacitive materials. As stated above, MnO_2 had a theoretical SC of 1380 F g^{-1}.[53] Because of its low conductivity, the high SC could only be achieved for thin film electrodes with a thickness of nanometers. The total energy stored in the electrodes was very low due to limitation of MnO_2 mass loading. However,

if the MnO_2 nanoparticles were distributed on carbon materials with large specific surface area, the high SC of MnO_2 and large mass loading could be achieved simultaneously, as proposed in Fig.2.16.[14]

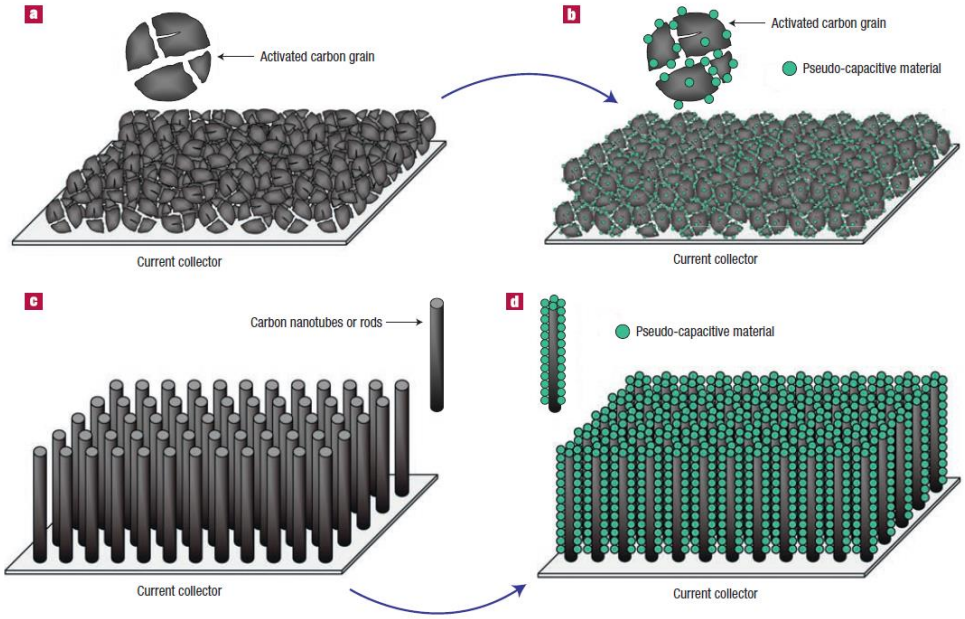

Fig.2.16 Possible strategies to improve both energy and power densities for electrochemical capacitors. Decorating activated carbon grains (a) with pseudo-capacitive materials (b). Achieving conformal deposit of pseudo-capacitive materials (d) onto highly ordered high-surface-area CNT (c).[14]

2.5 Fundamentals of electrophoretic and electrolytic deposition

Electrophoretic deposition (EPD) is one of the methods of preparing thin film electrode for ES. To achieve a successful EPD, particles must be dispersed in one solvent homogeneously to form a stable suspension. The stability of particles in a suspension is predicted by the DLVO theory, which is named after Dejaguin, Landau, Verwey, and Overbeek.

Fig.2.17 illustrates the interaction between two particles in a suspension. The total energy of two particles in a suspension is dominated by two energies, energy due to van der Waals attraction energy (V_A) and energy due to electrostatic double layer repulsion energy (V_R). The total internal energy between the two particles (V_T) in suspension was given in Eq.2.12.

$$V_T = V_A + V_R \quad \textbf{(Eq.}2.12\textbf{)}$$

The V_A and V_R were expressed in detail in Eq.2.13 and Eq.2.14, respectively.

$$V_A = \frac{-A}{12\pi D^2} \quad \textbf{(Eq.}2.13\textbf{)}$$

$$V_R = 2\pi\varepsilon a\xi^2 e^{-\kappa D} \quad \textbf{(Eq.}2.14\textbf{)}$$

Where A is the Hamaker constant, D is the particle separation, a is the particle radius, π is the solvent permeability, ξ is the zeta potential, and κ is a function of the ionic composition.

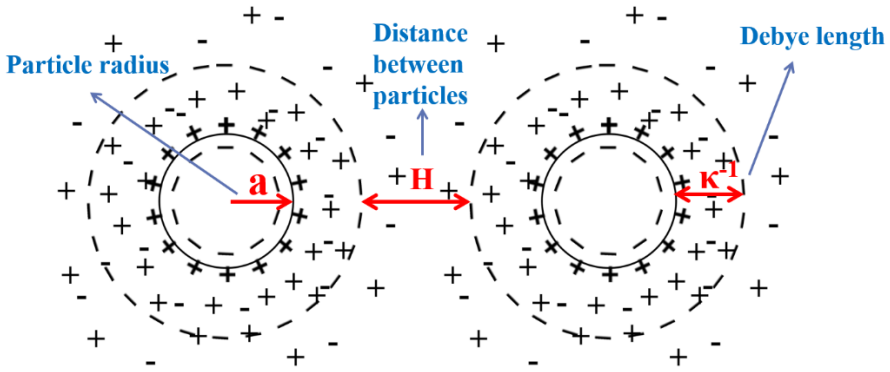

Fig.2.17 Schematic illustration of interaction between two particles in suspension.

The Debye length is defined as κ^{-1}, which is expressed in Eq.2.15 and showed in Fig.2.17.

$$\kappa = \left(\frac{e_0^2 \sum n_i z_i^2}{\varepsilon\varepsilon_0 kT}\right)^{1/2} \quad \textbf{(Eq.}2.15\textbf{)}$$

where e_0 is the electron charge, k is the Boltzmann constant, T is the absolute temperature, n_i is the concentration of ions with valence z_i. The increase of free ion concentration and/or valence causes a reduction of Debye length and hence repulsive energy.

V_T varies with the D, with their relationship showed schematically in Fig.2.18. The primary minimum in the interaction energy curve results at particle/particle contact (D=0). As particles separation increases, the role of repulsive energy increases and becomes the domination of total internal energy. An energy barrier (E_B) exists, which prevents particle coagulation and agglomeration in suspension. Beyond the energy barrier, a secondary shallow minimum develops. Particles could form a reversible coagulation at the distance secondary minimum. However, once particles have enough energy to pass the energy barrier, irreversible coagulation occurs.

To maintain stability of a suspension, the repulsive energy should be the dominate factor in the total internal energy. Electrostatic, steric, and electrosteric stabilization are widely used to improve stability of colloidal suspension. The steric stability involves the adding of polymer to a colloidal suspension. The polymer molecules are attached to the particles and prevent them from contacting each other. Electrostatic stability is using the electrostatic force between particles to avoid contacting of particles. Colloidal particles adsorb ions and carry same charges in the suspension. The same charges create electrostatic repulsive force and hence improve colloidal stability. Polymer with appropriate functionalities can improve colloidal stability with both steric stabilization and electrostatic stabilization, which is referred as electrosteric stabilization. Such polymers are named ionic polymeric dispersants.[81]

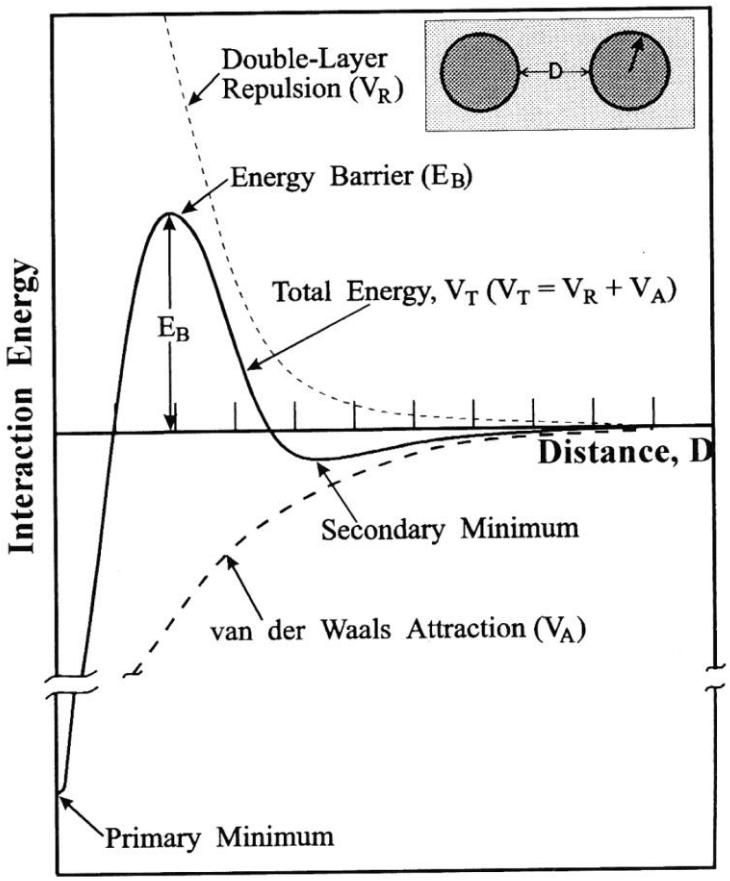

Fig.2.18 Schematic of the interaction energy as a function of separation between two particles in suspension.[82]

EPD is a colloidal process of moving stable dispersed colloidal particles from suspension to electrode forming coating on substrates. The schematic process is shown in Fig.2.19. The motivation of particles movement is the DC field and particles charges.

EPD is a combination of two process, electrophoresis and deposition. Electrophoresis is the motion of charged particles in a suspension under influence of an electric field. Deposition is the coagulation of particles to a dense mass on a substrate. In order to achieve efficient EPD, particles must be dispersed into solvent forming a stable colloidal suspension, where charged particles are free to move inside the suspension. Compared to

other techniques, EPD is versatile for many applications. It also has precise control of film thickness and quality by adjusting voltage, concentration, and dispersants. Depending on which electrode the EPD film forming on, the EPD could be categorized into anodic EPD and cathodic EPD.

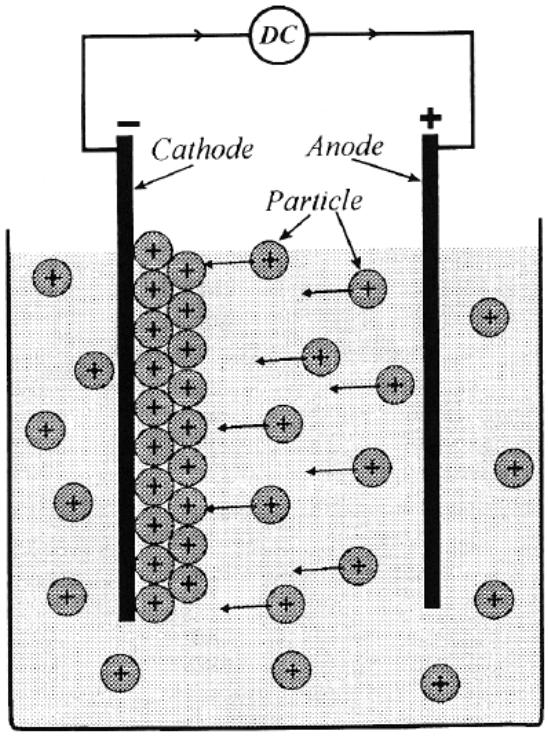

Fig.2.19 Schematic drawing of EPD cell showing the process[82]

Electrolytic deposition (ELD) is the procedure of producing ceramic thin films from solutions of metal salts. According to the places of electrode reaction, ELD can be categorized to cathodic ELD and anodic ELD. The mechanism of ELD can be explained by DLVO theory. Applied voltage causes ions movement and creates regions with high ion concentration. According to the DLVO theory, flocculation is observed once electrolyte concentration exceeds its critical value. The deposition during ELD is caused by formation of a flocculate introduced by the electrolyte.[83]

In cathodic ELD, cathodic reaction generates large amount of OH^- groups. Therefore the local pH increases near electrode. Metal ions adsorb OH^- and hydrolyzed on electrode surface to form colloidal particles (Eq.2.16). The particles coagulated and deposited on the electrode gradually. In the bulk solution, metal ions are stable in the environment of low pH.

$$M^{n+} + n(OH^-) \rightarrow M(OH)_n\downarrow \quad (\textbf{Eq.}2.16)$$

Anodic ELD is an oxidation process, where metal ion in lower oxidation state is oxidized to higher oxidation state (Eq.2.17). So the criteria of electrolyte is that metal ion in lower oxidation state is stable. Metal ion in higher oxidation state is rapidly hydrolyzed to yield metal oxide or hydroxide (Eq.2.18).

$$M^{z+} \rightarrow M^{(z+\Delta)+} + \Delta e^- \quad (\textbf{Eq.}2.17)$$

$$M^{(z+\Delta)+} + (z+\Delta)\ OH^- \rightarrow M(OH)_{z+\Delta} \rightarrow MO_{(z+\Delta)/2}\downarrow + (z+\Delta)/2\ H_2O \quad (\textbf{Eq.}2.18)$$

2.6 Applications of ES

ES were used when high power delivery and long cycle life were needed, such as power buffers and energy recovery systems. Supercapacitors were not invented to substitute batteries in market, but as a complementary for batteries to provide uninterruptible power supply. Because of small ESR compared with battery, the power delivery of ES was much faster than that of battery, which made ES to supply large amount of energy in a very short time without side effects such as heating and reducing lifetime. Another advantage of ES was its extremely long cycle life, up to 10^6 times, under fast charge-discharge.[24, 84] For comparison, Li-ion batteries had a cycle life of only hundreds times, which could even be dramatically reduced under fast charge-discharge because of

degradation of active materials in electrode.[9] The comprehensive comparison between battery and supercapacitor was listed in Table 2.6.[85] So the ES was also widely used in applications where long cycle life was demanded, such as wind farm.

Table 2.6 Comprehensive comparison between supercapacitor and battery[85]

Attribute	Supercapacitor	Battery
Power Density	>1000 W kg^{-1}	<500 W kg^{-1}
Energy Density	< 20 Wh kg^{-1}	10-300 Wh kg^{-1}
Cold Temperature	<-40 ℃	-20 ℃
Hot Temperature	+65 ℃	+40 ℃
Columbic Efficiency	98%	95%
Charging Time	<1 min	>30 min
Energy Efficiency	88%-98%	70%-85%
Self-Discharge	Hours	Days
Cycle life	10^6-10^8	10^2-10^3
Lifetime	8-14 years	1-5 years
Toxicity	Non-toxic	Partially
Monitoring	Not Required	Sophisticated
Handing	Human Handing	Requires Equipment

Uninterruptible power supply was demanded in many systems including microelectronics and electronic vehicles. However, peak power demands were frequently needed in many circumstances, such as flash light of cameras and engine cranking. Batteries couldn't afford such high power demands because of intrinsic limitations such as large internal resistance, or frequent peak power supply could dramatically reduce batteries lifetime. Power density for supercapacitor typically ranges from 10^3 to 10^4 W kg^{-1}. In contrast, power density for the Li-ion battery is typically from 300 to 1500 W kg^{-1}. The role of ES is to supply pulse power demand and maintain a constant current output from battery, which could result in a longer lifetime for battery.

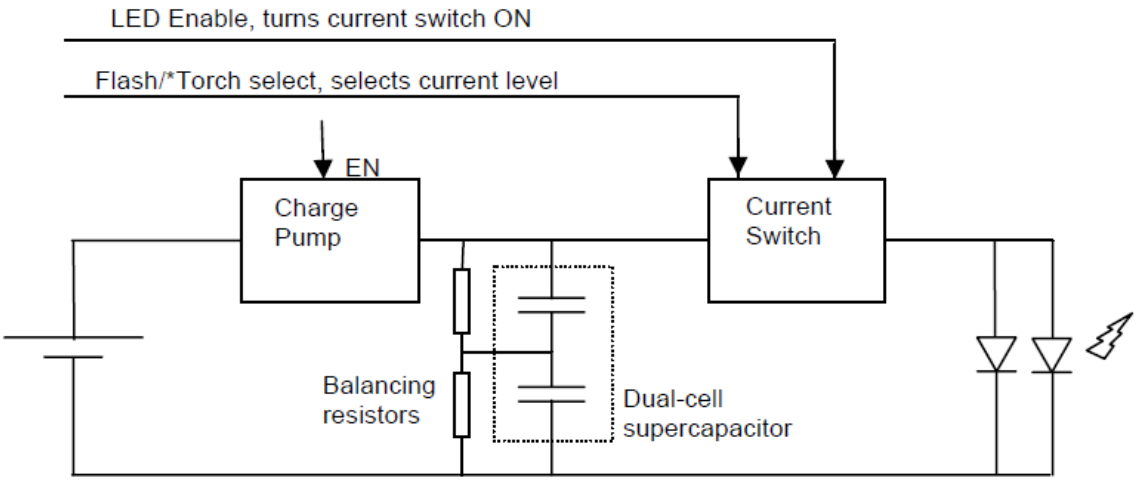

Fig.2.20 High power LED supercapacitor solution block diagram[86]

Fig.2.20 shows the circuit using ES to power LED flash for high resolution camera phones.[86] When LED flash was not in use, battery was charging the supercapacitor series. Once charged, supercapacitor series was capable to deliver high current in a very short time (<0.2 s) to power the LED flash. Once discharge finished, the battery started to charge the supercapacitor series again. With the use of supercapacitor, battery doesn't participate in the peak power supply for LED flash and hence the lifetime was extended. Other usage of ES included backup power for computer memories, power for cordless tools such as screwdrivers and electric cutters.

The ERS of ES was much smaller than that of battery and fuel cell, so the ES could be charged or discharged with extremely high current without heating problem. In comparison, the overheating was inevitable for battery under large current charge/discharge, so the charge/discharge current must be limited. Another advantage of supercapacitor is that it can accept a large range of charging/discharging currents. The energy of a supercapacitor is dependent on its voltage. So the monitoring of an ES is simpler and cheaper. The properties of an ES are determined by electrolytes, such as

electrochemical stability voltage, freezing point of electrolyte and ion mobility in electrolyte. The temperature range of an ES varies from -45 ℃ to 60 ℃ with no significant changes of capacitance and ESR.[87] In contrast, the Li-ion battery has a dramatically decrease of performance under 0 ℃.[88] These features of ES makes them suitable for energy recycling applications. For conventional vehicles, braking energy is transformed to heat and wasted. The regenerative braking application can transfer braking energy to electric energy with high current, which can be absorbed by and stored in supercapacitor.[89]

Comparing with battery, ES has much longer cycle life and lifetime as indicated in Table 2.6. The good cycling performance (10^6-10^8 cycles) and long lifetime (~15 year) make the ES a good candidate for hybrid vehicles to improve fuel economy and reduce emission gas in the whole lifespan of this vehicle.[90, 91] Moreover, ES are environmental friendly in operating, and waste disposing. So the use of ES for hybrid vehicles brings no environmental pollution.[92]

References

[1] Helmholtz Hv. Journal of Chemical Society. 1881;39.

[2] Samec Z. Charge-transfer between two immiscible electrolyte-solutions: part 3 stationary curve of current vs potential of electron-transfer across interface. Journal of Electroanalytical Chemistry 1979;103:1-9.

[3] Centeno TA, Stoeckli F. The role of textural characteristics and oxygen-containing surface groups in the supercapacitor performances of activated carbons. Electrochimica Acta 2006;52:560-6.

[4] Pistoia G, Rosan R. Electrochemical synthesis of poly(2,5-dimetheoxyaniline) - evaluation of the equivalent - circuit associated with the film and its stability in solution. Electrochimica Acta 1994;39:333-8.

[5] Bai LJ, Conway BE. AC impedance of faradaic reactions involving electrosorbed intermediates - examination of conditions leading to pseudoinductive behavior represented in 3-dimensional impedance spectroscopy diagrams. Journal of the Electrochemical Society 1991;138:2897-907.

[6] Robertson J. High dielectric constant oxides. The European Physical Journal-Applied Physics. 2004;28:265-91.

[7] Grahame DC. The electrical double layer and the theory of electrocapillarity. Chemical Reviews 1947;41:441-501.

[8] Zhu Y, Murali S, Stoller MD, Ganesh KJ, Cai W, Ferreira PJ, et al. Carbon-based supercapacitors produced by activation of graphene. Science. 2011;332:1537-41.

[9] Miller JR, Burke AF. Electrochemical capacitors: challenges and opportunities for real-world applications. The Electrochemical Society Interface. 2008;17:53.

[10] Conway B. Electrochemical supercapacitors: scientific fundamentals and technological applications. New York: Kluwer Academic; 1999.

[11] Shukla A.K., Sampath S., Vijayamohanan K. Electrohcemical supercapacitor: energy storage beyond batteries. Current Science. 2000;79.

[12] Conway BE, Pell WG. Double-layer and pseudocapacitance types of electrochemical capacitors and their applications to the development of hybrid devices. Journal of Solid State Electrochemistry 2003;7:637-44.

[13] Zhi M, Xiang C, Li J, Li M, Wu N. Nanostructured carbon-metal oxide composite electrodes for supercapacitors: Review. Nanoscale. 2012.

[14] Simon P, Gogotsi Y. Materials for electrochemical capacitors. Nature Materials 2008;7:845-54.

[15] Kazaryan SA, Razumov SN, Litvinenko SV, Kharisov GG, Kogan VI. Mathematical model of heterogeneous electrochemical capacitors and calculation of their parameters. Journal of the Electrochemical Society 2006;153:A1655-A71.

[16] Portet C, Taberna PL, Simon P, Laberty-Robert C. Modification of Al current collector surface by sol–gel deposit for carbon–carbon supercapacitor applications. Electrochimica Acta 2004;49:905-12.

[17] Zhu Y, Zhitomirsky I. Influence of dopant structure and charge on supercapacitive behavior of polypyrrole electrodes with high mass loading. Synthetic Metals 2013;185–186:126-32.

[18] Su Y, Zhitomirsky I. Electrophoretic nanotechnology of composite electrodes for electrochemical supercapacitors. The Journal of Physical Chemistry B. 2012;117:1563-70.

[19] Shi K, Su Y, Zhitomirsky I. Characterization of Ni plaque based polypyrrole electrodes prepared by pulseelectropolymerization. Materials Letters 2013;96:135-8.

[20] Chen W, Rakhi RB, Hu L, Xie X, Cui Y, Alshareef HN. High-performance nanostructured supercapacitors on a sponge. Nano Letters 2011;11:5165-72.

[21] Pekala RW, Farmer JC, Alviso CT, Tran TD, Mayer ST, Miller JM, et al. Carbon aerogels for electrochemical applications. Journal of Non-Crystalline Solids 1998;225:74-80.

[22] Zhang L, Holt CMB, Luber EJ, Olsen BC, Wang H, Danaie M, et al. High rate electrochemical capacitors from three-dimensional arrays of vanadium nitride functionalized carbon nanotubes. The Journal of Physical Chemistry C. 2011;115:24381-93.

[23] Ruiz V, Blanco C, Raymundo-Piñero E, Khomenko V, Béguin F, Santamaría R. Effects of thermal treatment of activated carbon on the electrochemical behaviour in supercapacitors. Electrochimica Acta 2007;52:4969-73.

[24] Burke A. Ultracapacitors: why, how, and where is the technology. Journal of Power Sources 2000;91:37-50.

[25] Kötz R, Carlen M. Principles and applications of electrochemical capacitors. Electrochimica Acta 2000;45:2483-98.

[26] Ue M. Chemical capacitors and quaternary ammonium salts. Electrochemistry. 2007;75:565-72.

[27] Mastragostino M, Soavi F. Strategies for high-performance supercapacitors for HEV. Journal of Power Sources 2007;174:89-93.

[28] Rogers RD, Seddon KR. Ionic liquids-solvents of the future? Science. 2003;302:792-3.

[29] Seddon KR. Ionic liquids: A taste of the future. Nat Mater. 2003;2:363-5.

[30] Weingarth D, Noh H, Foelske-Schmitz A, Wokaun A, Kötz R. A reliable determination method of stability limits for electrochemical double layer capacitors. Electrochimica Acta 2013;103:119-24.

[31] Nanbu N, Ebina T, Uno H, Ishizawa S, Sasaki Y. Physical and electrochemical properties of quaternary ammonium bis(oxalato)borates and their application to electric double-layer capacitors. Electrochimica Acta 2006;52:1763-70.

[32] Gamby J, Taberna PL, Simon P, Fauvarque JF, Chesneau M. Studies and characterisations of various activated carbons used for carbon/carbon supercapacitors. Journal of Power Sources 2001;101:109-16.

[33] Shi H. Activated carbons and double layer capacitance. Electrochimica Acta 1996;41:1633-9.

[34] Qu D, Shi H. Studies of activated carbons used in double-layer capacitors. Journal of Power Sources 1998;74:99-107.

[35] Qu D. Studies of the activated carbons used in double-layer supercapacitors. Journal of Power Sources 2002;109:403-11.

[36] Kim YJ, Horie Y, Ozaki S, Matsuzawa Y, Suezaki H, Kim C, et al. Correlation between the pore and solvated ion size on capacitance uptake of PVDC-based carbons. Carbon. 2004;42:1491-500.

[37] Jurewicz K, Vix-Guterl C, Frackowiak E, Saadallah S, Reda M, Parmentier J, et al. Capacitance properties of ordered porous carbon materials prepared by a templating procedure. Journal of Physics and Chemistry of Solids 2004;65:287-93.

[38] Fernández JA, Morishita T, Toyoda M, Inagaki M, Stoeckli F, Centeno TA. Performance of mesoporous carbons derived from poly(vinyl alcohol) in electrochemical capacitors. Journal of Power Sources 2008;175:675-9.

[39] Salitra G, Soffer A, Eliad L, Cohen Y, Aurbach D. Carbon electrodes for double - layer capacitors I. relations between ion and pore dimensions. Journal of the Electrochemical Society 2000;147:2486-93.

[40] Gogotsi Y, Nikitin A, Ye H, Zhou W, Fischer JE, Yi B, et al. Nanoporous carbide-derived carbon with tunable pore size. Nat Mater. 2003;2:591-4.

[41] Béguin F, Presser V, Balducci A, Frackowiak E. Carbons and electrolytes for advanced supercapacitors. Advanced Materials 2014;26:2219-51.

[42] Frackowiak E. Carbon materials for supercapacitor application. Physical Chemistry Chemical Physics 2007;9:1774-85.

[43] Regisser F, Lavoie M-A, Champagne GY, Bédanger D. Randomly oriented graphite electrode. Part 1. Effect of electrochemical pretreatment on the electrochemical behavior and chemical composition of the electrode. Journal of Electroanalytical Chemistry 1996;415:47-54.

[44] Momma T, Liu X, Osaka T, Ushio Y, Sawada Y. Electrochemical modification of active carbon fiber electrode and its application to double-layer capacitor. Journal of Power Sources 1996;60:249-53.

[45] Béguin F, Szostak K, Lota G, Frackowiak E. A self-supporting electrode for supercapacitors prepared by one-step pyrolysis of carbon nanotube/polyacrylonitrile blends. Advanced Materials 2005;17:2380-4.

[46] Hulicova D, Yamashita J, Soneda Y, Hatori H, Kodama M. Supercapacitors prepared from melamine-based carbon. Chemistry of Materials 2005;17:1241-7.

[47] Pan H, Poh CK, Feng YP, Lin J. Supercapacitor electrodes from tubes-in-tube carbon nanostructures. Chemistry of Materials 2007;19:6120-5.

[48] Raymundo-Piñero E, Leroux F, Béguin F. A high-performance carbon for supercapacitors obtained by carbonization of a seaweed biopolymer. Advanced Materials 2006;18:1877-82.

[49] Baxter JB, Aydil ES. Nanowire-based dye-sensitized solar cells. Applied Physics Letters 2005;86:-.

[50] Novoselov KS, Geim AK, Morozov SV, Jiang D, Zhang Y, Dubonos SV, et al. Electric field effect in atomically thin carbon films. Science. 2004;306:666-9.

[51] Conway BE. Electrochemical supercapacitors: scientific fundamentals and technological applications: Springer US; 1999.

[52] Lee HY, Goodenough JB. Supercapacitor behavior with KCl electrolyte. Journal of Solid State Chemistry 1999;144:220-3.

[53] Toupin M, Brousse T, Bélanger D. Charge storage mechanism of MnO_2 electrode used in aqueous electrochemical capacitor. Chemistry of Materials 2004;16:3184-90.

[54] Yan W, Kim JY, Xing W, Donavan KC, Ayvazian T, Penner RM. Lithographically patterned gold/manganese dioxide core/shell nanowires for high capacity, high rate, and

high cyclability hybrid electrical energy storage. Chemistry of Materials 2012;24:2382-90.

[55] Ghodbane O, Pascal J-L, Favier F. Microstructural effects on charge-storage properties in MnO_2-based electrochemical supercapacitors. ACS Applied Materials & Interfaces 2009;1:1130-9.

[56] Hsieh Y-C, Lee K-T, Lin Y-P, Wu N-L, Donne SW. Investigation on capacity fading of aqueous $MnO_2 \cdot nH_2O$ electrochemical capacitor. Journal of Power Sources 2008;177:660-4.

[57] Hadži-Jordanov S, Angerstein-Kozlowska H, Conway BE. Surface oxidation and H deposition at ruthenium electrodes: Resolution of component processes in potential-sweep experiments. Journal of Electroanalytical Chemistry and Interfacial Electrochemistry 1975;60:359-62.

[58] Zheng JP, Cygan PJ, Jow TR. Hydrous ruthenium oxide as an electrode material for electrochemical capacitors. Journal of the Electrochemical Society 1995;142:2699-703.

[59] Hu C-C, Chen W-C, Chang K-H. How to achieve maximum utilization of hydrous ruthenium oxide for supercapacitors. Journal of the Electrochemical Society 2004;151:A281-A90.

[60] Lee JW, Hall AS, Kim J-D, Mallouk TE. A facile and template-free hydrothermal synthesis of Mn_3O_4 nanorods on graphene sheets for supercapacitor electrodes with long cycle stability. Chemistry of Materials 2012;24:1158-64.

[61] Wang S-Y, Ho K-C, Kuo S-L, Wu N-L. Investigation on capacitance mechanisms of Fe_3O_4 electrochemical capacitors. Journal of the Electrochemical Society 2006;153:A75-A80.

[62] Xia X-H, Tu J-P, Wang X-L, Gu C-D, Zhao X-B. Mesoporous Co_3O_4 monolayer hollow-sphere array as electrochemical pseudocapacitor material. Chemical Communications 2011;47:5786-8.

[63] Kuo S-L, Wu N-L. Electrochemical characterization on $MnFe_2O_4$/carbon black composite aqueous supercapacitors. Journal of Power Sources 2006;162:1437-43.

[64] Yuan C, Li J, Hou L, Lin J, Pang G, Zhang L, et al. Template-engaged synthesis of uniform mesoporous hollow $NiCo_2O_4$ sub-microspheres towards high-performance electrochemical capacitors. RSC Advances. 2013;3:18573-8.

[65] Choi D, Blomgren GE, Kumta PN. Fast and reversible surface redox reaction in nanocrystalline vanadium nitride supercapacitors. Advanced Materials 2006;18:1178-82.

[66] Xiao X, Peng X, Jin H, Li T, Zhang C, Gao B, et al. Freestanding mesoporous VN/CNT hybrid electrodes for flexible all-solid-state supercapacitors. Advanced Materials 2013/09/25;25:5091-7.

[67] Dong S, Chen X, Zhang X, Cui G. Nanostructured transition metal nitrides for energy storage and fuel cells. Coordination Chemistry Reviews 2013;257:1946-56.

[68] Eustache E, Frappier R, Porto RL, Bouhtiyya S, Pierson J-F, Brousse T. Asymmetric electrochemical capacitor microdevice designed with vanadium nitride and nickel oxide thin film electrodes. Electrochemistry Communications 2013;28:104-6.

[69] Pande P, Rasmussen PG, Thompson LT. Charge storage on nanostructured early transition metal nitrides and carbides. Journal of Power Sources 2012;207:212-5.

[70] Kelsall GH, Thompson I, Francis PA. Redox chemistry of H_2S oxidation by the British Gas Stretford process part IV: V-S-H2O thermodynamics and aqueous vanadium (v) reduction in alkaline solutions. Journal of Applied Electrochemistry 1993;23:417-26.

[71] Lu X, Wang G, Zhai T, Yu M, Xie S, Ling Y, et al. Stabilized TiN nanowire arrays for high-performance and flexible supercapacitors. Nano Letters 2012;12:5376-81.

[72] Shu D, Lv CJ, Cheng FK, He C, Yang K, Nan JM, et al. Enhanced capacitance and rate capability of nanocrystalline VN as electrode materials for supercapacitors. International Journal of Electrochemical Science 2013;8:1209-25.

[73] Sivakkumar SR, Saraswathi R. Performance evaluation of poly(N-methylaniline) and polyisothianaphthene in charge-storage devices. Journal of Power Sources 2004;137:322-8.

[74] Snook GA, Kao P, Best AS. Conducting-polymer-based supercapacitor devices and electrodes. Journal of Power Sources 2011;196:1-12.

[75] Lota K, Khomenko V, Frackowiak E. Capacitance properties of poly(3,4-ethylenedioxythiophene)/carbon nanotubes composites. Journal of Physics and Chemistry of Solids 2004;65:295-301.

[76] Mastragostino M, Arbizzani C, Soavi F. Polymer-based supercapacitors. Journal of Power Sources 2001;97–98:812-5.

[77] Ryu KS, Kim KM, Park N-G, Park YJ, Chang SH. Symmetric redox supercapacitor with conducting polyaniline electrodes. Journal of Power Sources 2002;103:305-9.

[78] Stejskal J, Gilbert R. Polyaniline. Preparation of a conducting polymer (IUPAC technical report). Pure and Applied Chemistry 2002;74:857-67.

[79] Ryu KS, Kim KM, Park YJ, Park N-G, Kang MG, Chang SH. Redox supercapacitor using polyaniline doped with Li salt as electrode. Solid State Ionics 2002;152–153:861-6.

[80] Faverolle F, Attias AJ, Bloch B, Audebert P, Andrieux CP. Highly conducting and strongly adhering polypyrrole coating layers deposited on glass substrates by a chemical process. Chemistry of Materials 1998;10:740-52.

[81] Farrokhpay S. A review of polymeric dispersant stabilisation of titania pigment. Advances in Colloid and Interface Science. 2009;151:24-32.

[82] Sarkar P, Nicholson PS. Electrophoretic deposition (EPD): Mechanisms, kinetics, and application to ceramics. Journal of the American Ceramic Society 1996;79:1987-2002.

[83] Boccaccini AR, Zhitomirsky I. Application of electrophoretic and electrolytic deposition techniques in ceramics processing. Current Opinion in Solid State and Materials Science 2002;6:251-60.

[84] Winter M, Brodd RJ. What are batteries, fuel cells, and supercapacitors? Chemical Reviews 2005;105:1021-.

[85] Mallika S, Kumar RS. Review on ultracapacitor-battery interface for energy management system. System. 2011;1:2.

[86] Mars P. Using supercapacitors to solve LED flash power issues for high resolution camera phones. Electronics world wireless world. 2006;113:34-9.

[87] Chan MS, Chau K, Chan C. Effective charging method for ultracapacitors. Journal of Asian Electric Vehicles. 2005;3:771-6.

[88] Lukic SM, Cao J, Bansal RC, Rodriguez F, Emadi A. Energy storage systems for automotive applications. IEEE Transactions on Industrial Electronics 2008;55:2258-67.

[89] Zheng J, Jow T, Ding M. Hybrid power sources for pulsed current applications. IEEE Transactions on Aerospace and Electronic Systems 2001;37:288-92.

[90] Dougal RA, Liu S, White RE. Power and life extension of battery-ultracapacitor hybrids. IEEE Transactions on Components and Packaging Technologies 2002;25:120-31.

[91] Sikha G, Popov BN. Performance optimization of a battery–capacitor hybrid system. Journal of Power Sources 2004;134:130-8.

[92] Catherino HA, Burgel JF, Shi PL, Rusek A, Zou X. Hybrid power supplies: A capacitor-assisted battery. Journal of Power Sources 2006;162:965-70.

Chapter 3 Problem statements and proposals

3.1 Problem statements

(i) Challenges of EPD technology for films forming of nanostructured materials

EPD is an important colloidal technique for the fabrication of inorganic, polymer and composite films for electronic, catalytic, biomedical, energy storage and other applications.[1] EPD is achieved via motion of charged particles in a suspension under an applied electric field, followed by particle coagulation and deposition at the electrode surface[2]. EPD technology has faced a new challenge with increasing interest in nanostructured materials[3]. The dispersion of nanoparticles in suspensions presents difficulties, attributed to their high surface area and strong tendency for agglomeration. It was found that particle size reduction introduced problems related to electric field induced agglomeration during EPD[4]. Moreover, stirring of suspensions containing very fine particles promoted their agglomeration and sedimentation, which reduced the EPD yield[4].

Despite the impressive progress achieved in the EPD of various materials, there is a need for simple and versatile methods for efficient chemical modification, dispersion, charging and deposition of colloidal nanoparticles. The chemical interactions of inorganic nanoparticles with charging or dispersing agents are especially important and must be well understood to predict the adsorption mechanism and dispersion efficiency[5].

(ii) Problems related to cathodic EPD of composite films

The electrochemical strategies for the fabrication of composite materials combined EPD of CNT or graphene and various electrochemical methods for the electrodeposition of inorganic and organic materials[6]. Composite films were obtained by cathodic and anodic EPD[7]. It is important to note that anodic EPD introduces inherent problems related to anodic oxidation and dissolution of non-noble metallic substrates. Moreover, anodic deposition has limited applications for the fabrication of composites. It is in this regard that metals can be deposited by cathodic electroplating methods. Various electrochemical techniques were developed for the cathodic electrosynthesis of oxides and hydroxides[4], whereas only limited number of oxide materials can be produced by anodic electrosynthesis methods.

(iii) Problems related to the forming of composite films

There is increasing interest in the EPD of nanocomposites, combining advanced functional properties of oxide nanoparticles and CNT[8]. EPD is especially attractive for the fabrication of MnO_2-CNT or MnO_2-graphene composites for application in electrochemical supercapacitors (ES). The interest in application of MnO_2 for electrodes of ES is attributed to high specific capacitance of this material. However, difficulties are attributed to the dispersion of MnO_2 nanoparticles and fabrication of suspensions of sufficient concentration [9] for application in EPD. CNT or graphene are usually added to MnO_2 in order to increase the electronic conductivity of the composite electrodes and improve the power density of ES[10]. The use of CNT or graphene as conductive additives offers benefits of their high surface area and low percolation threshold. However, the specific capacitances of CNT and graphene are low. Therefore, the

fabrication of MnO_2-CNT or MnO_2-graphene electrodes requires efficient dispersion of CNT and graphene and optimization of the CNT and graphene contents in the composites.

Significant effort has been invested in the development of functionalization strategies, which included both covalent and supramolecular approaches[11]. However, polymer "wrapping" and supramolecular dispersion methods often result in the formation of CNT and graphene bundles[12]. Many attempts have been made to improve wetting properties of CNT in solvents by oxidation in strong acids or mixtures of acids[13]. It was shown that under acidic conditions, defective sites in the CNT and graphene are attacked, resulting in the formation of fragmented CNT and graphene decorated with carboxylic and other oxygen-containing groups on their surface. These acidic groups electrostatically stabilized the CNT and graphene in suspensions and provided a negative charge for EPD[7]. However, the oxidation and functionalization strategies introduce defects on its sidewalls and reduce its electronic conductivity. In another approach, the charging of CNT for EPD was achieved by adsorption of metal ions from added metal salts[7]. It should be noted that the addition of metal salts results in lower suspension stability, attributed to increasing ionic strength of the suspension. The metal ions usually incorporate into the cathodic deposits as corresponding hydroxides and contaminate the deposits. However, metal hydroxides[14] or polymers[12] incorporated into the deposits provided improved film adhesion, due to their binding properties.

(iv) Additives with dual roles of dopants for PPy and dispersants for MWCNT

The success in application of PPy for energy storage in ES devices will depend largely on the development of efficient electrodes with high specific capacitance at high PPy mass loadings. However, it was found that the increase in active mass loading resulted in

increased electrode resistance and reduced capacitance[15]. Moreover, high active material loading results in worse capacitance retention at high scan rates or fast charge-discharges[16]. To solve this problem, composite electrodes of PPy and CNT were proposed[17], utilizing high capacitance of PPy and high conductivity of CNT.

The development of advanced dopants for PPy polymerization is a subject of intense experimental work[18]. It was demonstrated that with the variation of the dopant anion, the conductivity of the PPy thin films can differ by three orders of magnitude[19]. Considerable attention[20] has been given to the development of polyaromatic dopants, which promoted preferred orientation of pyrrole ring parallel to the electrode or growth surface and allowed enhanced conductivity. It was found[21] that dopants showed significant influence on the size and shape of PPy particles, electrochemical performance, voltage window and cyclic stability of PPy, prepared by chemical polymerization.

The use of polyaromatic dopants offers additional benefits for the fabrication of PPy - MWCNT composites. The dispersion of MWCNT in the PPy matrix is important for the fabrication of efficient electrodes. A critical property of the dispersant is its adsorption on the MWCNT surface.

(v) Improving energy and power density through enlarging voltage window

The voltage windows of aqueous symmetric ES, containing two similar MnO_2[22], PPy[23], or PPy-CNT composite[24] electrodes are typically about 0.9 V. The improvement in power-energy characteristics of ES can be achieved by the increase of voltage window. Larger voltage windows were achieved in asymmetric ES, containing polypyrrole based composites as positive electrodes and activated carbon as negative electrodes[25]. However, difficulties were attributed to low specific capacitance of

activated carbon electrodes, especially at high mass loadings[26]. Recent studies revealed high capacitance of VN-MWCNT electrodes at relatively high active mass loadings in the negative potential range in the Na_2SO_4 electrolyte. Therefore, VN-MWCNT composites are promising materials for the fabrication of asymmetric ES with increased voltage window.

3.2 Proposals and approaches

The objective of this investigation was the development and testing of supercapacitor electrodes and devices. It was achieved by

(i) Development of new methods for dispersion, electrophoretic deposition and co-deposition of MWCNT and MnO_2.

(ii) Development of new methods for cathodic deposition of MWCNT-graphene composites.

(iii) Development of pulse electrolytic deposition of porous MnO_2

(iv) Development of VN-MWCNT synthesis and its application for ES

(v) Discovery of new dopants and electrochemical active dopants for PPy

(vi) Synthesis of PPy coated MWCNT and its application for ES.

(vii) Analysis and optimization of microstructure of new materials

(viii) Fabrication and testing of symmetric and asymmetric devices, investigation of capacitance, impedance, power-energy characteristics, capacitance retention at different charge-discharge rates and cyclic stability.

References

[1] Boccaccini AR, Keim S, Ma R, Li Y, Zhitomirsky I. Electrophoretic deposition of biomaterials. Journal of the Royal Society Interface. 2010;7:S581-S613.

[2] Somarajan S, Hasan SA, Adkins CT, Harth E, Dickerson JH. Controlled electrophoretic deposition of uniquely nanostructured star polymer films. Journal of Physical Chemistry B. 2008;112:23-8.

[3] Boccaccini AR, Roether JA, Thomas BJC, Shaffer MSP, Chavez E, Stoll E, et al. The electrophoretic deposition of inorganic nanoscaled materials. Journal of the Ceramic Society of Japan. 2006;114:1-14.

[4] Zhitomirsky I. Cathodic electrodeposition of ceramic and organoceramic materials. Fundamental aspects. Advances in Colloid and Interface Science. 2002;97:277-315.

[5] Wu K, Wang Y, Zhitomirsky I. Electrophoretic deposition of TiO_2 and composite TiO_2-MnO_2 films using benzoic acid and phenolic molecules as charging additives. Journal of Colloid and Interface Science. 2010;352:371-8.

[6] Li X, Zhitomirsky I. Electrodeposition of polypyrrole-carbon nanotube composites for electrochemical supercapacitors. Journal of Power Sources 2013;221:49-56.

[7] Boccaccini AR, Cho J, Roether JA, Thomas BJC, Jane Minay E, Shaffer MSP. Electrophoretic deposition of carbon nanotubes. Carbon. 2006;44:3149-60.

[8] Boccaccini AR, Cho J, Subhani T, Kaya C, Kaya F. Electrophoretic deposition of carbon nanotube-ceramic nanocomposites. Journal of the European Ceramic Society. 2010;30:1115-29.

[9] Chin S-F, Pang S-C, Anderson MA. Material and electrochemical characterization of tetrapropylammonium manganese oxide thin films as novel electrode materials for electrochemical capacitors. Journal of the Electrochemical Society 2002;149:A379-A84.

[10] Li J, Yang QM, Zhitomirsky I. Nickel foam-based manganese dioxide-carbon nanotube composite electrodes for electrochemical supercapacitors. Journal of Power Sources. 2008;185:1569-74.

[11] Casagrande T, Lawson G, Li H, Wei J, Adronov A, Zhitomirsky I. Electrodeposition of composite materials containing functionalized carbon nanotubes. Materials Chemistry and Physics 2008;111:42-9.

[12] Grandfield K, Sun F, FitzPatrick M, Cheong M, Zhitomirsky I. Electrophoretic deposition of polymer-carbon nanotube-hydroxyapatite composites. Surface and Coatings Technology 2009;203:1481-7.

[13] Esumi K, Ishigami M, Nakajima A, Sawada K, Honda H. Chemical treatment of carbon nanotubes. Carbon. 1996;34:279-81.

[14] Nie C, Pan L, Liu Y, Li H, Chen T, Lu T, et al. Electrophoretic deposition of carbon nanotubes-polyacrylic acid composite film electrode for capacitive deionization. Electrochimica Acta. 2012;66:106-9.

[15] Shi K, Zhitomirsky I. Influence of current collector on capacitive behavior and cycling stability of Tiron doped polypyrrole electrodes. Journal of Power Sources 2013;240:42-9.

[16] Zhu Y, Zhitomirsky I. Influence of dopant structure and charge on supercapacitive behavior of polypyrrole electrodes with high mass loading. Synthetic Metals. 2013;185:126-32.

[17] Frackowiak E, Khomenko V, Jurewicz K, Lota K, Beguin F. Supercapacitors based on conducting polymers/nanotubes composites. Journal of Power Sources 2006;153:413-8.

[18] Carrillo I, De La Blanca ES, Redondo MI, Garcia MV, Gonzalez-Tejera MJ, Fierro JLG, et al. Influence of dopant anions on properties of polypyrrole nanocoated poly(styrene-co-methacrylic acid) particles. Synthetic Metals 2012;162:136-42.

[19] Mitchell GR, Davis FJ, Legge CH. Effect of dopant molecules on the molecular order of electrically-conducting films of polypyrrole. Synthetic Metals 1988;26:247-57.

[20] Hakansson E, Lin T, Wang H, Kaynak A. The effects of dye dopants on the conductivity and optical absorption properties of polypyrrole. Synthetic Metals 2006;156:1194-202.

[21] Han M, Chu Y, Han D, Liu Y. Fabrication and characterizations of oligopyrrole doped with dodecylbenzenesulfonic acid in reverse microemulsion. Journal of Colloid and Interface Science 2006;296:110-7.

[22] Su X, Yu L, Cheng G, Zhang H, Sun M, Zhang L, et al. Controllable hydrothermal synthesis of Cu-doped δ-MnO_2 films with different morphologies for energy storage and conversion using supercapacitors. Applied Energy 2014;134:439-45.

[23] Zhu Y, Zhitomirsky I. Influence of dopant structure and charge on supercapacitive behavior of polypyrrole electrodes with high mass loading. Synthetic Metals 2013;185–186:126-32.

[24] Zhu Y, Shi K, Zhitomirsky I. Polypyrrole coated carbon nanotubes for supercapacitor devices with enhanced electrochemical performance. Journal of Power Sources 2014;268:233-9.

[25] Fan L-Q, Liu G-J, Wu J-H, Liu L, Lin J-M, Wei Y-L. Asymmetric supercapacitor based on graphene oxide/polypyrrole composite and activated carbon electrodes. Electrochimica Acta 2014;137:26-33.

[26] Liu Y, Shi K, Zhitomirsky I. New colloidal route for electrostatic assembly of oxide nanoparticle-carbon nanotube composites. Colloids and Surfaces A: Physicochemical and Engineering Aspects. 2014;446:15-22.

Chapter 4 Experimental Procedures

4.1. Materials synthesis

(i) MnO_2 nanoparticles

MnO_2 nanoparticles were prepared by reduction of $KMnO_4$ using ethanol (Eq.4.1).

$$4MnO_4^- + 3CH_3CH_2OH \rightarrow 4MnO_2 + 3CH_3COO^- + OH^- + 4H_2O \quad (\textbf{Eq}.4.1)$$

50 mL dehydrated ethanol was added into 100 mL 0.21 M $KMnO_4$ solution under vigorous stirring for 24 hours. The black precipitation was collected using filtration and washed using 2 L water and 0.5 L dehydrated ethanol to remove ions and organics. The final powder was further dried in air for 48 hours and stored in desiccator. The full process is schematically shown in Fig.4.1 MnO_2 nanoparticles obtained using this method had an diameters varying from 30 to 60 nm.[1]

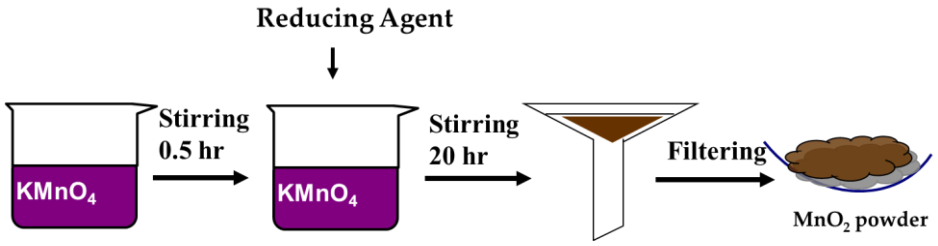

Fig.4.1 Schematic illustration of MnO_2 synthesizing process

(ii) VN nanoparticles and VN-MWCNT composite

The method for the fabrication of VN from V_2O_5 and melamine was similar to that described in the literature.[2, 3] In a typical procedure 0.5 g of V_2O_5 was dissolved in 80 mL of 0.14 M oxalic acid aqueous solution. After drying, the obtained powder was mixed

with 2.5 g of melamine and annealed at 800 ℃ in N_2 gas atmosphere during 3 h. This procedure was modified for the fabrication of a composite, containing VN (67 wt%) and MWCNT (33 wt%). In the modified procedure, MWCNT were dispersed in the oxalic acid solution, containing dissolved V_2O_5, using ultrasonication. After drying and mixing with melamine the obtained material was annealed at 800 ℃ in N_2 gas atmosphere during 3 h. The full process was illustrated schematically in Fig.4.2.

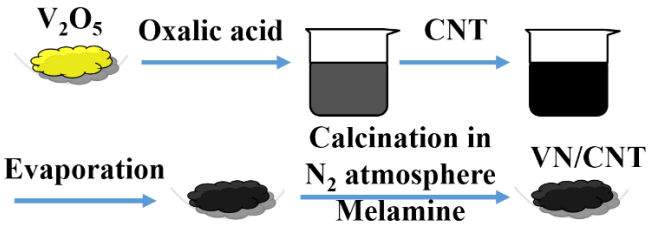

Fig.4.2 Schematic illustration of VN-MWCNT synthesizing process

(iii) PPy nanoparticles PPy coated MWCNT

In this synthesis, additives played both roles of dispersants for MWCNT and graphene and dopants for PPy. The additives used for the preparation of PPy included sulfanilic acid azochromotrop (SPADNS), sulfonazo III sodium salt (CHR-BS), 4-amino-5-hydroxynaphthalene-2,7-disulfonic acid monosodium salt hydrate (AHDA), and diamine green black (DAGB).

The method for the synthesis of PPy coated MWCNT (PPy-MWCNT) was based on the use of anionic dopants for PPy polymerization and dispersants for MWCNT. In a typical procedure, 1.25 g L^{-1} MWCNT was dispersed in 80 ml of ethanol using 5 mM dispersants (e.g. SPADNS, CHR-BS, AHDA, DAGB etc.) to form a homogeneous suspension under ultrasonication. The suspension was kept in ice-water bath for 1 hour under magnetic

stirring and then pyrrole (Py) was added. The MWCNT:PPy mass ratio was in the range of 1:9 to 3:7. Polymerization was performed by very slow addition of 55 mM APS to the suspension with the adding rate of 2 mL per minute. The reaction was performed during 24 h using ice-water bath. The precipitate was filtrated and dried in air for 24 hours. PPy nanoparticles were synthesized in the same way without MWCNT.

4.2 Film preparation using EPD and ELD techniques

ELD and EPD were performed using a constant current/constant voltage power supply (EPS 2A200, Amersham Biosciences). The whole procedure was schematically illustrated in Fig.4.3, where solvent was used for ELD and suspension was used for EPD. Stainless steel foils (2.5×5 cm) and Ni foams (1×3 cm) were used as substrates with platinum counter electrode. The distance between substrate and platinum counter electrode was 15 mm. Depending on whether it was cathodic reaction or anodic reaction, proper potential difference was applied to two electrodes. The deposition yield was measured using balance with 0.01 mg accuracy. The deposition yield-deposition time, deposition yield-concentration, and deposition yield-deposition voltage could be obtained with varying proper parameters during EPD and ELD.

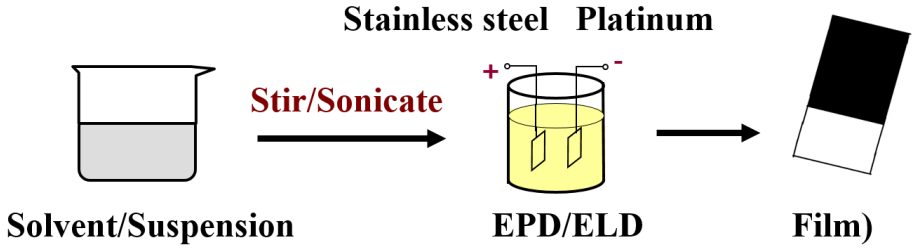

Fig.4.3 Schematic illustration of the procedure for EPD and ELD.

For pulse EPD and ELD (Keithley modle 2400 series sourcemeter), the voltage was

controlled to apply and stop for a very short time (less than 1 s). The ON time and OFF time and the ratio between them had great influence to the morphology of deposited film.

4.3 Materials characterization techniques

(i) Crystallinity study

X-ray diffraction (XRD) investigations were carried out using Bruker D8 diffractometer and Co Kα radiation.

(ii) Morphology study

Electron microscopy studies were performed using JEOL JSM-7000F scanning electron microscope (SEM) and FEI Tecnai Osiris transmission electron microscope (TEM) equipped with super X field emission gun (X-FEG) and ChemiSTEM^{TM} X-ray detection system for energy-dispersive X-ray (EDX) spectroscopy. High angle annular dark field (HAADF) method in the STEM mode was used to form images and perform EDX analysis. The Esprit software was used for elemental mapping.

(iii) Composition study

Fourier transform infrared spectroscopy (FTIR) studies were performed on Bio-Rad FTS-40 instrument. The Ultraviolet-Visible (UV-vis) spectra were obtained using a Cary-50 UV-Vis spectrophotometer. The thermogravimetric analysis (TGA) and differential thermal analysis (DTA) investigations were carried out in air at a heating rate of 5 ℃ min^{-1} using a Netzsch STA-409 thermoanalyzer.

(iv) *In-situ* deposit yield study

The deposition kinetics has been investigated in-situ using a quartz crystal microbalance

(QCM 922, Princeton Applied Research) controlled by a computer. The deposit mass Δm was calculated using Sauerbrey's equation (Eq.4.2).[4, 5]

$$\Delta F = \frac{2F_0^2}{A\sqrt{\rho_q \mu_q}} \times \Delta m \qquad \textbf{(Eq.}4.2\textbf{)}$$

where ΔF is the frequency decrease of the QCM, F_0 is the parent frequency of QCM (9 MHz), A is the area of the gold electrode (0.2 cm^2), ρ_q is the density of quartz (2.65 gcm^{-3}) and μ_q is the shear modulus of quartz (2.95×10^{11} dyne cm^{-2}).

4.4 Electrode fabrications using EPD and ELD

(i) MWCNT-MnO_2 composite films using 1-pyrenebutyric acid (PBH) as dispersant. PBH was dissolved in water at pH=8. The pH of the solutions was adjusted using NaOH. The aqueous EPD baths for deposition of PBH and composite films contained 0.1-2 g L^{-1} PBH, 0-1 g L^{-1} MWCNT and 0-4 g L^{-1} MnO_2. Before the deposition, the suspensions, containing MWCNT and MnO_2, were ultrasonicated for 30 min to achieve a homogeneous dispersion. Electrophoretic deposits were obtained on various conductive substrates, such as stainless steel and Pt foils and platinized silicon wafers (30×50 mm). The deposition was performed at constant voltages of 1-10 V. The deposition time was varied in the range of 0-10 min. After deposition, the deposits were dried in air for 48 h.

(ii) MWCNT-MnO_2 composite films using calconcarboxylic acid (CCA) as a dispersant

Electrophoretic deposits were obtained on stainless steel substrates (25×50 mm) using suspensions, containing 0-1 g L^{-1} MWCNT and 0-10 g L^{-1} MnO_2 in ethanol. The concentration of chromotrope FB (CFB) and CCA in the suspensions was varied in the range of 0-1 g L^{-1}. Before the deposition, the suspensions were ultrasonicated for 30 min

to achieve a homogeneous dispersion. The deposition was performed at constant voltages of 20-60 V. The deposition time was varied in the range of 0-10 min. After deposition, the deposits were dried in air for 48 h.

(iii) MWCNT-graphene composite film using crystal violet as a dispersant

EPD was performed from aqueous 0.1-1 g L^{-1} crystal violet solutions containing 0-1 g L^{-1} MWCNT or graphene. The solutions were ultrasonicated for 10 min in order to achieve homogeneous dispersions of MWCNT or graphene. The deposition voltage for MWCNT dispersions was varied in the range of 1-10V, whereas the deposition from graphene dispersions was achieved at voltages of 10-50V. Cathodic deposits were obtained on stainless steel and platinized silicon wafer substrates. The deposition time was varied in the range of 0-10 min. After deposition, the deposits were dried in air for 48 h.

(iv) MWCNT-graphene composite film using methyl violet as a dispersant

The deposition of methyl violet was performed at constant voltages in the range of 5-20 V from aqueous 0.1-1 g L^{-1} MV solutions. The deposition process was studied using CV at a scan rate of 20 mV s^{-1}. Aqueous MWCNT and graphene suspensions for EPD, containing dissolved methyl violet as dispersant, were ultrasonicated for 30 min to achieve homogeneous dispersions. EPD was performed at deposition voltages of 1-11 V and 20-50 V for MWCNT and graphene suspensions, respectively, from their aqueous suspensions with concentrations varying in the range of 0.1-1 g L^{-1}. Stainless steel foils (2.5×5 cm) were polished, washed with distilled water and used as substrates for EPD. A constant voltage EPD was performed using a power supply. The deposits were dried in air for 24 hours.

(v) Pulse deposition of porous MnO_2 films on Ni foam electrode

Commercial Ni plaques with 80% volume porosity and thickness of 1.8 mm (Vale Company) were used as substrates. Pulse electrosynthesis was performed from prepared 10 mM $KMnO_4$ solutions, containing 50 mM Na_2SO_4 as a supporting electrolyte. Electrosynthesis was performed in a pulse regime at a current density of 1 mA cm^{-2} during the ON time, which was varied from 0.01 to 0.5 s, and ON/OFF time ratio of 0.5.

4.5 Electrode and ES device fabrications using impregnation

Powder was fabricated into electrode using slurry impregnation. In a typical procedure, nanoparticles of electrochemical active materials (e.g. MnO_2, VN etc.) and carbon materials (e.g. AC, MWCNT, graphen etc.) with proper mass ratio were mixed under grinding in ethanol with 5 wt% PVB (Polyvinyl butyral) binder. The slurry was then pasted on Ni foam current collector (95 vol% porosity) in an area of 1×1 cm^2 with an areal density from 5 mg cm^{-2} to 50 mg cm^{-2}. Once dried, the electrode was pressed into 20% of its original thickness using roller to improve contacting between electrode material and current collector.

Different types of ES devices were prepared. The separator of all ES device was a porous polyethylene membrane (mean pore size 0.4 μm, Vale, Canada). The coin cell devices (CR2032 type, MTI Corporation, USA) were sealed using a hydraulic crimping machine (MSK-110, MTI Corporation, USA). The fabricated devices included (i) VN-MWCNT/MnO_2-MWCNT asymmetric ES device, (ii) PPy-MWCNT/PPy-MWCNT symmetric ES device, and (iii) VN-MWCNT/PPy-MWCNT symmetric ES device.

4.6 Electrochemical characterization

(i) Cyclic voltammetry

Cyclic voltammety (CV) of single electrodes, coin cell devices, and modules of several devices was tested using a potentiostat (PARSTAT 2273, Princeton Applied Research). Single electrodes were tested using three electrodes setup (Fig.4.4), where the reference electrode and counter electrode were the standard calomel electrode (SCE) and platinum gauze, respectively.

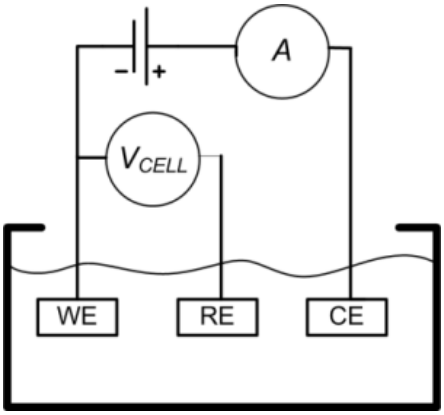

Fig.4.4 Three electrodes sensor topology.

CV was performed in 0.5 M Na_2SO_4 aqueous electrolyte. The scan rates for CVs were varying from 2 mV s^{-1} to 100 mV s^{-1}. The SC was calculated using half the integrated area of the CV curve to obtain the charge (Q), and subsequently dividing the charge by the width of the potential window (ΔU) and film mass (m) for gravimetric SC (C_m, Eq.4.3) or area (S) for areal SC (C_S, Eq.4.4).

$$C_m = \frac{Q}{\Delta U \cdot m} \quad \textbf{(Eq.}4.3\textbf{)}$$

$$C_S = \frac{Q}{\Delta U \cdot S} \quad \textbf{(Eq.}4.4\textbf{)}$$

(ii) Electrochemical impedance spectroscopy

The electrochemical impedance spectroscopy (EIS) was also tested using a potentiostat (PARSTAT 2273, Princeton Applied Research) in a frequency (*f*) range of 10 mHz-100 kHz under sinusoidal signal with amplitude of 5 mV to obtain the complex impedance (Eq.4.5). The EIS in Nyquist plot were simulated using a ZSimpWin (Princeton Applied Research) and equivalent circuit was given to each Nyquist plot.

$$Z^{*}=Z'-i\cdot Z'' \quad \textbf{(Eq.}4.5\textbf{)}$$

The complex capacitance (C^{*}, Eq.4.6) was calculated from corresponding impedance data. The real part (C', Eq.4.7) reflected the capacitance performance and the imaginary part (C'', Eq.4.8) reflected the energy dispersion of ES electrode or device.[6]

$$C^{*}=C'-iC'' \quad \textbf{(Eq.}4.6\textbf{)}$$

$$C' = \frac{Z''}{2\pi f Z^2} \quad \textbf{(Eq.}4.7\textbf{)}$$

$$C'' = \frac{Z'}{2\pi f Z^2} \quad \textbf{(Eq.}4.8\textbf{)}$$

(iii) Cyclic charge-discharge

Cyclic charge-discharge is a technique to characterize capacitive performance and cyclic stability of ES devices. A complete charge and discharge loop is called one charge-discharge cycle.

The charge-discharge loops were conducted at constant current (I) varying from 0.1 mA to 50 mA with voltage limits (ΔU) of 0.9 V for PPy-PPY devices, 1.3 V for PPy-VN devices, and 1.8 V for MnO_2-VN devices using charge-discharge analyzer (BST8, MTI

Corporation). The total charge (Q) was calculated (Q=I ŧ, t-discharging time) from each cycle and the capacitance (C) is calculated from Eq.4.3 and Eq.4.4.

The energy density (E_d) and power density (P_d) was calculated from Eq.4.9 and Eq.4.10, respectively, for each charge-discharge at different constant currents, where t is the discharging time and m is the electrode mass. Ragone plot was obtained from energy density and power density data.

$$E_d = \frac{\int_0^t UIdt}{m} \quad \textbf{(Eq.}4.9\textbf{)}$$

$$P_d = \frac{E_d}{t} \quad \textbf{(Eq.}4.10\textbf{)}$$

References

[1] Cheong M, Zhitomirsky I. Electrophoretic deposition of manganese oxide films. Surface Engineering 2009;25:346-52.

[2] Shu D, Lv CJ, Cheng FK, He C, Yang K, Nan JM, et al. Enhanced capacitance and rate capability of nanocrystalline VN as electrode materials for supercapacitors. International Journal of Electrochemical Science 2013;8:1209-25.

[3] Cheng F, He C, Shu D, Chen H, Zhang J, Tang S, et al. Preparation of nanocrystalline VN by the melamine reduction of V_2O_5 xerogel and its supercapacitive behavior. Materials Chemistry and Physics 2011;131:268-73.

[4] Sauerbrey G. Verwendung von schwingquarzen zur wägung dünner schichten und zur mikrowägung. Zeitschrift für Physik A Hadrons and Nuclei. 1959;155:206-22.

[5] Deakin MR, Buttry DA. Electrochemical applications of the quartz crystal microbalance. Analytical Chemistry 1989;61:1147A-54A.

[6] Taberna PL, Simon P, Fauvarque JF. Electrochemical characteristics and impedance spectroscopy studies of carbon-carbon supercapacitors. Journal of the Electrochemical Society 2003;150:A292-A300.

Chapter 5 Pulse electrosynthesis of MnO_2 electrodes for supercapacitors

5.1 Electrosynthesis of MnO_2 from $KMnO_4$ solution using pulse ELD

Cathodic electrosynthesis allowed the impregnation of Ni plaques with MnO_2. Fig.5.1 shows electrosynthesis yield data for various conditions. The deposit mass increased with increasing deposition time (Fig.5.1A), indicating the possibility of mass loading variation in the range of 0.1-13 mg cm^{-2}. The deposition rate increased with increasing pulse duration (ON) in the range of 0.01-0.1 s and remained nearly constant at higher pulse duration (Fig.5.1B). The result indicated that the use of Ni plaque current collectors allowed significantly higher deposition yields, compared to the metal foil substrates[1, 2].

It is in this regard that for commercial applications in supercapacitors, materials loading of about 10 mg cm^{-2} are required[3]. The results presented in Fig.5.1A indicated that such materials loadings can be achieved by cathodic electrosynthesis using $KMnO_4$ solutions. In this strategy, the difficulties related to anodic electrodeposition on non-noble substrates with high surface area can be avoided. Anodic electrodeposition on non-noble substrates of high surface area presents difficulties, related to the anodic oxidation and dissolution of the substrates.

The deposition yield in the impregnation process is influenced by various factors. The method used in this investigation involved the application of anionic MnO_4^- species for cathodic electrosynthesis of MnO_2. Therefore, electric field provided electromigration of the anionic species away from the electrode. When a negatively charged MnO_4^- ion is reduced cathodically, it has to approach the cathode by diffusion against an adverse

potential gradient. However, electric screening effect can be expected inside the porous metallic Ni plaque structure. The OFF time in the pulse deposition process was essential for the supply of MnO_4^- ions to the inner surfaces of the Ni plaque substrates.

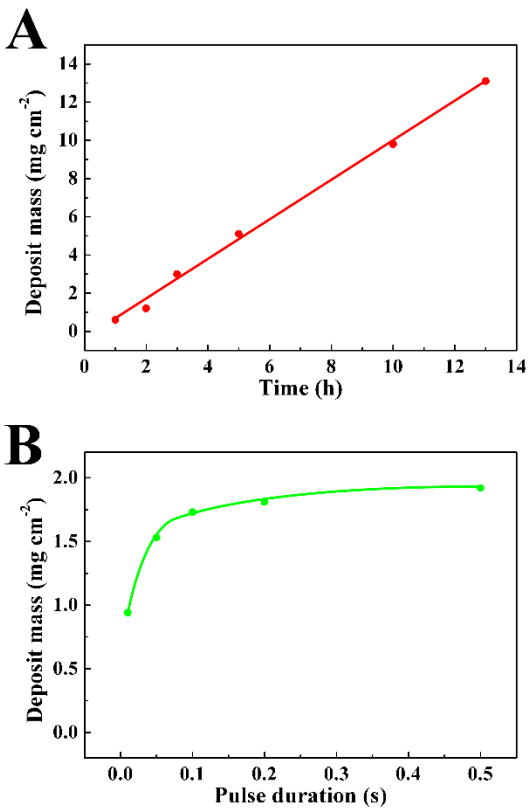

Fig.5.1 Deposit mass (A) versus total deposition (ON) time at a pulse duration (ON) of 0.05 s and (B) versus pulse duration at a total deposition time of 2 h.

5.2 Morphology study of electrosynthesized MnO_2 film on Ni plaques

The Ni plaques, impregnated with MnO_2 were studied by SEM. Fig.5.2 shows impregnated Ni plaque with MnO_2 loading of 3 mg cm^{-2}. The SEM images shown in Fig.5.2A,B indicated that individual Ni particles were coated with MnO_2 and large pores of Ni plaques remained open. Such pores are beneficial for good electrolyte access to the active material. The SEM image at higher magnification (Fig.5.2C) showed that MnO_2

formed porous coating on Ni particles with typical pore size of about 50 nm. Further increase in materials loading resulted in gradual filling the voids between the individual Ni particles.

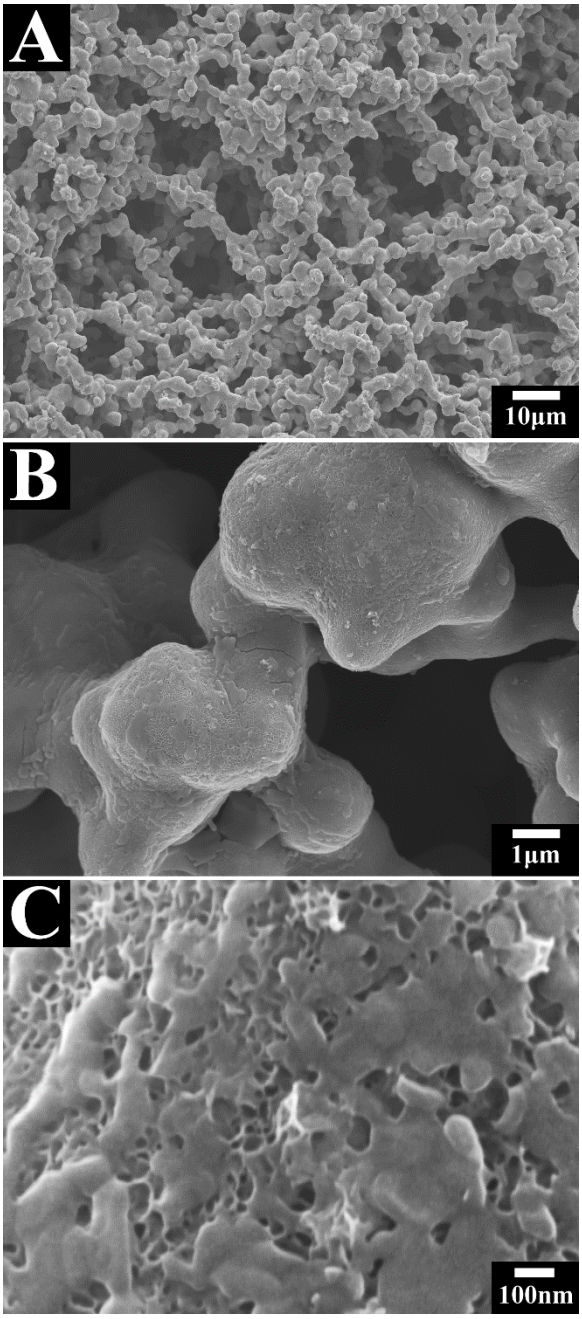

Fig.5.2 (A, B, C) SEM images at different magnifications for impregnated Ni plaque with MnO_2 loading of 3 mg cm^{-2}.

Fig.5.3 shows SEM images at different magnifications for impregnated Ni plaque with materials loading of 13 mg cm^{-2}. The low magnification image (Fig.5.3A) indicates significant reduction in porosity, compared with Fig.5.2(A), however many large pores remained open. The MnO_2 surface layer showed cracks. The observation of a cracked area (Fig.5.3B) indicated that relatively dense surface layer was formed, however inner layer has higher microporosity. Figs.5.3C,D shows microstructures of porous inner layer and dense surface layers, respectively, at higher magnification. The inner layer has typical pores of about 200-300 nm (Fig.5.3C). The pore size of the surface layer was below 20 nm.

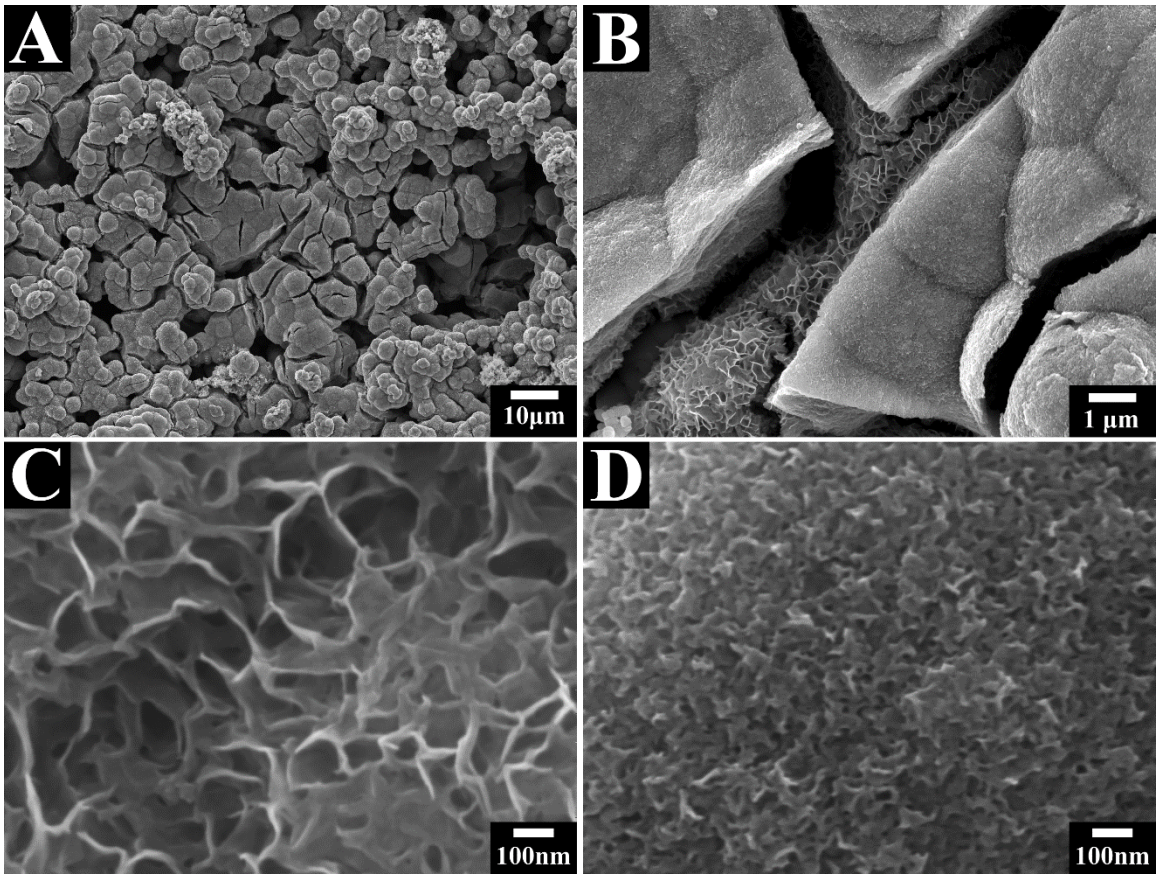

Fig.5.3 (A, B, C, D) SEM images at different magnifications for impregnated Ni plaque with MnO_2 loading of 13 mg cm^{-2}, where (C) shows the structure of an inner porous

layer and (D) shows the structure of a surface dense layer.

5.3 Electrochemical capacitive performance of porous MnO_2 films

Fig.5.4 shows typical CVs for electrodes prepared by pulse electrosynthesis. The box shape of the CVs obtained at a scan rate as high as 200 mV s^{-1} indicated good capacitive behavior. The electrodes, prepared at a pulse duration of 0.05 s showed improved CV shape and higher capacitance, compared to the electrodes prepared at pulse duration of 0.5 s. Good capacitance retention was observed in the range of 2-200 mV s^{-1}. The electrodes with mass loading of 1.5 mg cm^{-2} showed a specific capacitance of 252 F g^{-1} at a scan rate of 2 mV s^{-1} for single electrode.

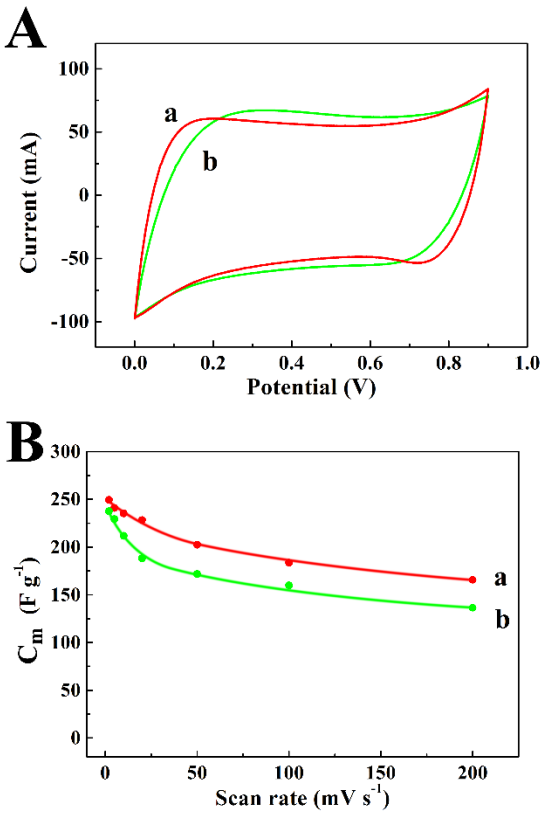

Fig.5.4 (A) CVs at a scan rate of 200mV s^{-1} and (B) specific capacitance versus scan rate for 1.5 mg cm^{-2} MnO_2 electrodes prepared at pulse duration of (a) 0.05 s and (b) 0.5 s.

Fig.5.5 compares CV data for electrodes of different mass prepared at a pulse duration of 0.05 s. The box shape CVs and the increase in current with increasing scan rate and increasing mass loading indicated good capacitive behavior.

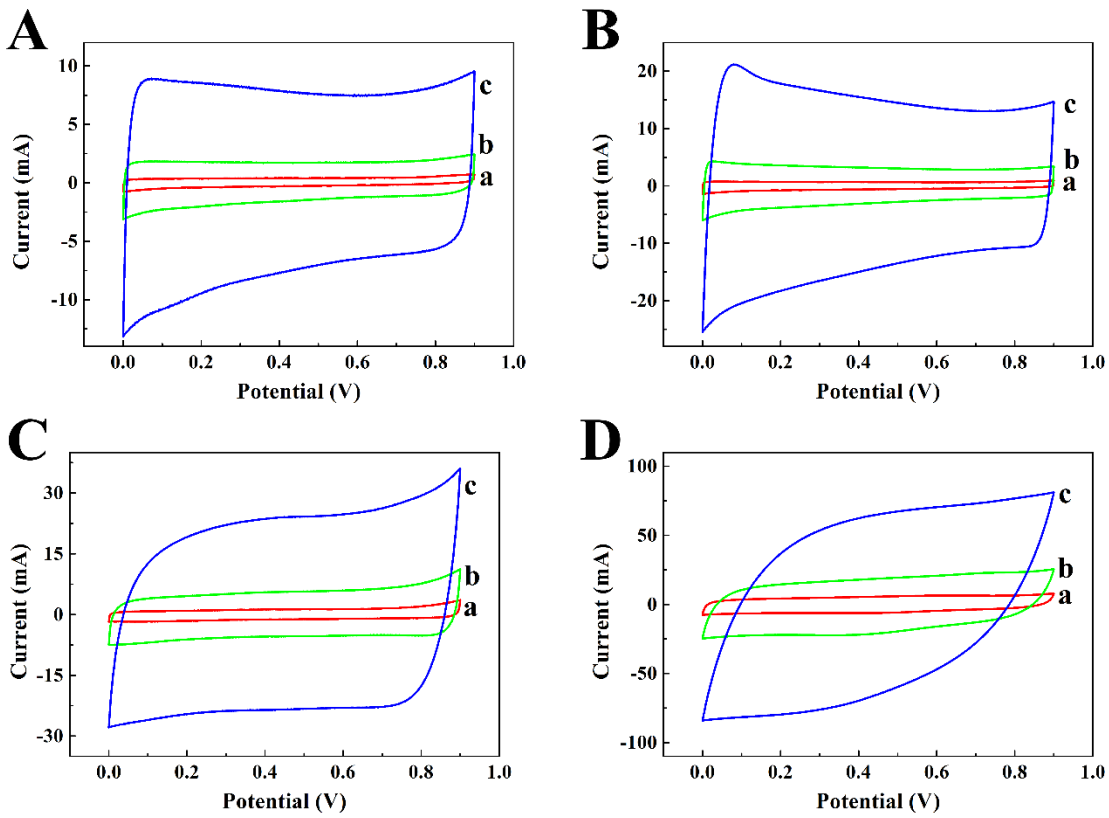

Fig.5.5 CVs for electrodes with mass loading of (A)0.6, (B)1.2, (C)3.0 and (D) 13 mg cm^{-2} prepared at a pulse duration of 0.05 s at scan rates of (a) 2, (b) 10 and (c) 50 mV s^{-1}.

The specific capacitance was calculated from the CV data and presented in Fig.5.6. The electrodes with mass loading of 0.6 and 1.2 mg cm^{-2} showed C_m of 320 and 270 F g^{-1}, respectively at a scan rate of 2 mV s^{-1}. The electrodes showed a capacitance retention above 90% at a scan rate of 100 mV s^{-1} and above 85% at a scan rate of 200 mV s^{-1}. In contrast, thin film electrodes[1] with mass loading of 0.1 mg cm^{-2} showed a capacitance retention of only 28% at a scan rate of 100 mV s^{-1}. The increase in film mass above 0.1

mg cm^{-2} resulted in further reduction of capacitance retention[1]. Fig.5.6 indicates that electrodes with mass loading of 3 and 13 mg cm^{-2} showed C_m of 248 and 199 F g^{-1} and capacitance retention of 68 and 40%, respectively, at a scan rate of 100 mV s^{-1}. Therefore, the use of Ni plaques allowed significant increase in materials loading, relatively high C_m and improved capacitance retention.

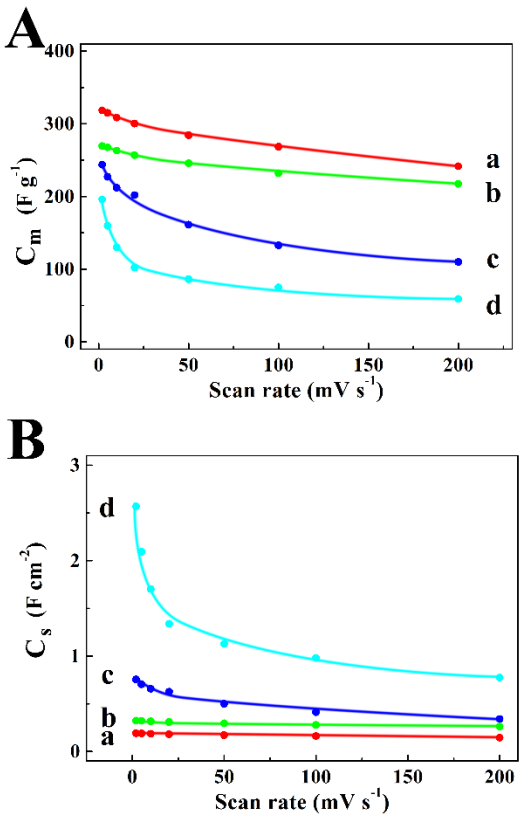

Fig.5.6 (A) C_m and (B) C_s versus scan rate for electrodes with mass loading of (a)0.6, (b)1.2, (c)3.0 and (d) 13 mg cm^{-2} prepared at a pulse duration of 0.05 s.

It is important to note that high mass normalized specific capacitance C_m doesn't necessarily indicate good capacitive behavior[3]. High C_m can be achieved in thin films with low materials loadings at low scan rates. The increase in materials loadings and increasing scan rates results in lower C_m. The analysis of area normalized specific

capacitance (C_s) showed that limited electrolyte access to the bulk of a thick dense film resulted in poor capacitive behavior[4]. Such a bulk layer behaved as a capacitor with low capacitance, connected in series with a capacitive surface layer, and reduced the total capacitance of the film. In the previous investigations the increase in electrode mass resulted in increasing C_s at low scan rate, but decreasing C_s at high scan rates[4]. In contrast, the experimental results, presented in Fig.5.6B, indicated that the increase in mass loading resulted in increasing C_s at scan rates in the range of 2-200mVs^{-1}. The C_s of 2.6 F cm^{-2} was achieved at materials loading of 13 mg cm^{-2}.

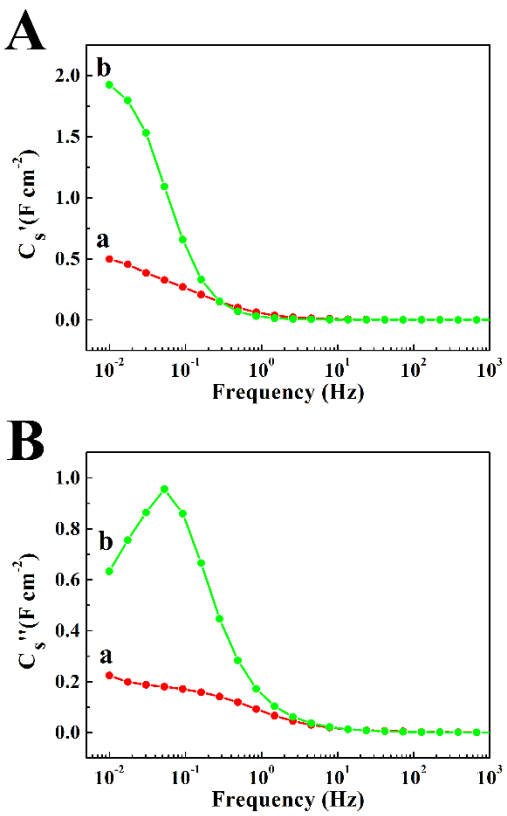

Fig.5.7 (A) C_s' and (B) C_s" calculated from EIS data versus frequency for MnO_2 electrodes with mass loadings of (a) 3 and (b) 13 mg cm^{-2}.

Fig.5.7A,B shows frequency dependencies of components of complex AC capacitance,

calculated from the EIS data. Fig.5.7A indicates that C_s' decreased with increasing frequency, indicating relaxation type of frequency dispersion[5]. The C_s'' for 13 mg cm^{-2} electrode showed (Fig.5.7B) well defined relaxation maximum[5]. The increase in mass loading resulted in increasing C_s'.

It is important to compare the specific capacitances derived from the CV and EIS data. Such data analysis is usually performed at the same time scale, because the voltammetric capacitance depends on a scan rate, whereas AC capacitance depends on frequency. The comparison of experimental data at the same time scale showed that C_s'=1.09 F cm^{-2} at 56 mHz is comparable with C_s=0.97 F cm^{-2} obtained at a scan rate of 100 mV s^{-1} for the electrode with mass loading of 13 mg cm^{-2}.

Fig.5.8A,B shows galvanostatic charge-discharge behavior at different current densities for 3 and 13 mg cm^{-2} electrodes. The charging and discharging curves were nearly linear and symmetrical, indicating good capacitive performance. The reduced discharge times for 13 mg cm^{-2} electrode, compared to 3 mg cm^{-2} electrode, was attributed to lower C_m in agreement with the data presented in Fig.5.6A. The Power density and Energy density, calculated from the galvanostatic discharge data were presented in a Ragone plot, shown in Fig.5.8C. The reduction in C_m, Power density and Energy density with increasing materials loading is usually attributed to diffusion limitation of electrolyte in pores of electrode materials[6]. The analysis of the Ragone plots indicated that SE of 20 Wh kg^{-1} and SP of 28 kW kg^{-1} for 13 mg cm^{-2} electrodes are relatively high in comparison with the literature data[3]. The electrode with lower mass showed higher Power density and Energy density.

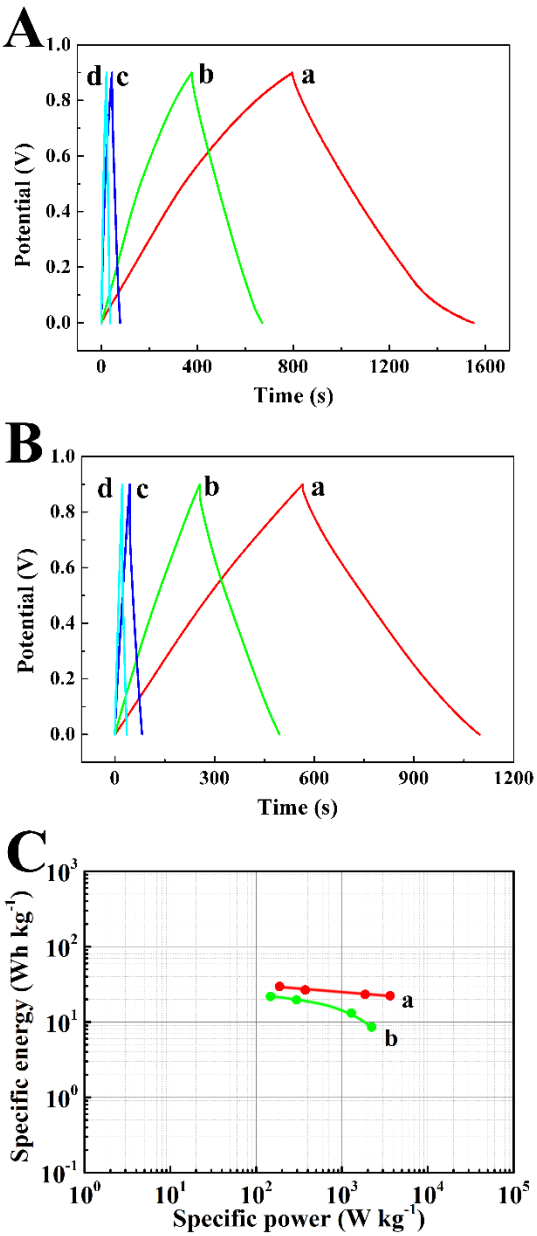

Fig.5.8 (A,B) Galvanostatic charge-discharge curves at currents of (a) 0.39, (b) 0.78, (c) 3.9 and (d) 7.8 A g^{-1} for electrodes with MnO_2 mass loading of (A) 3 and (B) 13 mg cm^{-2}. (C) Ragone plots for electrodes with MnO_2 mass loading of (a) 3 and (b) 13 mg cm^{-2}.

According to the literature [7-10] MnO_2 electrodes with high materials loading exhibit low capacitance and low power-energy characteristics due to the insulating properties of MnO_2. Improved capacitive behavior is usually achieved using conductive additives, such

as carbon nanotubes and graphene[7, 8]. Difficulties are attributed to relatively high cost of such additives and their poor dispersibility. In contrast, in this investigation relatively high capacitance, good capacitance retention at high scan rates and good power-energy characteristics were achieved without additives. Therefore the MnO_2 electrodes prepared by the pulse deposition method using Ni plaque current collectors are promising for application in supercapacitors.

5.4 Conclusions

Cathodic pulse deposition method has been developed for the electrosynthesis of MnO_2 electrodes using porous Ni plaque current collectors. The method allowed the variation of materials loading in the range of 0.1-13 mg cm^{-2}. The C_s of 2.6 F cm^{-2} (199 F g^{-1}), Energy density of 20 Wh kg^{-1} and Power density of 28 kW kg^{-1} were achieved for 13 mg cm^{-2} electrodes. The electrodes with lower mass loadings showed higher specific capacitance and higher power-energy characteristics. The electrodes showed improved capacitance retention at high scan rates.

Good electrochemical performance of MnO_2 electrodes was achieved without conductive additives. The Ni plaque based MnO_2 electrodes are promising for energy storage applications in electrochemical supercapacitors.

References

[1] Wei J, Nagarajan N, Zhitomirsky I. Manganese oxide films for electrochemical supercapacitors. Journal of Materials Processing Technology 2007;186:356-61.

[2] Wei J, Zhitomirsky I. Electrosynthesis of manganese oxide films. Surface Engineering. 2008;24:40-6.

[3] Gogotsi Y, Simon P. True performance metrics in electrochemical energy storage. Science. 2011;334:917-8.

[4] Shi K, Zhitomirsky I. Influence of current collector on capacitive behavior and cycling stability of Tiron doped polypyrrole electrodes. Journal of Power Sources 2013;240:42-9.

[5] Shi K, Zhitomirsky I. Polypyrrole nanofiber-carbon nanotube electrodes for supercapacitors with high mass loading obtained using an organic dye as a co-dispersant. Journal of Materials Chemistry A. 2013;1:11614-22.

[6] Kötz R, Carlen M. Principles and applications of electrochemical capacitors. Electrochimica Acta 2000;45:2483-98.

[7] Zhang S, Peng C, Ng KC, Chen GZ. Nanocomposites of manganese oxides and carbon nanotubes for aqueous supercapacitor stacks. Electrochimica Acta. 2010;55:7447-53.

[8] Brousse T, Taberna P-L, Crosnier O, Dugas R, Guillemet P, Scudeller Y, et al. Long-term cycling behavior of asymmetric activated carbon/MnO_2 aqueous electrochemical supercapacitor. Journal of Power Sources. 2007;173:633-41.

[9] Reddy RN, Reddy RG. Sol-gel MnO_2 as an electrode material for electrochemical capacitors. Journal of Power Sources. 2003;124:330-7.

[10] Jiang R, Huang T, Tang Y, Liu J, Xue L, Zhuang J, et al. Factors influencing MnO_2/multi-walled carbon nanotubes composite's electrochemical performance as supercapacitor electrode. Electrochimica Acta 2009;54:7173-9.

Chapter 6 Electrophoretic nanotechnology of composite electrodes for ESs

6.1 Structure comparison between CCA and CFB

Fig.6.1A,B compares structures of CFB and CCA used in this investigation. CFB and CCA are aromatic compounds with conjugated bonds. The anionic properties of CFB (Fig.6.1A) are related to SO_3^- groups, whereas the anionic properties of CCA (Fig.6.1B) are attributed to SO_3^- and COO^- groups. The structures of CFB and CCA include OH groups bonded to the aromatic rings. CFB and CCA were investigated for the dispersion of MnO_2 and MWCNT in ethanol and EPD of MnO_2, MWCNT and composite films.

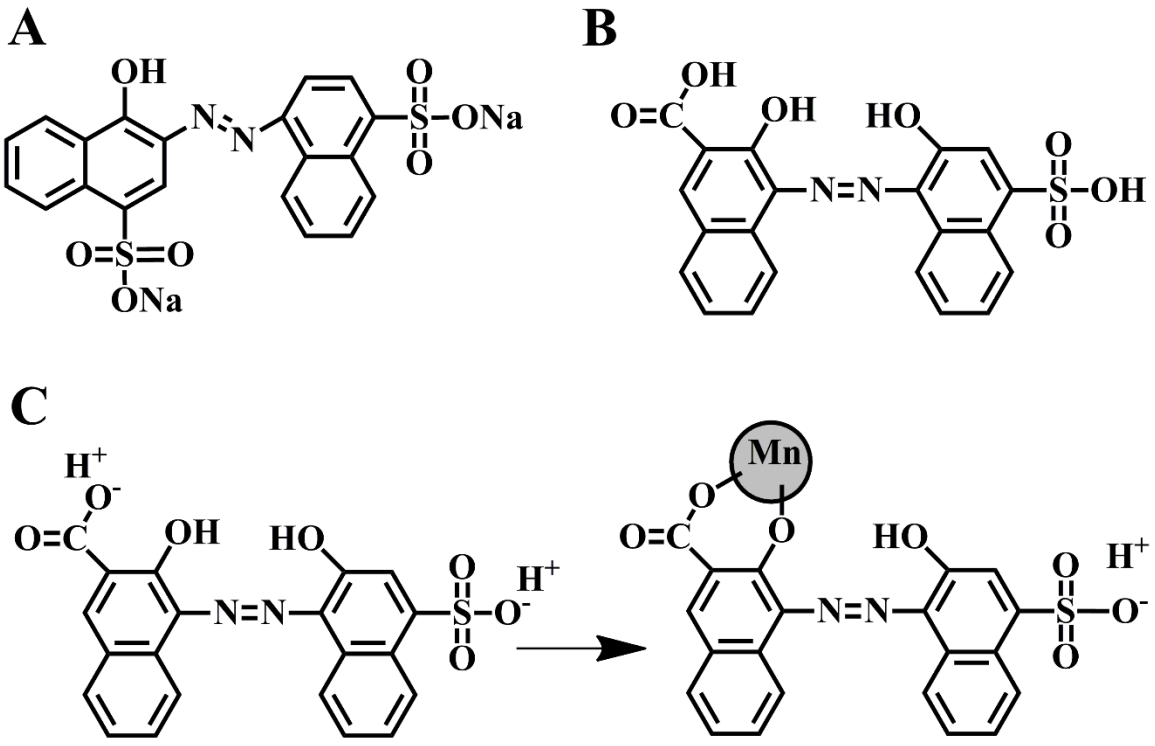

Fig.6.1 (A) Chemical structure of CFB, (B) chemical structure of CCA and (C) mechanism of CCA adsorption on MnO_2 particles.

6.2 Adsorption mechanism of CCA on MnO_2 nanoparticles

The suspensions of MnO_2 in ethanol were unstable and showed significant sedimentation 10h after the ultrasonic agitation. The addition of 0.05-0.8 g L^{-1} CFB or 0.05-0.15 g L^{-1} CCA to the MnO_2 suspensions resulted in reduced suspension stability. However, stable suspensions of MnO_2 were obtained at CCA concentrations of 0.3-0.8 g L^{-1}. Fig.6.2a,b shows 4 g L^{-1} MnO_2 suspensions without CCA and containing 0.8 g L^{-1} CCA 3 months after the ultrasonic agitation. Fig.6.2b indicates excellent colloidal stability of the MnO_2 suspension, containing CCA. It is known that the formation of stable suspensions of MnO_2 nanoparticles with concentration above 1 mM (0.09 g L^{-1}) presents difficulties[1]. The dilute suspensions with MnO_2 concentration below 1mM cannot be used for practical applications of EPD because the deposition rate in the EPD process is proportional to the particle concentration in the suspensions[2]. The use of CCA allowed the formation of stable suspensions of MnO_2 with concentration of 1-10 g L^{-1}.

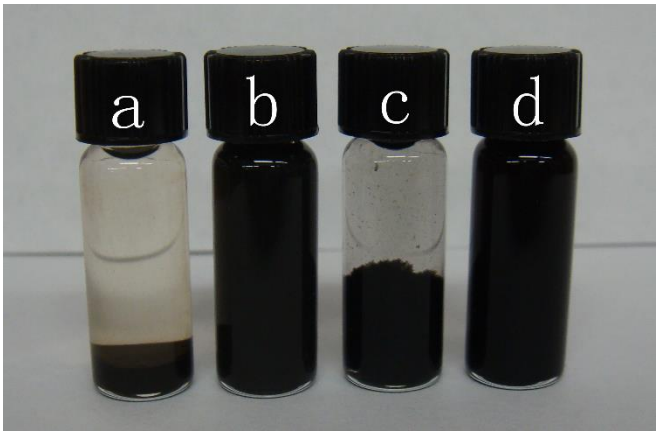

Fig.6.2 Suspensions of MnO_2: (a) without CCA and (b) containing CCA and suspensions of MWCNTs: (c) without CCA and (d) containing CCA. Suspensions (b) and (d) were stable for more than 3 months.

EPD from MnO_2 suspensions in ethanol resulted in the formation of cathodic deposits, indicating that MnO_2 particles were positively charged in the suspensions. However, as pointed out above, the suspensions exhibited very poor stability. As a result, the cathodic deposits obtained from the MnO_2 suspensions were non-uniform and contained agglomerated particles. The mechanism of inorganic particle charging in ethanol was discussed in the literature. Damodaran and Moudgil have proposed[3] a mechanism, in which the alcohol, adsorbed on a particle, ionized into a protonated alcohol and an alkoxide ion, followed by the dissociation of the protonated alcohol. Pure alcohols can ionize in the following way

$$RCH_2OH + RCH_2OH \rightarrow RCH_2O^- + RCH_2OH_2^+ \quad (\textbf{Eq.}6.1)$$

The dissociated alcohol and alkoxide ion desorbed into the solution, leaving a proton on the particle surface. This resulted in the formation of positively charged particles in the suspensions. This mechanism can also explain the positive charge of MnO_2 particles in ethanol suspensions.

The addition of CFB to the MnO_2 suspensions resulted in a reduced deposition rate and no deposition, either cathodic or anodic, was observed at CFB concentrations higher than 0.15 g L^{-1}. The addition of CCA to MnO_2 suspensions also resulted in the reduced cathodic deposition rate (Fig.6.3A) in the concentration range of 0-0.15 g L^{-1} CCA. However, anodic deposition was observed at higher CCA concentrations. The anodic deposition rate increased with increasing CCA concentration in the range of 0.15-0.8 g L^{-1} CCA. The anodic deposition resulted in the formation of uniform films. The formation of anodic deposits indicated that MnO_2 nanoparticles were negatively charged at CCA concentrations above 0.15 g L^{-1}. The film mass increased with increasing deposition time

(Fig.6.3B). Therefore, films of different mass can be obtained and deposition yield can be controlled.

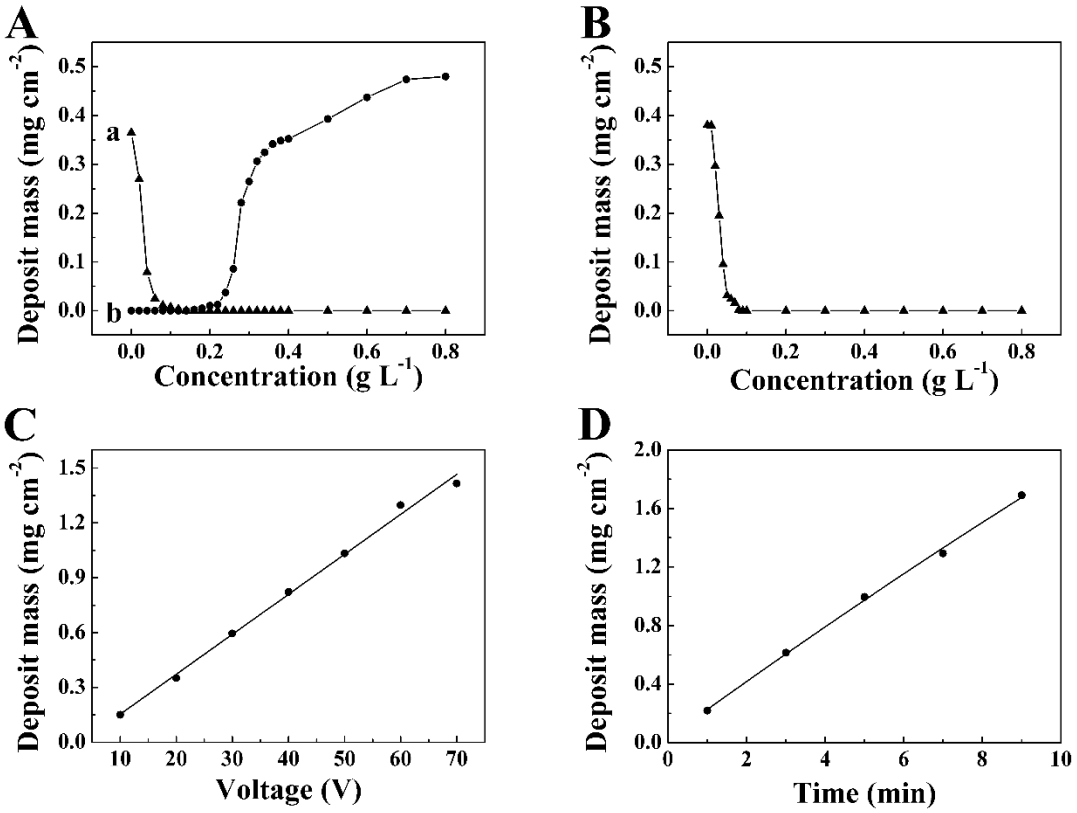

Fig.6.3 (A) deposit mass versus CCA concentration in the 4 g L^{-1} MnO_2 suspensions for (a) cathodic deposits and (b) anodic deposits at a deposition voltage of 20 V and deposition time of 2 min; (B) deposit mass versus CFB concentration in the 4 g L^{-1} MnO_2 suspensions for cathodic deposits at a deposition voltage of 20 V and deposition time of 2 min; (C) deposit mass versus deposition voltage for anodic deposits obtained from 4 g L^{-1} MnO_2 suspensions containing 0.4 g L^{-1} CCA for the deposition time of 2 min; (D) deposit mass versus deposition time for anodic deposits obtained from 4 g L^{-1} MnO_2 suspensions containing 0.4 g L^{-1} CCA at a deposition voltage of 20 V.

The reduction of the cathodic deposition yield with increase of CFB and CCA

concentration in the range of 0-0.15 g L^{-1} can be attributed to the adsorption of anionic CFB and CCA on the positively charged MnO_2 particles and charge compensation. The electrostatic attraction of the anionic molecules and positively charged MnO_2 promoted the adsorption of the molecules on the particle surfaces. However, the electrostatic interactions cannot explain the charge reversal of the MnO_2 particles at CCA concentrations above 0.15 g L^{-1}. Turning again to the structures of CFB and CCA, shown in Fig.6.1, it can be concluded that the electrostatic interactions are governed by the COO^- and SO_3^- functional groups of the organic molecules. The dissociation of the organic molecules resulted in the formation of corresponding anions and Na^+ or H^+. Therefore, a competitive adsorption of the anions and Na^+ or H^+ on the MnO_2 particles can be expected. However, only anionic CCA showed strong adsorption to the MnO_2 particles, which resulted in charge reversal and improved suspension stability. In contrast, the adsorption of CFB on MnO_2 nanoparticles was weak. As a result, no charge reversal was observed and the suspensions were unstable. The comparison of the chemical structures of CFB and CCA indicated that strong adsorption of CCA is attributed to the salicylate type of bonding[4, 5], involving COOH and OH groups. It should be noted that previous investigation[6] showed that the addition of benzoic acid to MnO_2 suspensions resulted in an increasing cathodic deposition rate. This was attributed to weak interaction of COO^- groups of benzoic acid with MnO_2 nanoparticles and preferred adsorption of H^+ on the particle surface. The analysis of the experimental data for CCA, containing COOH and OH groups bonded to the aromatic ring, and benzoic acid[6] without OH groups, indicated that that OH groups play an important role in the adsorption of the CCA molecules. It is known that the salicylic acid, containing COOH and OH groups bonded

to adjacent carbon atoms of the aromatic ring, is a powerful complexing agent[4, 5]. It is able to coordinate metals with complete deprotonation of the COOH and OH groups. Similar to salicylic acid, CCA was found to be a strong complexing agent, which was used for the voltammetric determination of Co, Cu, Ni, Ca, Zn, Pb and Hf in solutions[7, 8]. The suggested mechanism of salicylate type bonding of CCA to MnO_2 particles is shown in Fig.6.1C. It involves the complexation of Mn atoms on the MnO_2 surface.

6.3 Adsorption mechanism of CCA on MWCNT

CFB and CCA were also investigated for the dispersion and deposition of MWCNT. The suspensions of MWCNT in ethanol were unstable and showed rapid sedimentation immediately after the ultrasonic agitation. No EPD was achieved from such suspensions. The addition of CFB and CCA allowed the formation of stable suspensions. Fig.6.2c,d compares the MWCNT suspensions without CCA and with CCA. The suspension, containing CCA, was stable for more than 3 months.

It is suggested that CFB and CCA adsorbed on the MWCNT and provided electrosteric stabilization. The chemical structure of the molecules was beneficial for their adsorption on the MWCNT. It is in this regard that aromatic molecules are known[9-11] to interact strongly with sidewalls of CNTs through π-π stacking. It was demonstrated[9] that the adsorption affinity of the phenolic molecules to CNT increased with the increasing number of aromatic rings and OH groups. As a result 1-naphthol and pyrogallol showed better adsorption on CNT[9] compared to phenol. Small cationic and anionic aromatic molecules from the catechol and pyrogallol families were investigated for the EPD of MnO_2-MWCNT composites[6, 12]. However, no EPD of pure MWCNT films was

achieved. It was found that electric field promoted MWCNT aggregation and sedimentation. The electric field induced agglomeration was also observed during EPD of ceramic nanoparticles[13]. These investigations highlighted the importance of efficient dispersing agents for the application in electrophoretic nanotechnology.

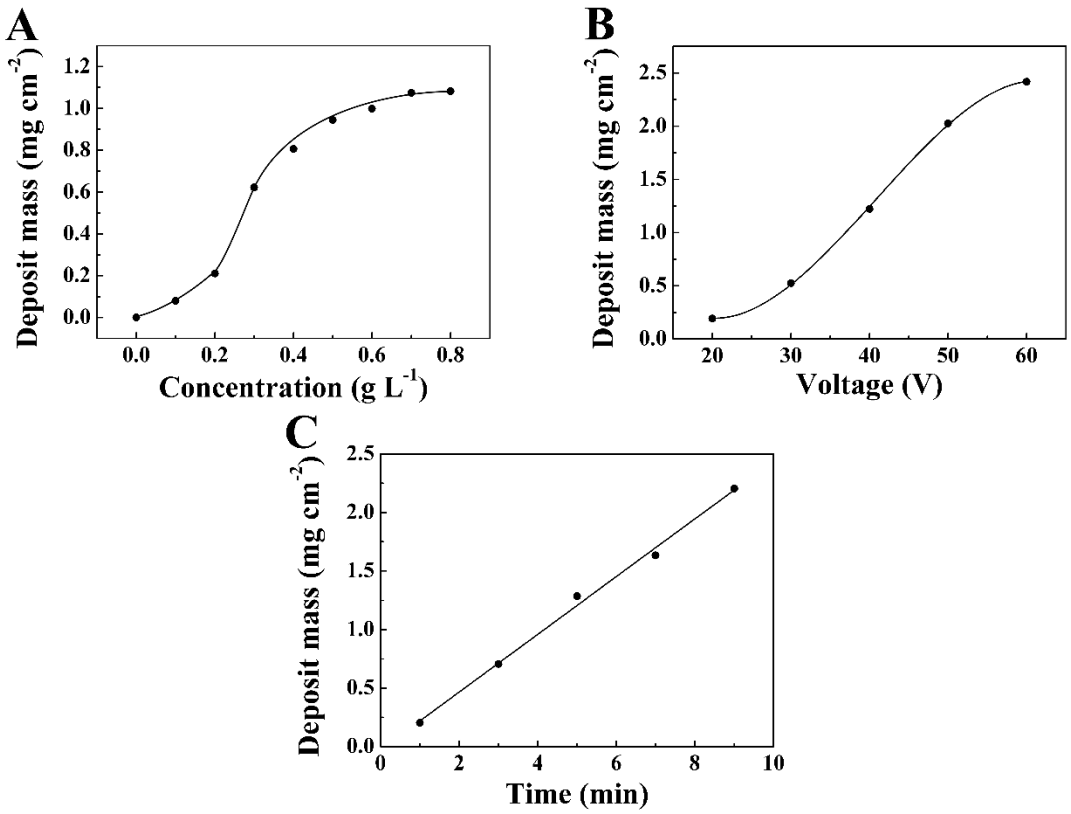

Fig.6.4 (A) Deposit mass versus CCA concentration in 1 g L^{-1} MWCNT suspension at a deposition voltage of 60 V and deposition time of 5 min.; (B) deposit mass versus deposition voltage for 1 g L^{-1} MWCNT suspension, containing 0.8 g L^{-1} CCA and deposition time of 10 min; (C) deposit mass versus deposition time for 1 g L^{-1} MWCNT suspension, containing 0.8 g L^{-1} CCA at a deposition voltage of 60 V.

A critical property of a dispersant is its adsorption on the material surface. Due to the strong adsorption of CFB and CCA on the MWCNT, the MWCNT suspensions showed

excellent stability in an electric field. In contrast to the results of previous investigations of aromatic molecules from the catechol and pyrogallol families[6, 12], the use of CFB and CCA as charging and dispersing agents allowed the formation of pure MWCNT films by EPD. The EPD method provided controlled deposition of MWCNT films. Fig.6.4A shows film mass versus CCA concentration in suspensions. The increase in CCA concentration in the suspensions resulted in increasing deposition yield. The data indicated that the increase in the CCA concentration in the suspension resulted in an increasing amount of adsorbed CCA, which provided electrosteric stabilization and electric charge for EPD of MWCNT. The increase in the deposition voltage resulted in significant increase of the deposition yield (Fig.6.4B). Relatively high deposition yield can be achieved at deposition voltages of 40-60 V.

6.4 FTIR characterization of CCA adsorptions

The results presented above indicated that CCA is an efficient dispersing and charging agent for EPD of two different materials: MnO_2 and MWCNT. However, CFB cannot be used for the EPD of MnO_2. Therefore, further investigation was focused on the use of CCA. The adsorption of CCA on MnO_2 and MWCNT was confirmed by the FTIR method. Fig.6.5 shows FTIR spectra for the deposits obtained from MnO_2 and MWCNT suspensions, containing CCA. The peak assignments are presented in Table 6.1. The FTIR spectrum of MnO_2 deposit showed absorptions attributed to stretching vibrations of the aromatic ring, SO_3^- group and other vibrations of adsorbed CCA. The SO_3^- vibrations of adsorbed CCA were observed in the spectrum of deposited MWCNT. The FTIR results confirmed that CCA was adsorbed on two different materials: MnO_2 and MWCNT. The CCA adsorption on MnO_2 was attributed to calicylate type of bonding.

The mechanism of CCA adsorption on MWCNT was related to π-π interactions.

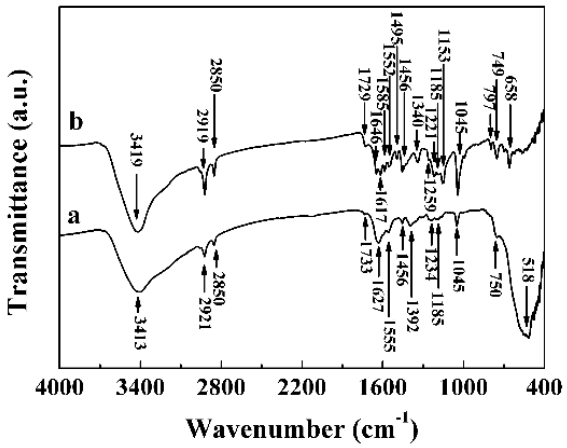

Fig.6.5 FTIR spectra of (a) a deposit prepared from 4 g L^{-1} MnO_2 suspensions containing 0.4 g L^{-1} CCA and (b) a deposit prepared from 1 g L^{-1} MWCNTs suspensions containing 0.4 g L^{-1} CCA.

Table 6.1 Band assignments for MnO_2 and MWCNT deposits obtained using CCA additive.

MnO_2	MWCNT	Band assignment
3405	3419	ν (O−H)[14]
2923, 2852	2916, 2850	ν (C−H)[14]
1733	1729	ν (C=O)[15]
1627, 1558	1646,1617,1552	ν (C−C)[16]
1453	1456	ν (C−C)[16, 17]
1394, 1234	1340, 1216	δ (C−OH)[17]
1185	1153	ν (SO3-)[18, 19]
1040	1040	ν (SO3-)[19, 20]
756	749, 658	δ (C−H)[21]
511		ν (Mn−O)[22]

The wavenumbers were given in cm^{-1}. ν-stretching mode, δ-bending mode

The adsorbed CCA provided a charge, required for the electrophoresis of MnO_2 and MWCNT. The fundamental aspects of electrophoresis of charged particles were discussed in many investigations[2, 23]. The concept of zeta potential was developed for hard particles. In contrast, the equations for electrophoretic mobility of polymers or

ceramic nanoparticles, containing adsorbed organic molecules do not include zeta potential[24, 25]. It was shown that the concept of zeta potential, which is important in the electrokinetics of hard particles, loses its physical meaning in the electrokinetics of soft particles[26]. The high particle charge or high zeta potential of particles are important factors controlling suspension stability. However, high charge or high zeta potential of ceramic particles does not necessarily allow their EPD. The particles must coagulate at the electrode surface in order to form a film. It was shown that mutual repulsion of the charged particles or polymer macromolecules, accumulated at the electrode surface due to electrophoresis, can prevent their coagulation and deposition[27]. However, using CCA as a dispersing and charging agent, efficient deposition of MnO_2 and MWCNT was achieved. It is important to note that for ES applications, that depends on the electronic conductivity of CNTs, the use of CCA for MWCNT dispersion and charging offers advantages, because this approach does not introduce defects on the MWCNT sidewalls. This in contrast to other methods, which are based on CNT chemical functionalization[28] and oxidation in acidic solutions[29, 30].

6.5 Co-deposition of MWCNT and MnO_2 nanoparticles

The possibility of deposition of MnO_2 and MWCNT using CCA as a co- dispersing agent paves the way for the fabrication of composite MnO_2-MWCNT materials by EPD. The composite films were obtained from the suspensions containing MnO_2 and MWCNT, which were dispersed using CCA. The amount of MnO_2 and MWCNT in the suspensions was varied. Fig.6.6 shows deposit mass versus MWCNT concentration in the 1 g L^{-1} MnO_2 suspensions at a deposition voltage of 40 V and deposition time of 2 min. The addition of MWCNT to the MnO_2 suspension resulted in increased deposition yield,

indicating co-deposition of MnO_2 and MWCNT. The increase in MWCNT concentration in the suspensions in the range of 0-0.53 g L^{-1} resulted in continuous increase in the deposit mass in the range of 0.11-0.47 mg cm^{-2}, attributed to increased amount of the deposited MWCNT. Therefore, the amount of MWCNT in the deposits can be varied.

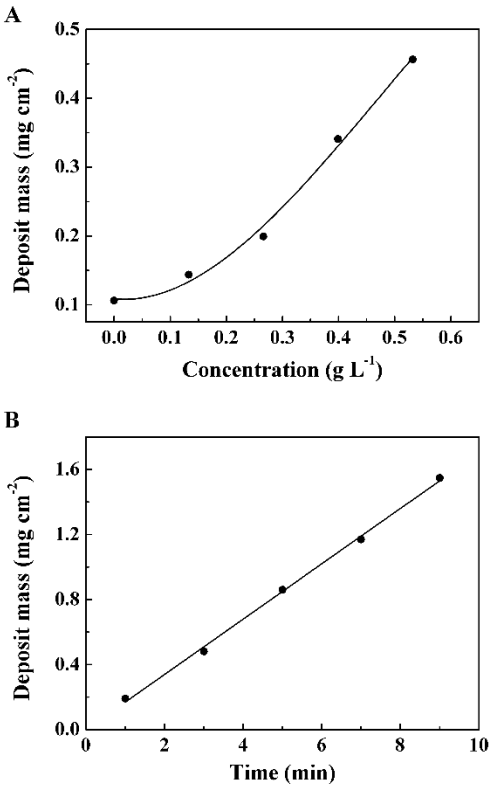

Fig.6.6 (A) Deposit mass versus MWCNT concentration in 2 g L^{-1} MnO_2 suspensions, containing 0.4 g L^{-1} CCA at a deposition voltage of 40 V and deposition time of 2 min; (B) deposit mass versus deposition time for 2 g L^{-1} MnO_2 suspensions, containing 0.4 g L^{-1} CCA and 0.5 g L^{-1} MWCNT at a deposition voltage of 40 V.

6.6 Morphology study of MnO_2-MWCNT composite films

The films prepared by the EPD method were investigated by SEM. Fig.6.7A shows a surface of the MnO_2 deposit. The deposit was crack free and contained MnO_2 nanoparticles. The porosity can be attributed to packing of the particles and gas evolution at the electrode. Fig.6.7B shows a surface of a MWCNT deposit. The deposit was porous with a typical pore size of 100 nm. The MWCNT were non-agglomerated due to the use of CCA dispersant. The SEM images of the deposits prepared from MnO_2 suspensions, containing MWCNT, showed that the deposits contained MnO_2 particles and MWCNT. A typical image of a composite MnO_2-MWCNT film is shown in Fig.6.7C.

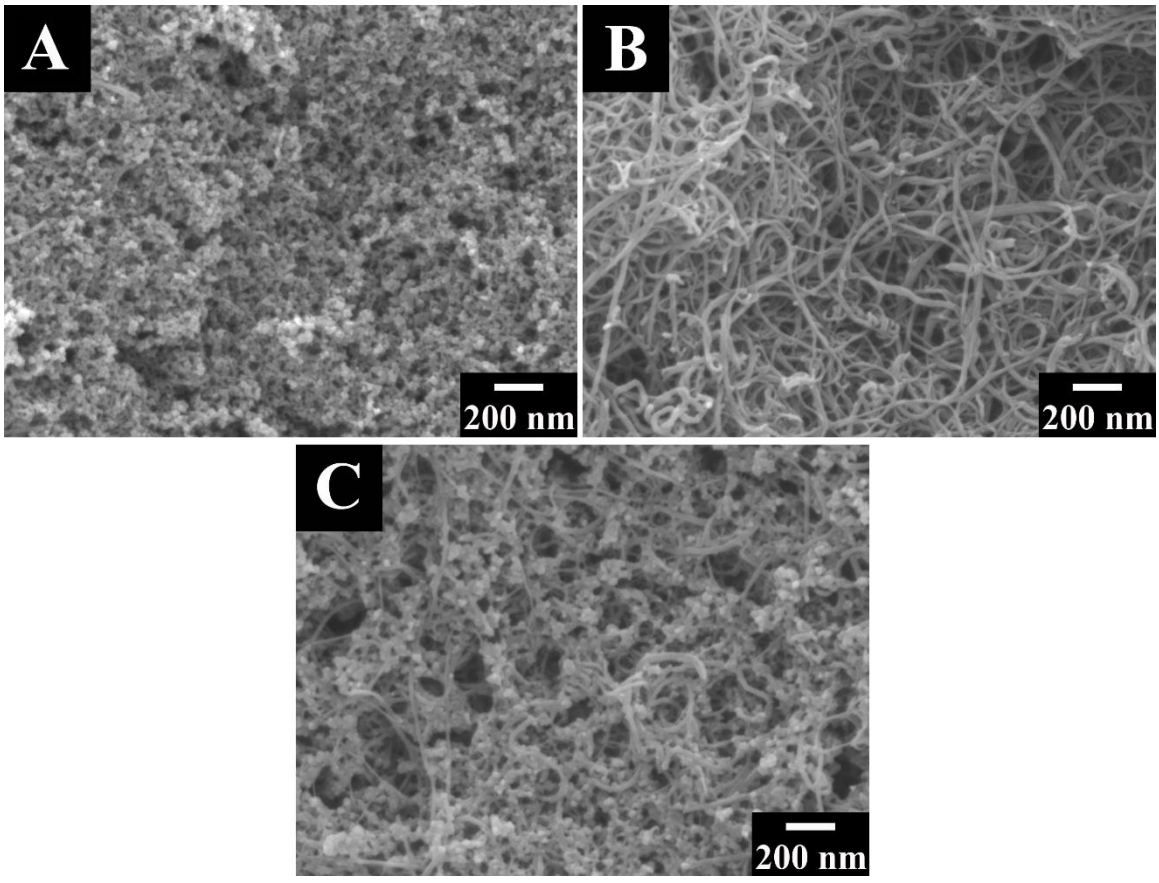

Fig.6.7 SEM images of films prepared from (A) 4 g L^{-1} MnO_2 suspensions (B) 1 g L^{-1} MWCNT suspensions (C) 1 g L^{-1} MnO_2 suspensions, containing 0.13 g L^{-1} MWCNT.

6.7 Composition study of MnO_2-MWCNT composite films

The formation of composite electrodes was confirmed by TGA and DTA studies. Fig.6.8 shows TGA and DTA data for the deposit, prepared from the 1g L^{-1} MnO_2 suspension, containing 0.13 g L^{-1} MWCNT and 0.2 g L^{-1} CCA. The TGA data showed several steps in mass loss below 600 ℃. The mass loss below 200 ℃ can be mainly attributed to dehydration. The corresponding DTA data showed a broad endotherm centered at 100 ℃. The mass loss at higher temperatures can be mainly attributed to burning out of MWCNT. However, the mass loss can be partially attributed to burning out of CCA, which was adsorbed on MnO_2 particles and MWCNT and incorporated into the deposit. The DTA data showed exothermic peaks at 305, 467, and 556 ℃, which corresponded to different steps in mass loss. The total mass loss at 700 ℃ was found to be 38% of the initial sample mass, indicating that MnO_2 content in the composite material was 62%.

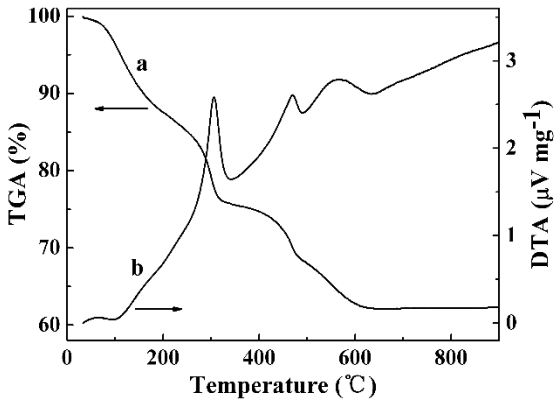

Fig.6.8 (a) TGA and (b) DTA data for the deposit obtained from 1g L^{-1} MnO_2 suspensions, containing 0.13 g L^{-1} MWCNT at a constant voltage of 40 V.

6.8 Capacitive performance of MnO_2-MWCNT composite films

The composite films prepared by EPD were investigated for application in ES. The charge-discharge behavior of MnO_2 is given by the following reaction[31]:

$$MnO_2 + A^+ + e^- \leftrightarrow MnO_2A^+ \qquad (\textbf{Eq.}6.2)$$

where $A^+ = Li^+, Na^+, K^+, H^+$. Eq.6.2 indicates that high electronic and ionic conductivity are necessary in order to utilize capacitive properties of MnO_2. The incorporation of MWCNT into the MnO_2 matrix allowed improved electronic conductivity of the composite material. The porous structure of the composite was beneficial for Na^+ ion access from the electrolyte to the MnO_2 particles.

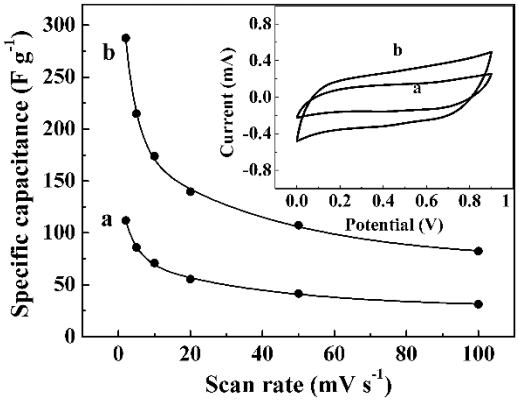

Fig.6.9 SC versus scan rate and (inset) corresponding CVs at 10 mV s^{-1} for the films, prepared from 1g L^{-1} MnO_2 suspensions, containing 0.2 g L^{-1} CCA: (a) without MWCNT and (b) with 0.13 g L^{-1} MWCNT, sample mass 0.15 mg cm^{-2}.

Fig.6.9 compares capacitive behavior of the MnO_2 and composite films. The box shape of the CVs indicated capacitive properties of the films in the voltage window of 0-0.9 V. The larger area of the CV of the composite film was attributed to higher SC compared to pure MnO_2 film. The SC calculated from the CV data decreased with increasing scan rate

due to the electrolyte diffusion limitations in the pores of the composite material. The composite material showed higher SC in the scan rate of 2-100 mVs^{-1} compared to SC of pure MnO_2 films. The highest SC of 290 F g^{-1} was obtained at a scan rate of 2 mV s^{-1}.

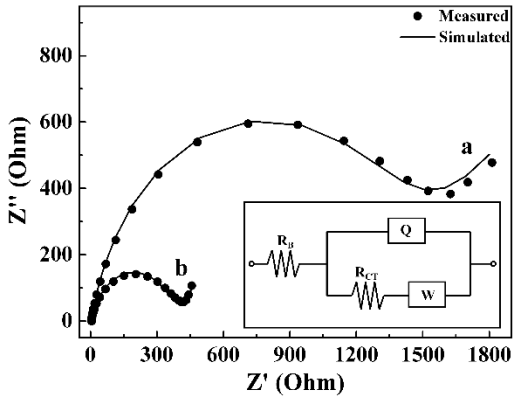

Fig.6.10 Nyquist plot of complex impedance *Z*=Z'-iZ''* for the films, prepared from 1 g L^{-1} MnO_2 suspensions, containing 0.2 g L^{-1} CCA: (a) without MWCNT and (b) with 0.13 g L^{-1} MWCNT, sample mass 0.15 mg cm^{-2}, inset shows equivalent circuit, used for simulation.

Impedance spectroscopy data for the MnO_2-MWCNT composite and pure MnO_2 films are presented in Fig.6.10. The Nyquist plots for the complex impedance *Z*=Z'-iZ''* showed significantly lower impedance values for composite films, compared to the corresponding values for pure MnO_2 films. The equivalent circuit[32] of the electrode included bulk electrolyte resistance (R_B), double layer capacitance, represented by a constant phase element (Q_{DL}), charge transfer resistance (R_{CT}) and Warburg element (W). The lower impedance of the composite films containing MWCNT resulted in higher SC (Fig.6.9). However, further optimization of the deposition conditions and deposit composition would be beneficial for the fabrication of MnO_2-MWCNT composite electrodes for ES. The approach developed in this investigation can be used for the

fabrication of other composites containing oxide nanoparticles and CNT.

6.9 Conclusions

New EPD method has been developed for the fabrication of MnO_2-MWCNT composites. CFB and CCA showed strong adsorption on MWCNT, allowed good MWCNT dispersion in the bulk of suspensions and controlled EPD of MWCNT films. The adsorption of CCA on MnO_2 nanoparticles allowed the formation of concentrated suspensions of well dispersed MnO_2 nanoparticles and fabrication of MnO_2 films. The mechanism of CCA adsorption on MWCNT was related to π-π interactions. The CCA adsorption on MnO_2 was attributed to calicylate type of bonding. It was found that CCA can be used as a co-dispersing and charging agent for EPD of two different types of materials: MWCNT and MnO_2. Composite MnO_2-MWCNT films prepared by EPD showed capacitive behavior in the 0.5M Na_2SO_4 aqueous electrolyte. The composite films showed higher SC compared to SC of pure MnO_2 films. The improved capacitive behavior was attributed to lower impedance of the composite films. The composite films showed a SC of 290 F g^{-1} and can be used for the fabrication of electrodes of ES. The EPD method developed in this investigation can be utilized for the fabrication of other composites containing ceramic particles and CNT.

References

[1] Chin S-F, Pang S-C, Anderson MA. Material and electrochemical characterization of tetrapropylammonium manganese oxide thin films as novel electrode materials for electrochemical capacitors. Journal of the Electrochemical Society 2002;149:A379-A84.

[2] Van der Biest OO, Vandeperre LJ. Electrophoretic deposition of materials. Annual Review of Materials Science 1999;29:327-52.

[3] Damodaran R, Moudgil BM. Electrophoretic deposition of calcium phosphates from non-aqueous media. Colloids and Surfaces A: Physicochemical and Engineering Aspects. 1993;80:191-5.

[4] Dobson KD, McQuillan AJ. In situ infrared spectroscopic analysis of the adsorption of aromatic carboxylic acids to TiO_2, ZrO_2, Al_2O_3, and Ta_2O_5 from aqueous solutions. Spectrochimica Acta A. 2000;56:557-65.

[5] Tunesi S, Anderson MA. Surface effects in photochemistry: an in situ cylindrical internal reflection-Fourier transform infrared investigation of the effect of ring substituents on chemisorption onto TiO_2 ceramic membranes. Langmuir. 1992;8:487-95.

[6] Wang Y, Zhitomirsky I. Effect of phenolic molecules on electrophoretic deposition of manganese dioxide-carbon nanotube nanocomposites. Colloids and Surfaces A: Physicochemical and Engineering Aspects. 2010;369:211-17.

[7] Levytska H, Orshuliak O. Voltammetric determination of hafnium with calconcarboxylic acid. Talanta. 2007;71:1441-3.

[8] Kocjan R, Błażewicz A, Blicharska E. LiChroprep-nH_2 modified with calconcarboxylic acid as a sorbent in trace analysis of metal ions. Journal of Separation Science 2002;25:891-6.

[9] Lin D, Xing B. Adsorption of phenolic compounds by carbon nanotubes: Role of aromaticity and substitution of hydroxyl groups. Environmental Science & Technology. 2008;42:7254-9.

[10] Woods LM, Badescu SC, Reinecke TL. Adsorption of simple benzene derivatives on carbon nanotubes. Physical Review B. 2007;75:155415-9.

[11] Star A, Han T-R, Gabriel J-CP, Bradley K, Grüner G. Interaction of aromatic compounds with carbon nanotubes: Correlation to the hammett parameter of the substituent and measured carbon nanotube fet response. Nano Letters 2003;3:1421-3.

[12] Wang Y, Zhitomirsky I. Electrophoretic deposition of manganese dioxide - Multiwalled carbon nanotube composites for electrochemical supercapacitors. Langmuir. 2009;25:9684-9.

[13] Zhitomirsky I. Cathodic electrodeposition of ceramic and organoceramic materials. Fundamental aspects. Advances in Colloid and Interface Science. 2002;97:279-317.

[14] Rajh T, Chen LX, Lukas K, Liu T, Thurnauer MC, Tiede DM. Surface restructuring of nanoparticles: An efficient route for ligand−metal oxide crosstalk. The Journal of Physical Chemistry B. 2002;106:10543-52.

[15] Liu G, Wu T, Zhao J, Hidaka H, Serpone N. Photoassisted degradation of dye pollutants. 8. Irreversible degradation of alizarin red under visible light radiation in air-equilibrated aqueous TiO_2 dispersions. Environmental Science & Technology. 1999;33:2081-7.

[16] Weisz AD, Garcia Rodenas L, Morando PJ, Regazzoni AE, Blesa MA. FTIR study of the adsorption of single pollutants and mixtures of pollutants onto titanium dioxide in water: Oxalic and salicylic acids. Catalysis Today. 2002;76:103-12.

[17] Janković IA, Šaponjić ZV, Čomor MI, Nedeljković JM. Surface modification of colloidal TiO_2 nanoparticles with bidentate benzene derivatives. The Journal of Physical Chemistry C. 2009;113:12645-52.

[18] Santos LRB, Chartier T, Pagnoux C, Baumard JF, Santillii CV, Pulcinelli SH, et al. Tin oxide nanoparticle formation using a surface modifying agent. Journal of the European Ceramic Society 2004;24:3713-21.

[19] Jayaweera PM, Jayarathne TAU. Acid/base induced linkage isomerization of alizarin red adsorbed onto nano-porous TiO_2 surfaces. Surface Science 2006;600:L297-L300.

[20] Guedes M, Ferreira JMF, Ferro AC. A study on the aqueous dispersion mechanism of CuO powders using Tiron. Journal of Colloid and Interface Science. 2009;330:119-24.

[21] Kawaguti CA, Santilli CV, Pulcinelli SH. Effect of the surfactant nature on the thermo-stability of surface modified SnO_2 nanoparticles. Journal of Non-Crystalline Solids 2008;354:4790-4.

[22] Yang R, Wang Z, Dai L, Chen L. Synthesis and characterization of single-crystalline nanorods of α-MnO_2 and γ-MnOOH. Materials Chemistry and Physics. 2005;93:149-53.

[23] Sarkar P, Nicholson PS. Electrophoretic deposition (EPD): Mechanisms, kinetics, and application to ceramics. Journal of the American Ceramic Society 1996;79:1987-2002.

[24] Ohshima H. Electrophoretic mobility of soft particles. Colloids and Surfaces A: Physicochemical and Engineering Aspects. 1995;103:249-55.

[25] Ohshima H. Dynamic electrophoretic mobility of a soft particle. Journal of Colloid and Interface Science. 2001;233:142-52.

[26] Ohshima H. Theory of electrostatics and electrokinetics of soft particles. Science and Technology of Advanced Materials. 2009;10:063001.

[27] Zhitomirsky I. Cathodic electrodeposition of ceramic and organoceramic materials. Fundamental aspects. Advances in Colloid and Interface Science. 2002;97:277-315.

[28] Casagrande T, Lawson G, Li H, Wei J, Adronov A, Zhitomirsky I. Electrodeposition of composite materials containing functionalized carbon nanotubes. Materials Chemistry and Physics 2008;111:42-9.

[29] Vaisman L, Wagner HD, Marom G. The role of surfactants in dispersion of carbon nanotubes. Advances in Colloid and Interface Science. 2006;128-130:37-46.

[30] Esumi K, Ishigami M, Nakajima A, Sawada K, Honda H. Chemical treatment of carbon nanotubes. Carbon. 1996;34:279-81.

[31] Devaraj S, Munichandraiah N. High capacitance of electrodeposited MnO_2 by the effect of a surface-active agent. Electrochemical and Solid-State Letters 2005;8:A373-A7.

[32] Jo C, Hwang I, Lee J, Lee CW, Yoon S. Investigation of pseudocapacitive charge-storage behavior in highly conductive ordered mesoporous tungsten oxide electrodes. The Journal of Physical Chemistry C. 2011;115:11880-6.

Chapter 7 Cataphoretic assembly of cationic dyes and deposition of CNT and graphene films

7.1 Mechanism of crystal violet film formation using ELD

Thin films were obtained by cathodic ELD from 0.1-1 g L^{-1} crystal violet solutions. The deposition process involved the dissociation of crystal violet in aqueous solutions, formation of cationic crystal violet (Fig.7.1A) species and their electrophoretic transport towards cathode. The pH at the cathode surface increased due to electrochemical decomposition of water

$$2H_2O + 2e^- \rightarrow H_2 + 2OH^- \quad (\textbf{Eq.}7.1)$$

and other cathodic reactions discussed in ref.[1]. The following cathodic reduction reaction[2] resulted in charge neutratization and deposition (Fig.7.1A):

$$\text{Cationic crystal violet} + OH^- \rightarrow \text{Crystal violet} \quad (\textbf{Eq.}7.2)$$

It is suggested that charge neutralization in reaction (Eq.7.2) prevented mutual electrostatic repulsion of cationic crystal violet species at the electrode surface and promoted film formation. Fig.7.1B shows deposit mass measured *in situ* during the deposition process versus deposition time. The QCM data at a deposition voltage of 5 V revealed small mass gain during the first 11 min of deposition, then deposit mass increased rapidly with increasing deposition duration. The deposition rate decreased with increasing deposition time at deposition times above 20 min. The reduction in the deposition rate was attributed to the formation of electrically insulating deposit and reduced voltage drop in the bulk of the solution[3]. The QCM data at 10 V showed very

small mass gain during the first 2 min, and then significant increase in deposit mass was observed. The deposition rate decreased with time at deposition times above 8 min. The deposition yield achieved at 10 V was higher, compared to that at 5 V.

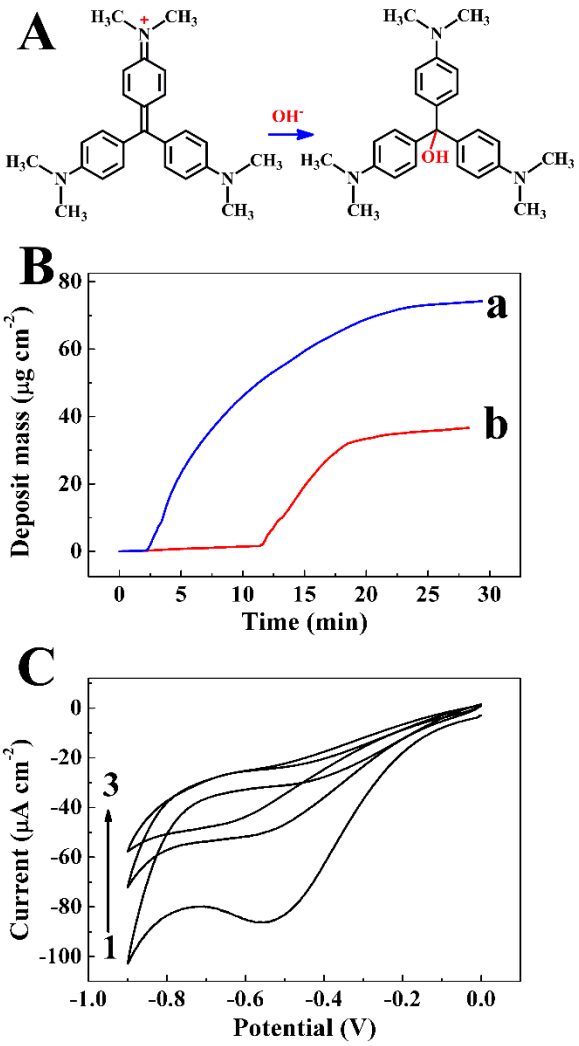

Fig.7.1 (A) Cathodic reaction of cationic crystal violet with electrogenerated OH^- ion and (B) deposit mass measured in-situ using QCM versus time for films prepared from 0.1 g L^{-1} crystal violet solutions at deposition voltages of (a) 5 and (b) 10 V. (C) crystal violet data for Pt electrode in 0.1 g L^{-1} crystal violet solution at a scan rate of 20 mV s^{-1} (arrow shows increasing cycle number).

The low deposition yield at the initial stage of deposition is in agreement with literature data[4-6], which showed that a certain period (critical time) has to elapse before the formation of a deposit starts. It was suggested that such a critical time is necessary for the accumulation of sufficient amount of material at the electrode surface. However, it can also be attributed to the formation of high pH surface layer by OH^- generation[6] in reaction (Eq.7.1). Higher deposition voltage promoted electromigration of cationic crystal violet species and their accumulation at the electrode surface[6]. Moreover, higher voltage promoted OH^- generation. As a result, the increase in the deposition voltage resulted in the reduced critical time (Fig.7.1B). It is important to note, that such a critical time was observed only in dilute solutions at low deposition voltages.

The deposition process was also studied using crystal violet. Fig.7.1C shows the CV data obtained by potential cycling of a Pt electrode in the crystal violet solution. The first cycle showed cathodic peak at -0.55 V, which can be attributed to reaction (Eq.7.2). A thin film was formed at the working electrode at a potential of -0.9 V. The cathodic current and intensity of the peak decreased with increasing cycle number. The decrease in current with increasing cycle number indicated growth of non-conductive crystal violet films.

7.2 Morphology study of crystal violet films

The films prepared from crystal violet solutions were studied by SEM. Fig.7.2 shows films surface at different magnifications. The films (Fig.7.2A) contained particles with diameters in the range of 0.2-0.5 μm. The SEM image at higher magnification (Fig.7.2B) revealed necks formation between the individual particles.

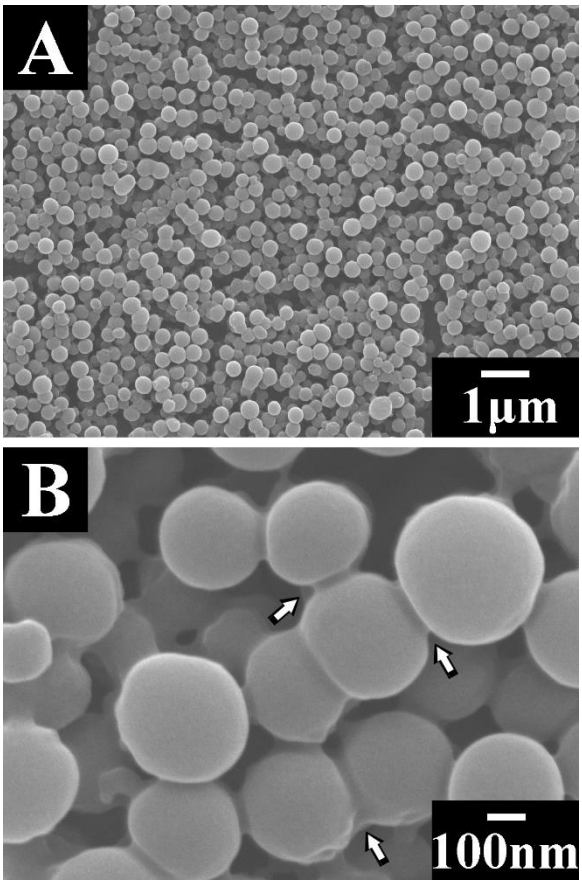

Fig.7.2 (A and B) SEM images of film surfaces at different magnifications for the films prepared from 1 g L^{-1} crystal violet solutions at a deposition voltage of 5 V, arrows show neck formation between the particles.

The analysis of film cross sections at different magnifications (Fig.7.3A,B) showed that most of the particles had a rod-like shape with the long axis perpendicular to the substrate surface. The diameter of some particles increased from bottom to the top (Fig.7.3B). The increase in particle diameter resulted in the formation of necks between the particles. Such particles limited the growth of some small particles nucleated at the substrate surface (Fig.7.3B). The formation of rod-like particles can be attributed to π-π interactions of the crystal violet dyes. It is in this regard that anisotropic particle growth

was also observed in investigations focused on chemical assembly of other polyaromatic molecules. The π-π interactions of molecules from pyrene family allowed the fabrication of fibers, nanotubes, nanowires and nanorods by chemical assembly methods.[7-11] Such materials exhibited advanced and tunable photovoltaic, optical and fluorescence properties.

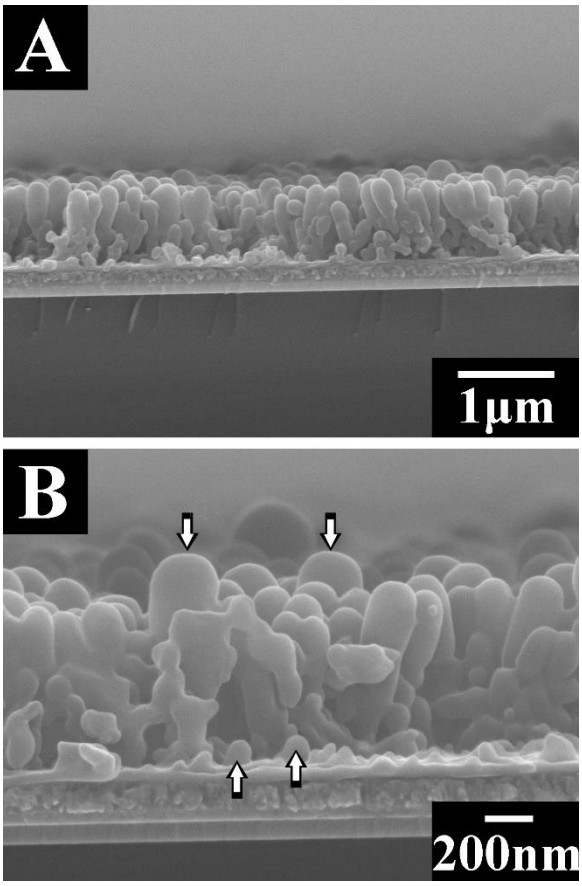

Fig.7.3 (A and B) SEM images of film cross-sections at different magnifications for the films prepared from 1 g L^{-1} crystal violet solutions at a deposition voltage of 5 V, up arrows show small crystal violet particles nucleated at the substrate surface, down arrows show top of growing particles with increased diameter.

The results of our investigation indicated that electrochemical cathodic assembly can be used for synthesis of similar particles. Moreover, electrochemical assembly allowed the formation of films, containing oriented rod-like particles. The π-π stacking of crystal violet molecules resulted in anisotropic particle growth during electrophoretic deposition.

7.3 Dispersion of MWCNT and graphene using crystal violet

The results of EPD of pure crystal violet paved the way for the fabrication of MWCNT and graphene films by cathodic EPD. The use of crystal violet as a dispersing agent allowed efficient dispersion of MWCNT and graphene. The aqueous suspensions of MWCNT and graphene without crystal violet were unstable and showed rapid precipitation (Fig.7.4). In contrast, the addition of crystal violet allowed the formation of stable suspensions, which didn't show precipitation for more than 3 months.

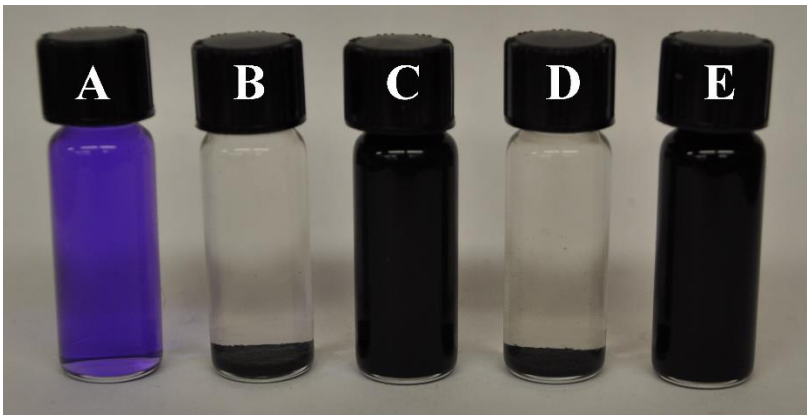

Fig.7.4 (a) Crystal violet solution, (b) MWCNT in water, (c) MWCNT dispersed in crystal violet solution, (d) graphene in water, (e) graphene dispersed in crystal violet solution.

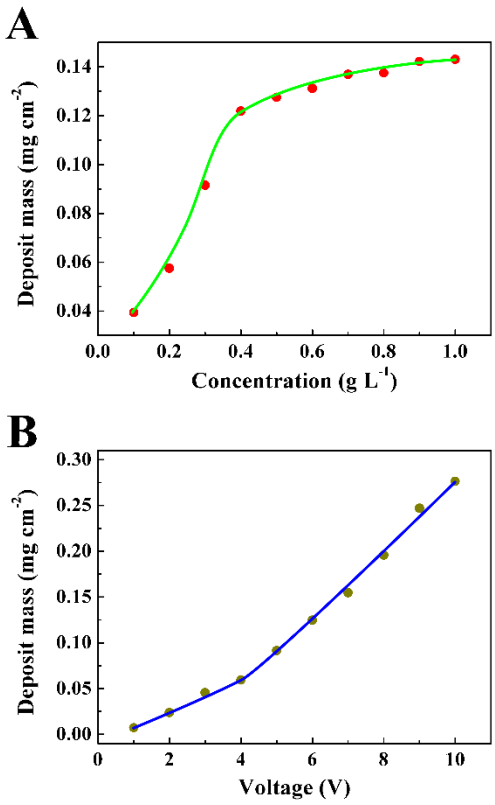

Fig.7.5 Deposit mass for films prepared from 1 g L^{-1} MWCNT suspension at a deposition time of 2 min versus (A) crystal violet concentration at the deposition voltage of 5 V and (B) deposition voltage at crystal violet concentration of 0.3 g L^{-1}.

7.4 Fabrication of MWCNT films using EPD

Adsorbed crystal violet provided electrosteric stabilization of MWCNT and graphene and allowed their cathodic EPD. The deposit mass of MWCNT increased with increasing crystal violet concentration (Fig.7.5A) at a constant deposition voltage and deposition time. It is important to note that efficient dispersion and deposition of MWCNT can be achieved at relatively low crystal concentrations. The crystal violet/MWCNT mass ratio was by 1-2 orders of magnitude lower compared to surfactant/CNT mass ratio reported for various CNT dispersions, containing cationic surfactants.[12-15] The film mass

increased with increasing deposition voltage (Fig.7.5B). The slope of the curve increased at deposition voltages above 4 V. The influence of deposition voltage on the deposition rate was discussed in the literature.[16, 17] In the EPD process, electric field drives particles towards the electrode. Therefore, the increase in the deposition voltage results in increasing deposition yield. However, a certain value of electric field is necessary in order to overcome interparticle interactions and to allow particle bonding to the substrate. Such interparticle interactions can result in reduced deposition rates at low voltages.

7.5 Morphology study of MWCNT films

The MWCNT films prepared by EPD were studied by SEM. Fig.7.6 compares SEM images at different magnifications for MWCNT films prepared from MWCNT suspension with different concentrations of crystal violet. The SEM images at lower magnification (Fig.7.6A,C,E) indicated that the deposition method resulted in the formation of continuous films. The images at higher magnifications (Fig.7.6B,D,F) showed that the films were porous with typical pore size of 100-200 nm. The SEM image (Fig.7.6D) for the deposit prepared from the MWCNT suspension, containing 0.6 g L^{-1} crystal violet, shows larger diameters of MWCNT, compared to the deposit prepared from MWCNT suspension, containing 0.2 g L^{-1} crystal violet. This observation indicated that the increase in crystal violet concentration in the solutions resulted in the formation of crystal violet coatings on MWCNT. Further increase in the crystal violet concentration resulted in the formation of crystal violet coatings on MWCNT and deposition of crystal violet in the voids between MWCNT (Fig.7.6F).

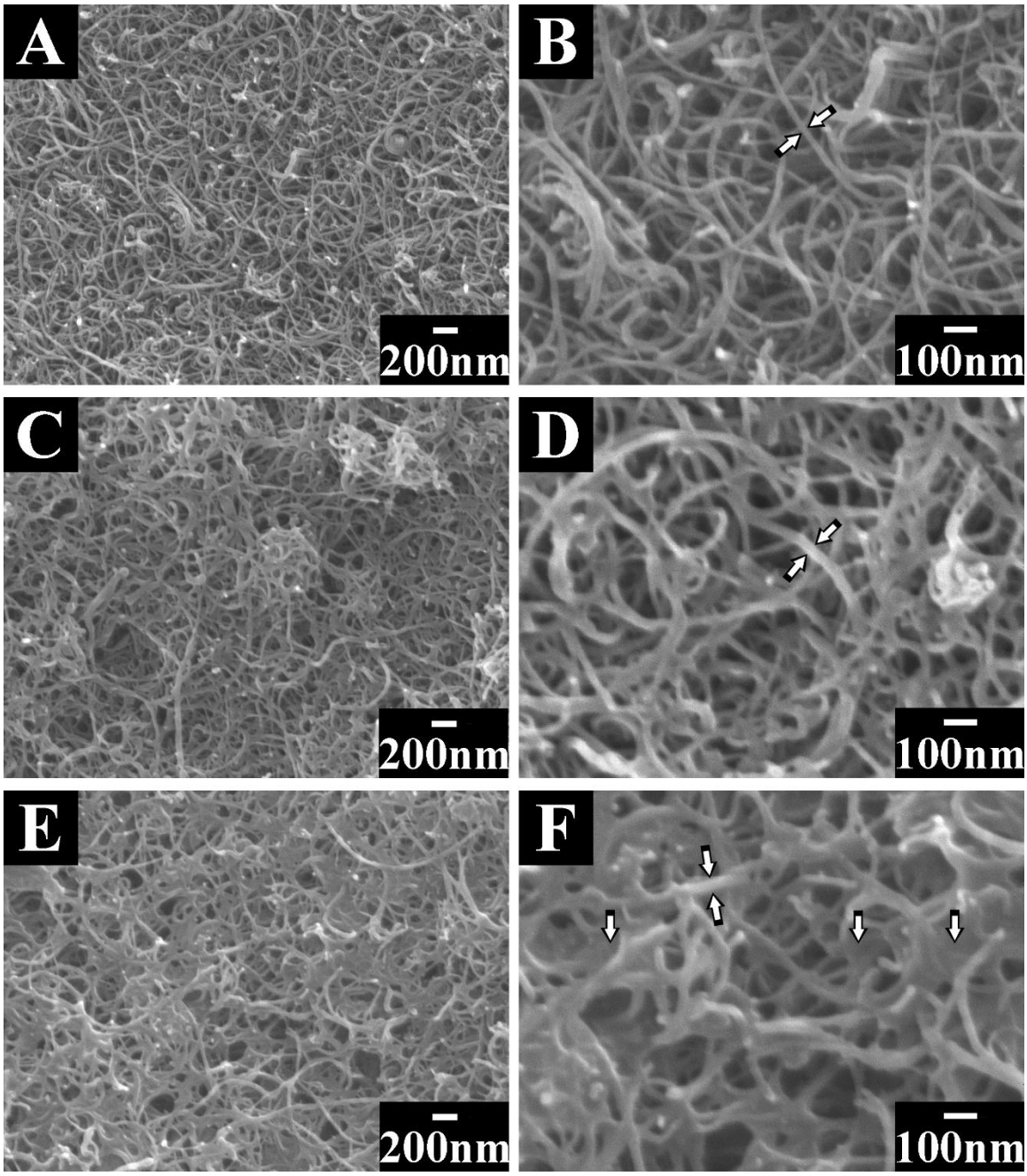

Fig.7.6 SEM images at different magnifications for films prepared from 1 g L^{-1} MWCNT suspensions containing (A,B) 0.2, (C,D) 0.6 (E,F) 1.0 g L^{-1} crystal violet at a deposition voltage of 5 V and deposition time of 2 min, arrows show (B, D, F) MWCNT diameter and (F) crystal violet in voids between MWCNT.

The analysis of SEM images of films obtained at different voltages showed that the increase in the deposition voltage promoted crystal violet deposition (Fig.7.7). The SEM image of MWCNT film, prepared from the MWCNT suspension, containing 0.3 g L^{-1} crystal violet at a deposition voltage of 5 V, shows only MWCNT (Fig.7.7A). The film prepared from the same suspension at a deposition voltage of 10 V shows MWCNT and rod-like crystal violet particles (Fig.7.7B). The MWCNT penetrated the rod-like crystal violet particles (Fig.7.7B).

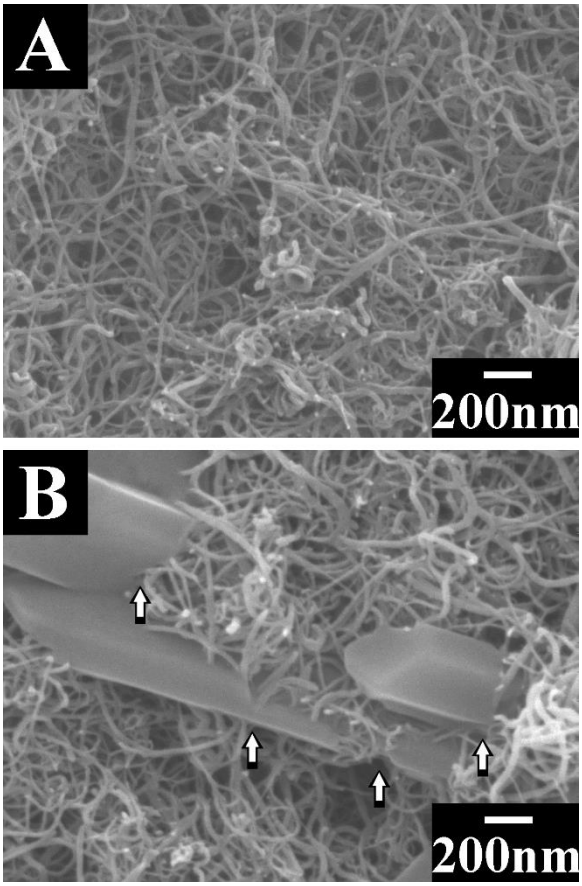

Fig.7.7 SEM images of MWCNT films deposited from 1 g L^{-1} MWCNT suspensions, containing 0.3 g L^{-1} crystal violet at deposition voltages of (A) 5 V and (B) 10 V, arrows show crystal violet particles.

7.6 Fabrication of graphene films using EPD and morphology study

EPD from the graphene suspensions, containing crystal violet allowed the formation of cathodic deposits. The deposit mass increased with increasing crystal violet concentration in the suspensions and deposition voltage (Fig.7.8). The deposition of graphene was achieved at higher voltages, compared to the voltages used for the deposition of MWCNT. The difference in the deposition voltages was due to larger mass of graphene particles compared to that of MWCNT.

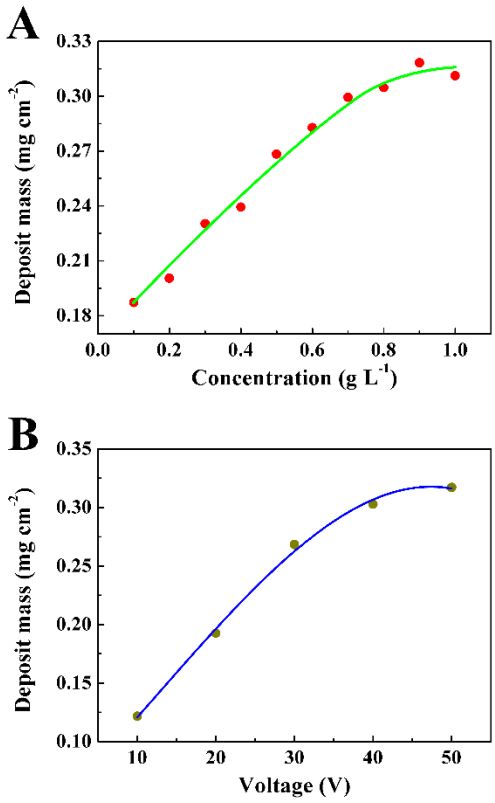

Fig.7.8 Deposit mass for films prepared from 1 g L^{-1} graphene suspension at a deposition time of 2 min versus (A) crystal violet concentration at a deposition voltage of 30 V and (B) deposition voltage at crystal violet concentration of 0.5 g L^{-1}.

Fig.7.9 shows SEM images of films prepared from graphene suspensions with different crystal violet concentrations. The SEM images of the films prepared from graphene suspensions, containing 0.4 g L^{-1} crystal violet, showed the formation of continuous films (Fig.7.9A,B). The increase in the crystal violet concentration in the solutions resulted in enhanced deposition of crystal violet. The comparison of the SEM images at low magnification (Fig.7.9A,C) revealed the formation of crystal violet particles at crystal violet concentration of 0.6 g L^{-1} (Fig.7.9C). Moreover, crystal violet covered graphene particles. Fig.7.9D shows pin holes in such crystal violet layers on the graphene particles. Such pin holes resulted from hydrogen gas evolution at the cathode surface during EPD. Further increase in the crystal violet concentration resulted in increasing number of crystal violet particles. Fig.7.9E,F showed that the shape and size of the particle was similar to those shown in Fig.7.2 and Fig.7.3. The crystal violet particles covered the graphene particles.

The results presented above showed that the use of crystal violet offers many benefits for EPD of CNT and graphene. Crystal violet allowed efficient dispersion and charging of MWCNT and graphene. As pointed out above the critical property of dispersant is its adsorption on particle surface. It is suggested that π-π interactions promoted crystal violet adsorption on MWCNT and graphene. As a result, efficient dispersion was achieved at relatively low crystal violet concentrations, compared to cationic surfactants with long hydrocarbon chains[12-15]. Adsorbed cationic crystal violet allowed electrophoretic transport of MWCNT and graphene to the electrode surface. The discharge of cationic crystal violet in reaction (Eq.7.2) promoted film formation. Moreover, the film forming properties of crystal violet were beneficial for deposition of MWCNT and graphene. It is

suggested that crystal violet formed at the electrode surface acted as a binder promoting coagulation of MWCNT and graphene and their binding to the substrate surface.

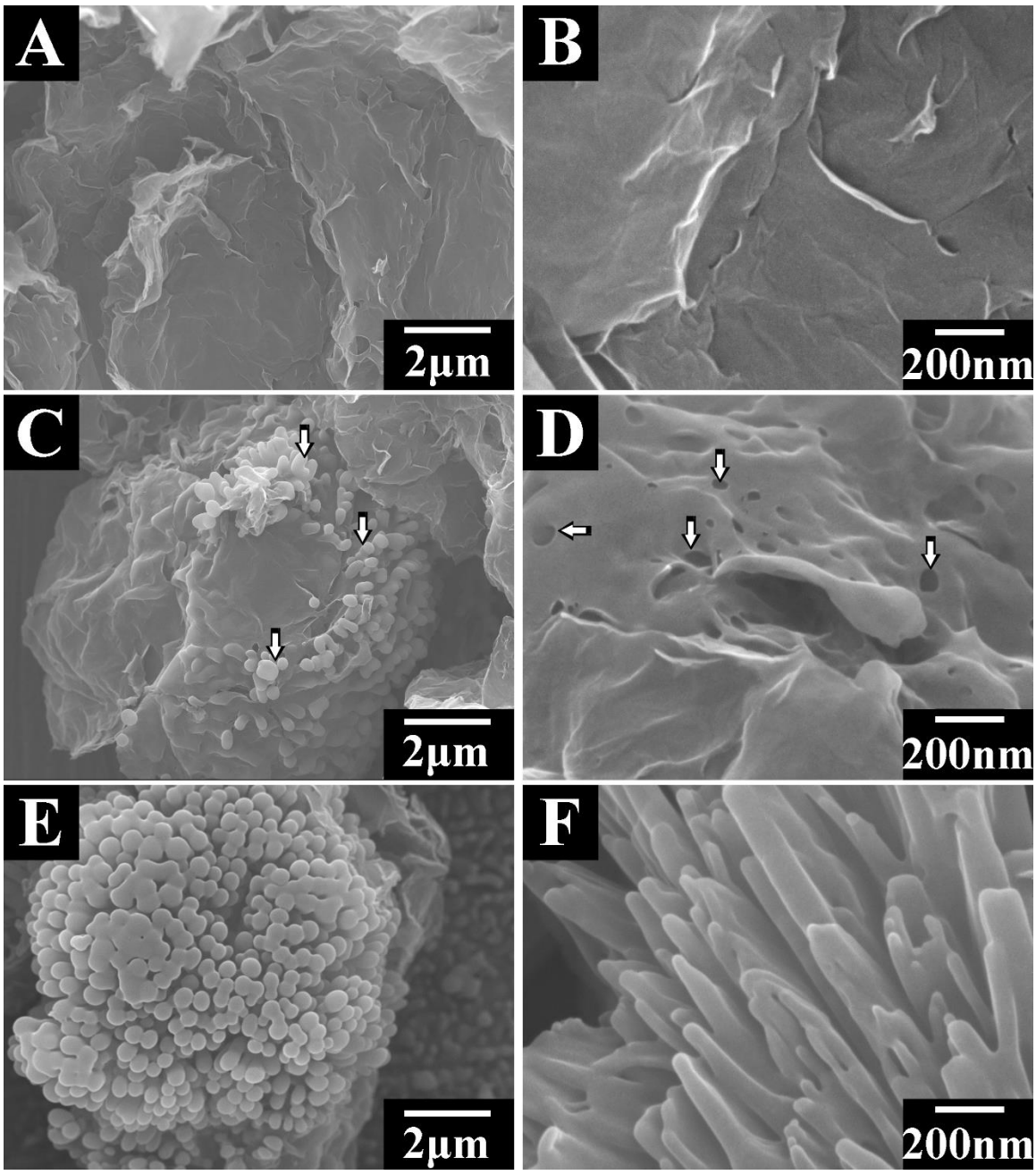

Fig.7.9. SEM images at different magnifications for films prepared from 1 g L^{-1} graphene suspensions containing (A and B) 0.4, (C and D) 0.6 (E and F) 1.0 g L^{-1} crystal violet at a deposition voltage of 30 V and deposition time of 2 min, arrows show (C) crystal violet

particles and (D) pin holes in crystal violet layers on graphene particles.

However, the amount of crystal violet in the suspensions and deposition voltage must be optimized in order to minimize the amount of crystal violet in the deposits. The EPD and graphene can be combined with other cathodic electrodeposition strategies for the deposition of metals and oxides and fabrication of advanced nanocomposites. Moreover, the results of this investigations pave the way for the fabrication of MWCNT-graphene nanocomposites using crystal violet as a dispersing agent for both materials. Such graphene-MWCNT nanocomposites are currently under intensive investigation for application in solar cells, electrochemical supercapacitors and other energy storage devices[18].

7.7 Conclusions

Cathodic EPD method has been developed for the fabrication of thin films from aqueous solutions of crystal violet dyes. The films contained rod-like particles with a long axis perpendicular to the substrate surface. The deposition mechanism involved cataphoresis of charged cationic crystal violet species, base generation in cathodic reactions, charge neutralization and film formation. The assembly of rod-like particles was governed by π-π interactions of polyaromatic crystal violet molecules. The efficient dispersion of MWCNT and graphene was achieved in crystal violet solutions of relatively low concentration. The feasibility of cathodic EPD of MWCNT and graphene using crystal violet as a dispersing, charging and film forming agent has been demonstrated. The deposition yield measurements revealed relatively high deposition yield, which can be varied by the variation of deposition time, voltage and crystal violet concentration. SEM

data showed that at low crystal violet concentrations in MWCNT and graphene suspensions and low deposition voltages the films contained MWCNT and graphene. The increase in the crystal violet concentration and/or deposition voltage resulted in enhanced deposition of crystal violet. The EPD method developed in this investigation paves the way for the fabrication of advanced nanocomposites by cathodic electrodeposition methods.

References

[1] Zhitomirsky I. Cathodic electrodeposition of ceramic and organoceramic materials. Fundamental aspects. Advances in Colloid and Interface Science. 2002;97:277-315.

[2] Mao L, Zhang K, On Chan HS, Wu J. Surfactant-stabilized graphene/polyaniline nanofiber composites for high performance supercapacitor electrode. Journal of Materials Chemistry 2012;22:80-5.

[3] Zhitomirsky I. Electrophoretic hydroxyapatite coatings and fibers. Materials Letters 2000;42:262-71.

[4] Koelmans H. Philips ResRep. 1955;10:161.

[5] Hamaker HC. Trans Faraday Soc. 1940;36:279.

[6] Koelmans H, Overbeek JTG. Discuss Faraday Soc. 1954;18:52.

[7] Kamikawa Y, Kato T. Color-tunable fluorescent organogels: Columnar self-assembly of pyrene-containing oligo(glutamic acid)s. Langmuir. 2007;23:274-8.

[8] Xiao J, Liu Y, Li Y, Ye J, Li Y, Xu X, et al. Self-assembly and optical properties of hydrogen bonded nanostructures containing C60 and pyrene. Carbon. 2006;44:2785-92.

[9] Chen Y, Zhu B, Han Y, Bo Z. Self-assembly of cationic pyrene nanotubes. Journal of Materials Chemistry 2012;22:4927-31.

[10] Zhang X, Zhang X, Shi W, Meng X, Lee C, Lee S. Morphology-controllable synthesis of pyrene nanostructures and its morphology dependence of optical properties. Journal of Physical Chemistry B 2005;109:18777-80.

[11] Wang Z, Liu M, Xie Y, Gao C. In situ fabrication of pyrene derivative nanorods inside polyelectrolytes microcapsules with tunable fluorescent properties. Journal of Materials Chemistry 2012;22:2855-8.

[12] Bai Y, Park IS, Lee SJ, Bae TS, Watari F, Uo M, et al. Aqueous dispersion of surfactant-modified multiwalled carbon nanotubes and their application as an antibacterial agent. Carbon. 2011;49:3663-71.

[13] Sun Z, Nicolosi V, Rickard D, Bergin SD, Aherne D, Coleman JN. Quantitative evaluation of surfactant-stabilized single-walled carbon nanotubes: Dispersion quality and its correlation with zeta potential. Journal of Physical Chemistry C 2008;112:10692-9.

[14] Clark MD, Subramanian S, Krishnamoorti R. Understanding surfactant aided aqueous dispersion of multi-walled carbon nanotubes. Journal of Colloid and Interface Science 2011;354:144-51.

[15] Chen L, Xie H, Li Y, Yu W. Applications of cationic gemini surfactant in preparing multi-walled carbon nanotube contained nanofluids. Colloids and Surfaces A: Physicochemical and Engineering Aspects. 2008;330:176-9.

[16] Van der Biest OO, Vandeperre LJ. Electrophoretic deposition of materials. Annual Review of Materials Science 1999;29:327-52.

[17] Zhitomirsky I, Gal-Or L. Electrophoretic deposition of hydroxyapatite. Journal of Materials Science: Materials in Medicine. 1997;8:213-9.

[18] Huang L, Wu B, Yu G, Liu Y. Graphene: learning from carbon nanotubes. Journal of Materials Chemistry 2011;21:919-29.

Chapter 8 Electrophoretic deposition of graphene, carbon nanotubes and composite films using methyl violet dye as a dispersing agent

8.1 Mechanism of MV deposition

Fig.8.1 shows a chemical structure of the methyl violet (MV) dye, which includes 3 aromatic rings and sp^2 hybridized central carbon atom (Fig.8.1A). The cationic properties of MV are attributed to the $-NH^+$ group. It was found that electrodeposition from 0.1-1 g L^{-1} MV solutions resulted in the formation of films on the cathodic substrates. The suggested deposition mechanism is based on the literature data on behavior of MV in basic solutions [1].

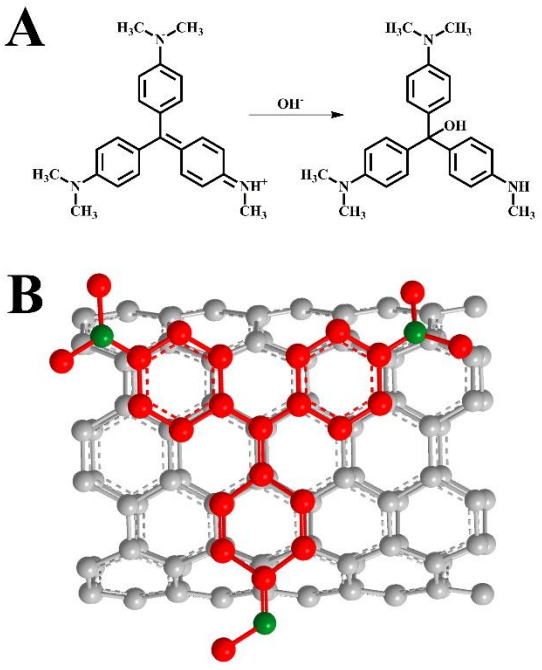

Fig.8.1 (A) Cathodic reaction of MV with hydroxide groups, (B) schematic of MV adsorption on the surface of MWCNT.

It is known that cationic MV molecules react with hydroxide groups in basic environment as shown in Fig.8.1A. This reaction results in charge neutralization and the changes from sp^2 to sp^3 hybridization of the central carbon atom. It is suggested that electric field provided electrophoresis of cationic MV towards the cathode. The following cathodic reaction resulted in the pH increase at the cathode surface:

$$2H_2O + 2e^- \rightarrow H_2 + 2OH^- \quad \textbf{(Eq.}8.1\textbf{)}$$

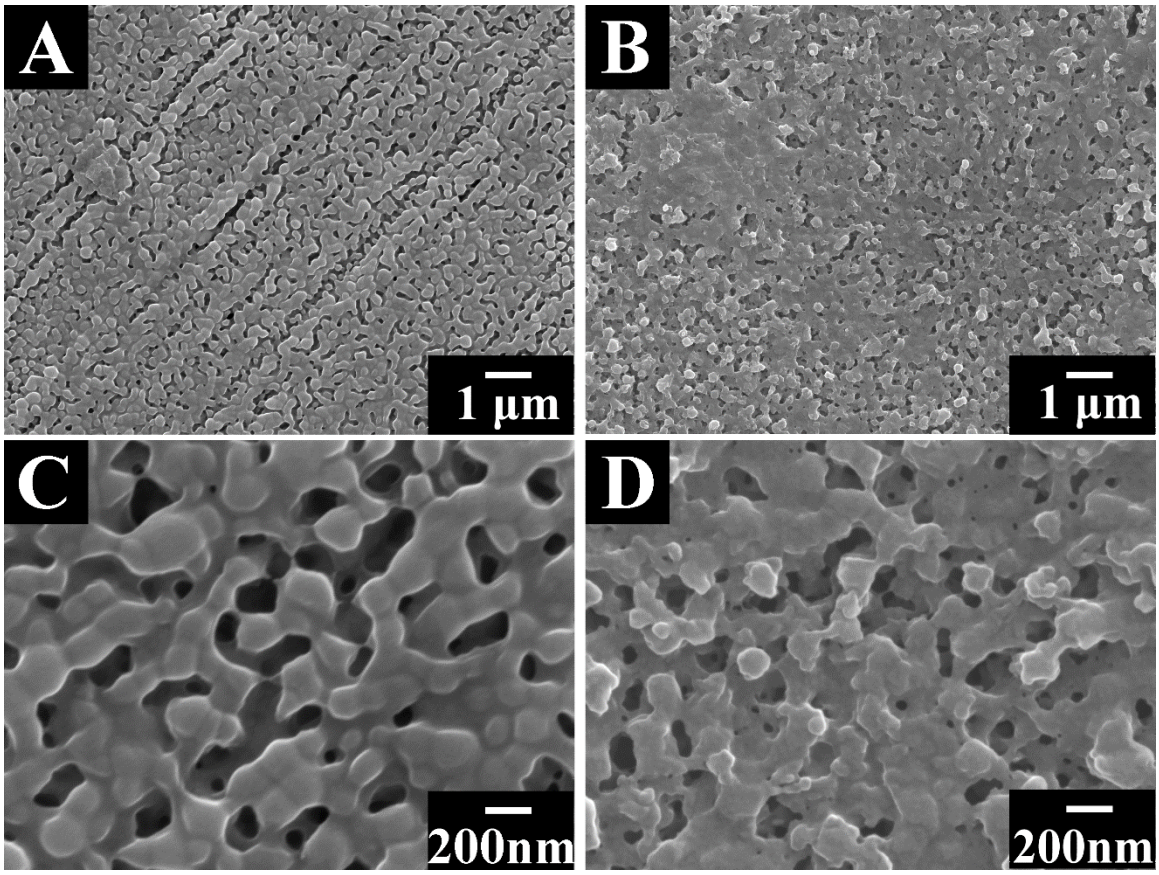

Fig.8.2 SEM images of cathodically deposited MV films from 1 g L^{-1} MV solutions at (A, C) 5 V and (B, D) 20 V.

The charge neutralization (Fig.8.1A) in the high pH region at the cathode promoted MV film formation. Fig.8.2A,C shows the microstructures of deposited MV films for different

magnification at 5 V, which were porous and contained MV particles with an average diameter of ~ 100 nm. The increase in the deposition voltage from 5 to 20 V resulted in reduced porosity (Fig.8.2B,D). The reduction in porosity was attributed to faster deposition at higher deposition voltage, which led to the necks formation between the particles and filling voids between the particles.

The deposition process was studied by potentiodynamic cycling. Fig.8.3 shows the CVs in the 0.1 g L^{-1} MV aqueous solution in the potential range from -0.9 to 0 V versus SCE. Fig.8.3 shows a peak at ~ -0.55 V versus SCE which was attributed to the electrochemical reduction (Fig.8.1A) of MV molecules. Thin film formation was observed after the first cycle. The decrease of current with cycle number indicated the formation of insulating film on the cathodic substrate.

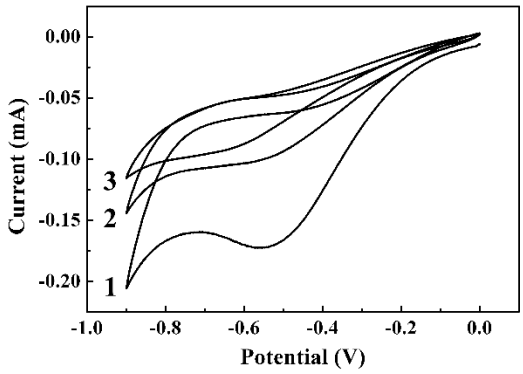

Fig.8.3 CV data for Pt electrode in 0.1 g L^{-1} MV solution at a scan rate of 20 mV s^{-1} for cycles 1–3.

8.2 EPD of MWCNT and graphene

MV was investigated for the dispersion of MWCNT and graphene in aqueous suspensions. The suspensions of MWCNT and graphene in water were unstable and

showed rapid sedimentation immediately after ultrasonic agitation. No EPD was achieved from such suspensions. The addition of MV to the suspensions of MWCNT and graphene resulted in improved suspension stability. The suspensions were stable for more than 2 months. It is suggested that MV was adsorbed on MWCNT and graphene and provided a positive charge for electrostatic stabilization. The adsorption of MV on MWCNT and graphene was governed by π-π interactions. Fig.8.1B shows a schematic of adsorption of polyaromatic MV molecule on the MWCNT surface.

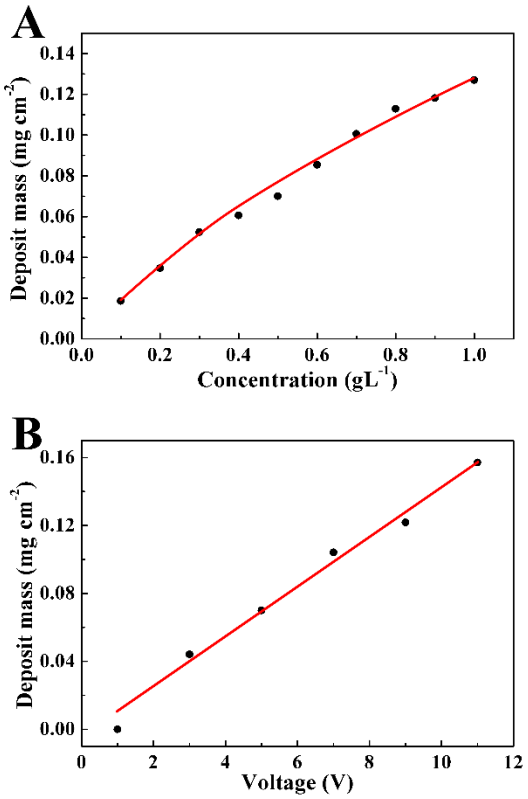

Fig.8.4 Deposit mass for films prepared from 1 g L^{-1} MWCNT suspension at a deposition time of 2 min versus (A) MV concentration at the deposition voltage of 5 V and (B) deposition voltage at MV concentration of 0.5 g L^{-1}.

The adsorbed MV imparted a positive charge to the MWCNT and graphene and allowed

their EPD. In this investigation, the EPD kinetics was studied by the analysis of deposition yield measurements due to limitations of zeta potential concept for application to particles, containing adsorbed organic molecules [2, 3]. The deposition yield of MWCNT was recorded to analyze the influences of both MV concentration (Fig.8.4A) and deposition voltage (Fig.8.4B). Under a constant deposition voltage of 5 V, the deposition yield of MWCNT increased with MV concentration as shown in Fig.8.4A. The data indicated that adsorbed MV allowed charging and deposition of MWCNT, even at MV concentration as low as 0.1 g L^{-1} in the 1 g L^{-1} MWCNT suspensions. The increase in MV concentration resulted in increasing adsorption of cationic MV molecules on MWCNT surface, and increased MV charge, which, in turn, resulted in higher deposition rate. The results indicated that deposition yield can be varied by variation of MV concentration. The deposition yield increased with increasing deposition voltage (Fig.8.4B). Nearly linear relationship dependence was observed in agreement with Hamaker equation [4].

Similar dependences were observed for graphene suspensions, where the deposition yield increased with the MV concentration (Fig.8.5A) due to increased charge of the graphene particles, containing adsorbed MV molecules [5]. However, a higher deposition voltage was required for the deposition of graphene due to the larger mass of the graphene particles. A linear dependence of the deposition yield versus deposition voltage was observed in the range of 0-30 V, and significant deviation from the linear dependence was observed at higher voltage range (Fig.8.5B). The linear part is in agreement with Hamaker equation [4]. The deviation from the linear dependence can be attributed to different factors, such as deposit spalling, increased voltage drop in thick deposit and

corresponding reduction in electric field in the bulk of the suspensions, electrode reactions and other factors discussed in the literature [6]. The results indicated that the deposition yield for MWCNT films and graphene films can be controlled by changing MV concentration and deposition voltage.

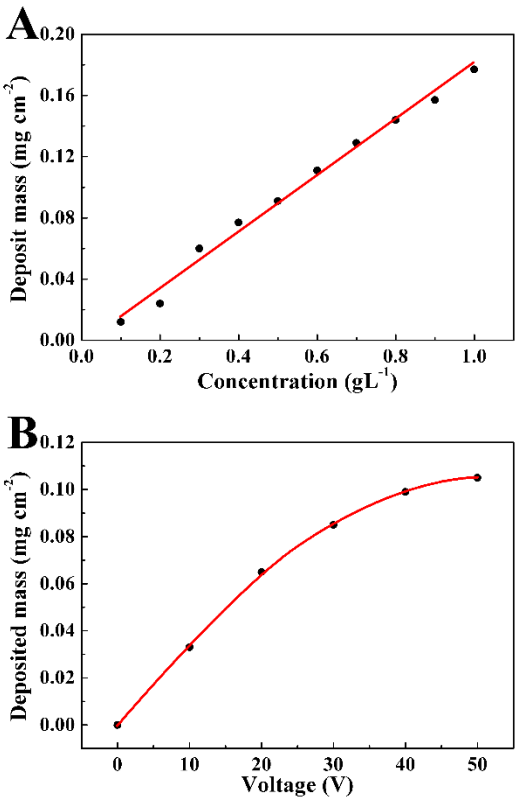

Fig.8.5 Deposit mass for films prepared from 1 g L^{-1} graphene suspension at a deposition time of 2 min versus (A) MV concentration at the deposition voltage of 30 V and (B) deposition voltage at CV concentration of 0.5 g L^{-1}.

8.3 Adsorption of MV on MWCNT and graphene

FTIR studies were performed in order to confirm the MV adsorption. Fig.8.6 compares the FTIR spectra of MV, MWCNT, graphene and deposited materials. The absorption assignments are summarized in Table 8.1.

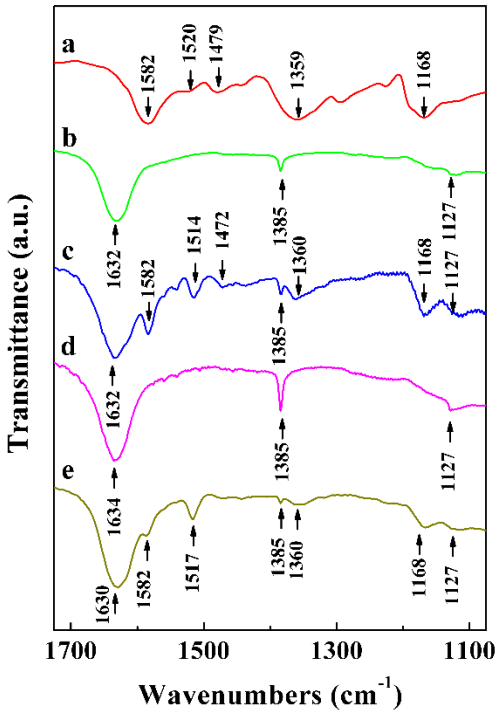

Fig.8.6 FTIR spectra of (a) MV, (b) pristine MWCNT, (c) deposited MWCNT, (d) pristine graphene, and (e) deposited graphene.

Table 8.1 Band Assignments for MWCNT, graphene, and MV

MV	Pristine MWCNT	Deposited MWCNT	Pristine Graphene	Deposited Graphene	Band Assignments
(cm^{-1})	(cm^{-1})	(cm^{-1})	(cm^{-1})	(cm^{-1})	
	1632	1632	1634	1630	C-C stretch in CNT[7]
1582 1479		1582 1472		1582	C=C in aromatic ring[8]
1520		1514		1517	N-H stretch[8]
	1385 1127	1385 1127	1385 1127	1385 1127	C-O stretch[9]
1359		1360		1360	C-H in CH3[8]
1168		1168		1168	C-N stretch[8]

In comparison with the spectra of pristine MWCNT and graphene, the spectra of deposited materials (Fig.8.6) showed additional absorptions at 1582, 1514, 1472, 1360

and 1168 cm^{-1} for deposited MWCNT and at 1582, 1517, 1360 and 1168 cm^{-1} for deposited graphene. Taking into account that similar absorptions were observed in the spectra of MV (Table 8.1), it was concluded that deposited MWCNT and graphene contained adsorbed MV.

8.4 Co-deposition of MWCNT and graphene

Fig.8.7 shows the SEM images of MWCNT (Fig.8.7A), graphene (Fig.8.7B), and MWCNT-graphene composite (Fig.8.7C). Fig.8.7A showed a continuous and uniform MWCNT film with an average pore size of ~ 100 nm. As shown in Fig.8.7B, graphene were dispersed from particles to sheets, and the substrate was fully covered. The possibility of deposition of MWCNT and graphene paved the way for the co-deposition of both materials from one suspension using MV as a charging and dispersing agent for both materials.

Literature data [10, 11] indicates that mixed suspensions of CNT and graphene exhibit improved stability, compared to the suspensions of individual materials. The results of sedimentations tests of mixed MWCNT-graphene suspension without dispersants are in agreement with the literature data and indicate that MWCNT-graphene suspensions without MV were stable for 3-4 hours. In contrast, MWCNT-graphene suspensions containing MV as a dispersant were stable for more than 2 months.

Mixed suspensions, containing MWCNT, graphene and MV dispersant were used for the formation of composite MWCNT-graphene films by EPD. The SEM image of the composite material shows graphene and MWCNT (Fig.8.7C). As pointed out above, the MWCNT-graphene composites have potential applications in many fields, including ES

[12] and batteries [13], due to improved electrolyte access to graphene layers, separated by MWCNT.

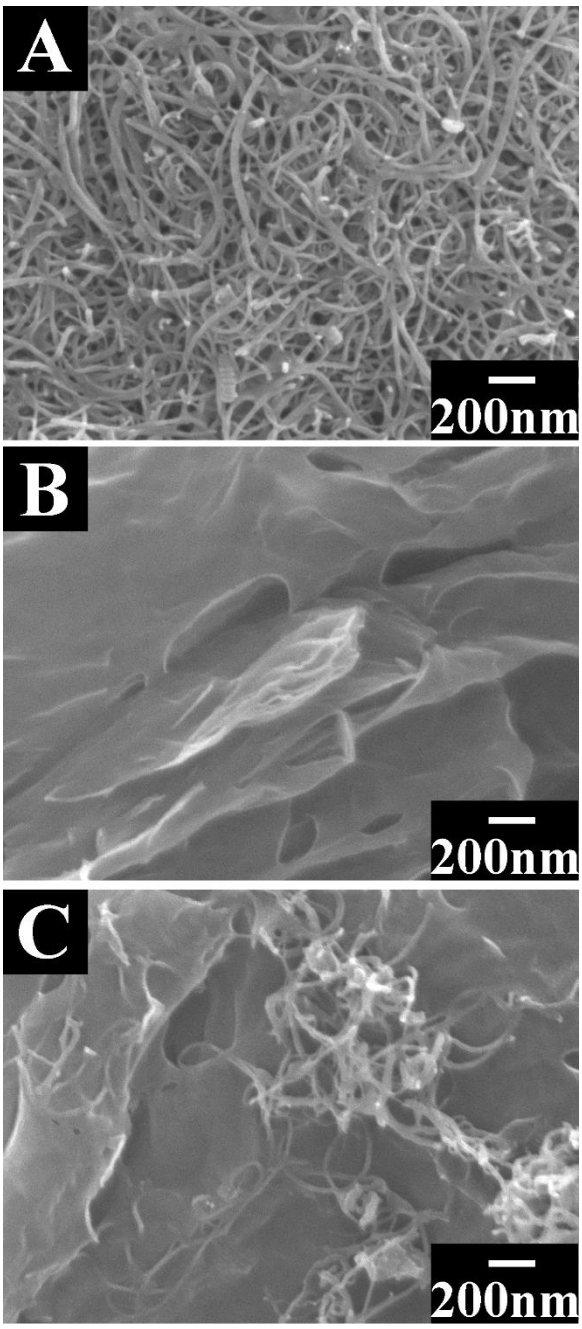

Fig.8.7 SEM images of (A) MWCNT, (B) graphene and (C) composite films, deposited from (A) 1 g L^{-1} MWCNT and 0.5 g L^{-1} MV suspensions at 5 V, (B) 1 g L^{-1} graphene

and 0.5 g L^{-1} MV suspension at 30 V, and (C) 1 g L^{-1} MWCNT, 1 g L^{-1} graphene and 1 g L^{-1} MV suspension at 20 V.

8.5 Electrochemical characterization of deposited films

The capacitive behavior of the composite films was studied using CV. The CVs were obtained within the potential range between -0.4 and 0.6 V versus SCE. The SC was calculated at each scan rate from CV data and plotted in Fig.8.8A.

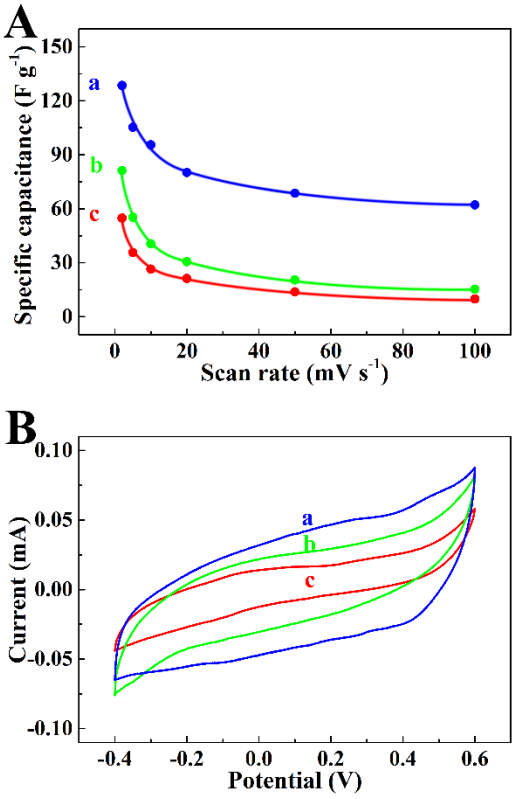

Fig.8.8 (A) SC versus scan rate and (B) corresponding CV at 10 mV s^{-1} for (a) composite film, prepared from a suspension containing 1 g L^{-1} MWCNT, 1 g L^{-1} graphene and 1 g L^{-1} MV (b) MWCNT film, prepared from 1 g L^{-1} MWCNT suspension, containing 0.5 g L^{-1} MV.

At the scan rate of 2 mV s^{-1}, a SC of ~ 130 F g^{-1} was achieved for a composite film with the mass loading of 0.04 mg cm^{-2}. With the increase of the scan rate, the SC decreased to ~ 63 F g^{-1} at 100 mV s^{-1}. This decrease was attributed to diffusion limitations of the electrolyte in the pores of the composite material. For comparison, the graphene film and MWCNT film with approximately the same active material areal density only had a SC of ~ 55 F g^{-1} and ~ 81 F g^{-1}, respectively, at a scan rate of 2 mV s^{-1}, which indicated the benefaction of composite film in the application of ES.

The Fig.8.8B shows CVs at 10 mV s^{-1} scan rate for graphene, MWCNT, and composite films. The CV of composite film has nearly box-shape, indicating good capacitive behavior. The CVs of graphene film and MWCNT film were both distorted in this potential range, which caused deterioration of capacitive performance. The smaller areas of these two samples indicated their less lower SC at a scan rate of 10 mV s^{-1}, as shown in Fig.8.8A.

The graphene, MWCNT, and composite films were studied by EIS and the data was shown in Fig.8.9. The equivalent circuit, presented in the inset of Fig.8.9, was used for the analysis of the impedance spectroscopy data. It included two RQ transmission lines, describing the porous electrode [14, 15]. The diffusion resistance of electrolyte inside the pores was represented by the Warburg impedance (W) [16, 17]. In this circuit, R_1 element represented the electrolyte resistance while R_2 represented the film resistance. Q elements represented the double-layer capacitance and pseudocapacitance of the composite film, with the consideration of microscopic roughness of the surface and capacitance dispersion of interfacial origin [12]. To simulate an impedance spectrum using an equivalent circuit, a minimum set of model parameters was used and good agreement of

the experimental data and the results of simulation was achieved. By comparing the EIS of three samples, it was found that composite film had the smallest film resistance, especially at low frequency range. For graphene and MWCNT films, Warburg diffusion resistance dominated impedance behavior at low frequency range. It was found that the mixing of MWCNT and graphene could improve the conductivity of composite film and hence enhance its capacitive behavior.

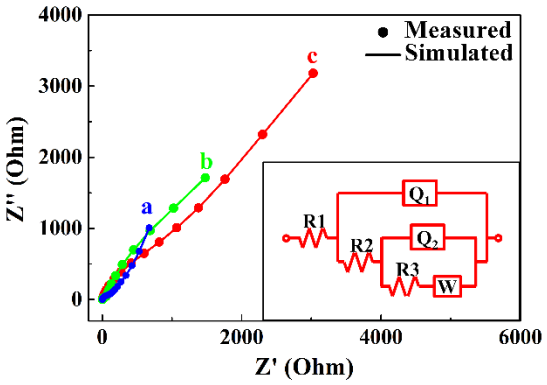

Fig.8.9 Nyquist plot of a complex impedance $Z^* = Z - iZ$ in the frequency range of 0.1 Hz–100 kHz for (a) composite, (b) MWCNT, and (c) graphene films; the suspensions for film preparation are the same as in Fig.8.8. The inset shows the equivalent circuit used for the simulation.

EPD offers many processing advantages, compared to other methods for the fabrication of MWCNT-graphene composites. The EPD method is simple and suitable for controlled deposition of well dispersed MWCNT and graphene on high surface area substrates. This method is especially attractive for application in ES. The SC of composite films prepared by this method is comparable with SC of the MWCNT-graphene composites synthesized by other methods [11, 18]. The method developed in this investigation gives an alternative route to achieve nanoscale fabrication of MWCNT-graphene composites,

utilizing processing advantages of EPD technology.

8.6 Conclusions

Cathodic EPD method has been developed for the fabrication of MV films, which were deposited by a constant voltage EPD or potentiodynamically. The deposition mechanism involved electrophoresis of cationic MV, pH increase at the cathode due to the electrode reactions, charge neutralization of the cationic MV at the electrode surface and film formation. MV allowed efficient dispersion, charging and cathodic EPD of MWCNT and graphene at relatively low dispersant concentrations. The deposition yield can be varied by variation of dispersant concentration and deposition voltage. FTIR data proved the adsorption of MV molecules on MWCNT and graphene surface. The use of MV as a co-dispersing agent for MWCNT and graphene allowed the fabrication of MWCNT-graphene composite films for application in electrodes of ES. The composite films showed capacitive behavior. The SC of ~ 130 F g^{-1} was obtained at a scan rate of 2 mV s^{-1}. The MWCNT-graphene composites are promising materials for ES.

References

[1] Creighton HJM. A method for making methyl violet. Proceedings of the Nova Scotian Institute of Science. 1919;15:57-61.

[2] Ohshima H. Electrophoretic mobility of soft particles. Journal of Colloid and Interface Science 1994;163:474-83.

[3] Zhitomirsky I. Cathodic electrodeposition of ceramic and organoceramic materials. Fundamental aspects. Advances in Colloid and Interface Science. 2002;97:279-317.

[4] Hamaker H. The London-van der Waals attraction between spherical particles. Physica. 1937;4:1058-72.

[5] O'Brien RW, White LR. Electrophoretic mobility of a spherical colloidal particle. Journal of the Chemical Society, Faraday Transactions 2: Molecular and Chemical Physics. 1978;74:1607-26.

[6] Besra L, Liu M. A review on fundamentals and applications of electrophoretic deposition (EPD). Progress in Materials Science 2007;52:1-61.

[7] Titus E, Ali N, Cabral G, Gracio J, Ramesh Babu P, Jackson MJ. Chemically functionalized carbon nanotubes and their characterization using thermogravimetric analysis, fourier transform infrared, and raman spectroscopy. Journal of Materials Engineering and Performance 2006;15:182-6.

[8] Sunil Kumar Bajpai AJ. Equilibrium and thermodynamic studies for adsorption of crystal violet onto spent tea leaves (STL). Water Journal. 2012;4:52-71.

[9] Janković IA, Šaponjić ZV, Čomor MI, Nedeljković JM. Surface modification of colloidal TiO_2 nanoparticles with bidentate benzene derivatives. The Journal of Physical Chemistry C. 2009;113:12645-52.

[10] Yu D, Dai L. Self-assembled graphene/carbon nanotube hybrid films for supercapacitors. Journal of Physical Chemistry Letters. 2009;1:467-70.

[11] Cheng Q, Tang J, Ma J, Zhang H, Shinya N, Qin L-C. Graphene and carbon nanotube composite electrodes for supercapacitors with ultra-high energy density. Physical Chemistry Chemical Physics 2011;13:17615-24.

[12] Su Y, Zhitomirsky I. Electrophoretic assembly of organic molecules and composites for electrochemical supercapacitors. Journal of Colloid and Interface Science 2012;392:247-55.

[13] Zhao M-Q, Liu X-F, Zhang Q, Tian G-L, Huang J-Q, Zhu W, et al. Graphene/single-walled carbon nanotube hybrids: one-step catalytic growth and applications for high-rate Li–S batteries. ACS Nano. 2012;6:10759-69.

[14] Conway BE, Pell WG. Power limitations of supercapacitor operation associated with resistance and capacitance distribution in porous electrode devices. Journal of Power Sources 2002;105:169-81.

[15] Huai Y, Hu X, Lin Z, Deng Z, Suo J. Preparation of nano-TiO_2/activated carbon composite and its electrochemical characteristics in non-aqueous electrolyte. Materials Chemistry and Physics 2009;113:962-6.

[16] Kötz R, Carlen M. Principles and applications of electrochemical capacitors. Electrochimica Acta 2000;45:2483-98.

[17] Sawai K, Ohzuku T. A method of impedance spectroscopy for predicting the dynamic behavior of electrochemical system and its application to a high-area carbon electrode. Journal of the Electrochemical Society 1997;144:988-95.

[18] Yang X, Zhu J, Qiu L, Li D. Graphene assembly: bioinspired effective prevention of restacking in multilayered graphene films: towards the next generation of high-performance supercapacitors. Advanced Materials 2011;23:2771-.

Chapter 9 Electrophoretic deposition of PBH and composite films

9.1 Mechanism of electrodeposition of PBH

Pyrenebutyric acid (PBH) films were deposited on anodic substrates from 0.1-2 g L^{-1} PBH solutions. Fig.9.1A shows the deposition yield, measured using QCM. The deposit mass increased with increasing deposition time at a constant deposition voltage. Therefore, the amount of the deposited material can be varied and controlled. The deposition rate decreased with increasing time due to the increase in voltage drop in the growing film and corresponding decrease in electric field in the bulk of the solution[1].

The PBH films were also obtained potentiodynamically. Fig.9.1B shows CVs obtained by potential cycling of a stainless steel electrode in the PBH solution. The first cycle showed anodic peaks, which can be attributed to oxidation of the stainless steel[2, 3]. A thin film was formed at the stainless steel electrode at a potential of ~ 1 V. The anodic peaks were not observed during the second and following cycles. This can attributed to the formation of PBH film, which prevented oxidation of the substrate. The decrease of current with increasing cycle number indicated film growth. Similar cycling behavior was observed during potentiodynamic deposition of other organic materials and attributed to film growth[4].

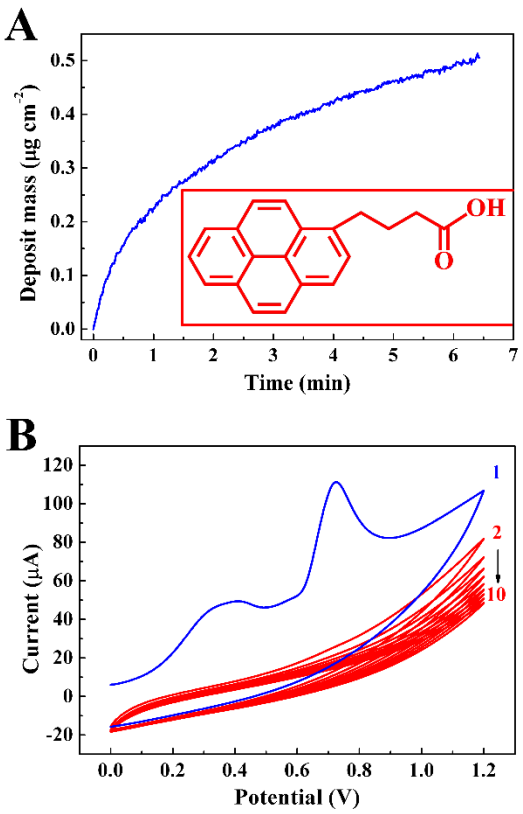

Fig.9.1 (A) Deposit mass, measured using QCM, versus deposition time for 1 g L^{-1} PBH aqueous solution at a deposition voltage of 3 V, inset shows chemical structure of PBH; (B) cyclic voltammetry data for a stainless steel electrode in the 1 g L^{-1} PBH aqueous solution at a scan rate of 20 mV s^{-1}, arrow shows increasing cycle number.

The results indicated that EPD method can used for the deposition of small organic molecules, such as PBH. The deposition mechanism involved the electrophoresis of dissociated PBH molecules, electrode reactions and film formation. The dissolution of PBH in water at pH=8 resulted in the deprotonation of the COOH group (Fig.9.1A, inset):

$$PBH \rightarrow PB^- + H^+ \qquad (\textbf{Eq.}9.1)$$

The electrophoresis of negatively charged PB^- resulted in the accumulation of PB^- at the anode surface, where pH decreased due to the following reaction:

$$2H_2O \rightarrow O_2 + 4H^+ + 4e^- \quad \textbf{(Eq.}9.2\textbf{)}$$

The protonation and charge neutralization of PB^- at the anode surface resulted in the deposition of PBH films:

$$PB^- + H^+ \rightarrow PBH \quad \textbf{(Eq.}9.3\textbf{)}$$

It is important to note that PBH is insoluble in water at neutral and acidic pH. Therefore, the deposition process resulted in the formation of insoluble PBH films. The charge neutralization and formation of insoluble PBH are important factors, controlling film deposition.

Fig.9.2 shows typical SEM images of (A) cross section and (B) surface of a PBH film. The analysis of SEM images showed that film thickness can be varied in the range of 0.1-2 μm by the variation of PBH concentration in the range of 0.1-2 g L^{-1}, deposition voltage in the range of 1-10 V and deposition time 1-10 min. The SEM image of the film surface indicated that the film was porous and contained needle-shape particles with the typical width and length of 150-200 nm and 0.5-1.5 μm, respectively.

It is suggested that particle formation is governed by π-π interactions of the PBH molecules. Turning again to the chemical structure of PBH shown in Fig.9.1A, it should be noted that PBH is a polyaromatic molecule, containing conjugated bonds. The π-π stacking of such molecules can result in anisotropic particle growth during electrophoretic deposition. The anisotropic particle growth was observed in other investigations focused on chemical assembly of molecules from pyrene family. The π-π stacking interactions of pyrene moieties allowed the columnar self-assembly of pyrene-containing oligo(glutamic acid)s[5]. The resulting fibrous materials showed tunable

fluorescence properties[5], which were utilized in new fluorescent devices.

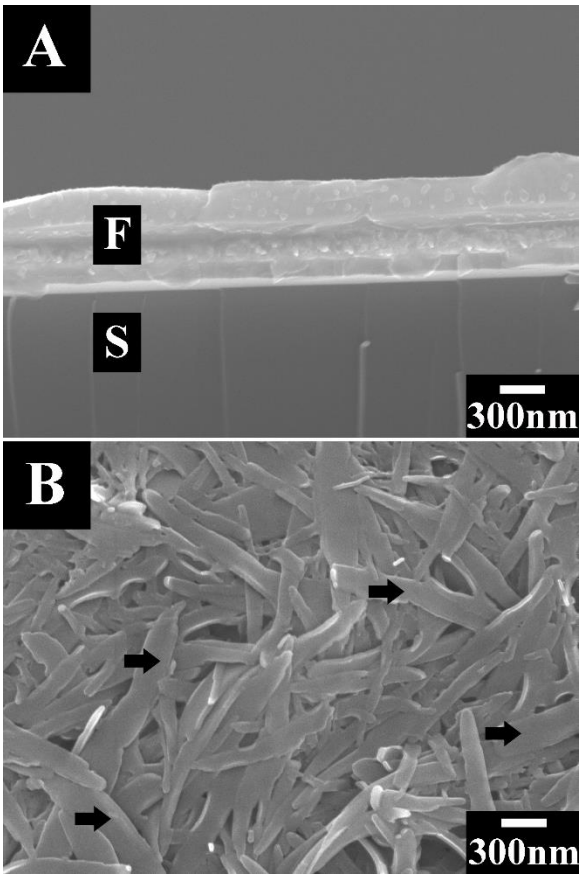

Fig.9.2 (A) Cross section of the PBH film (F) on a platinized silicon wafer substrate (S) and (B) surface of the PBH film, prepared from the 2 g L^{-1} PBH solution at a deposition voltage of 5 V and deposition time of 5 min. Black arrows show PBH particles.

Pyrene directed chemical self-assembly is currently under intensive investigation for the fabrication of efficient small molecule bulk heterojunction solar cells[6]. The π-π stacking provided enhanced electron transfer between the molecules. This approach resulted in record-high efficiency of small molecule organic photovoltaic devices[6]. In another investigation[7] π-π stacking interactions of pyrene allowed the formation of nanorods by chemical self-assembly. The films prepared by this method were used for the fabrication of photovoltaic devices. Chemical self-assembly of pyrene containing cationic

amphiphiles[8] allowed the formation of uniform nanotubes for application in sensors and optoelectronic devices. Pyrene nanowires and nanorods with tunable optical properties were prepared by chemical synthesis[9]. Pyrene-derivative nanorods with tunable fluorescent properties were formed by chemical precipitation inside the microcapsules, which were used for biomedical applications[10]. These studies have generated tremendous interest in chemical self-assembly of pyrene based molecules[8-11], formation of particles of special shapes with tunable properties, and investigation of physical properties of new materials. To this end, the electrochemical self-assembly approach offers new opportunities in the fabrication of advanced materials and devices.

Compared to chemical self-assembly methods, electrochemistry provides significantly higher deposition rates. Electrochemical methods offer many other advantages, such as possibility of co-deposition of a large variety of materials, good control of film morphology, microstructure, particle size and composition. It is important to note that pyrene derivatives played a leading role[12] in immobilization of various electroactive materials on CNT for applications as diverse as fluorescent [13], photovoltaic devices[12] and biosensors[14]. Therefore, new composite materials can be prepared by combined methods, based on electrochemical self-assembly and other electrochemical strategies. As a step in this direction, we utilized PBH for the fabrication of composite materials, containing MWCNT and MnO_2 nanoparticles.

9.2 EPD of MWCNT using PBH as a dispersant

It is known that electronic conductivity and mechanical properties of organic and inorganic materials can be improved by the development of composites, containing CNT. However, the fabrication of composites by colloidal methods presents difficulties,

attributed to agglomeration of CNT. The dispersion of CNT in suspensions and in final products is of critical importance for the fabrication of advanced composites.

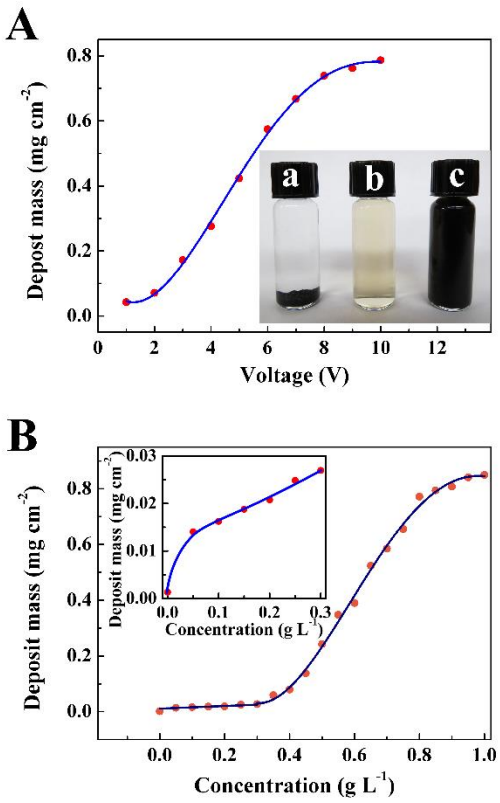

Fig.9.3 (A) Deposit mass versus deposition voltage for 1 g L^{-1} MWCNT suspension and deposition time of 5 min, inset shows (a) MWCNT, (b) PBH and (c) MWCNT and PBH in water, (B) deposit mass versus PBH concentration in 1 g L^{-1} MWCNT suspension at a deposition voltage of 7 V, inset shows low concentration range.

It was found that the suspensions of MWCNT in water were unstable and showed rapid precipitation immediately after the ultrasonic treatment. No EPD was achieved from such suspensions. In contrast, Fig.9.3A (inset) indicates good stability of the MWCNT suspension, containing PBH. The suspension was stable for more than 4 months. Moreover, EPD of MWCNT was achieved using PBH as a dispersing and charging agent. Fig.9.3A shows deposit mass as a function of deposition voltage for 1 g L^{-1} MWCNT

suspension, containing 1 g L^{-1} PBH. The deposition can be achieved at relatively low voltages with rapid increase in the deposition yield at voltages above 2 V (Fig.9.3A). The influence of PBH concentration on the deposition yield is shown in Fig.9.3B. It is seen that deposition can be achieved at relatively low PBH concentrations Fig.3B (inset). Significant increase in the deposition yield was observed (Fig.9.3B) at PBH concentrations above 0.4 g L^{-1}.

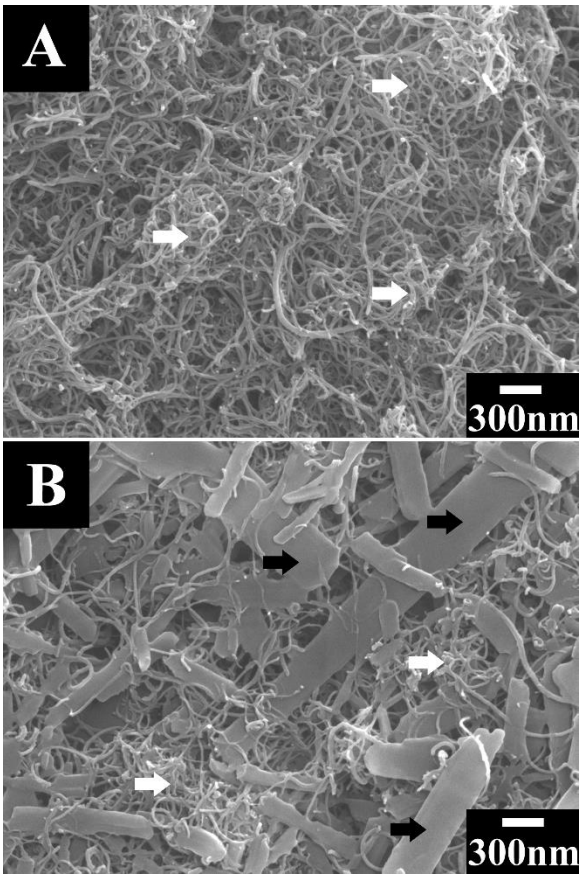

Fig.9.4 SEM images of deposits, prepared from 1 g L^{-1} MWCNT suspension, containing 1 g L^{-1} PBH, at deposition voltages of (A) 1 and (B) 3 V. White arrows show MWCNT, black arrows show PBH particles.

9.3 Influence of deposition voltage on MWCNT morphology

The films deposited at different conditions were studied by SEM. Fig.9.4 shows the influence of applied voltage on film microstructure and composition. EPD from 1 g L^{-1} MWCNT suspension, containing 1 g L^{-1} PBH at a deposition voltage of 1 V, resulted in the formation of a continuous MWCNT film (Fig.9.4A).

The increase in the deposition voltage resulted in significant changes in film microstructure and composition. SEM images of the films prepared at deposition voltages of 3-10V showed microstructures, containing MWCNT and relatively large PBH particles (Fig.9.4B). The size and shape of the PBH particles were similar to those shown in Fig.9.2B. The MWCNT were bonded to the surfaces of the PBH particles (Fig.9.4B). Moreover, the SEM investigations showed that some MWCNT were located inside the PBH particles.

9.4 Influence of PBH concentration on MWCNT morphology

The SEM analysis revealed the influence of PBH concentration on the film morphology and composition. Fig.9.5 compares the SEM images of films prepared at a deposition voltage of 7 V from the suspensions, containing different amounts of PBH. The film, prepared from 1 g L^{-1} MWCNT and 0.1 g L^{-1} PBH showed a porous microstructure, containing MWCNT (Fig.9.5A). However, the SEM image at higher magnification (Fig.9.5B) indicated that MWCNT were coated with PBH. The coating was non-uniform with higher coating thickness at junctions of individual nanotubes. It is suggested that higher local current density at the junction points can result in enhanced deposition of PBH. The increase in the PBH concentration resulted in changes in film morphology and

composition. Fig.9.5C showed PBH particles in addition to MWCNT. The SEM image at higher magnification (Fig.9.5D) indicated that MWCNT were bonded to the surface of PBH particles or located inside the PBH particles. The increase in the PBH concentration in the suspension resulted in increasing amount of the particles in the deposit (Fig.9.5E). The comparison of the images at higher magnification (Fig.9.5D,F) showed that the increase in the PBH concentration in the suspension resulted in the larger size of the deposited particles. The size and shape of PBH particles shown in Fig.9.4B and Fig.9.5C-F are comparable with those, presented in Fig.9.2B.

SEM investigations showed that the deposits contained mainly MWCNT at low deposition voltages or low PBH concentrations. The increase in deposition voltage and PBH concentration in the solutions promoted the deposition of PBH particles. Such observations correlate with deposition yield data presented in Fig.9.3, which showed rapid increase in the deposition yield at deposition voltages above 2 V and PBH concentration above 0.4 g L^{-1}. However, the changes in the deposition yield cannot be solely attributed to the deposition of PBH particles. It is important to see that the deposition yield for MWCNT-PBH deposits (Fig.9.3) was significantly higher than that for pure PBH (Fig.9.1A). Therefore, the rapid increase in the deposition yield at deposition voltages above 2 V (Fig.9.3A) and PBH concentration above 0.4 g L^{-1} (Fig.9.3B) can be attributed to enhanced deposition of both materials: MWCNT and PBH. Indeed, the electronic conductivity of PBH is low, therefore the charge transfer through the growing PBH film presents difficulties. The porous structure formed by conductive MWCNT facilitated charge transfer during electrodeposition and allowed a higher deposition rate. It is in this regard that EPD method allowed significant increase in

thickness of composite MWCNT-polymer films, compared to pure polymer films[15].

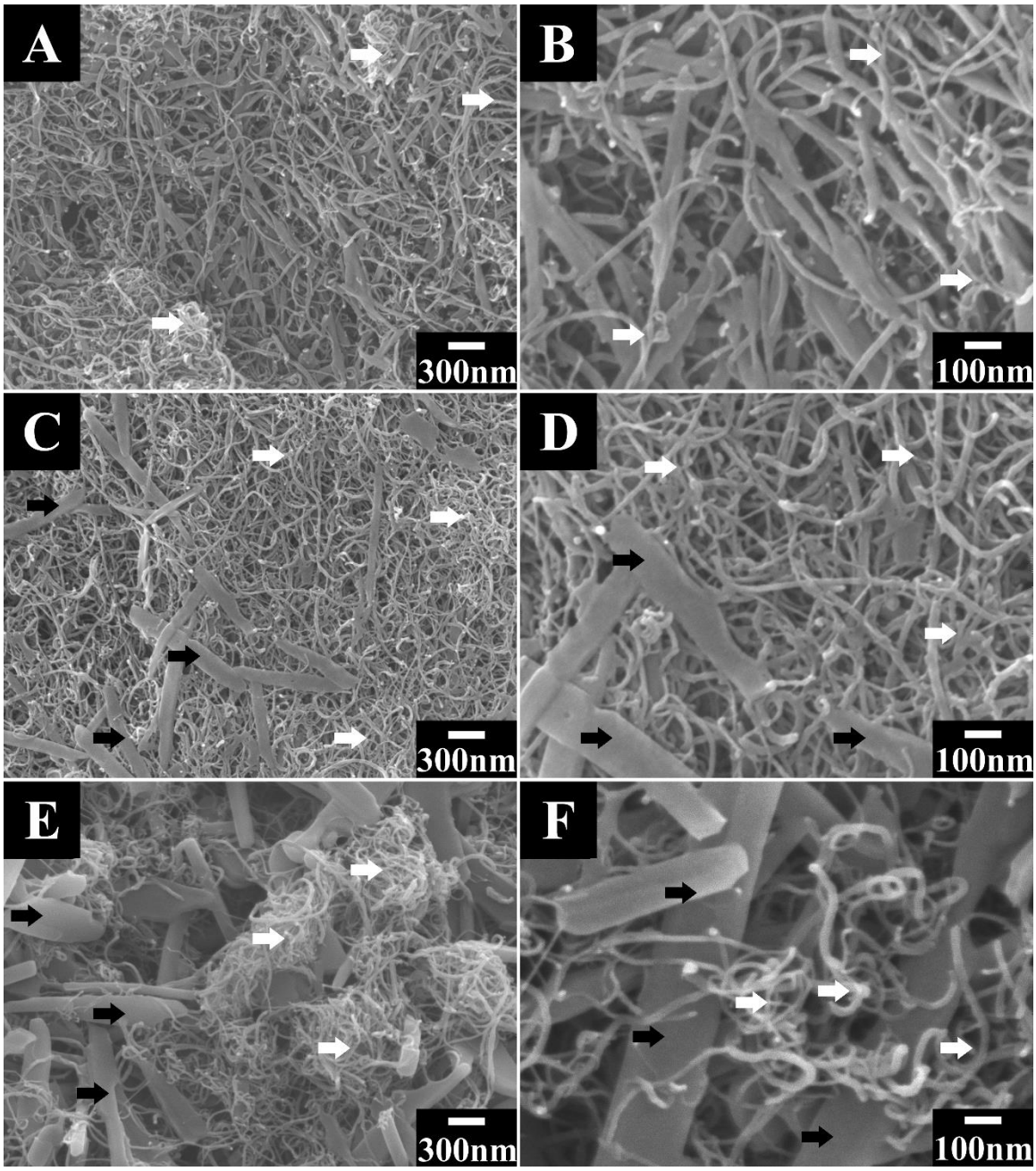

Fig.9.5 SEM images at different magnifications for deposits prepared from 1 g L^{-1} MWCNT suspension, containing (A and B) 0.1, (C and D) 0.2, and (E and F) 0.6 g L^{-1} PBH at a deposition voltage of 7 V. White arrows show MWCNT, black arrows show PBH particles.

9.5 Advantages of using PBH as a dispersant for MWCNT

The use of PBH as a dispersing and charging agent offers important advantages for EPD of MWCNT. In the previous investigations, various methods were developed for the dispersion, charging and EPD of CNT. It was found that adsorbed anionic and cationic polyelectrolytes provided charging of CNT in suspensions and allowed the formation of anodic or cathodic deposits by EPD[16]. Investigations were focused on the development of functionalization strategies, which included both covalent and supramolecular approaches[17-19]. However, polymer "wrapping" and supramolecular dispersion methods often result in the formation of CNT bundles.

The interactions of CNT with charging additives and solvents are especially important for dispersion and charging[20]. Many attempts have been made to improve wetting properties of CNT in solvents by oxidation in strong acids or mixtures of acids[20, 21]. It was shown that under acidic conditions, defective sites in the CNT are attacked, resulting in the formation of fragmented CNT, decorated with carboxylic and other oxygen-containing groups on their surface. These acidic groups electrostatically stabilized the CNT in suspensions and provided a negative charge for EPD. However, the oxidation and functionalization strategies introduce defects on the CNT sidewalls and reduce electronic conductivity of CNT. In another approach, the charging of CNT for EPD was achieved by adsorption of metal ions from added metal salts[20, 22]. It should be noted that the addition of metal salts results in lower suspension stability, attributed to increasing ionic strength of the suspension. The metal ions usually incorporate into the deposits as corresponding hydroxides or oxides and contaminate the deposits.

The dispersion and EPD of CNT using surfactants is of special interest[19]. Sodium

dodecyl sulfate (SDS) is one of the most promising anionic surfactants for the fabrication of stable suspensions of charged CNT[19]. However, relatively large concentration of SDS is required for CNT dispersion and EPD[23]. SDS form micelles, which induce a depletion attraction between the nanotubes [24, 25]. The strength of the attraction increases with increasing micelle concentration. Therefore, the increase in SDS concentration results in CNT aggregation. Van der Waals - induced aggregation at low SDS concentration and depletion-induced aggregation at high SDS concentration define an intermediate concentration range, where CNT can be homogeneously dispersed. The width of this SDS concentration range decreases drastically with increasing CNT concentration[24, 25], preventing the dispersion. It should be noted that the mechanism of PBH adsorption on MWCNT is different from the mechanism of SDS adsorption. The π-π interactions provided adsorption of polyaromatic PBH molecules on MWCNT. The dispersant adsorption is critical for efficient dispersion of MWCNT. PBH showed remarkable adsorption on SWCNT [26]. PBH offers other advantages for EPD, such as pH-dependent charge, film forming and binding properties. It is in this regard that colloidal stability and charge of MWCNT not necessarily allow for their deposition. Previous investigations showed that mutual electrostatic repulsions of particles at the electrode surface and poor particle adhesion to the electrode can prevent film formation[27]. Therefore, the pH-dependent charge, binding and film forming properties of PBH promoted the formation of MWCNT films. The co-deposition of MWCNT and materials from pyrene family, such as PBH, can be used for applications in electronic, photovoltaic and optical devices[5, 6, 9, 11], utilizing functional properties of pyrene based materials and high electronic conductivity of MWCNT. The EPD of MWCNT is

of special interest for the fabrication of composite MnO_2-MWCNT electrodes of electrochemical supercapacitors. The charging mechanism of MnO_2 is given by the following equation[28]:

$$MnO_2 + A^+ + e^- \leftrightarrow MnOOA \qquad (\textbf{Eq.}9.4)$$

where $A^+ = Li^+, Na^+, K^+, H^+$. Equation (6) indicates that high electronic and ionic conductivities of the electrode material are important in order to utilize the high theoretical SC of MnO_2 (1370 Fg^{-1}[29]). A complicating factor in the application of MnO_2 in ES is low electronic conductivity of this material. This problem can be addressed by the development of porous composites, containing MWCNT.

9.6 Co-deposition of MWCNT and MnO_2 nanoparticles

MnO_2 were negatively charged in aqueous suspensions at pH=8. EPD from the suspensions resulted in the formation of anodic deposits. In order to obtain composite MnO_2-MWCNT films by EPD, PBH and MWCNT were added to the MnO_2 suspensions. Fig.9.6A shows deposit mass as a function of deposition voltage for 4 g L^{-1} MnO_2 suspension, containing 1 g L^{-1} PBH. The deposit mass increased with increasing deposition voltage at a constant deposition time. The deposit mass increased with increasing PBH concentration (Fig.9.6B). Such increase cannot be solely attributed to PBH deposition, because the deposition rate of pure PBH is relatively low (Fig.9.1A). It is suggested that anionic PB^- was adsorbed on MnO_2 particles in the suspension and promoted their anodic deposition. The adsorption mechanism is similar to that of benzoic acid adsorption on oxide particles [30]. It can be attributed to interactions of COO^- group of PBH with Mn ions at the particle surface.

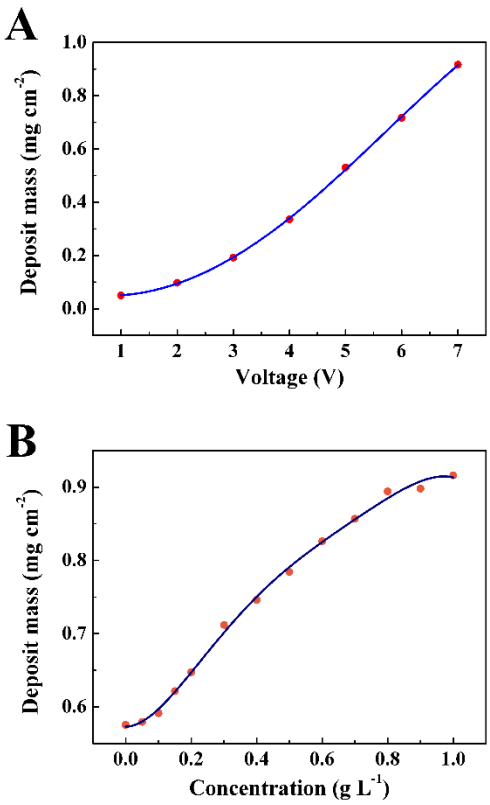

Fig.9.6 Deposit mass for 4 g L^{-1} MnO_2 suspension and deposition time of 5 min versus (A) deposition voltage at PBH concentration of 1 g L^{-1} and (B) PBH concentration at a deposition voltage of 7 V.

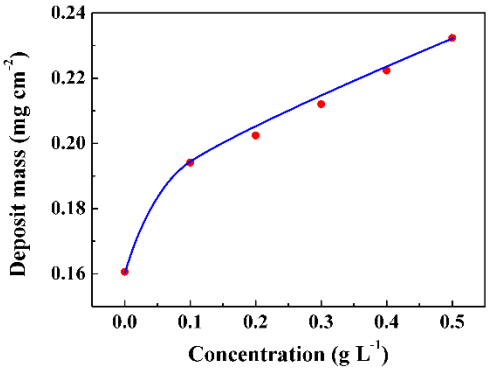

Fig.9.7 Deposit mass versus MWCNT concentration in 2 g L^{-1} MnO_2 suspension, containing 0.5 g L^{-1} PBH, at a deposition voltage of 7 V and deposition time of 2 min.

The MnO_2 deposits prepared from 2-4 g L^{-1} MnO_2 suspensions, containing 0.1-1.0 g L^{-1} PBH, at deposition voltages of 1-10 V were studied by SEM. In contrast to the SEM data for MWCNT deposits (Fig.9.4, 9.5), individual PBH particles were not observed in the MnO_2 deposits. The addition of MWCNT to the MnO_2 suspensions, containing PBH, resulted in increasing deposition rate, which indicated co-deposition of MnO_2 and MWCNT (Fig.9.7).

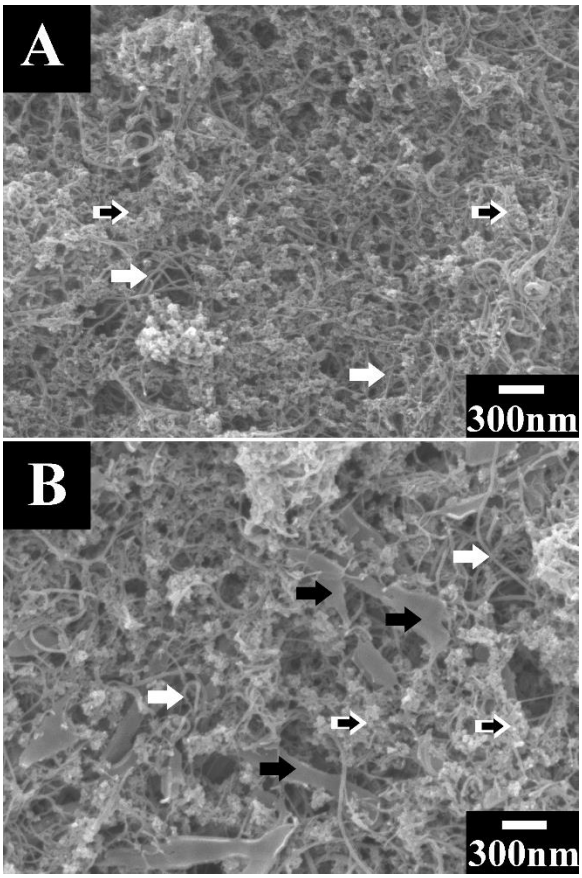

Fig.9.8 SEM images of deposits, prepared from 2 g L^{-1} MnO_2 suspension, containing 0.5 g L^{-1} MWCNT and (A) 0.1 and (B) 0.5 g L^{-1} PBH at a deposition voltage of 7 V. White arrows show MWCNT, black arrows show PBH particles, white-black arrows show MnO_2 particles.

The formation of composite deposits was confirmed by the SEM studies. Fig.9.8A shows

SEM image of the deposit, prepared from 2 g L^{-1} MnO_2 suspension, containing 0.5 g L^{-1} MWCNT and 0.1 PBH. The deposit was porous, it contained MnO_2 particles and MWCNT. The increase in PBH concentration from 0.1 to 0.5 g L^{-1} resulted in the deposition of PBH particles (Fig.9.8B). As pointed out above, the PBH particles were not observed in the SEM images of MnO_2 deposits, however similar particles were observed in the MWCNT deposits, prepared using PBH (Fig.9.4,9.5).

9.7 Composition study of MWCNT-MnO_2 composite film

Fig.9.9 compares TGA and DTA data for PBH, MWCNT, MnO_2, and composite deposits. The TGA data for PBH (Fig.9.9A) showed 2 steps in the mass loss in the range of 360-400 and 500-650 ℃, attributed to burning out of PBH. The corresponding DTA data showed broad exotherms in the same temperature range in agreement with the TGA data. The thermal analysis of MWCNT (Fig.9.9B) showed mass loss in the range of 500-700 ℃ in the TGA data and corresponding broad exotherm in the DTA data, attributed to burning out of MWCNT.

The TGA data for MnO_2 showed a sharp reduction of sample mass below 200 ℃, and then, the sample mass decreased gradually with increasing temperature (Fig.9.9C). The reduction in sample mass was attributed to dehydration of the birnessite phase. The corresponding DTA data showed an endotherm at ~ 120 ℃. A small mass gain in the range of 430-475 ℃ and a corresponding exotherm in the DTA curve could be attributed to the oxidation of non-stoichiometric birnessite phase. The total mass loss at 800 ℃ was found to be 13.4%.

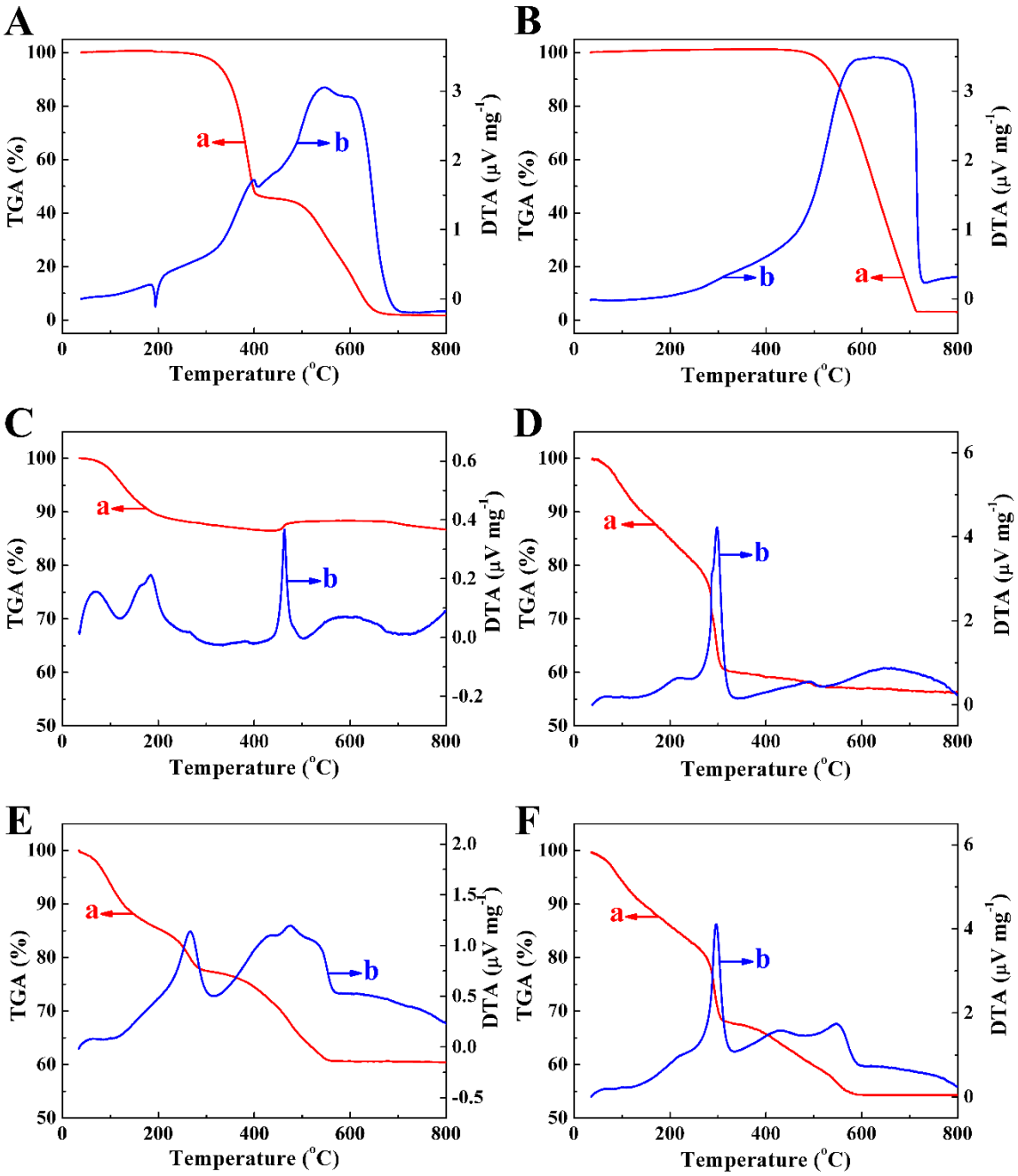

Fig.9.9 (a) TGA and (b) DTA data for (A) PBH, (B) MWCNT, (C) MnO_2 and composite deposits prepared at a constant voltage of 7 V from suspensions, containing (D) 4 g L^{-1} MnO_2 and 1 g L^{-1} PBH, (E) 2 g L^{-1} MnO_2, 0.5 g L^{-1} MWCNT and 0.1 g L^{-1} PBH, (F) 2 g L^{-1} MnO_2, 0.5 g L^{-1} MWCNT and 0.5 g L^{-1} PBH.

The TGA data (Fig. 9.9D) for deposit, prepared from 4 g L^{-1} MnO_2 suspension,

containing 1 g L^{-1} PBH, showed significant mass loss below 300 ℃, at higher temperatures relatively small reduction in sample mass were observed. The corresponding DTA data showed exothermic peak at ~300 ℃. The total mass loss of 43.6% at 800 ℃ was attributed to burning out of PBH and dehydration of the birnessite phase of MnO_2. Taking into account, the mass loss for MnO_2 (Fig.9.9C), the PBH content in the composite sample calculated from the TGA data (Fig. 9.9D) was 34.9%. The TGA data were in agreement with deposition yield measurements, presented in Fig.9.6B and indicated co-deposition of MnO_2 and PBH and the formation of composite films.

Fig.9.9E and F shows TGA and DTA data for deposits, prepared from 2 g L^{-1} MnO_2 suspensions, containing 0.5 g L^{-1} MWCNT and 0.1 or 0.5 g L^{-1} PBH. The TGA data showed several steps in mass loss attributed to thermal dehydration of the birnessite phase of MnO_2, burning out of MWCNT and PBH. The total mass loss was found to be (Fig.9.9E) 39.6 and (Fig.9.9F) 45.8%. The difference can be attributed to larger PBH content in the deposit prepared from the suspension with larger PBH concentration.

The TGA data are in agreement with SEM observations of the same samples (Fig.9.8), which showed large amount of PBH particles in the sample prepared from the suspension containing 0.5 g L^{-1} PBH. The comparison of the TGA data for the deposit (Fig. 9.9D) without MWCNT and (Fig.9.9E and F) with MWCNT showed relatively large mass changes (Fig.9.9E and F) in the range above 300 ℃, which are especially evident (Fig.9.9E) for the deposit, prepared from the suspension with lower PBH concentration. This mass loss above 300 ℃ can mainly be attributed to burning out of MWCNT, because burning out of MWCNT was observed at higher temperatures (Fig.9.9B), compared to PBH (Fig.9.9A). Moreover, the corresponding DTA data (Fig.9.9E and F)

revealed additional exotherms, attributed to burning out of MWCNT in the range of 400-600 ℃, which were not observed in Fig.9.9D.

9.8 Capacitive performance of MWCNT-MnO_2 composite film

The composite films showed capacitive behavior in the 0.5M Na_2SO_4 electrolyte. Fig.9.10(A,B) presents SC versus scan rate dependencies and corresponding CVs at scan rate of 10 mVs^{-1} for 0.3 mg cm^{-2} samples. The deposit prepared from the 2 g L^{-1} MnO_2 suspension, containing 0.5 g L^{-1} MWCNT and 0.1 g L^{-1} PBH, showed a SC of 250 and 90 Fg^{-1} at scan rates of 2 and 100 mV s^{-1}, respectively. The decrease in SC with increasing scan rate is attributed to diffusion limitations of electrolyte in pores. The increase in the PBH concentration in the suspension from 0.1 to 0.5 g L^{-1} resulted in significant reduction in specific capacitance at high scan rates (Fig.9.10A). The corresponding CVs deviated significantly from box shape (Fig.9.10B). This can be attributed to increased resistance. Turning again to the SEM images for corresponding samples, shown in Fig.9.8, it should be noted that the deposition of PBH particles (Fig.9.8B) can result in reduced porosity of the deposit prepared from suspension, containing 0.5 g L^{-1} PBH. The reduced porosity led to diffusion limitation in pores and reduced capacitance, especially at high scan rates. The sample, prepared from the suspension containing 0.5 g L^{-1} PBH, but without MWCNT, showed a SC of 40 Fg^{-1} at a scan rate of 2 mVs^{-1} and significant reduction in the area of corresponding CV (Fig.9.10A,B)

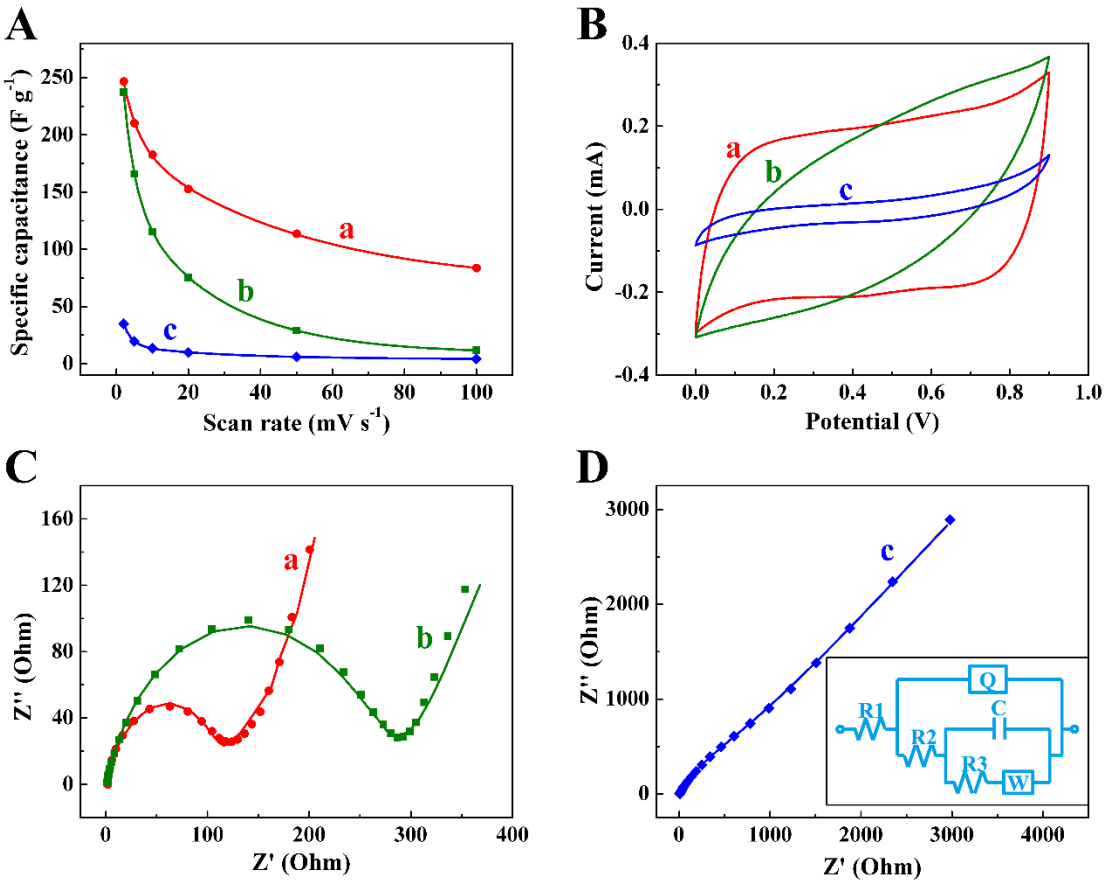

Fig.9.10 (A) SC versus scan rate, (B) corresponding CVs at a scan rate of 10 mV s^{-1} and (C and D) Nyquist plots for complex impedance $Z^* = Z' - iZ''$ for deposits prepared from 2 g L^{-1} MnO_2 suspensions, containing (a) 0.5 g L^{-1} MWCNT and 0.1 g L^{-1} PBH, (b) 0.5 g L^{-1} MWCNT and 0.5 g L^{-1} PBH, (c) 0.5 g L^{-1} PBH, solid lines are simulation results, obtained using an equivalent circuit shown in (D, inset), film mass 0.3 mg cm^{-2}.

The impedance spectroscopy data for corresponding samples were presented in Nyquist plots in Fig.9.10C,D. The equivalent circuit of ES (Fig.9.10D, inset) was discussed in several investigations[31-33]. It included RC-RQ transmission line, describing the porous electrode, and Warburg impedance W[33, 34], representing the diffusion resistance of electrolyte inside the pores. In this circuit, C elements represent double-layer capacitance and preudocapacitance, whereas R elements represent electrolyte resistance in pores,

Faradaic resistance and equivalent series resistance of the electrodes. The CPE element (Q)[35] describes a capacitor with microscopic roughness of the surface and capacitance dispersion of interfacial origin. Solution resistance is usually combined in series with RC-RQ transmission line[36].

The equivalent circuit should allow an optimum representation of the analyzed impedance data with a minimum set of model parameters. Conway and Pell described the impedance of the porous electrode using a five RC element circuit[31]. Good agreement of simulated and measured (Fig.9.10C,D) data was found for the equivalent circuit containing a transmission line with two RC(RQ) elements (Fig.9.10D, inset). The analysis of the impedance data, shown in Fig.9.10D, indicated significant increase in impedance with increased PBH concentration in the solution. This is in good agreement with corresponding SEM data, presented in Fig.9.8, which indicated that some pores can be blocked by PBH particles. The deposit prepared from suspension without MWCNT showed significantly higher resistance. The slope of the curve presented in Fig.10D is close to 45 º, indicating significant contribution of Warburg impedance. The relatively high impedance (Fig.9.10C(b) and Fig.9.10D) of the deposits prepared from the suspensions containing 0.5 g L^{-1} PBH resulted in lower SC (Fig.9.10A(b,c)).

The obtained SC (Fig.9.10Aa) was higher than that reported in a previous investigation [59] for MnO_2-MWCNT electrodes of similar mass prepared by EPD. The difference can be attributed to improved dispersion of MWCNT, achieved using PBH as a dispersant. However, the SC is lower compared to that achieved in the redox method [60]. However, in the redox method, CNT are used as a sacrificial reducing agent. The degradation of CNT results in reduced conductivity. It is important to note that in Ref. [60], the SC was

presented for MnO_2 component only, whereas in our investigation, the total mass of the deposited electrode material was used for SC calculation.

9.9 Conclusions

EPD method has been developed for the fabrication of PBH films from aqueous solutions. The films can be obtained at constant voltage or potentiodynamic conditions. The deposition mechanism involved the electrophoresis of anionic PB^- species, pH decrease at the anode surface, charge neutralization and formation of insoluble PBH films. The film morphology and shape of the PBH particles are controlled by the π-π stacking mechanism of the polyaromatic PBH molecules. The use of PBH as a charging, dispersing and film forming agent allowed the fabrication of stable suspensions of MWCNT and their anodic deposition by EPD. The deposition yield, deposit microstructure and composition can be varied by the variation of deposition voltage and PBH concentration. The increase in the deposition voltage and PBH concentration in the suspensions promoted the co-deposition of PBH particles together with MWCNT. The new approach to the deposition of MWCNT was used for the fabrication of composite MnO_2-MWCNT films for electrodes of ES, which showed a SC of 250 Fg^{-1}. The EPD method developed in this investigation paves the way for the deposition of other organic molecules and composites and their applications in new materials and devices, utilizing the functional properties of the organic molecules, CNT and other advanced materials.

References

[1] Zhitomirsky I. Electrophoretic hydroxyapatite coatings and fibers. Materials Letters 2000;42:262-71.

[2] Vukovic M. The formation and growth of hydrous oxide film on stainless steel in alkaline solution by potential cycling. Corrosion Science 1995;37:111-20.

[3] Freire L, Novoa XR, Pena G, Vivier V. On the corrosion mechanism of AISI 204Cu stainless steel in chlorinated alkaline media. Corrosion Science 2008;50:3205-12.

[4] Zhang YZ, Luo HQ, Li NB. Polyaniline coating on 304 stainless steel by electropolymerisation from aqueous NaOH solution for corrosion protection in NaCl medium. Corrosion Engineering, Science and Technology. 2011;46:580-4.

[5] Kamikawa Y, Kato T. Color-tunable fluorescent organogels: Columnar self-assembly of pyrene-containing oligo(glutamic acid)s. Langmuir. 2007;23:274-8.

[6] Lee OP, Yiu AT, Beaujuge PM, Woo CH, Holcombe TW, Millstone JE, et al. Efficient Small Molecule Bulk Heterojunction Solar Cells with High Fill Factors via Pyrene-Directed Molecular Self-Assembly. Advanced Materials 2011;23:5359-63.

[7] Xiao J, Liu Y, Li Y, Ye J, Li Y, Xu X, et al. Self-assembly and optical properties of hydrogen bonded nanostructures containing C60 and pyrene. Carbon. 2006;44:2785-92.

[8] Chen Y, Zhu B, Han Y, Bo Z. Self-assembly of cationic pyrene nanotubes. Journal of Materials Chemistry 2012;22:4927-31.

[9] Zhang X, Zhang X, Shi W, Meng X, Lee C, Lee S. Morphology-controllable synthesis of pyrene nanostructures and its morphology dependence of optical properties. Journal of Physical Chemistry B 2005;109:18777-80.

[10] Wang Z, Liu M, Xie Y, Gao C. In situ fabrication of pyrene derivative nanorods inside polyelectrolytes microcapsules with tunable fluorescent properties. Journal of Materials Chemistry 2012;22:2855-8.

[11] Uji-I H, Nishio S, Fukumura H. Electronic properties of a -stacked pyrene derivative at a liquid-solid interface studied with scanning tunneling spectroscopy. Chemical Physics Letters 2005;408:112-7.

[12] Ehli C, Guldi DM, Angeles Herranz M, Martin N, Campidelli S, Prato M. Pyrene-tetrathiafulvalene supramolecular assembly with different types of carbon nanotubes. Journal of Materials Chemistry 2008;18:1498-503.

[13] Tasis D, Mikroyannidis J, Karoutsos V, Galiotis C, Papagelis K. Single-walled carbon nanotubes decorated with a pyrene-fluorenevinylene conjugate. Nanotechnology. 2009;20:135606.

[14] Haddad R, Holzinger M, Maaref A, Cosnier S. Pyrene functionalized single-walled carbon nanotubes as precursors for high performance biosensors. Electrochimica Acta 2010;55:7800-3.

[15] Wang Y, Deen I, Zhitomirsky I. Electrophoretic deposition of polyacrylic acid and composite films containing nanotubes and oxide particles. Journal of Colloid and Interface Science 2011;362:367-74.

[16] Grandfield K, Sun F, FitzPatrick M, Cheong M, Zhitomirsky I. Electrophoretic deposition of polymer-carbon nanotube-hydroxyapatite composites. Surface and Coatings Technology 2009;203:1481-7.

[17] Casagrande T, Lawson G, Li H, Wei J, Adronov A, Zhitomirsky I. Electrodeposition of composite materials containing functionalized carbon nanotubes. Materials Chemistry and Physics 2008;111:42-9.

[18] Wu K, Imin P, Sun Y, Pang X, Adronov A, Zhitomirsky I. Electrophoretic deposition of composite films from solutions of conjugated polymers and their supramolecular complexes with carbon nanotubes. Materials Letters 2012;67:248-51.

[19] Vaisman L, Wagner HD, Marom G. The role of surfactants in dispersion of carbon nanotubes. Advances in Colloid and Interface Science. 2006;128-130:37-46.

[20] Boccaccini AR, Cho J, Roether JA, Thomas BJC, Jane Minay E, Shaffer MSP. Electrophoretic deposition of carbon nanotubes. Carbon. 2006;44:3149-60.

[21] Esumi K, Ishigami M, Nakajima A, Sawada K, Honda H. Chemical treatment of carbon nanotubes. Carbon. 1996;34:279-81.

[22] Du C, Pan N. High power density supercapacitor electrodes of carbon nanotube films by electrophoretic deposition. Nanotechnology. 2006;17:5314-8.

[23] Pei S, Du J, Zeng Y, Liu C, Cheng H-M. The fabrication of a carbon nanotube transparent conductive film by electrophoretic deposition and hot-pressing transfer. Nanotechnology. 2009;20:235707.

[24] Vigolo B, Coulon C, Maugey M, Zakri C, Poulin P. An experimental approach to the percolation of sticky nanotubes. Science. 2005;309:920-3.

[25] Vigolo B, Pénicaud A, Coulon C, Sauder C, Pailler R, Journet C, et al. Macroscopic fibers and ribbons of oriented carbon nanotubes. Science. 2000;290:1331-4.

[26] Rogers RE, Bardsley TI, Weinstein SJ, Landi BJ. Solution-phase adsorption of 1-pyrenebutyric acid using single-wall carbon nanotubes. Chemical Engineering Journal 2011;173:486-93.

[27] Zhitomirsky I. Cathodic electrodeposition of ceramic and organoceramic materials. Fundamental aspects. Advances in Colloid and Interface Science. 2002;97:277-315.

[28] Athouel L, Moser F, Dugas R, Crosnier O, Belanger D, Brousse T. Variation of the MnO_2 birnessite structure upon charge/discharge in an electrochemical supercapacitor electrode in aqueous Na_2SO_4 electrolyte. The Journal of Physical Chemistry C. 2008;112:7270-7.

[29] Devaraj S, Munichandraiah N. High capacitance of electrodeposited MnO_2 by the effect of a surface-active agent. Electrochemical and Solid-State Letters 2005;8:A373-A7.

[30] Tunesi S, Anderson MA. Surface effects in photochemistry: an in situ cylindrical internal reflection-Fourier transform infrared investigation of the effect of ring substituents on chemisorption onto TiO_2 ceramic membranes. Langmuir. 1992;8:487-95.

[31] Conway BE, Pell WG. Power limitations of supercapacitor operation associated with resistance and capacitance distribution in porous electrode devices. Journal of Power Sources 2002;105:169-81.

[32] Huai Y, Hu X, Lin Z, Deng Z, Suo J. Preparation of nano-TiO_2/activated carbon composite and its electrochemical characteristics in non-aqueous electrolyte. Materials Chemistry and Physics 2009;113:962-6.

[33] Kötz R, Carlen M. Principles and applications of electrochemical capacitors. Electrochimica Acta 2000;45:2483-98.

[34] Sawai K, Ohzuku T. A method of impedance spectroscopy for predicting the dynamic behavior of electrochemical system and its application to a high-area carbon electrode. Journal of the Electrochemical Society 1997;144:988-95.

[35] Pell WG, Zolfaghari A, Conway BE. Capacitance of the double-layer at polycrystalline Pt electrodes bearing a surface-oxide film. Journal of Electroanalytical Chemistry 2002;532:13-23.

[36] Zhang G-Q, Zhao Y-Q, Tao F, Li H-L. Electrochemical characteristics and impedance spectroscopy studies of nano-cobalt silicate hydroxide for supercapacitor. Journal of Power Sources 2006;161:723-9.

Chapter 10 Asymmetric MnO_2-MWCNT/VN-MWCNT supercapacitors

10.1 Synthesis of VN-MWCNT composites

Fig.10.1A shows an SEM image of the V_2O_5 powder, used in this investigation. The particle size of V_2O_5 was in the range of 0.2-1.0 μm. The SEM image of the VN powder (Fig.10.1B) showed that primary particle size is on the nanometric scale. However, some particles formed agglomerates. The size of the agglomerates was comparable with the size of V_2O_5 particles (Fig.10.1A), used for the synthesis of VN. Such agglomerates were not observed in the SEM images of VN-MWCNT composites.

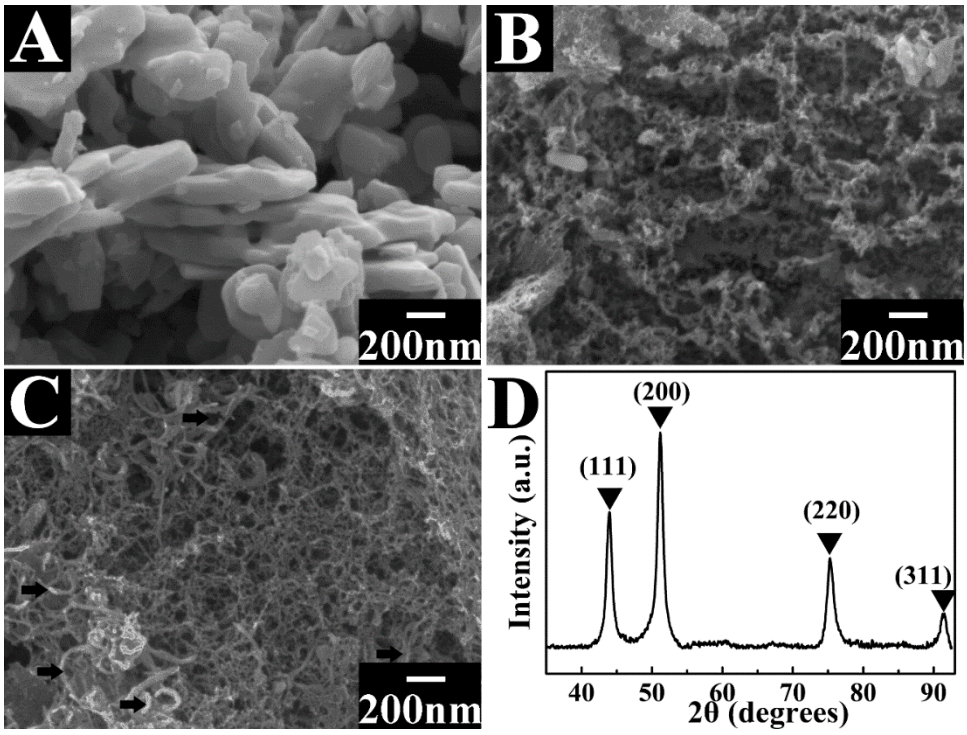

Fig.10.1 SEM images of (A) V_2O_5, (B) VN, (C) VN-MWCNT composite, arrows show MWCNT, and (D) XRD spectrum of VN, ▼- peaks corresponding to JCPDS 35-0768

file.

Fig.10.1C shows the typical SEM image of a VN-MWCMT composite. The microstructure of the composite included fibrous nanoparticles of VN, which had smaller diameter, compared to the diameter of MWCNT. The XRD studies confirmed the formation of pure VN phase. The XRD pattern of VN corresponds to the JCPDS 35-0768 file (Fig.10.1D).

10.2 Electrochemical capacitive performance of VN-MWCNT electrodes

The VN electrodes with mass loading of 15 mg cm^{-2} showed a C_m of 38.5 F g^{-1} (C_s =0.58 F cm^{-2}) in 0.5 M Na_2SO_4 electrolyte at a scan rate of 2 mV s^{-1}. The MWCNT electrodes of the same mass showed a C_m of 49.8 F g^{-1} (C_s=0.75 F cm^{-2}). The SC decreased with increasing scan rate due to diffusion limitations of the electrolyte in pores. The VN-MWCNT composite electrode with mass loading of 15 mg cm^{-2} showed C_m of 160.3 F g^{-1} (C_s=2.4 F cm^{-2}) at a scan rate of 2 mV s^{-1}. The SC decreased with increasing scan rate, showing C_m=65 F g^{-1} (C_s =0.97 F cm^{-2}) at a scan rate of 100 mV s^{-1}. The corresponding CVs, used for SC calculations are presented in Fig.10.2B. Nearly box shape CVs indicated good capacitive behavior in the voltage window of -0.9 ─ 0 V versus SCE. The increase in current with increasing scan rate indicated good capacitance retention. The higher SC of the composite, compared to VN electrode, can be attributed to lower agglomeration of VN particles and higher conductivity of the VN-MWCNT composite. It is suggested that the MWCNT network provided improved electronic conductivity of the composite material, which was beneficial for the charge-discharge reactions.

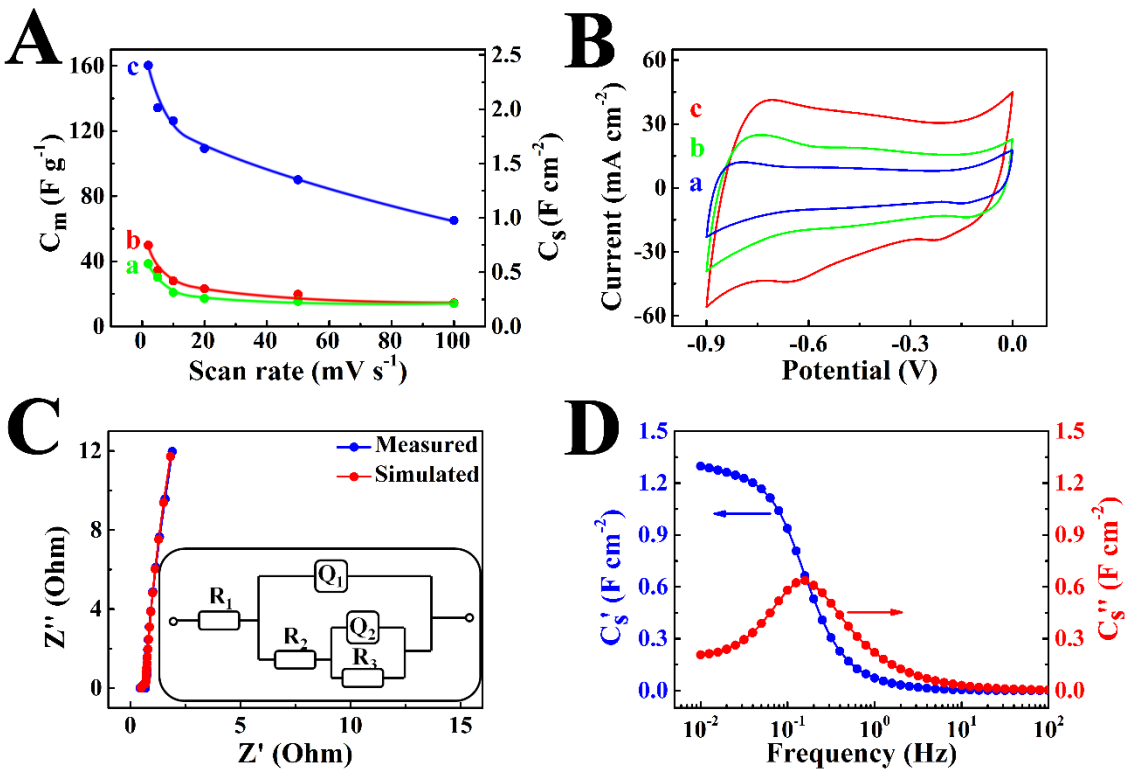

Fig.10.2 (A) CVs for VN-MWCNT electrode at scan rates of (a) 5, (b) 10, and (c) 20 mV s^{-1}, (B) C_m and C_s versus scan rate for (a) VN, (b) CNT, and (c) VN-MWCNT composite electrodes, (C) Nyquist plot of complex impedance and corresponding simulation data for the VN-MWCNT composite electrode, inset shows the equivalent circuit used for the simulation, (D) real and imaginary components of capacitance for the VN-MWCNT composite electrode, calculated from the impedance data. Mass loading for all electrodes is 15 mg cm^{-2}.

The EIS data presented in a Nyquist plot of Z'' versus Z' showed nearly linear dependence with the line slope close to 90 º, indicating good capacitive behavior and low resistance R=Z'. The Nyquist plot was simulated using an equivalent circuit shown in the inset of Fig.10.2C, which included two R-Q transmission lines, describing the porous electrode [1, 2]. In this circuit, R_1, R_2 and R_3 represented the electrolyte resistance, electrode material

resistance and charge transfer resistance, respectively. Q_1 and Q_2 elements represent pseudocapacitance and double-layer capacitance [3, 4], respectively, with consideration of surface roughness and capacitance dispersion of interfacial origin. Fig.10.2D shows frequency dependence of components of AC capacitance, calculated from the EIS data. The electrodes showed a C_s' of 1.3 F cm^{-2} at a frequency of 0.01Hz, comparable with C_s, calculated from the CV data at a similar charge-discharge period. The spectrum revealed relaxation type of dispersion[5, 6] at frequencies above 0.1 Hz, as indicated by the reduction of C_s' with increasing frequency and corresponding maximum in C_s'' at 0.2 Hz.

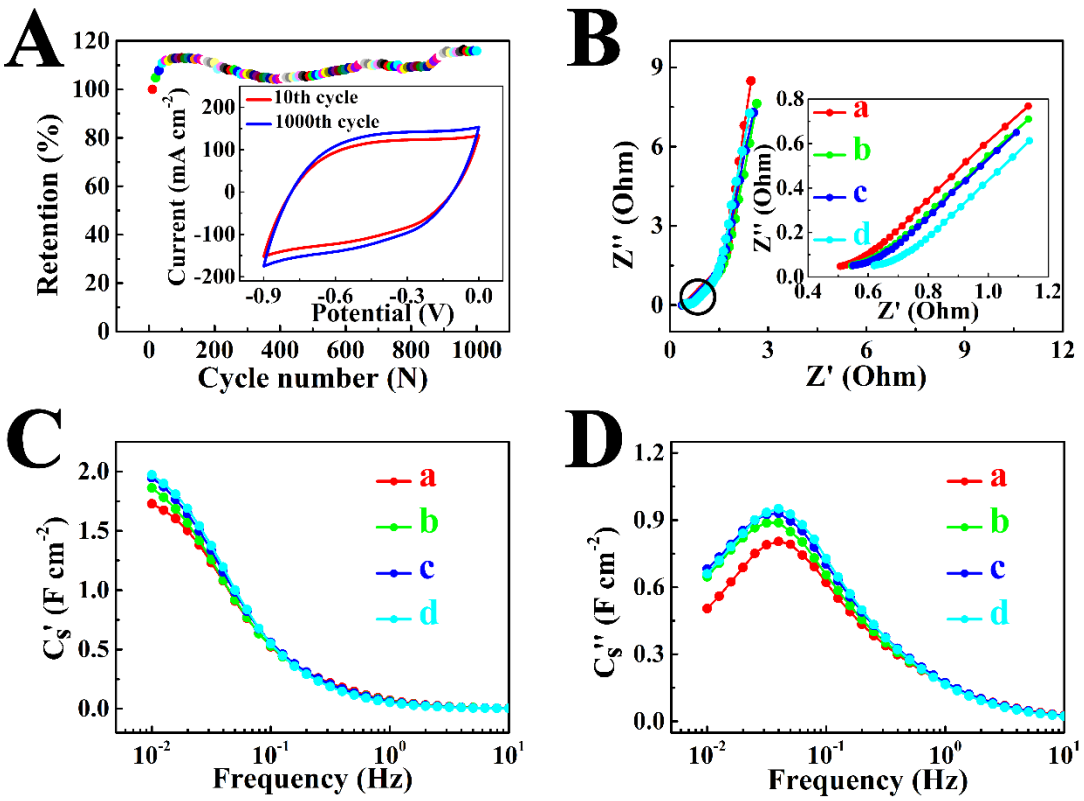

Fig.10.3 (A) Capacitance retention for 30 mg cm^{-2} VN-MWCNT composite electrode at a scan rate of 50 mV s^{-1}, inset shows CVs for 10^{th} and 1000^{th} cycles. (B) Nyquist plot of complex impedance, inset shows encircled high frequency range, (C) C_s', and (D) C_s'', calculated from the impedance data after (a) 250^{th}, (b) 500^{th}, (c) 750^{th}, and (d) 1000^{th}

cycle.

The investigation of the cycling behavior of the VN-MWCNT electrodes showed that capacitance increased by 15.9 % after 1000 cycles (Fig.10.3A). The inset in Fig.10.3A shows increased area of the CV after 1000 cycles. Similar capacitance increase was observed for other materials, it was attributed to microstructure changes during cycling[5]. The analysis of the impedance data (Fig.10.3B) showed small changes in Z' and Z" during cycling. The corresponding low frequency C_s' and C_s'' values increased slightly during cycling (Fig.10.3C,D). The increase in C_s' with increasing cycle number (Fig.10.3C) was in agreement with C_s increase (Fig.10.3A). No obvious frequency shift was observed for the peaks of C_s'', indicating that cycling had no influence on the frequency dependence of AC capacitance.

Previous investigations showed good cycling stability of VN electrodes in KOH electrolyte at low active mass loadings (0.21-0.41 mg cm^{-2}) [7]. The capacitance reduction was less than 10% after 1000 cycles a scan rate of 50 mV s^{-1}. In another investigation[8] the capacitance remained at the level of 60% of initial capacitance after 1000 cycles in KOH electrolyte. The VN functionalized carbon nanotube electrodes with VN loading of 0.135 mg cm^{-2} showed[9] capacitance retention of 64% after 600 cycles in a KOH electrolyte at a scan rate of 50 mV s^{-1}. However, it is important to achieve good electrochemical performance and cycling stability at materials loading of 10-20 mg cm^{-2}, which is desired for many commercial devices [10, 11]. The good capacitance retention, achieved at material loading of 30 mg cm^{-2} in Na_2SO_4 electrolyte (Fig.10.3), is promising for practical application of VN electrodes in electrochemical supercapacitors.

10.3 Charge-discharge mechanism of VN

The charging mechanism of VN in the 0.5 M Na_2SO_4 electrolyte is different from that, described for the 1 M KOH electrolyte[7, 12-14]. In the concentrated KOH solutions, the anionic OH^- species were involved in charge storage in the VN electrodes at negative electrode potentials. The suggested charge storage mechanisms included the double layer formation and Faradaic reactions [7, 12]. Numerous XPS studies revealed the formation of surface oxides on VN nanoparticles[7, 12-14] in aqueous solutions. It was suggested[7] that in the presence of OH^- ions, the following reactions occur on the oxy-nitride surface:

$$VN_xO_y + OH^- \leftrightarrow VN_xOy \| OH \qquad (\textbf{Eq.}10.1)$$

$$VN_xO_y + OH^- \leftrightarrow VN_xOy\text{-}OH \qquad (\textbf{Eq.}10.2)$$

Eq.10.1 and Eq.10.2 describe double layer ($VN_xOy \| OH$) and pseudocapacitance, respectively. The pseudocapacitance mechanism involved the electron transfer across the surface. Such mechanisms cannot explain the charge storage of VN in the Na_2SO_4 solutions due to the low concentration of OH^- ions. Moreover, it is important to note that the electric field moves OH^- ions away from the negative electrodes. The analysis of ion migration in supercapacitor electrode material is important for understanding the charge-discharge mechanisms. The QCM technique is an important tool for the analysis of ionic fluxes into porous electrode materials of electrochemical supercapacitors[15].

In this investigation the ionic fluxes in the VN-MWCNT electrodes were analyzed using QCM at galvanostatic conditions. Fig.10.4 compares the QCM data for VN-MWCNT coated and uncoated quartz resonators for applied positive and negative constant current pulses of 0.1 mA. For coated electrodes, the application of negative current pulses

resulted in a mass gain, which can be attributed to the insertion of Na^+ ions into the VN-MWCNT material. The application of positive current pulses resulted in the mass loss, attributed to electromigration of Na^+ in opposite direction. Literature data[15] on QCM analysis of porous electrode materials in periodic electric fields revealed periodic mass gains related to insertion of both: cations and anions. However, the QCM studies[16] of CNT electrodes in neutral aqueous solutions showed that mass gain was observed only when the potential was scanned in the negative direction. Such behavior indicated significant contribution of the cationic transport. Investigations[15-18] demonstrated that relative contributions of cationic and anionic transport to the mass changes of QCM resonator depend on the relative size of cations and anions and point of zero charge of the electrode material. It was demonstrated that negatively charged carbon nanotubes in aqueous solutions promoted cationic transport[16]. As a result, QCM studies revealed mass gain only for the negative scans[16]. A similar mechanism can explain the QCM data for VN-MWCNT coated resonators. As pointed out above, numerous XPS studies revealed the formation of surface oxides on VN nanoparticles[7, 12-14] in aqueous solutions. It is known[19] that vanadium oxides have low points of zero charge. Therefore, in neutral solutions the negatively charged surface oxide layers of VN can promote a cationic transport.

QCM studies of MnO_2 in NaCl and Na_2SO_4 solutions showed mass loss when positive potential was applied to the electrodes[20-22]. The investigations were performed in a wide potential range at different current and voltage conditions. It was shown that Na cations are involved in the charging of MnO_2 in the positive potential range, according to the following reaction[20, 21]:

$$MnO_2Na_\delta \leftrightarrow \delta Na^+ + \delta e^- + MnO_2 \quad \textbf{(Eq.}10.3\textbf{)}$$

The results of QCM studies of the VN electrodes showed that the insertion/deinsertion of Na^+ ions can be involved in the charge-discharge mechanism (Fig.10.4). The following charging mechanism, involving oxy-nitride surface, can be proposed in the Na_2SO_4 solutions:

$$VN_xO_y + \delta Na^+ + \delta e^- \leftrightarrow VN_xO_yNa_\delta \quad \textbf{(Eq.}10.4\textbf{)}$$

The presented results of the investigation of negative VN-MWVNT electrodes in the Na_2SO_4 electrolyte, coupled with literature data[23-28], demonstrating good electrochemical performance of MnO_2-MWCNT positive electrodes in the same electrolyte, paved the way to the fabrication of asymmetric devices with enlarged voltage window.

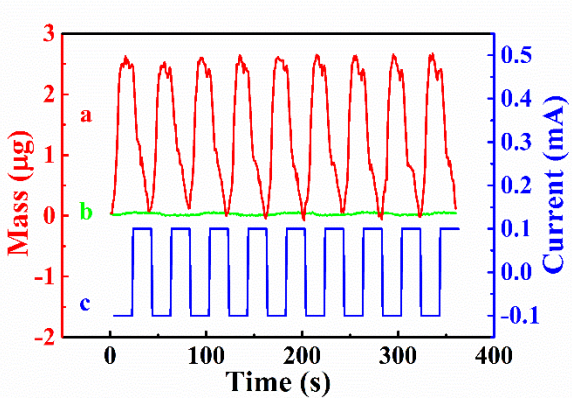

Fig.10.4 QCM data for (a) VN-MWCNT coated and (b) uncoated quartz resonators for (c) applied positive and negative constant current pulses of 0.1 mA.

10.4 Electrochemical capacitive performance of MnO_2-MWCNT/VN-MWCNT asymmetric supercapacitors

The VN-MWCNT negative electrodes were combined with MnO_2-MWCNT positive electrodes for the fabrication of supercapacitor cells. Compared with the previous investigations[28, 29], the MWCNT content in the MnO_2-MWCNT electrodes was increased to 50% in order to achieve comparable capacitances with VN-MWCNT electrodes at high scan rates. The capacitive behavior of MnO_2-MWCNT electrode is shown in Fig.10.5.

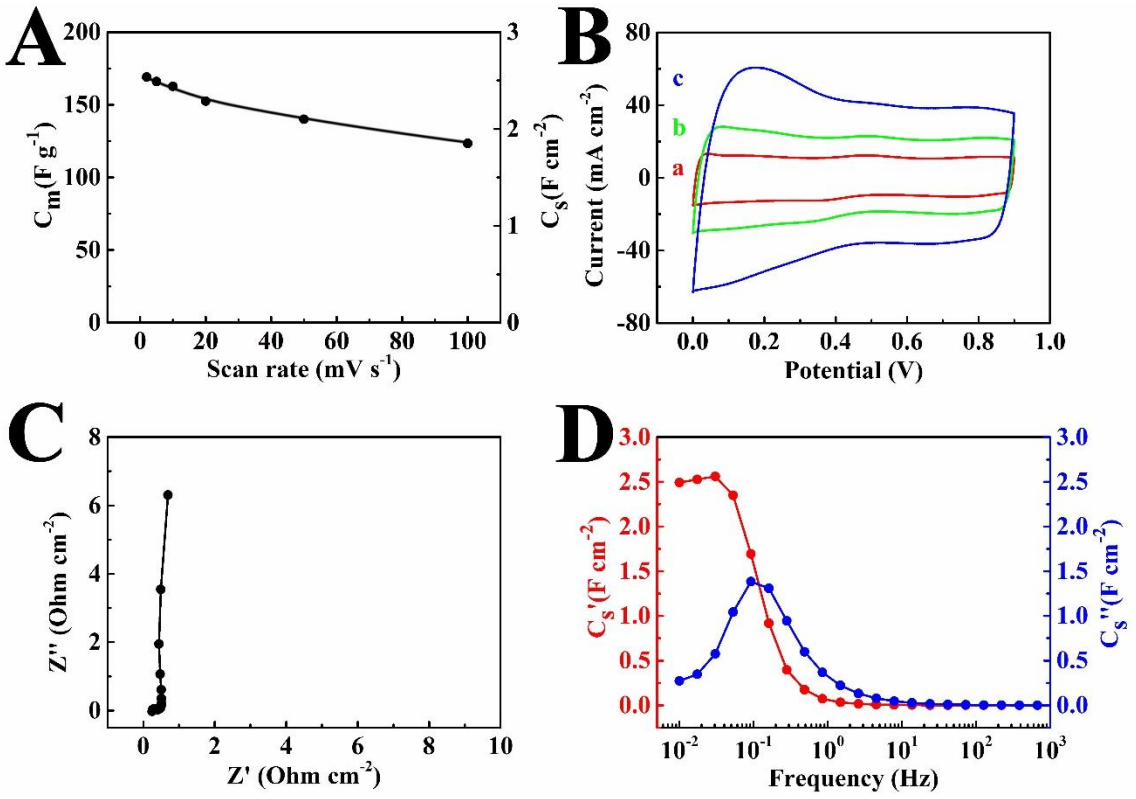

Fig.10.5 (A) Specific capacitance C_m and C_s of MnO_2-MWCNT with a material loading of 21 mg cm^2 on nickel foam. (B) Corresponding CVs at scan rate of (a) 5, (b) 10, and (c) 20 mV s^{-1}. (C) EIS and (D) real (C_s') and imaginary (C_s'') capacitances calculated from

the EIS data.

The asymmetric cells showed box shape CVs at different scan rates, indicating good electrochemical performance in a voltage window of 1.8 V (Fig.10.6A). The C_s of 1.33 F cm^{-2} (was achieved at a scan rate of 2 mV s^{-1} for mass loading of each individual electrode of 10 mg cm^{-2}. The increase in scan rate resulted in decreasing C_s. The asymmetric cells showed C_s of 0.48 F cm^{-2} at a scan rate of 100 mV s^{-1} (Fig.10.6B). The high mass loading allowed significant improvement in C_s compared to the C_s of 1.85 mF cm^{-2} reported for cell voltage window of 1.3 V[30]. The results of EIS studies of the asymmetric cells are presented in the Nyquist plot in Fig.10.6C. The EIS showed relatively low impedance, which is well described by the equivalent circuit, presented in

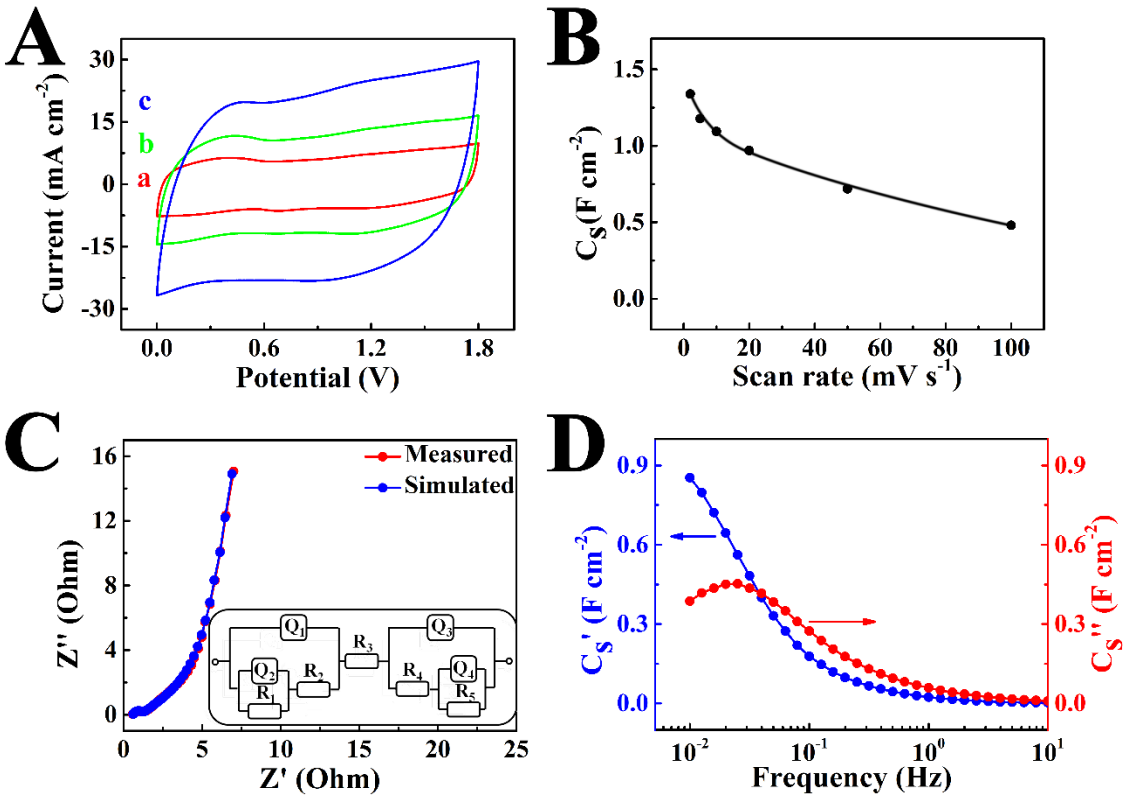

Fig.10.6 (A) CVs for two electrode asymmetric VN-MWCNT/MnO_2-MWCNT cell at scan rates of (a) 5, (b) 10, and (c) 20 mV s^{-1}, (B) C_s versus scan rate, calculated from the

CV data, (C) Nyquist plot of complex impedance for the asymmetric cell and corresponding simulation data, the inset shows the equivalent circuit, used for the simulation, (D) C_s', and C_s'', calculated from the impedance data.

Fig.10.6C (inset). The equivalent circuit of the device can be considered as a combination of two circuits of individual components, similar to the circuit shown in Fig.10.2C. The circuit includes electrode material resistances (R_2 and R_4) and charge transfer resistances (R_1 and R_5), electrolyte resistance R_3, pseudocapacitances (Q_1 and Q_3) and double-layer capacitances (Q_2 and Q_4). The capacitance C_s, calculated from the EIS data showed relaxation type frequency dispersion[5, 6], as indicated by the rapid decrease in Cs' in the range of 0.01-0.1 Hz and corresponding maximum in Cs'' at 0.03 Hz (Fig.10.6D).

Galvanostatic charge-discharge behavior of the asymmetric cells was investigated at different current densities in a voltage window of 1.8 V (Fig.10.7A). As shown in Fig.10.7A, the voltage-time curves were nearly symmetrical at all currents, indicating good Coulombic efficiency related to the reversible redox reactions of both MnO_2 and VN. No significant potential drops at low currents were observed, so the internal resistance was small. The energy density and power density were calculated from the discharges curves and plotted on a Ragone diagram in Fig.10.7B. The maximum energy density was 38.7 Wh kg^{-1} (19.4 mWh cm^{-3}) with a power density of 7.3 W kg^{-1} (3.7 mW cm^{-3}) under discharge current 0.25 mA, which gradually decreased to 13.3 Wh kg^{-1} (6.7 mWh cm^{-3}) with a power density of 316.2 W kg^{-1} (158.1 mW cm^{-3}) under discharge current of 10 mA.

For comparison, the energy and power density, reported[31] for asymmetric VN-CNT cells, were of 0.54 mWh cm^{-3} and 0.4 W cm^{-3}, respectively. In another investigation[32],

the maximum energy density and power density of 0.61 mWh cm^{-3} and 0.85 W cm^{-3}, respectively, were reported. Therefore, the approach, developed in this investigation allowed significant improvement in power-energy characteristics of the asymmetric cells, based on the VN electrode material. The insets in Fig.10.7B show coin cells, used in this investigation, and LED bulbs powered by the coin cells. The coin cells showed volumetric capacitance of 43 F cm^{-3} (86 F g^{-1}) at a constant current of 0.25 mA cm^{-2}, which is higher than the reported[31] value of 7.9 F cm^{-3} for asymmetric VN-CNT cells.

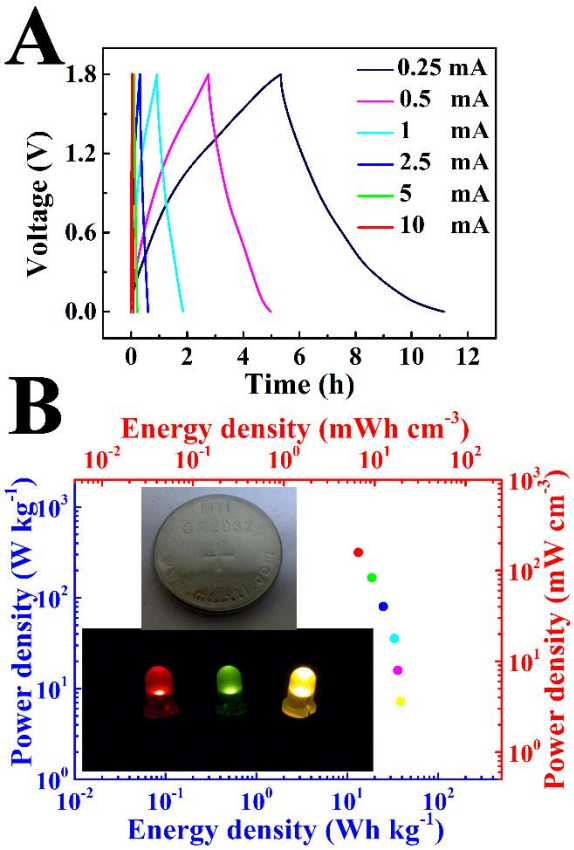

Fig.10.7 (A) Galvanostatic charge-discharge for two electrode asymmetric VN-MWCNT/MnO_2-MWCNT cell at different currents, (B) Ragone plot for the two electrode cell. The inset shows asymmetric VN-MWCNT/MnO_2-MWCNT coin cell used for the charge-discharge tests and LED bulbs powered by the coin cells.

The investigation of cyclic stability of the cells showed capacitance reduction with increasing cycle number. The capacitance retention after 1000 cycles was about 80% (Fig.10.8A). The capacitance decrease of asymmetric cells is not well understood, because individual electrodes showed good capacitance retention in corresponding voltage windows in the same electrolyte. It is suggested that capacitance reduction can be attributed to degradation of electrode materials or separator at operating conditions of 1.8 V. It is known that capacitance reduction during cycling of asymmetric capacitors can result from[33] excessive positive potential on the MnO_2 electrode and electrode matching problems. The analysis of the discharge curves showed that after 200 cycles a voltage drop V=IR appeared at the beginning of discharge (Fig.10.8B). The voltage drop increased with increasing cycle number and indicated the increasing cell resistance R.

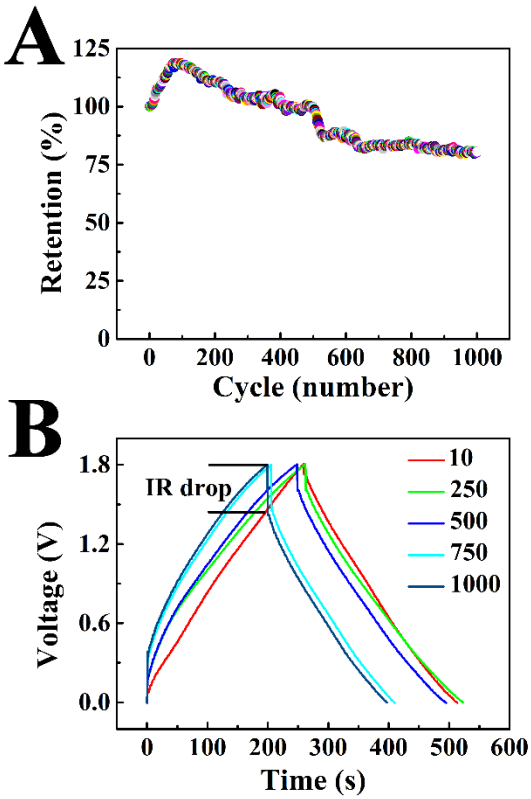

Fig.10.8 (A) Capacitance retention for asymmetric VN-MWCNT/MnO_2-MWCNT cell at

constant current of 10 mA, (B) Galvanostatic charge-discharge at a current of 10 mA for different cycles.

10.5 Conclusions

Nanostructured VN-MWCNT electrodes for electrochemical supercapacitors, prepared by a chemical method, showed good capacitive behavior in 0.5 M Na_2SO_4 electrolyte. The specific capacitance of VN-MWCNT was significantly higher compared to the capacitance of pure VN and MWCNT materials. QCM studies indicated that charge storage mechanism involves adsorption and desorption of Na^+ ions. The VN-MWCNT electrodes with high mass loading in the range of 10-30 mg cm^{-2} showed high specific capacitance, good capacitance retention in the range of 2-200 mV s^{-1} and good cycling stability. The highest capacitance of 160 F g^{-1} was achieved at a scan rate of 2 mV s^{-1}. Good electrochemical performance of the VN-MWCNT electrodes in the negative potential range in the 0.5 M Na_2SO_4 electrolyte allowed the fabrication of new type of asymmetric cells, containing VN-MWCNT negative and MnO_2-MWCNT positive electrodes. The asymmetric cells showed promising electrochemical performance in a voltage window of 1.8 V in aqueous 0.5 M Na_2SO_4 electrolyte with energy density of 38.7 Wh kg^{-1} (19.4 mWh cm^{-3} and a power density of 7.3 W kg^{-1} (3.7 mW cm^{-3}).

References

[1] Conway BE, Pell WG. Power limitations of supercapacitor operation associated with resistance and capacitance distribution in porous electrode devices. Journal of Power Sources 2002;105:169-81.

[2] Huai Y, Hu X, Lin Z, Deng Z, Suo J. Preparation of nano-TiO_2/activated carbon composite and its electrochemical characteristics in non-aqueous electrolyte. Materials Chemistry and Physics 2009;113:962-6.

[3] Su Y, Zhitomirsky I. Electrophoretic assembly of organic molecules and composites for electrochemical supercapacitors. Journal of Colloid and Interface Science 2012;392:247-55.

[4] Su Y, Zhitomirsky I. Electrophoretic deposition of graphene, carbon nanotubes and composite films using methyl violet dye as a dispersing agent. Colloids and Surfaces A: Physicochemical and Engineering Aspects. 2013;436:97-103.

[5] Shi K, Zhitomirsky I. Influence of current collector on capacitive behavior and cycling stability of Tiron doped polypyrrole electrodes. Journal of Power Sources 2013;240:42-9.

[6] Shi K, Zhitomirsky I. Polypyrrole nanofiber-carbon nanotube electrodes for supercapacitors with high mass loading obtained using an organic dye as a co-dispersant. Journal of Materials Chemistry A. 2013;1:11614-22.

[7] Choi D, Blomgren GE, Kumta PN. Fast and reversible surface redox reaction in nanocrystalline vanadium nitride supercapacitors. Advanced Materials. 2006;18:1178-82.

[8] Shu D, Lv CJ, Cheng FK, He C, Yang K, Nan JM, et al. Enhanced capacitance and rate capability of nanocrystalline VN as electrode materials for supercapacitors. International Journal of Electrochemical Science 2013;8:1209-25.

[9] Zhang L, Holt CM, Luber EJ, Olsen BC, Wang H, Danaie M, et al. High rate electrochemical capacitors from three-dimensional arrays of vanadium nitride functionalized carbon nanotubes. The Journal of Physical Chemistry C. 2011;115:24381-93.

[10] Wei L, Yushin G. Nanostructured activated carbons from natural precursors for electrical double layer capacitors. Nano Energy. 2012;1:552-65.

[11] Gogotsi Y, Simon P. True performance metrics in electrochemical energy storage. Science. 2011;334:917-8.

[12] Cheng F, He C, Shu D, Chen H, Zhang J, Tang S, et al. Preparation of nanocrystalline VN by the melamine reduction of V_2O_5 xerogel and its supercapacitive behavior. Materials Chemistry and Physics 2011;131:268-73.

[13] Gao Z-H, Zhang H, Cao G-P, Han M-F, Yang Y-S. Spherical porous VN and NiO_x as electrode materials for asymmetric supercapacitor. Electrochimica Acta. 2013;87:375-80.

[14] Ghimbeu CM, Raymundo-Pinero E, Fioux P, Beguin F, Vix-Guterl C. Vanadium nitride/carbon nanotube nanocomposites as electrodes for supercapacitors. Journal of Materials Chemistry 2011;21:13268-75.

[15] Levi MD, Salitra G, Levy N, Aurbach D, Maier J. Application of a quartz-crystal microbalance to measure ionic fluxes in microporous carbons for energy storage. Nature Materials. 2009;8:872-5.

[16] Barisci JN, Wallace GG, Baughman RH. Electrochemical quartz crystal microbalance studies of single-wall carbon nanotubes in aqueous and non-aqueous solutions. Electrochimica Acta. 2000;46:509-17.

[17] Sigalov S, Levi MD, Salitra G, Aurbach D, Maier J. EQCM as a unique tool for determination of ionic fluxes in microporous carbons as a function of surface charge distribution. Electrochemistry Communications. 2010;12:1718-21.

[18] Levy N, Levi MD, Aurbach D, Demadrille R, Pron A. Failure and stabilization mechanisms in multiply cycled conducting polymers for energy storage devices. Journal of Physical Chemistry C. 2010;114:16823-31.

[19] Livage J. Hydrothermal synthesis of nanostructured vanadium oxides. Materials. 2010;3:4175-95.

[20] Kuo S-L, Wu N-L. Investigation of pseudocapacitive charge-storage reaction of $MnO_2 \cdot nH_2O$ supercapacitors in aqueous electrolytes. Journal of the Electrochemical Society 2006;153:A1317-A24.

[21] Devaraj S, Munichandraiah N. EQCM investigation of the electrodeposition of MnO2 and its capacitance behavior. Electrochemical and Solid-State Letters. 2009;12:F21-F5.

[22] Sopcic S, Peter R, Petravic M, Mandic Z. New insights into the mechanism of pseudocapacitance deterioration in electrodeposited MnO2 under negative potentials. Journal of Power Sources. 2013;240:252-7.

[23] Jiang R, Huang T, Tang Y, Liu J, Xue L, Zhuang J, et al. Factors influencing MnO_2/multi-walled carbon nanotubes composite's electrochemical performance as supercapacitor electrode. Electrochimica Acta 2009;54:7173-9.

[24] Xia H, Huo C. Electrochemical properties of MnO_2/CNT nanocomposite in neutral aqueous electrolyte as cathode material for asymmetric supercapacitors. International Journal of Smart and Nano Materials. 2011;2:283-91.

[25] Li J, Zhitomirsky I. Electrophoretic deposition of manganese dioxide-carbon nanotube composites. Journal of Materials Processing Technology. 2009;209:3452-9.

[26] Fang H, Zhang S, Wu X, Liu W, Wen B, Du Z, et al. Facile fabrication of multiwalled carbon nanotube-α MnOOH coaxial nanocable films by electrophoretic deposition for supercapacitors. Journal of Power Sources. 2013;235:95-104.

[27] Zheng H, Wang J, Jia Y, Ma Ca. In-situ synthetize multi-walled carbon nanotubes@MnO_2 nanoflake core–shell structured materials for supercapacitors. Journal of Power Sources 2012;216:508-14.

[28] Li J, Yang QM, Zhitomirsky I. Nickel foam-based manganese dioxide-carbon nanotube composite electrodes for electrochemical supercapacitors. Journal of Power Sources. 2008;185:1569-74.

[29] Wang Y, Liu Y, Zhitomirsky I. Surface modification of MnO_2 and carbon nanotubes using organic dyes for nanotechnology of electrochemical supercapacitors. Journal of Materials Chemistry A. 2013;1:12519-26.

[30] Eustache E, Frappier R, Porto RL, Bouhtiyya Sd, Pierson J-F, Brousse T. Asymmetric electrochemical capacitor microdevice designed with vanadium nitride and nickel oxide thin film electrodes. Electrochemistry Communications. 2013;28:104-6.

[31] Xiao X, Peng X, Jin H, Li T, Zhang C, Gao B, et al. Freestanding mesoporous VN/CNT hybrid electrodes for flexible all-solid-state supercapacitors. Advanced Materials 2013/09/25;25:5091-7.

[32] Lu X, Yu M, Zhai T, Wang G, Xie S, Liu T, et al. High energy density asymmetric quasi-solid-state supercapacitor based on porous vanadium nitride nanowire anode. Nano Letters 2013;13:2628-33.

[33] Wu Z-S, Ren W, Wang D-W, Li F, Liu B, Cheng H-M. High-energy MnO_2 nanowire/graphene and graphene asymmetric electrochemical capacitors. ACS Nano. 2010;4:5835-42.

Chapter 11 Asymmetric electrochemical supercapacitor, based on polypyrrole coated carbon nanotube electrodes.

11.1 Adsorption and doping mechanism of additives for MWCNT-PPy composites.

Fig.11.1 (A,B) shows chemical structures of polyaromatic SPADNS and CHR-BS molecules. The anionic properties of both SPADNS and CHR-BS are attributed to their SO_3^- groups, bonded to the aromatic rings. The CHR-BS molecule has four SO_3^- groups, whereas SPADNS molecule has three SO_3^- groups. However, the molecules have comparable charge to mass ratio due to the larger size of CHR-BS. The interest in the application of SPADNS and CHR-BS as anionic dopants for PPy polymerization is attributed to their polyaromatic structure, large size and relatively high charge to mass ratio. The analysis of literature indicates that such structural characteristics of the dopants are beneficial for the formation of PPy particles with reduced particle size, enhanced conductivity and capacitance and improved cyclic stability.[1-4] Moreover, the SPADNS and CHR-BS molecules belong to the family of azo-dyes, which exhibit electroactive properties, attributed to $2e^-$ reductions of ─N═N─ groups and the formation of ─NH─NH─ hydrazo groups[5, 6]. Moreover, the redox-active properties of SPADNS and CHR-BS molecules are also attributed to their OH groups[7]. As pointed out above, the redox-active dopants can contribute to the capacitance of doped PPy electrodes.

The use of SPADNS and CHR-BS as anionic dopants offers additional benefits for the fabrication of PPy based composite electrodes. Recently, significant attention has been

given to the application of charged polyaromatic dyes for the dispersion of MWCNT in suspensions. The aromatic rings of the molecules promoted their adsorption on MWCNT due to the π-π interactions, whereas the charged groups of the adsorbed molecules provided electrostatic repulsion and dispersion of MWCNT[8-10].

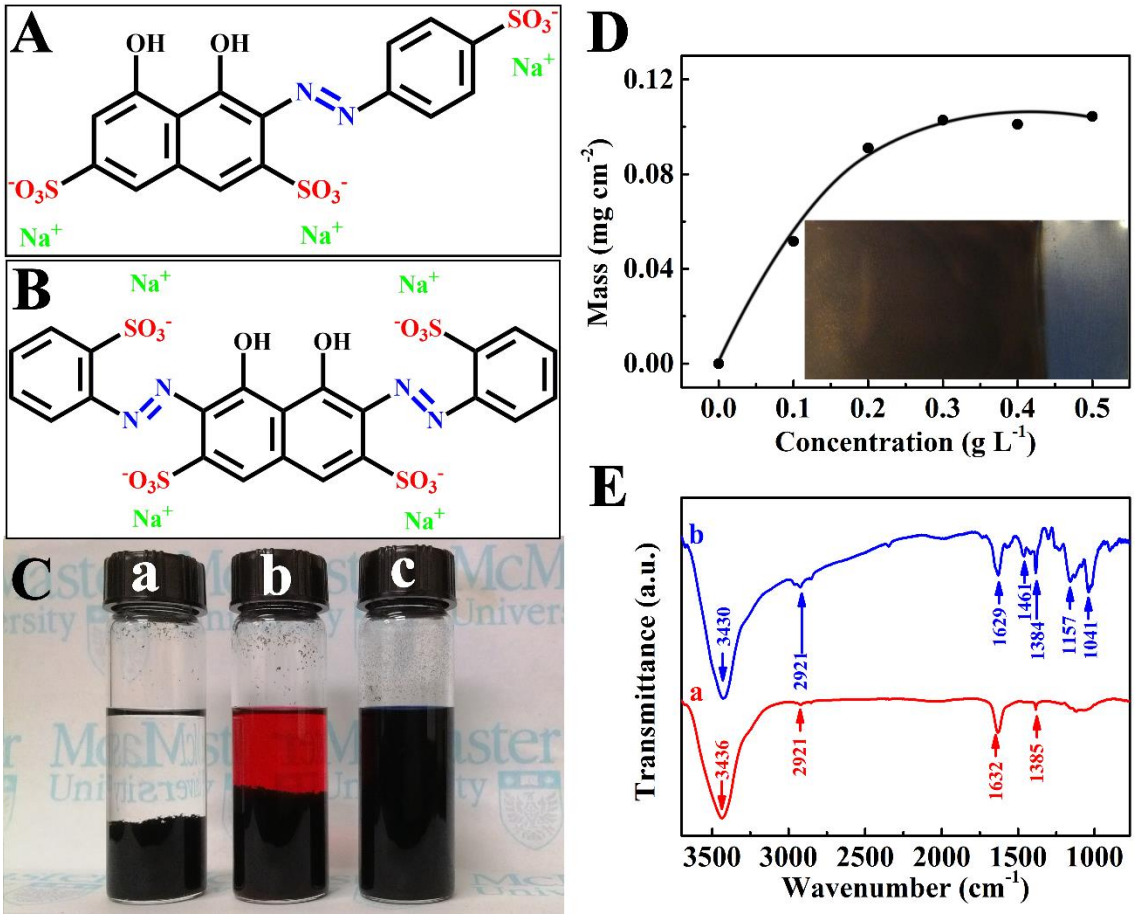

Fig.11.1 (A,B) Chemical structures of (A) SPADNS and (B) CHR-BS, (C) suspension stability of 1 g L^{-1} MWCNT in ethanol with (a) no dispersant, (b) 0.5 g L^{-1} SPADNS, and (c) 0.5 g L^{-1} CHR-BS after 24 hours, (D) deposit mass from 1 g L^{-1} MWCNT suspension versus CHR-BS concentration at a deposition voltage of 100 V and deposition time of 3 min, inset shows MWCNT film, (E) FTIR spectra of (a) pristine MWCNT and (b) MWCNT, deposited from 1 g L^{-1} MWCNT suspension, containing 0.5 g L^{-1} CHR-BS.

Based on these considerations, SPADNS and CHR-BS were investigated as dispersants for MWCNT and dopants for PPy in the synthesis of PPy coated MWCNT. The sedimentation tests showed that the stability of MWCNT suspensions prepared using SPADNS as a dispersant was 3 hours. In contrast, the MWCNT suspensions (Fig.11.1C), containing CHR-BS, were stable for several weeks. The improved dispersion of MWCNT can result from strong adsorption of CHR-BS on the MWCNT surface. The adsorption of CHR-BS was confirmed by electrophoretic deposition experiments and FTIR studies of the deposited MWCNT.

The adsorption of anionic CHR-BS on MWCNT provided negative charges on MWCNT surface, which were deposited on the anode under an electric field. The deposition yield increased with increasing CHR-BS concentration in the MWCNT suspensions (Fig.11.1D) and with increasing deposition voltage. The reason for these phenomena were that negative charges on MWCNT surface increased with increasing CHR-BS concentration, and hence resulting in increasing deposition yield. Relatively uniform deposits were obtained on the stainless steel substrates at deposition voltages of 50-150 V (Fig.11.1D, inset).

The adsorption of CHR-BS on MWCNT was confirmed by the FTIR analysis of the deposited material. In this case, the deposited material included only adsorbed dispersant, whereas the non-adsorbed dispersant remained in the solution. The FTIR spectra of as-received and deposited MWCNT are compared in Fig.11.1E. The band assignments, presented in Table 11.1, were based on literature[11-13] data. The comparison of the FTIR spectra indicates that the spectrum of deposited MWCNT contained additional absorptions, attributed to N=N and S=O groups of CHR-BS. Therefore, the FTIR data

confirmed the adsorption of CHR-BS on MWCNT.

Table 11.1 Band Assignments for pristine MWCNT and deposited MWCNT using CHR-BS as a dispersant.

MWCNT	CHR-BS/MWCNT	Band Assignment
3436	3430	ν(-OH)[12]
	2958 2921 2852	ν(-CH)[13]
	2347	ν(C-O)[13]
1632	1629	ν(C=C)[11, 13]
	1461	ν(N=N)[13]
1385	1384 1129	δ(C-H),δ(C-O)[11, 13]
	1157	ν (S=O) (asymmetric)[13]
	1041	ν (S=O) (symmetric)[13]

The wavenumbers were given in cm^{-1}, ν-stretching mode, δ-bending mode.

11.2 Morphology characterization of PPy coated MWCNT composite

Fig.11.2 (A,B) compares microstructure of PPy-MWCNT composites, prepared using SPADNS and CHR-BS. The PPy-MWCNT composites, prepared using SPADNS, contained PPy coated MWCNT and relatively large agglomerates, containing PPy material between PPy coated MWCNT. In contrast, the SEM images of the PPy-MWCNT composites, prepared using CHR-BS, contained only PPy coated MWCNT. The difference in the microstructure can be attributed to improved dispersion of MWCNT in the suspensions, containing CHR-BS. It is suggested that CHR-BS, adsorbed on the MWCNT surfaces, allowed MWCNT dispersion and promoted the PPy polymerization on the MWCNT surface. The hydrophobic and π-π interactions between MWCNT and PPy also promoted the polymerization of pyrrole on the surface of MWCNT.

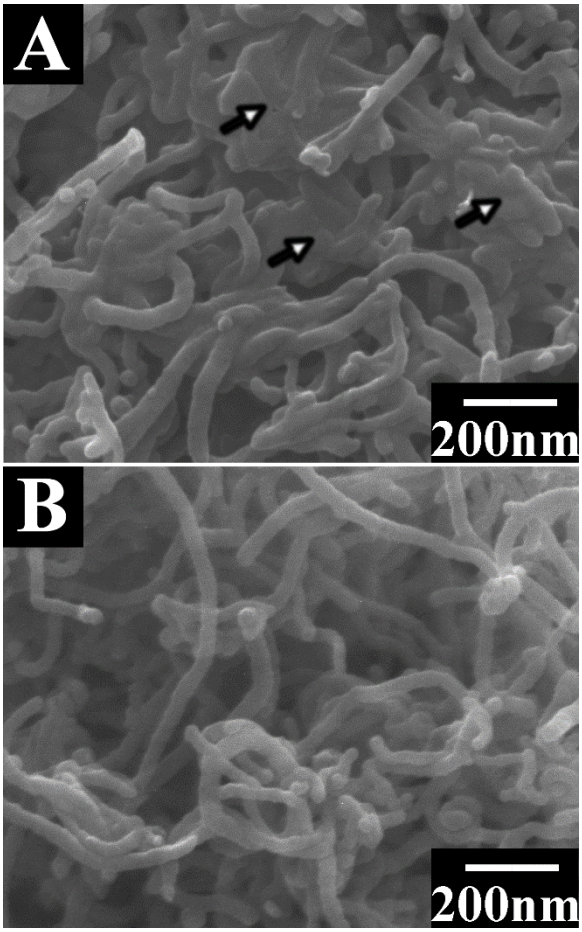

Fig.11.2 (A,B) SEM images of PPy coated MWCNT, prepared using (A) SPADNS and (B) CHR-BS as dispersants, the arrows in (A) show agglomerates, containing PPy between PPy coated MWCNT.

The formation of PPy coated MWCNT using CHR-BS as a dispersant for MWCNT and dopant for PPy polymerization was confirmed by TEM. The TEM image presented in Fig.11.3 shows a typical PPy coated MWCNT. The image indicated the formation of relatively uniform coating and good contact of PPy and MWCNT. Such microstructure offers the advantages of high conductivity of MWCNT, high capacitance of PPY and good electrical contact of both materials. It could reduce the pathway of electron transfer between PPy and MWCNT, so the electron transfer was more efficient than that in

mechanical mixture of PPy and MWCNT.

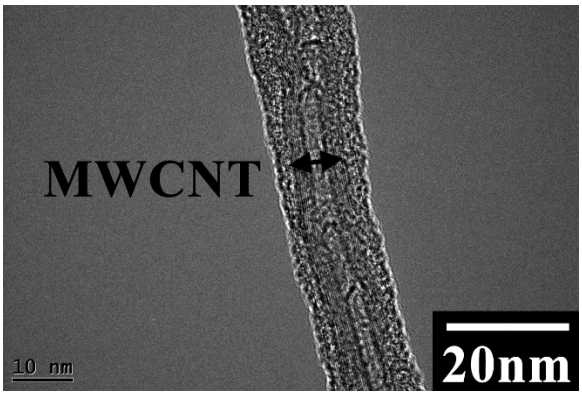

Fig.11.3 TEM image of PPy-MWCNT prepared using CHR-BS, the double arrow shows MWCNT.

The formation of PPy coated MWCNT was also confirmed by the results of EDX studies. The comparison of HAADF image and corresponding element distribution maps (Fig.11.4) indicated that MWCNT were coated with PPy polymer, containing nitrogen in its structure.

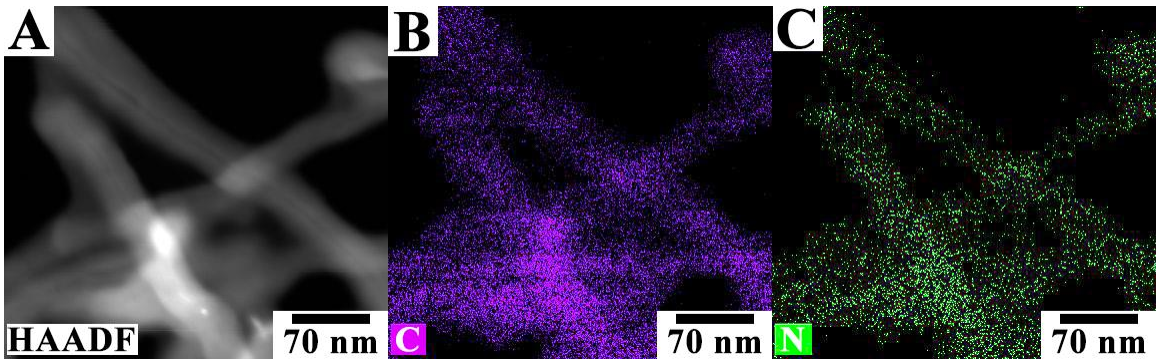

Fig.11.4 (A) HAADF and (B,C) EDX analysis for (B) carbon and (C) nitrogen elements of PPy-MWCNT, prepared using CHR-BS.

11.3 Capacitive performance of PPy coated MWCNT composites

The PPy coated MWCNT, prepared using SPADNS and CHR-BS were tested as ES electrode. Fig.11.5 (A,B) shows nearly box-shaped CVs for the electrodes with mass loading of 10 mg cm^{-2}, where the current increased with the increase of scan rate, indicating good electrochemical capacitive performance. The PPy-MWCNT composites, prepared using CHR-BS showed larger area of CVs, indicating higher capacitance. From CVs of electrodes prepared using CHR-BS, C_m and C_S were calculated and shown in Fig.11.5C, with highest C_m of 179 F g^{-1} (C_S of 1.8 F cm^{-2}) was observed at lowest scan rate of 2 mV s^{-1}. Even at highest scan rate of 100 mV s^{-1}, 52% of the highest capacitance was maintained. In contrast, the capacitance retention of PPy electrodes, prepared without MWCNT[14], was about 10% in the same scan rate range. Therefore, the PPy coating on MWCNT improved the capacitive retention significantly. Fig.11.5D shows Nyquist plot of electrochemical impedance together with the corresponding simulation data, obtained with an equivalent circuit[15]. The electrodes showed relatively small resistance R=Z'. The resistance of the electrodes, prepared using CHR-BS, was lower, compared to the resistance of electrodes prepared using SPADNS. The slopes of the Z'' versus Z' curves were close to 90 º, indicating good capacitive behavior. The impedance data is in good agreement with the results of simulation, obtained using a circuit[15]. The circuit used for simulation was the same as used in the literature[15], which included two R-Q transmission lines for the electrode porous surface[16, 17].

The frequency dependencies of complex AC capacitance are presented in Fig.11.5E. The dependencies showed typical relaxation type[11] dispersions, as indicated by the fast reduction in the real component C' with increasing frequency above 2 Hz and maxima in

the frequency dependencies of C'' at about 2.5 Hz. The relaxation frequencies, corresponding to the C'' maxima, were higher, compared to other PPy-MWCNT composites[11] of similar electrode mass. Therefore, the use of PPy coated MWCNT allows improved capacitance retention with increasing frequency. The electrodes, prepared using CHR-BS, showed higher capacitance at low frequencies, compared to the electrodes, prepared SPADNS. This result is in good agreement with capacitance data, obtained from the CVs.

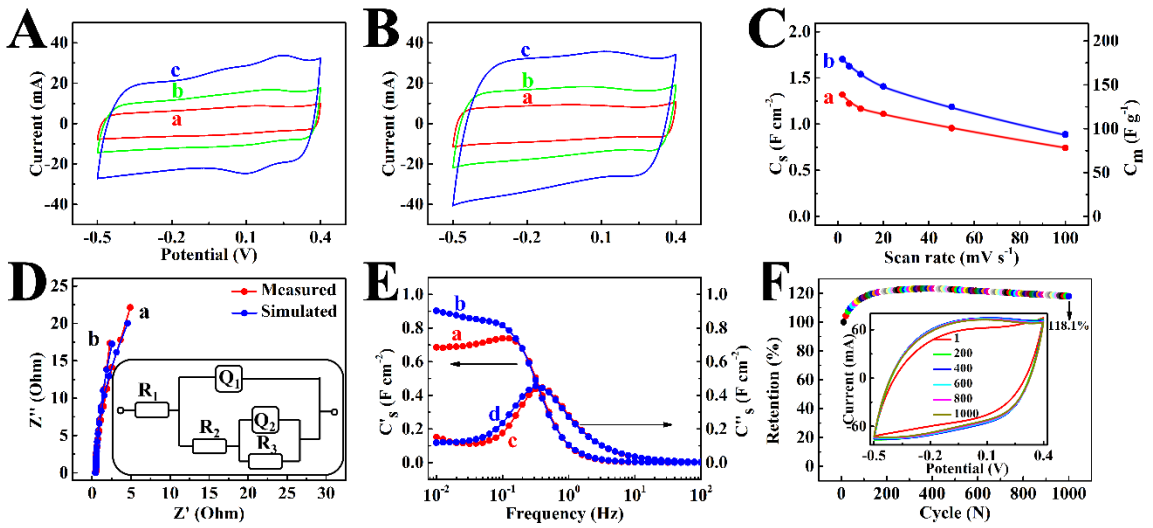

Fig.11.5 (A,B) CVs at (a) 5, (b) 10, and (c) 20 mV s^{-1} for PPy-MWCNT, prepared using (A) SPADNS and (B) CHR-BS, (C) C_s and C_m versus rate for PPy-MWCNT, prepared using (a) SPADNS and (b) CHR-BS, (D) EIS and corresponding simulation data for PPy-MWCNT electrodes, prepared using (a) SPADNS and (b) CHR-BS, inset shows the circuit for simulation, (E) (a,b) C_s' and (c,d) C_s'' versus frequency for PPy-MWCNT, prepared using (a,c) SPADNS and (b,d) CHR-BS, (F) Cyclic stability of PPy-MWCNT, prepared using CHR-BS, inset shows CVs at different cycles.

Due to the improved capacitive behavior of the electrodes, prepared using CHR-BS, such

electrodes were used for the fabrication of asymmetric devices. The cyclic stability of the electrodes is important for device performance. The investigation of cyclic stability of the CHR-BS electrodes (Fig.11.5F) showed that capacitance increased with increasing cycle number during the first 400 cycles and then slightly reduced with increasing cycle number. The inset in Fig.11.5F shows corresponding variations in CVs during cycling. It is seen that the area of the CVs increased during the initial 400 cycles. The increase in the capacitance of PPy electrodes during cycling can result from the changes in electrode microstructure[18]. The electrodes showed capacitance retention of 118.1% after 1000 cycles (Fig.5F).

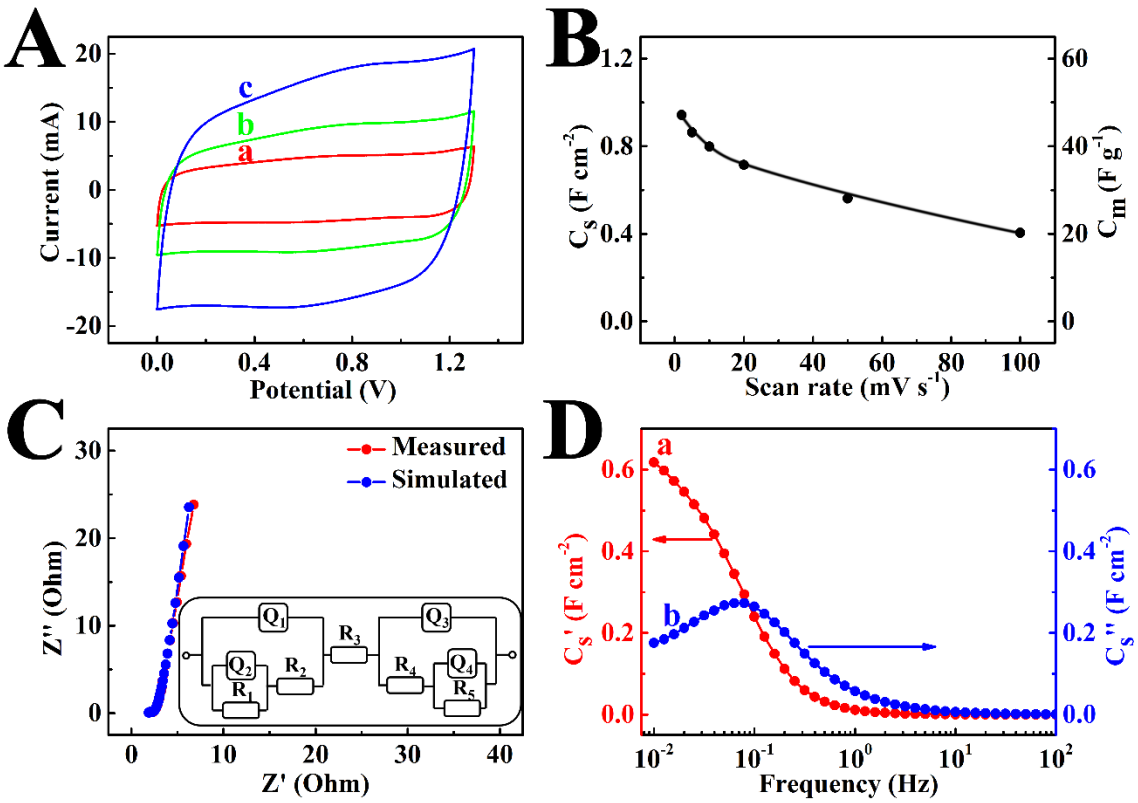

Fig.11.6 (A) CVs at (a) 5, (b) 10, and (c) 20 mV s^{-1}, (B) C_m and C_s versus scan rate, (C) EIS and corresponding simulation data, inset shows the circuit for simulation, (D) (a) C_s' and (b) C_s'' versus frequency for PPy-MWCNT/VN-MWCNT asymmetric device.

11.4 Capacitive performance of PPy-MWCNT/VN-MWCNT asymmetric devices

The asymmetric devices were fabricated using PPy-MWCNT as positive electrodes and VN-MWCNT as negative electrodes. The mass loading and MWCNT content of the negative VN-MWCNT electrodes was adjusted to balance the capacitances of positive PPy-MWCNT electrodes at whole charge-discharge rates. The devices showed box shape CVs in a voltage window of 1.3 V, indicating good capacitive behavior (Fig.11.6A). The current increased with increasing scan rate.

Fig.11.6B shows capacitance, calculated from the CV data, at different scan rates. The highest capacitance of 47.1 F g^{-1} (0.94 F cm^{-2}) was achieved at a scan rate of 2 mV s^{-1}. The devices showed a capacitance retention of 43.6% at a scan rate of 100 mV s^{-1}. The devices showed (Fig.11.6C) relatively low resistance R=Z'. The slope of the Z'' versus Z' curve was close to 90 º, indicating good capacitive behavior. However, the asymmetric cell has larger internal resistance, compared to the resistance of individual electrodes.The equivalent circuit (Fig.11.6C, inset) of the asymmetric cell was the same as used in the literature[15], which was a combination of two single electrode circuits, shown in Fig.11.5(D), with shared electrolyte resistance R_3. The results of simulation are in good agreement with the experimental data.

The AC capacitance of the cell was calculated from the impedance data and presented in Fig.11.6D in the form of frequency dependences of real C' and imaginary C'' components. Similar to the corresponding dependencies for individual electrodes (Fig.11.5E), the frequency dependencies of the AC capacitance (Fig.11.6D) for the cell showed relaxation

type dispersion, as indicated by the decrease in C' with increasing frequency and a maximum in the frequency dependence of C". The observed relaxation frequency of 0.09 Hz for the cell, corresponding to the C" maximum, was lower than the relaxation frequencies for the individual PPy-MWCNT (2.5 Hz, Fig.11.4E) and VN-MWCNT (0.2 Hz) electrodes. The difference in the relaxation frequencies can result from larger internal resistance of the cell.

The galvanostatic charge-discharge curves at different charging and discharging rates were shown Fig.11.7A in a voltage window of 1.3 V. The charge-discharge curves were of nearly triangular symmetrical shape, indicating good capacitive behavior. In contrast, the symmetrical device, containing two PPy-MWCNT can be charged and discharged in the voltage window of 0.9 V. As a result, the asymmetric device showed improved power-energy characteristics, compared to the symmetric device. The Ragone plots for asymmetric and symmetric devices are presented in Fig.11.7B. The highest energy density of 10.7 Wh kg^{-1} was obtained for the asymmetric device at a constant current of 0.5 mA. The energy density of the symmetric device at the same discharge current was only 4.5 Wh kg^{-1}. The asymmetric device showed significant improvement in power density, which was especially evident at higher discharge currents. The power density of the asymmetric device at a current of 50 mA was 1.99 kW kg^{-1}, whereas the power density of the symmetric device at the same current was only 0.69 kW kg^{-1}. The difference is attributed to larger voltage window of the asymmetric device. The asymmetric device showed capacitance retention of 84.3% after 1000 cycles (Fig.11.7C). The charge-discharge curves showed symmetric triangular shape during cycling. As a result, the charge efficiency of PPy-MWCNT/VN-MWCNT hybrid device was close to

100% during the cycling.

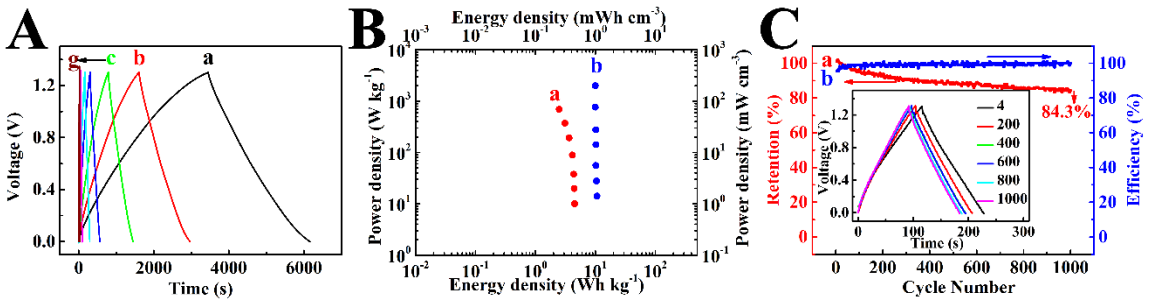

Fig.11.7 (A) Charge-discharges curves for PPy-MWCNT/VN-MWCNT hybrid device at constant currents of (a) 0.5, (b) 1, (c) 2, (d) 5, (e) 10, (f) 20, and (g) 50 mA. (B) Ragone plots for (a) PPy-MWCNT/PPY-MWCNT symmetric device and (b) PPy-MWCNT/VN-MWCNT asymmetric device, obtained from constant current charge-discharge data, (C) (a) cyclic stability and (b) Coulombic efficiency of PPy-MWCNT/VN-MWCNT hybrid device versus cycle number, inset shows charge-discharge curves for different cycles.

11.5 Capacitive performance of devices modules

The relatively low resistance and high capacitance of the asymmetric devices paved the way to the fabrication of modules with larger voltages. As a step in this direction, two asymmetric cells were combined and tested. Fig.11.8A shows CVs at different scan rates for two devices connected in series. The box shape CVs in a voltage window of 2.6 V were obtained, where current changed proportional to the scan rates, indicating good capacitive behavior. The charge-discharge curves at different currents in the same voltage window were of nearly ideal triangular symmetrical shape. A similar behavior was observed for the module, containing 3 cells in the voltage window of 3.9 V (Fig.11.9). The modules were used for the powering of LED bulbs (Fig.11.9).

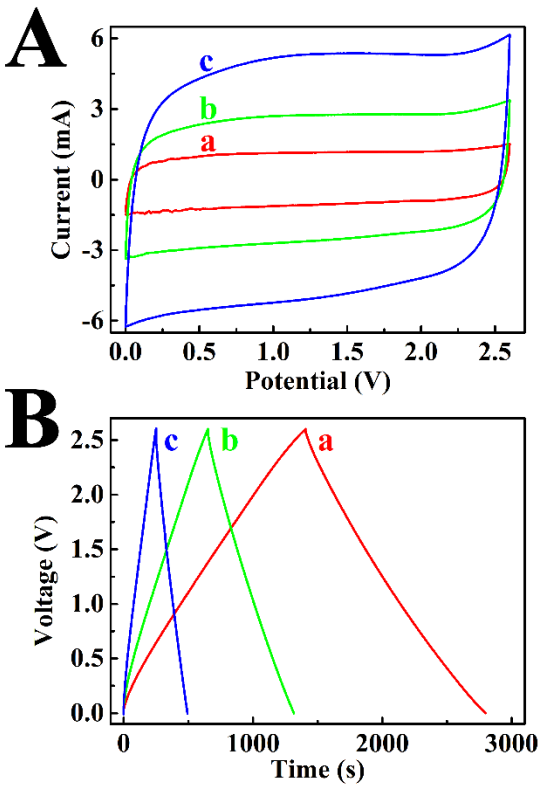

Fig.11.8 (A) CVs at (a) 2, (b) 5, and (c) 10 mV s^{-1}, and (B) charge-discharge curves at constant currents of (a) 1, (b) 2, and (c) 5 mA for two PPy-MWCNT/VN-MWCNT hybrid devices connected in series.

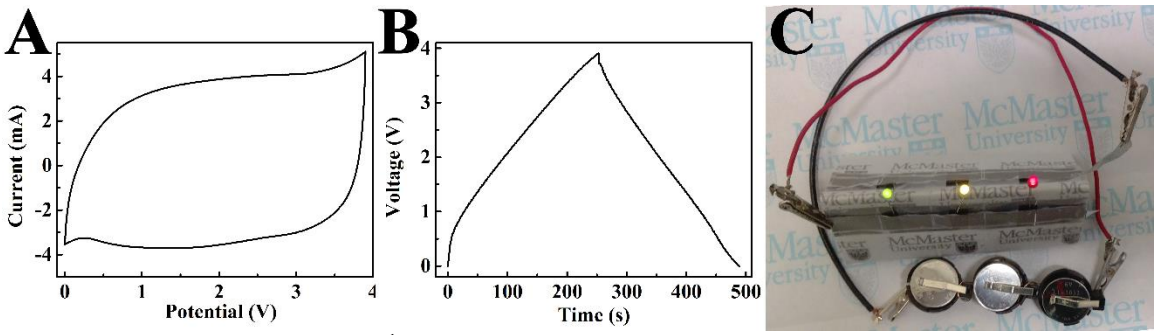

Fig.11.9 (A) CV at 10 mV s^{-1}, (B) charge-discharge at constant current of 10 mA for 3 PPy-MWCNT/VN-MWCNT hybrid devices connected in series. (C) Green, yellow and red LED bulbs powered by 3 hybrid devices in series.

11.6 Conclusions

The strong adsorption and dispersion ability of CHR-BS to MWCNT was proven by sedimentation tests, EPD experiments and FTIR investigations. The use of CHR-BS as an anionic dopant for PPy polymerization and dispersant for MWCNT allowed the fabrication of PPy coated MWCNT. The analysis of the experimental data for PPy-MWCNT composites, prepared using CHR-BS and SPADNS, indicated that CHR-BS molecules allowed improved MWCNT dispersion, reduced agglomeration of PPy coated MWCNT and improved electrochemical performance. The data indicated that the structure and size of the molecules are important factors controlling the microstructure and properties of the PPy-MWCNT composites. The PPy coated MWCNT showed a capacitance of 179 F g^{-1} at a scan rate of 2 mV s^{-1} for mass loading of 10 mg cm^{-2}, good capacitance retention at high charge-discharge rates and excellent cyclic stability. Asymmetric ES devices, containing PPy coated MWCNT positive electrodes and VN-MWCNT negative electrodes showed significant improvement in energy density and power density, compared to the symmetric ES due to the larger voltage window. The low impedance and high capacitance of the individual cells paved the way to the fabrication of modules with higher voltage, which showed good electrochemical performance.

References

[1] Mitchell GR, Davis FJ, Legge CH. Effect of dopant molecules on the molecular order of electrically-conducting films of polypyrrole. Synthetic Metals 1988;26:247-57.

[2] Zhu Y, Zhitomirsky I. Influence of dopant structure and charge on supercapacitive behavior of polypyrrole electrodes with high mass loading. Synthetic Metals 2013;185–186:126-32.

[3] Weng B, Shepherd R, Chen J, Wallace GG. Gemini surfactant doped polypyrrole nanodispersions: an inkjet printable formulation. Journal of Materials Chemistry 2011;21:1918-24.

[4] Lang X, Wan Q, Feng C, Yue X, Xu W, Li J, et al. The role of anthraquinone sulfonate dopants in promoting performance of polypyrrole composites as pseudo-capacitive electrode materials. Synthetic Metals 2010;160:1800-4.

[5] Jain R, Sharma N, Radhapyari K. Electrochemical treatment of pharmaceutical azo dye amaranth from waste water. Journal of Applied Electrochemistry 2009;39:577-82.

[6] Dossi N, Piccin E, Bontempelli G, Carrilho E, Wang J. Rapid analysis of azo-dyes in food by microchip electrophoresis with electrochemical detection. Electrophoresis. 2007;28:4240-6.

[7] Ensafi AA, Taei M, Khayamian T, Arabzadeh A. Highly selective determination of ascorbic acid, dopamine, and uric acid by differential pulse voltammetry using poly(sulfonazo III) modified glassy carbon electrode. Sensors and Actuators B: Chemical 2010;147:213-21.

[8] Su Y, Zhitomirsky I. Electrophoretic deposition of graphene, carbon nanotubes and composite films using methyl violet dye as a dispersing agent. Colloids and Surfaces A: Physicochemical and Engineering Aspects. 2013;436:97-103.

[9] Ata M, Liu Y, Zhitomirsky I. A review of new methods of surface chemical modification, dispersion and electrophoretic deposition of metal oxide particles. RSC Advances. 2014;4:22716-32.

[10] Su Y, Zhitomirsky I. Electrophoretic nanotechnology of composite electrodes for electrochemical supercapacitors. The Journal of Physical Chemistry B. 2012;117:1563-70.

[11] Shi K, Zhitomirsky I. Polypyrrole nanofiber-carbon nanotube electrodes for supercapacitors with high mass loading obtained using an organic dye as a co-dispersant. Journal of Materials Chemistry A. 2013;1:11614-22.

[12] Rajh T, Chen LX, Lukas K, Liu T, Thurnauer MC, Tiede DM. Surface restructuring of nanoparticles: An efficient route for ligand−metal oxide crosstalk. The Journal of Physical Chemistry B. 2002;106:10543-52.

[13] Yuen C, Ku S, Choi P, Kan C, Tsang S. Determining functional groups of commercially available ink-jet printing reactive dyes using infrared spectroscopy. Res J Text Appar. 2005;9:26-38.

[14] Zhu Y, Zhitomirsky I. Influence of dopant structure and charge on supercapacitive behavior of polypyrrole electrodes with high mass loading. Synthetic Metals. 2013;185:126-32.

[15] Su Y, Zhitomirsky I. Hybrid MnO_2/carbon nanotube-VN/carbon nanotube supercapacitors. Journal of Power Sources 2014;267:235-42.

[16] Conway BE, Pell WG. Power limitations of supercapacitor operation associated with resistance and capacitance distribution in porous electrode devices. Journal of Power Sources 2002;105:169-81.

[17] Huai Y, Hu X, Lin Z, Deng Z, Suo J. Preparation of nano-TiO_2/activated carbon composite and its electrochemical characteristics in non-aqueous electrolyte. Materials Chemistry and Physics 2009;113:962-6.

[18] Shi K, Zhitomirsky I. Influence of current collector on capacitive behavior and cycling stability of Tiron doped polypyrrole electrodes. Journal of Power Sources 2013;240:42-9.

Chapter 12 Influence of dopants on performance of polypyrrole coated CNT electrodes and devices

12.1 Adsorption and doping mechanisms

Fig.12.1A,B shows chemical structures of the polyaromatic anionic molecules used in this investigation. The two SO_3^- groups, OH and NH_2 groups are bonded to a fused pair of benzene rings of AHDA and DAGB. It is suggested that AHDA and DAGB molecules are promising for application as dopants for polymerization of PPy due to their polyaromatic nature and two charged SO_3^- groups. The comparison of AHDA and DAGB indicates that the DAGB structure includes four additional aromatic rings and three redox-active N═N groups. DAGB belongs to the family of azo-dyes, which exhibit electroactive properties, attributed to $2e^-$ reductions of ─N═N─ groups and the formation of ─NH─NH─ hydrazo groups[1, 2]. As pointed out above, the redox-active dopants can contribute to the capacitance of doped PPy electrodes.

The use of polyaromatic dopants offers additional benefits for the fabrication of PPy – MWCNT composites. The dispersion of MWCNT in the PPy matrix is important for the fabrication of efficient electrodes. A critical property of the dispersant is its adsorption on the MWCNT surface. Charged polyaromatic molecules showed strong adsorption on the MWCNT surface due to the π-π interactions and provided electrostatic dispersion[3-5]. The analysis of experimental data[3-6] for different molecules indicated that the molecular structure is an important factor, governing the adsorption of the aromatic molecules and efficiency of MWCNT dispersion. However, the influence of the molecular structure on the adsorption and dispersion is not well understood. The

investigation of various phenolic molecules and organic dyes[6, 7] showed that OH, NH_2, and other functional groups of the aromatic molecules promoted their adsorption on the MWCNT surface. Therefore, it is suggested that OH and NH_2 groups of the dyes, selected for this investigation, can be beneficial for their adsorption on MWCNT. The comparison of the experimental data for AHDA and DAGB can provide insight into the influence of the dopant structure on electrochemical performance of PPy electrodes and MWCNT dispersion.

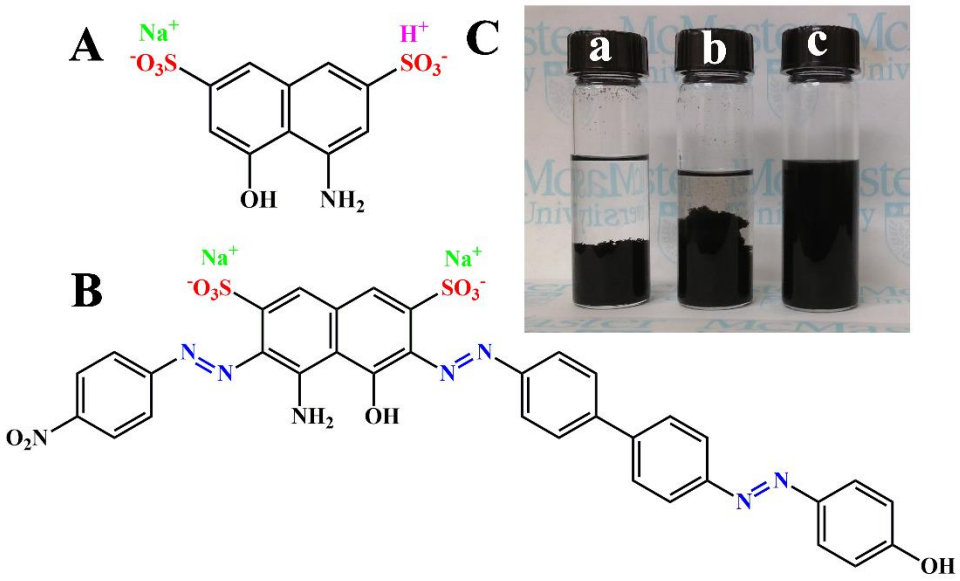

Fig.12.1 (A,B) Chemical structures of (A) AHDA, (B) DAGB and (C) suspensions of 1 g L^{-1} MWCNT in ethanol 24 h after the ultrasonic agitation: (a) without additives and containing (b) 0.5 g L^{-1} AHDA and (c) 0.5 g L^{-1} DAGB.

Sedimentation tests (Fig.12.1C(a)) showed poor stability of the pure MWCNT suspensions in ethanol. The MWCNT suspension, containing AHDA (Fig.12.1C(b)) showed precipitation 24 h after the ultrasonic agitation. In contrast the use of DAGB resulted in improved stability of the MWCNT suspensions (Fig.12.1C(c)). It is suggested

that larger DAGB molecules provided improved electrosteric stabilization of MWCNT.

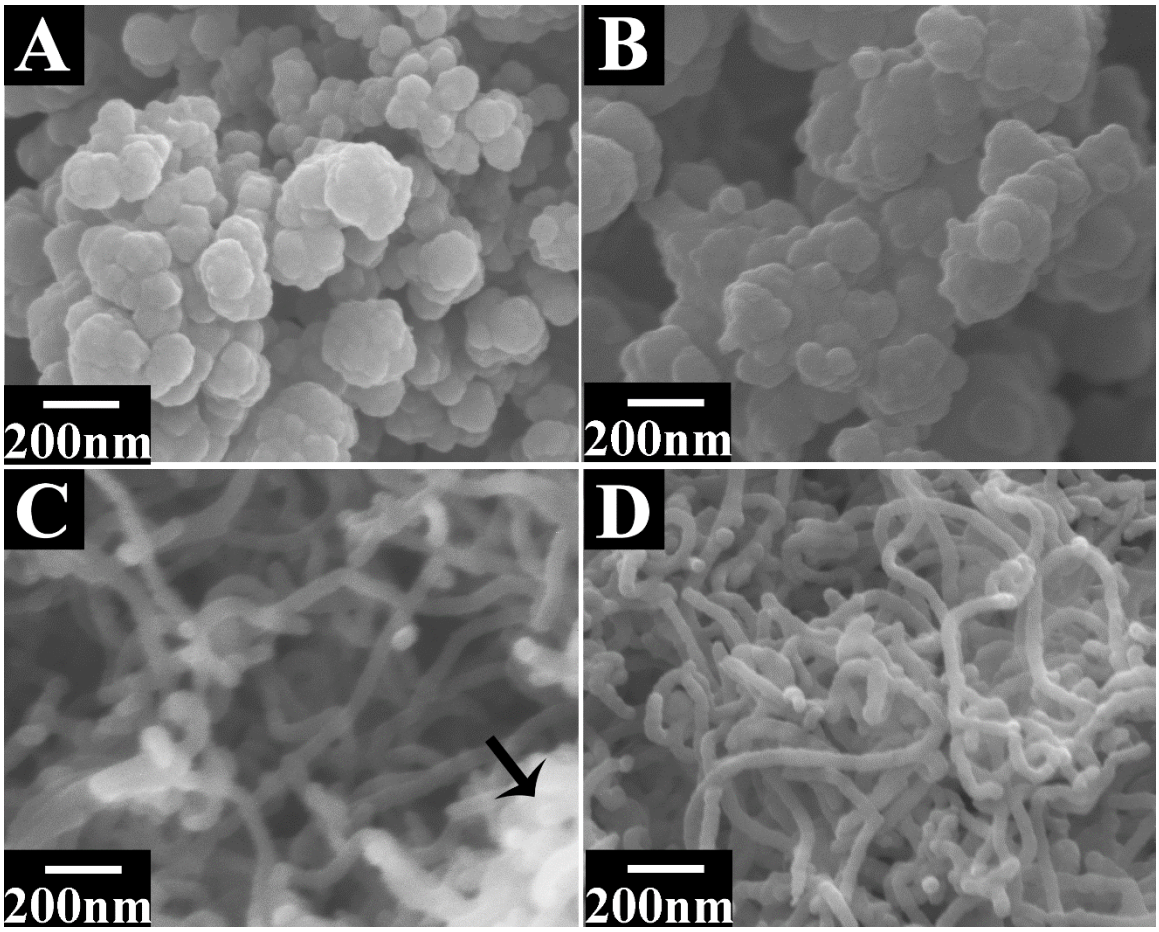

Fig.12.2 SEM images of (A,B) PPy and (C,D) PPy (80%)–MWCNT (20%) composites, prepared using (A,C) AHDA and (B,D) DAGB, arrow in (C) shows PPy agglomerate.

12.2 Microstructure and morphology characterization of PPy coated MWCNT

Fig.12.2(A,B) shows SEM images of PPy powders, prepared by chemical polymerization, using AHDA and DAGB as dopants. The SEM images show agglomerates, containing primary PPy particles with particle size of about 100 nm. The size of the agglomerates was in the range of 200 nm-1μm. The formation of agglomerates is detrimental for PPy

applications for ES electrodes due to the poor electrolyte access to the PPy material.

However, once the MWCNT were introduced into the systems, PPy was formed on the surface of MWCNT. Fig.12.2(C,D) shows SEM images of PPy-MWCNT composites, formed in the presence of AHDA and DAGB. The SEM image of PPy-MWCNT composites, prepared using AHDA shows PPy coated MWCNT, however some PPy agglomerates were also formed. In contrast, the SEM images of PPy-MWCNT composites, formed in the presence of DAGB contained only PPy coated MWCNT. The synthesis method allowed the formation of relatively uniform coatings. The difference in the microstructure of the composites can be attributed to improved dispersion of MWCNT in the presence of DAGB. In the synthesis method, DAGB was used as a dopant for PPy polymerization and a dispersant for MWCNT. The method of the synthesis of PPy coated MWCNT is simple and suitable for mass production.

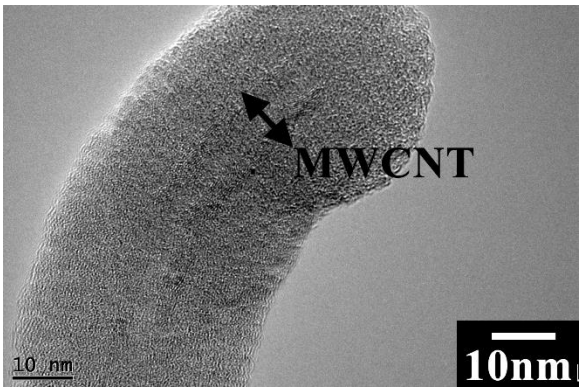

Fig.12.3 TEM image of PPy coated MWCNT, prepared using DAGB, double arrow shows MWCNT.

The formation of PPy coated MWCNT was also confirmed by TEM studies. Fig.12.3 shows a typical TEM image of a PPy coated MWCNT, prepared using DAGB. The thickness of the coating is about 12 nm. The formation of PPy coating was further proved

using EDX (Fig.12.4). Both carbon map and nitrogen map overlapped with the PPy coated MWCNT in the HAADF image. The PPy coating was a source of nitrogen, detected in the EDX studies. The electron microscopy and EDX data also illustrate the benefits of the PPy coated MWCNT for application in ES.

The charge storage mechanism of PPy is pseudocapacitive, it can be described by the reaction[8-10]:

$$[PPy+]A^- + e^- \leftrightarrow [PPy^0] + A^- \qquad (\textbf{Eq.}12.1)$$

where A^- is an anion (anionic dopant or SO_4^{2-} anion from the electrolyte). The Eq.12.1 indicates that high electronic conductivity and good electrolyte access to the active materials are required for the efficient charge storage. The conductive MWCNT core (Fig.12.3) provides good electronic conductivity. Compared to the agglomerated powders, the thin PPy coatings on MWCNT allow improved electrolyte access to the PPy material. As a result, PPy coated MWCNT showed better electrochemical performance, compared to pure PPy materials.

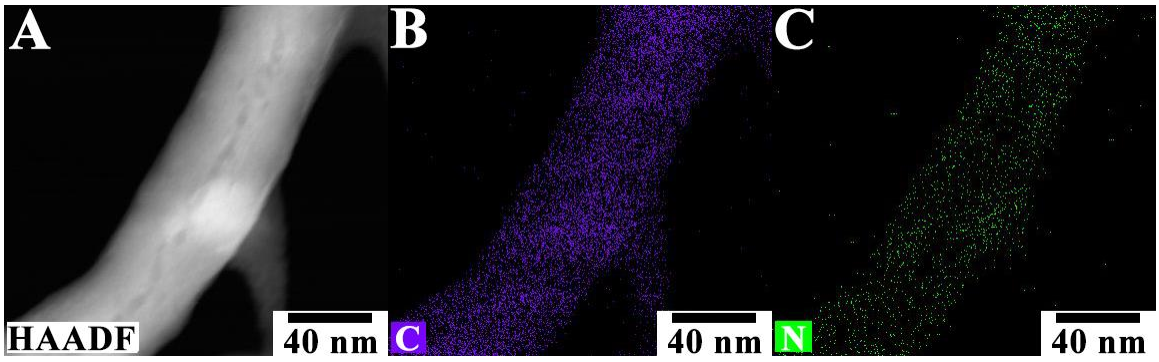

Fig.12.4 (A) HAADF and (B,C) EDX mapping analysis for (B) carbon and (C) nitrogen elements of PPy-MWCNT, prepared using DAGB.

The formation of PPy coated MWCNT was also confirmed by the results of EDX studies. The comparison of HAADF image and corresponding element distribution maps (Fig.12.4) indicated that MWCNT were coated with PPy polymer, containing nitrogen in its structure.

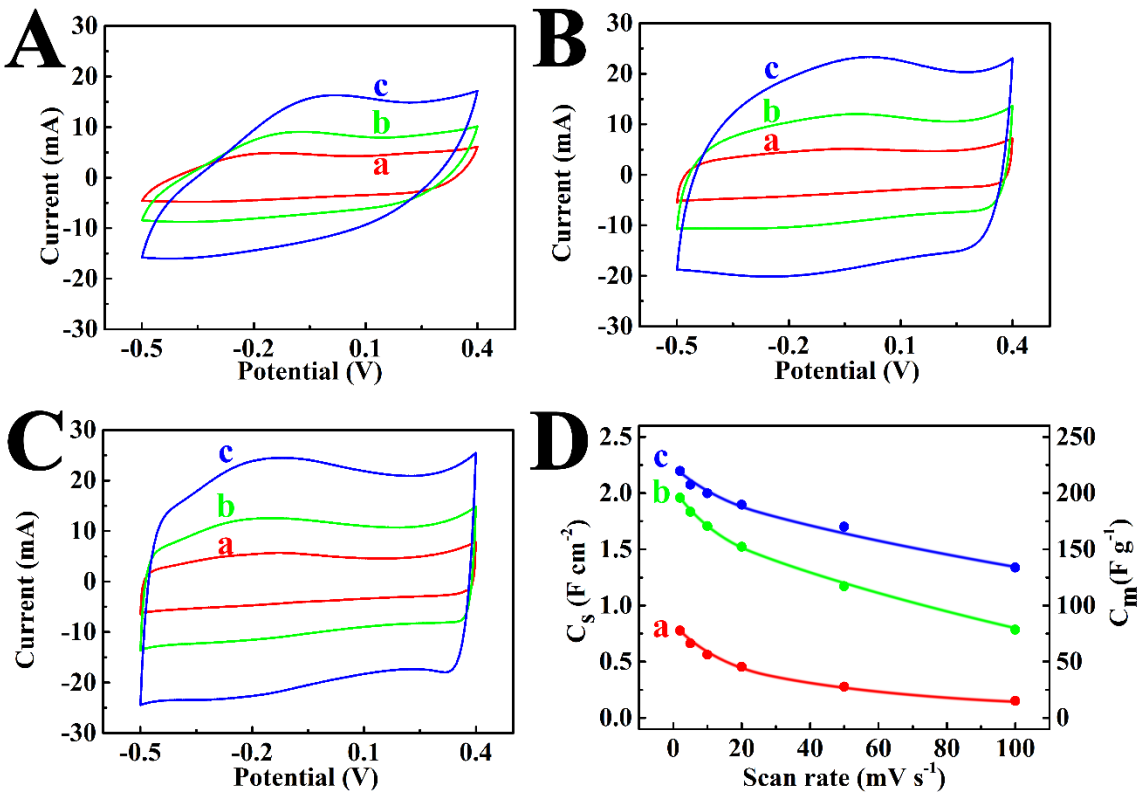

Fig.12.5 (A,B,C) CVs at scan rates of (a) 5, (b) 10, and (c) 20 mV s^{-1}, (D) specific capacitance versus scan rate for (A) and (D(a)) PPy, prepared using DAGB, (B) and (D(b)) PPy (80%)–MWCNT (20%) composite, prepared using AHDA, (C) and (D(c)) PPy(80%)–MWCNT(20%) composite, prepared using DAGB.

12.3 Influences of dopants on specific capacitance of PPy coated MWCNT

Fig.12.5 compares CV data for PPy powders and PPy coated MWCNT. The CVs for the PPy, doped with DAGB (Fig.12.5A), deviated significantly from the ideal box shape, even at relatively low scan rates, such as 20 mV s^{-1}. Similar results were obtained for the powders, prepared using AHDA. In contrast, the larger CV areas of the powders, prepared using MWCNT, and nearly box shape of the CVs indicated improved capacitive behavior (Fig.12.5B,C). The PPy-MWCNT composites, prepared using DAGB, showed larger CV areas, compared to the PPy-MWCNT composites, prepared using AHDA.

The capacitances, calculated from the CV data are presented in Fig.12.5D. The highest capacitance C_s=2.20 F cm^{-2} (C_m=220 F g^{-1}) was achieved at a scan rate of 2 mV s^{-1} for PPy-MWCNT composites, prepared using DAGB. Moreover, such composites showed significant improvement in capacitance at 100 mV s^{-1}. The capacitance retention at 100 mV s^{-1} was found to be 60.9 %. The PPy electrodes without MWCNT, prepared using DAGB, showed a capacitance of C_s=0.78 F cm^{-2} (C_m=77.6 F g^{-1}) at 2 mV s^{-1} and capacitance retention of 19.6% at 100 mV s^{-1}. The PPy-MWCNT electrodes, prepared using AHDA showed a capacitance of C_s=1.96 F cm^{-2} (C_m=195.9 F g^{-1}) at 2 mV s^{-1} and capacitance retention of 40.0% at 100 mV s^{-1}.

The impedance spectroscopy data for the same materials are shown in Fig.12.6A as a Nyquist plot of complex impedance. The PPy-MWCNT composite, synthesized using DAGB showed lower resistance R=Z', compared to pure PPy, prepared using DAGB, and compared to PPy-MWCNT composite, prepared using AHDA. The impedance data were

used for the calculation of components of complex AC capacitance. The frequency dependencies of real and imaginary components of complex capacitance (Fig.12.6B,C) provided additional information, related to capacitive behavior of the materials. It is important to note that CV and impedance measurements provide capacitive data at different conditions. The impedance spectroscopy measurements are usually performed at very low amplitude of AC field of about 5 mV. Therefore, the impedance spectroscopy data were used for the calculation of the differential capacitance. The CV data were accumulated in a voltage window of 0.9V and used to retrieve the integral capacitance.

The PPy-MWCNT composite, synthesized using DAGB showed the highest capacitance at a frequency of 0.01Hz. Relatively small changes in the capacitance were observed in the range of 0.01-0.1 Hz. In contrast the capacitance of PPy, prepared using DAGB without MWCNT and PPy-MWCNT composites, prepared using AHDA, decreased rapidly in the same frequency range. It is important to compare the differential and integral capacitance of the materials. Such comparison must be performed at the same time scale, because differential capacitance depends on frequency, whereas the integral capacitance depends on scan rate. The results indicated that the differential capacitance of the PPy-MWCNT composite, synthesized using DAGB was close to the integral capacitance of this composite material. The frequency dependencies of the capacitance (Fig.12.6B,C) showed relaxation type dispersions, as indicated by the decrease in C_s' with increasing frequency and relaxation maxima, observed in the frequency dependencies of C_s''. The PPy-MWCNT composite, synthesized using DAGB, showed relaxation maximum at higher frequency, compare to PPy-MWCNT composites, prepared using AHDA and pure PPy materials, prepared without MWCNT.

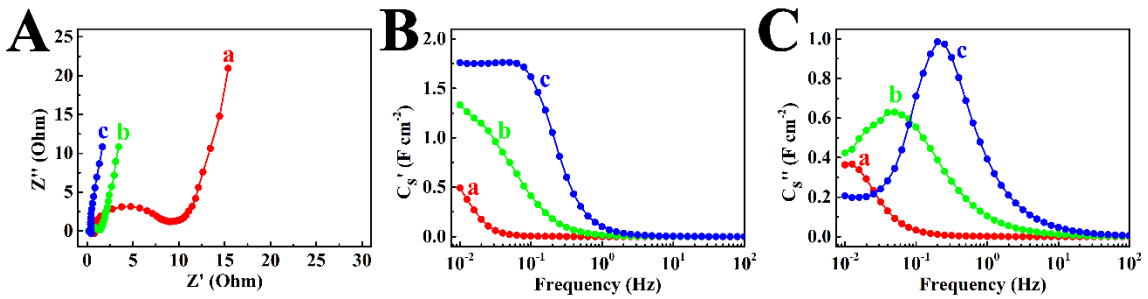

Fig.12.6 (A) Nyquist plot of complex impedance, (B) real part C'_s, and (C) imaginary part C''_s of complex capacitance, derived from the impedance data for (a) PPy, prepared using DAGB, (b) PPy(80%)-MWCNT(20%) composites, prepared using AHDA, (c) PPy(80%)–MWCNT(20%) composites, prepared using DAGB.

12.4 Influence of MWCNT content on capacitive behavior of PPy coated MWCNT composite electrodes

Fig.12.7 shows the influence of MWCNT content on the properties of the PPy-MWCNT composites. The composites with MWCNT content of 20% exhibited larger area of CVs, compared to composites, containing 10 and 30% MWCNT (Fg.12.7A). The larger CV area indicated larger capacitance (Fig.12.7B).

The analysis of the impedance data, presented in the Nyquist plot (Fig.12.7C), showed that the increase in MWCNT content in the composites resulted in reduced resistance Z'=R, which is especially evident from the Fig.12.7D, showing high frequency range of Fig.12.7C. The results indicated that the increase in the concentration of conductive MWCNT resulted in lower resistance of the composite. The analysis of the differential capacitances, calculated from the impedance data indicated that the composite with 20% MWCNT showed higher capacitance at low frequencies, compared to other composites

(Fig.12.7E). The relaxation frequencies were found to be 0.08, 0.2 and 0.5 Hz for composites, containing 10, 20 and 30% MWCNT, respectively (Fig.12.7F). The increase in the relaxation frequency with increasing MWCNT concentration resulted from reduced resistance of the composites.

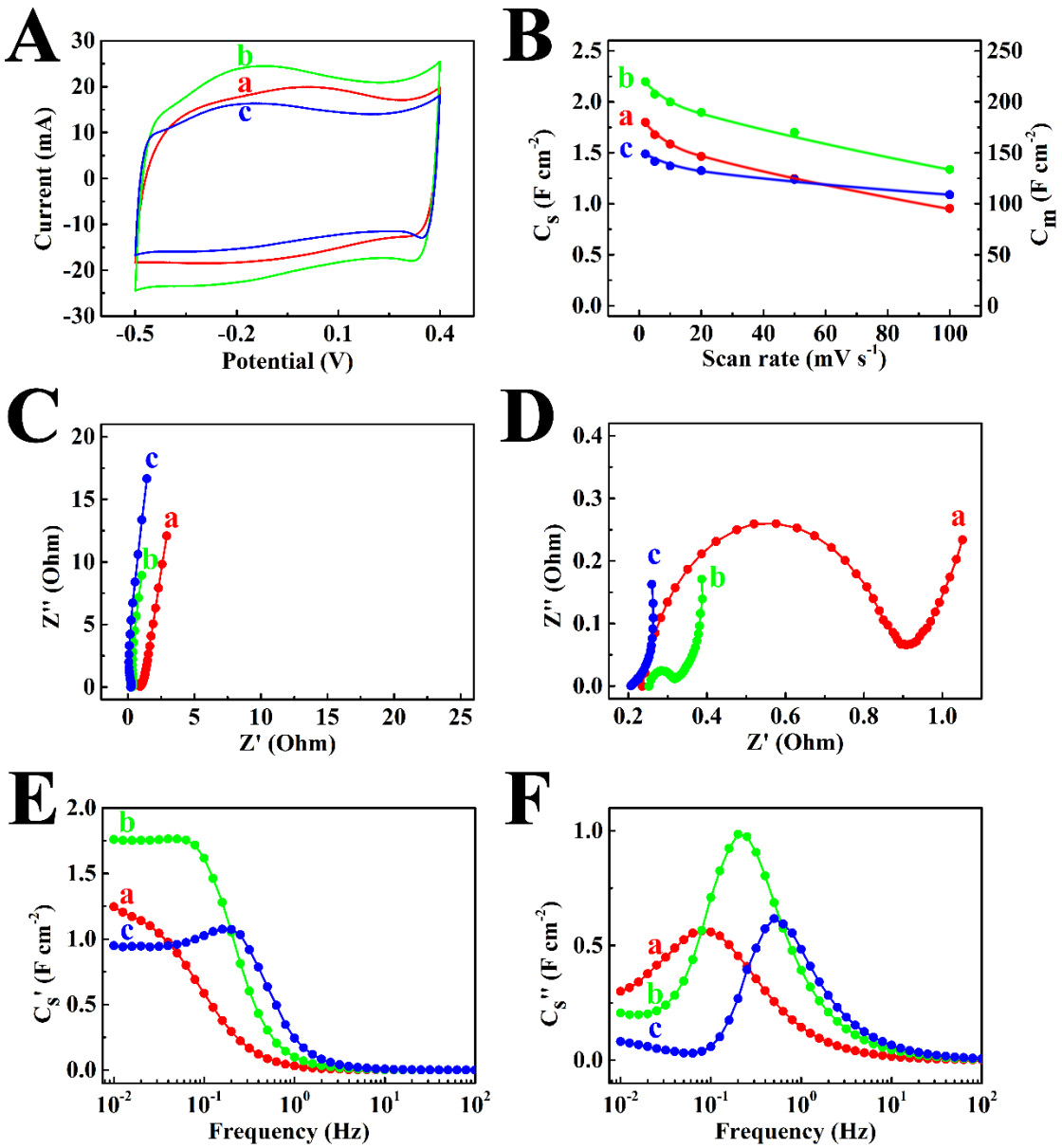

Fig.12.7 (A) CVs at a scan rate of 20 mV s^{-1}, (B) specific capacitance versus scan rate, (C) Nyquist plot of complex impedance, (D) high frequency range of (C), (E) real part C'$_s$, (F)

imaginary part C"$_s$ of complex capacitance for (a) PPy(90%)-MWCNT(10%), (b) PPy(80%)-MWCNT(20%) and (c) PPy(70%)-MWCNT(30%) composites, prepared using DAGB.

The results presented in Fig.12.7 revealed highest integrated and differential capacitances of the PPy(80%)–MWCNT(20%) composites, which were further utilized for the fabrication of ES cells. The PPy(80%)–MWCNT(20%) composites showed capacitance retention of 92.4% after 1000 cycles (Fig.12.8). The shape of the CV remained practically unchanged (Fig.12.8, inset) during cycling. The capacitance reduction can be attributed to changes in microstructure of the active material during cycling[11].

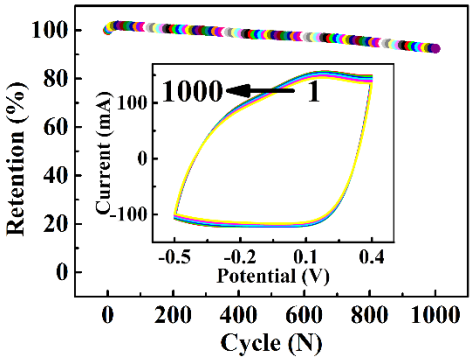

Fig.12.8 Capacitance retention versus cycle number for PPy(80%)-MWCNT(20%) composite, prepared using DAGB, inset shows CVs for different cycle numbers.

12.5 Influence of voltage window to capacitive performance of ES devices

The symmetric cells containing two similar PPy(80%)–MWCNT(20%) composite electrodes showed box shape CVs, indicating good capacitive behavior in a voltage window of 0.9V (Fig.12.9A). In order to increase the voltage window, asymmetric cells

were fabricated and tested. Recent studies showed that VN is a promising material for negative electrodes of aqueous ES[12-14]. In a previous investigation[15] composite VN-MWCNT electrodes with active mass loading of 10-30 mg cm^{-2} showed good capacitive behavior in Na_2SO_4 electrolyte. The capacitance of 160 F g^{-1} was achieved[15]. The asymmetric device, containing PPy(80%)-MWCNT(20%) positive electrode and VN(50%)-MWCNT(50%) negative electrode showed nearly box shape CVs in the voltage window of 1.3V (Fig.12.9B). The asymmetric devices showed larger capacitance, compared to symmetric devices (Fig.12.9C).

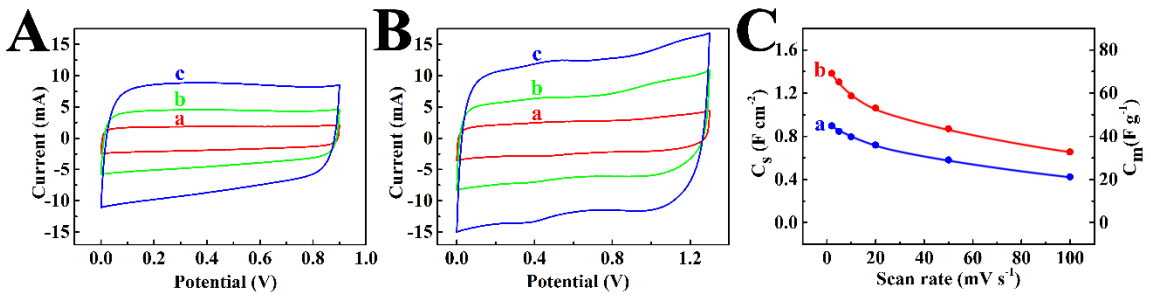

Fig.12.9 (A,B) CVs at scan rates of (a) 5, (b) 10, (c) 20 mV s^{-1}, (C) specific capacitance versus scan rate for (A) and C(a) symmetric PPy(80%)-MWCNT(20%) device, (B) and C(b) asymmetric PPy(80%)-MWCNT(20%) /VN(50%)-MWCNT(50%) device.

Impedance measurements (Fig.12.10A) showed slightly lower resistance R=Z', of the asymmetric device, compared to the symmetric device. The analysis of differential capacitance (Fig.12.10B), derived from the impedance data, showed higher C_s' at low frequencies and higher relaxation frequency, corresponding to the maximum in the frequency dependence of C_s'', of the asymmetric device.

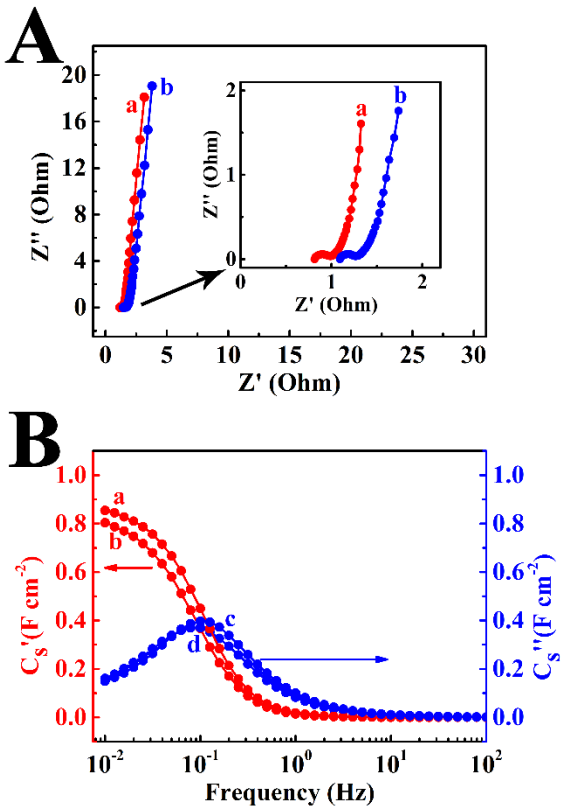

Fig.12.10 (A) Nyquist plot of complex impedance, inset shows a high frequency range, (B) (a,b) real part C'_s and (c,d) imaginary part C''_s of specific capacitance versus frequency for (A) (a) and (B) (a,c) asymmetric PPy(80%)-MWCNT(20%) /VN(50%)-MWCNT(50%) device, (A)(b) and (B) (b,d) symmetric PPy(80%)-WCNT(20%) device.

The galvanostatic charge-discharge curves (Fig.12.11A,B) for symmetric and asymmetric devices were of nearly linear and symmetrical shape. However, some voltage drop (U=IR, where I-current) was observed at the beginning of the discharge for the symmetric device (Fig.12.11A). The asymmetric devices (Fig.12.11B) showed longer discharge times in the larger voltage windows, when compared with symmetric devices (Fig.12.11A) at the same currents. As a result, the corresponding Ragone plot indicated that higher power and energy densities can be achieved using asymmetric devices (Fig.12.11C). The testing

results indicated that asymmetric devices showed improved capacitive properties and power-energy characteristics, compared to symmetric devices. The analysis of cyclic stability of the asymmetric devices (Fig.12.11D (a) and inset) showed a capacitance retention of 83.1% after 1000 cycles. The changes in capacitance can result from changes in microstructure of electrodes or membranes during cycling[11]. The Coulombic efficiency[16] remained at the level of about 99% after 1000 cycles.

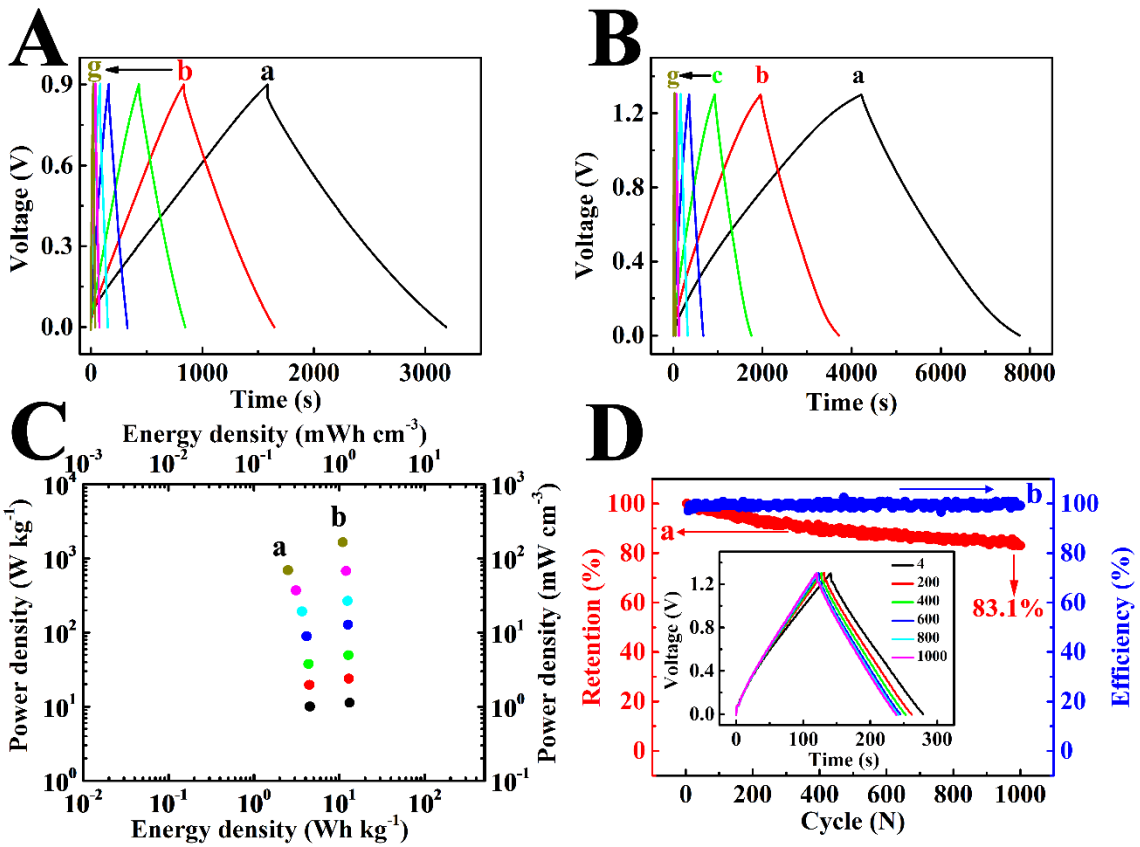

Fig.12.11 (A,B) Galvanostatic charge-discharge at current densities of (a) 0.5, (b) 1, (c) 2, (d) 5, (e) 10, (f) 20, and (g) 50 mA cm^{-2}, (C) Ragone plots for (A) and (C)(a) symmetric PPy(80%)-MWCNT(20%) device, (B) and C(b) asymmetric PPy (80%)-MWCNT(20%) /VN(50%)-MWCNT(50%) device, (D) (a) capacitance retention and (b) Coulombic efficiency versus cycle number for asymmetric PPy(80%)-MWCNT(20%)/VN(50%)-

MWCNT(50%) device, inset shows corresponding charge-discharge curves for different cycles.

The results of this investigation indicated that asymmetric PPy(80%)-MWCNT(20%) /VN(50%)-MWCNT(50%) devices are promising for energy storage applications. Larger voltage windows can be obtained by combining individual cells in series. As a step in this direction, we demonstrate performance of two asymmetric cells, connected in series, which showed box shape CVs (Fig.12.12A) and nearly linear charge-discharge (Fig.12.12B) in a voltage window of 2.6V. The combined coin cells allowed powering of LED bulbs with a current of 20 mA (Fig.12.12C).

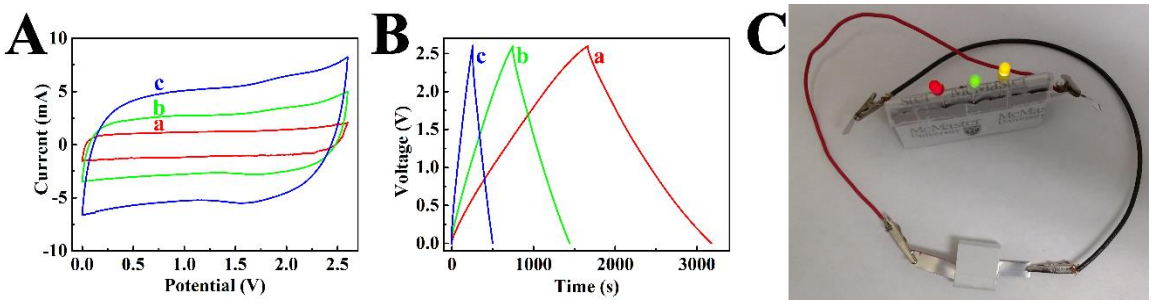

Fig.12.12 (A) CVs at scan rates of (a) 5, (b) 10, (c) 20 mV s^{-1} and (B) charge-discharge behavior at constant currents of (a) 1, (b) 2, and (c) 5 $mAcm^{-2}$ for two PPy (80%)-MWCNT(20%)/VN(50%)-MWCNT(50%) asymmetric devices in series (C) LED bulbs powered by the asymmetric devices.

12.6 Conclusions

PPy and PPy-MWCNT composites were prepared by chemical polymerization for charge storage application in electrodes of ES, using AHDA and DAGB as new anionic dopants. It was found that DAGB improved colloidal stability MWCNT dispersions and allowed

the fabrication of PPy coated MWCNT. The larger size of the DAGB molecules, compared to that of AHDA, was beneficial for electrosteric dispersion of MWCNT and formation of PPy coated MWCNT. The PPy-MWCNT composites showed significant improvement in capacitance, compared to pure PPy electrodes for active mass loading of 10 mg cm^{-2}. The higher capacitance of the composites and improved capacitance retention at high scan rates and high frequencies was attributed to high conductivity of MWCNT, and formation of PPy coated MWCNT. The highest capacitance of 220 F g^{-1} was achieved at a scan rate of 2 mV s^{-1} for PPy coated MWCNT, prepared using DAGB. The capacitance retention at 100 mV s^{-1} was found to be 60.9 %. The PPy coated MWCNT electrodes, prepared using DAGB, were used for the fabrication of symmetric devices, containing two similar PPy-MWCNT electrodes and asymmetric devices containing PPy-MWCNT positive electrode and VN-MWCNT negative electrodes. The asymmetric devices offered advantages of higher capacitance, lower impedance, larger voltage window and improved power-energy characteristics.

References

[1] Jain R, Sharma N, Radhapyari K. Electrochemical treatment of pharmaceutical azo dye amaranth from waste water. Journal of Applied Electrochemistry 2009;39:577-82.

[2] Dossi N, Piccin E, Bontempelli G, Carrilho E, Wang J. Rapid analysis of azo-dyes in food by microchip electrophoresis with electrochemical detection. Electrophoresis. 2007;28:4240-6.

[3] Su Y, Zhitomirsky I. Electrophoretic nanotechnology of composite electrodes for electrochemical supercapacitors. The Journal of Physical Chemistry B. 2012;117:1563-70.

[4] Su Y, Zhitomirsky I. Electrophoretic deposition of graphene, carbon nanotubes and composite films using methyl violet dye as a dispersing agent. Colloids and Surfaces A: Physicochemical and Engineering Aspects. 2013;436:97-103.

[5] Li X, Zhitomirsky I. Electrodeposition of polypyrrole-carbon nanotube composites for electrochemical supercapacitors. Journal of Power Sources 2013;221:49-56.

[6] Lin D, Xing B. Adsorption of phenolic compounds by carbon nanotubes: Role of aromaticity and substitution of hydroxyl groups. Environmental Science & Technology. 2008;42:7254-9.

[7] Gupta VK, Kumar R, Nayak A, Saleh TA, Barakat MA. Adsorptive removal of dyes from aqueous solution onto carbon nanotubes: A review. Advances in Colloid and Interface Science. 2013;193-194:24-34.

[8] Snook GA, Kao P, Best AS. Conducting-polymer-based supercapacitor devices and electrodes. Journal of Power Sources 2011;196:1-12.

[9] Wang J-G, Wei B, Kang F. Facile synthesis of hierarchical conducting polypyrrole nanostructures via a reactive template of MnO_2 and their application in supercapacitors. RSC Advances. 2014;4:199-202.

[10] Wu Q-F, He K-X, Mi H-Y, Zhang X-G. Electrochemical capacitance of polypyrrole nanowire prepared by using cetyltrimethylammonium bromide (CTAB) as soft template. Materials Chemistry and Physics 2007;101:367-71.

[11] Shi K, Zhitomirsky I. Influence of current collector on capacitive behavior and cycling stability of Tiron doped polypyrrole electrodes. Journal of Power Sources 2013;240:42-9.

[12] Choi D, Blomgren GE, Kumta PN. Fast and reversible surface redox reaction in nanocrystalline vanadium nitride supercapacitors. Advanced Materials 2006;18:1178-82.

[13] Porto RL, Frappier R, Ducros J, Aucher C, Mosqueda H, Chenu S, et al. Titanium and vanadium oxynitride powders as pseudo-capacitive materials for electrochemical capacitors. Electrochimica Acta 2012;82:257-62.

[14] Pande P, Rasmussen PG, Thompson LT. Charge storage on nanostructured early transition metal nitrides and carbides. Journal of Power Sources. 2012;207:212-5.

[15] Su Y, Zhitomirsky I. Hybrid MnO_2/carbon nanotube-VN/carbon nanotube supercapacitors. Journal of Power Sources 2014;267:235-42.

[16] Mallika S, Kumar RS. Review on ultracapacitor-battery interface for energy management system. System. 2011;1:2.